

Cell Reports

Best of 2014



Year 3 in Review

Patient
- derived
samples



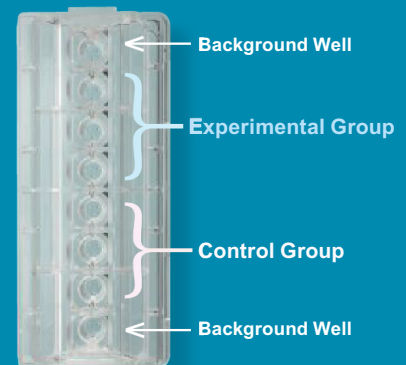
Functional
metabolic data
on live cells
in real time!

Phenotyping

Pairwise
comparisons

XFp Extracellular Flux Analyzer

The new, compact XFp Analyzer is built on innovative and proven XF Technology, and is ideal for use in pairwise comparisons, phenotyping and with patient-derived samples. The XFp Analyzer delivers the Gold Standard assays that are providing scientists with the necessary functional data that is enabling a greater understanding of cell metabolism.



See what's possible.

Scan this QR code to view videos and see what XF Technology Analyzer can achieve. Visit www.seahorsebio.com/XFp for more information!

Seahorse *Bioscience*

Visit Us at the 2014 ASCB/IFCB Meeting, Booth 505



Create Your Masterpiece

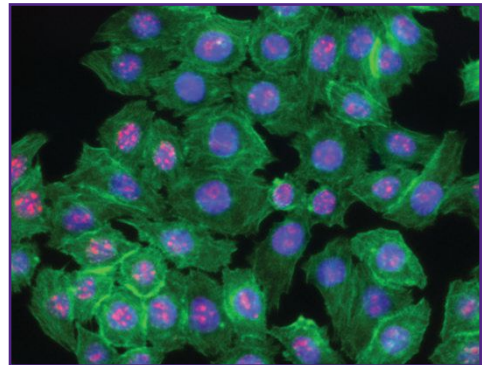
Direct Antibody Conjugates for Multicolor Microscopy

For multicolor fluorescence microscopy, bright fluorescence with little background is critical for specific detection of antigens. Furthermore, directly labeled antibodies are essential for multicolor microscopy. BioLegend now introduces our line of antibodies directly conjugated to **Alexa Fluor® 594**, a bright, stable fluorophore emitting into the red range of the color spectrum, ideal for imaging applications. **Brilliant Violet 421™** is an exceptionally bright and photostable fluorescent polymer well-suited for microscopy applications. BioLegend has over 100 IHC or IF suitable clones conjugated to Brilliant Violet™, Alexa Fluor®, and DyLight®, including secondary antibodies and streptavidin.

Learn more: biolegend.com/AF594
biolegend.com/brilliantviolet



Alexa Fluor® 594 anti-Ki-67



HeLa cells were fixed, permeabilized, and blocked, then intracellularly stained with Ki-67 (clone Ki-67) Alexa Fluor® 594 (red) and Alexa Fluor® 488 Phalloidin (green). Nuclei were counterstained with DAPI (blue). The image was captured with 40x objective.

Alexa Fluor® is a trademark of Life Technologies Corporation.
Brilliant Violet 421™ is a trademark of Sirigen Group Ltd.
DyLight® is a trademark of Thermo Fisher Scientific Inc. and its subsidiaries.

BioLegend is ISO 9001:2008 and ISO 13485:2003 Certified

Toll-Free Tel: (US & Canada): 1.877.BIOLEGEND (246.5343)
Tel: 1.858.768.5800
biolegend.com

08-0040-07

World-Class Quality | Superior Customer Support | Outstanding Value

Introducing

bio-technne®

HIGHEST QUALITY PRODUCT PORTFOLIO



TRUSTED GLOBAL BRANDS

R&D systems

NOVUS
BIOLOGICALS

TOCRIS

bio-technne

LEARN MORE

bio-technne.com/launch



Building
Innovation
Opportunities

bio-technne.com
info@bio-technne.com
techsupport@bio-technne.com

North America
TEL 800 343 7475

Europe • Middle East • Africa
TEL +44 (0)1235 529449

China
info.cn@bio-technne.com
TEL +86 (21) 52380373

Rest of World
bio-technne.com/find-us/distributors
TEL +1 612 379 2956

Bio-Technne is a trading name for R&D Systems

Foreword



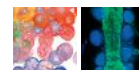
Welcome to the 2014 edition of *Best of Cell Reports*. It was a major year for *Cell Reports* in many respects, and it was truly interesting and enjoyable to look back over the papers that we published this year. It was almost impossible to select the papers that you'll find here because there were so many strong papers that truly advanced their fields across the very broad scope of the journal. The lineup in this supplement was chosen to represent various fields covered by *Cell Reports* and is based on a number of metrics, including Almetrics scores, citations, and reader downloads.

We are really looking forward to 2015, when there will be some major changes at *Cell Reports*. Starting in January, a fresh new issue of *Cell Reports* will arrive in your inbox every week—yes, we are going weekly! One of the consistent pieces of positive feedback we receive is that our speed of publication is much appreciated. To further facilitate this, in the coming months, we will move to two online publication dates each week. In addition, we plan to expand our social media and blogging efforts on the *Cell Reporter* and have lots of fresh ideas that we look forward to sharing with you. We are also planning some exciting meetings and events, so hold the following dates. In 2015, *Cell Reports* will be involved in organizing meetings on both sides of the Atlantic as well as across the Pacific. March 18th sees the Ubiquitous Ubiquitin Signaling Lablinks in Cambridge, UK, while July 14th sees the RNA in the Nervous System meeting in New York. In November 2015, we will cohost a major symposium in Singapore on Human Genomics. We hope to see you there!

We greatly value the support of the many researchers who are the authors, reviewers, readers, and editorial and advisory board members that make *Cell Reports* possible. We thank you all for your help in 2014, and we look forward to working with you, meeting you, and talking to you about your exciting research in 2015.

Finally, we are grateful for the generosity of our sponsors, who helped to make this reprint collection possible.

Cell Reports



For information for the Best of Series, please contact:
Jonathan Christison
Program Director, Best of Cell Press
e: jchristison@cell.com
p: 617-397-2893
t: @cellPressBiz

Does your
IHC antibody
measure up?

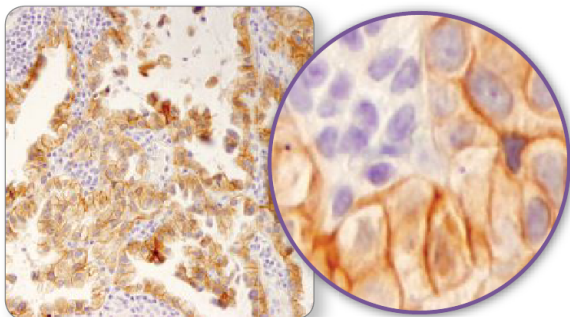
Rigorously Validated IHC Antibodies Against High Impact Research Targets

from Cell Signaling Technology

Paraffin-embedded human lung and ovarian carcinoma tissues using CST™ HER3/ErbB3 (D22C5) XP® Rabbit mAb #12708 or Company 2 mouse monoclonal antibody.

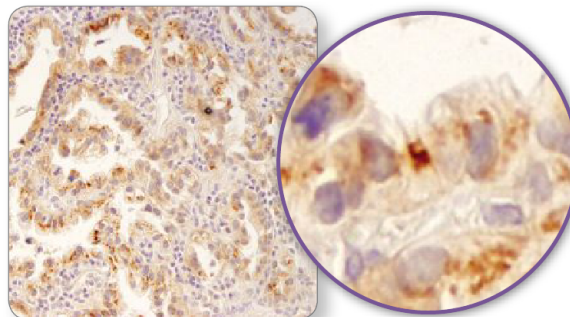
CST HER3/ErbB3 (D22C5) XP® Rabbit mAb #12708

Lung Carcinoma



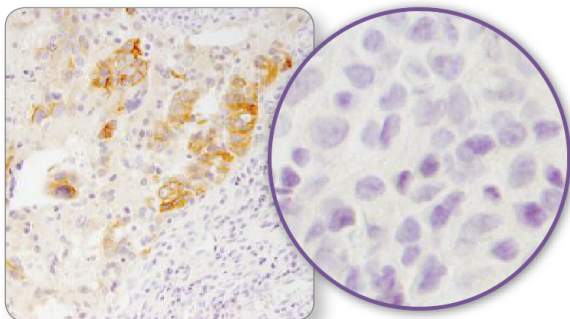
Strong, specific plasma membrane-associated
HER3 staining in the epithelium

Company 2 Mouse Monoclonal Antibody

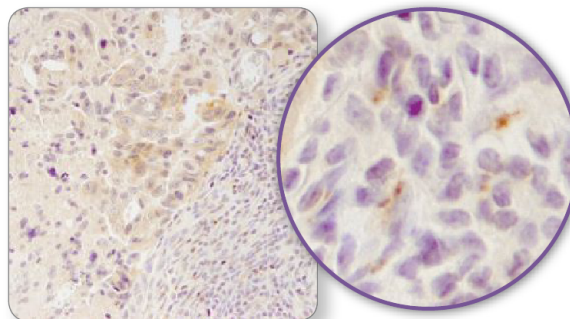


Non-specific, non-membranous
staining in the epithelium

Ovarian Carcinoma



Strong, specific signal in tumor cells,
and no staining seen in stromal cells



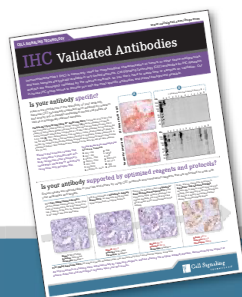
Weak signal in tumor cells, and
non-specific staining in stromal cells

14PAD1HC_NON00160ENG_00

WB IP IHC IF F CHIP

For Research Use Only. Not For Use In Diagnostic Procedures.

© 2014 Cell Signaling Technology, Inc. Cell Signaling Technology®, CST™, and XP® are trademarks of Cell Signaling Technology, Inc.



Skeptical? Go to www.cellsignal.com/ihcell to see more



Cell Signaling
TECHNOLOGY®

Cell Reports

Best of 2014

Perspective

Ruled by Ubiquitylation: A New Order for Polycomb Recruitment

Yuri B. Schwartz and Vincenzo Pirrotta

Reports

The Fungal Aroma Gene *ATF1* Promotes Dispersal of Yeast Cells through Insect Vectors

Joaquin F. Christiaens, Luis M. Franco, Tanne L. Cools, Luc De Meester, Jan Michiels, Tom Wenseleers, Bassem A. Hassan, Emre Yaksi, and Kevin J. Verstrepen

The Cytosolic DNA Sensor cGAS Forms an Oligomeric Complex with DNA and Undergoes Switch-like Conformational Changes in the Activation Loop

Xu Zhang, Jiayi Wu, Fenghe Du, Hui Xu, Lijun Sun, Zhe Chen, Chad A. Brautigam, Xuewu Zhang, and Zhijian J. Chen

Simple and Rapid In Vivo Generation of Chromosomal Rearrangements using CRISPR/Cas9 Technology

Rafael B. Blasco, Elif Karaca, Chiara Ambrogio, Taek-Chin Cheong, Emre Karayol, Valerio G. Minero, Claudia Voena, and Roberto Chiarle

Long-Term Health of Dopaminergic Neuron Transplants in Parkinson's Disease Patients

Penelope J. Hallett, Oliver Cooper, Damaso Sadi, Harold Robertson, Ivar Mendez, and Ole Isacson

The Role of the Endocrine System in Feeding-Induced Tissue-Specific Circadian Entrainment

Miho Sato, Mariko Murakami, Koichi Node, Ritsuko Matsumura, and Makoto Akashi

Articles

Inference of Tumor Evolution during Chemotherapy by Computational Modeling and In Situ Analysis of Genetic and Phenotypic Cellular Diversity

Vanessa Almendro, Yu-Kang Cheng, Amanda Randles, Shalev Itzkovitz, Andriy Marusyk, Elisabet Ametller, Xavier Gonzalez-Farre, Montse Muñoz, Hege G. Russnes, Åslaug Helland, Inga H. Rye, Anne-Lise Borresen-Dale, Reo Maruyama, Alexander van Oudenaarden, Mitchell Dowsett, Robin L. Jones, Jorge Reis-Filho, Pere Gascon, Mithat Gönen, Franziska Michor, and Kornelia Polyak

Gli Protein Activity Is Controlled by Multisite Phosphorylation in Vertebrate Hedgehog Signaling

Pawel Niewiadomski, Jennifer H. Kong, Robert Ahrends, Yan Ma, Eric W. Humke, Sohini Khan, Mary N. Teruel, Bennett G. Novitch, and Rajat Rohatgi

Fate of iPSCs Derived from Azoospermic and Fertile Men following Xenotransplantation to Murine Seminiferous Tubules

Cyril Ramathal, Jens Durruthy-Durruthy, Meena Sukhwani, Joy E. Arakaki, Paul J. Turek, Kyle E. Orwig, and Renee A. Reijo Pera

(continued)

Pain without Nociceptors? Nav1.7-Independent Pain Mechanisms

Michael S. Minett, Sarah Falk, Sonia Santana-Varela, Yury D. Bogdanov, Mohammed A. Nassar, Anne-Marie Heegaard, and John N. Wood

Ribosome Profiling Reveals Pervasive Translation Outside of Annotated Protein-Coding Genes

Nicholas T. Ingolia, Gloria A. Brar, Noam Stern-Ginossar, Michael S. Harris, Gaëlle J.S. Talhouarne, Sarah E. Jackson, Mark R. Wills, and Jonathan S. Weissman

Resource

Conservation of mRNA and Protein Expression during Development of *C. elegans*

Dominic Grün, Marieluse Kirchner, Nadine Thierfelder, Marlon Stoeckius, Matthias Selbach, and Nikolaus Rajewsky

A smarter approach to FLUORESCENCE IMAGING



Introducing the ZOE™ Fluorescent Cell Imager.
No darkroom, no training, no overwhelming user interface.

Combining brightfield capabilities with multichannel fluorescence, this cell imager is both affordable and easy to use — your perfect solution for routine cell culture and imaging applications.

Learn more at [bio-rad.com/info/newzoe](https://www.bio-rad.com/info/newzoe)

BIO-RAD

Dharmacon™
part of GE Healthcare



With Dharmacon, you can confidently silence, express and edit your genes.

In every experiment, you invest time, money and effort. Still, success is not a certainty – that's the nature of science. Fortunately, you can decrease the uncertainty with Dharmacon RNAi, gene expression and gene editing products. As scientists too, we know what you're feeling – and what you're facing – and can help you confidently achieve the best possible results.

Explore our advanced gene editing tools.

We make human cells.

We can't state it more simply: We manufacture human cells from induced pluripotent stem cells. Our highly pure iCell® and MyCell® products are consistent and reproducible from lot-to-lot, enabling you to focus on the biology . . . and what drives your research.

True Human Biology. Why use an animal or immortalized cell model as a proxy when a true human model, consistent across lots, is available? If you have a phenotype of interest, we can make iPSCs and terminal cells from your donors.

Highly Characterized. Highly Predictive.

Our cells have the appropriate gene and protein expression and the relevant physiological response of the target cell type, with numerous peer-reviewed publications detailing their characterization and predictivity of human response.

MORE Cells. CDI provides more cells than other providers: 96-well capacity per vial. GUARANTEED.

**Any cell type.
Any genotype.
Any quantity.**



**CELLular
Dynamics
international**

You make:

safer medicines
discoveries
therapies
breakthroughs
tenure
your peers envious with a tier 1 publication



Check out the iCell community of scientists who discuss the difference iCell products have made in their research:

www.cellulardynamics.com/community

Molecules That Count®

Gene Expression • miRNA Expression • Epigenomics • Copy Number Variation • Single Cell

www.nanostring.com

Multiplex REDEFINED

The nCounter® Analysis System offers digital detection of target molecules and high levels of multiplexing with no compromise between data quality and data quantity. Data output files include the target identifier and count number along with a comprehensive set of internal controls that enable each assay to be highly quantitative and reproducible.

- Multiplex up to 800 targets in a single tube
- Directly assay tissue, cell & blood lysates, FFPE
- No amplification*, no RT, no sample partitioning
- Fully automated with 15-min hands-on time
- Simple workflow – up to 800 targets in a single tube

www.nanostring.com/technology



nCounter® Analysis System

Direct Digital Quantification of Nucleic Acids



nanoString
TECHNOLOGIES®

www.nanostring.com | info@nanostring.com | 888 358 6266

© 2014 NanoString® Technologies, Inc. All rights reserved.
FOR RESEARCH USE ONLY. Not for use in diagnostic procedures.

*Single Cell assay requires reverse transcription and amplification prior to analysis on the nCounter System.

NEW

Sensor-based shRNA Pooled Screening Libraries

*Achieve greater confidence
in screen hits*

PLATINUM *Select* shRNA-mir screening libraries combine superior knockdown efficiency from sensor-based shERWOOD algorithm designs with a stringent equimolar pooling process for more consistent and sensitive hit detection from your pooled screen. Lentiviral pooled shRNA libraries are available targeting the whole genome, epigenome, kinome, cancer metabolism and more.

- **Powerful and consistent knockdown** - drives phenotypic change even at single copy
- **Increased confidence in screen hits** - more potent shRNA per gene for clearer hit identification
- **Flexible format options** - high titer lentiviral particles or plasmid DNA pool formats
- **Custom Pool Development** - Select gene list and vector options

NEW

Pooled Screening Deconvolution Service - Includes library preparation, sequencing and data analysis from your genomic DNA samples.

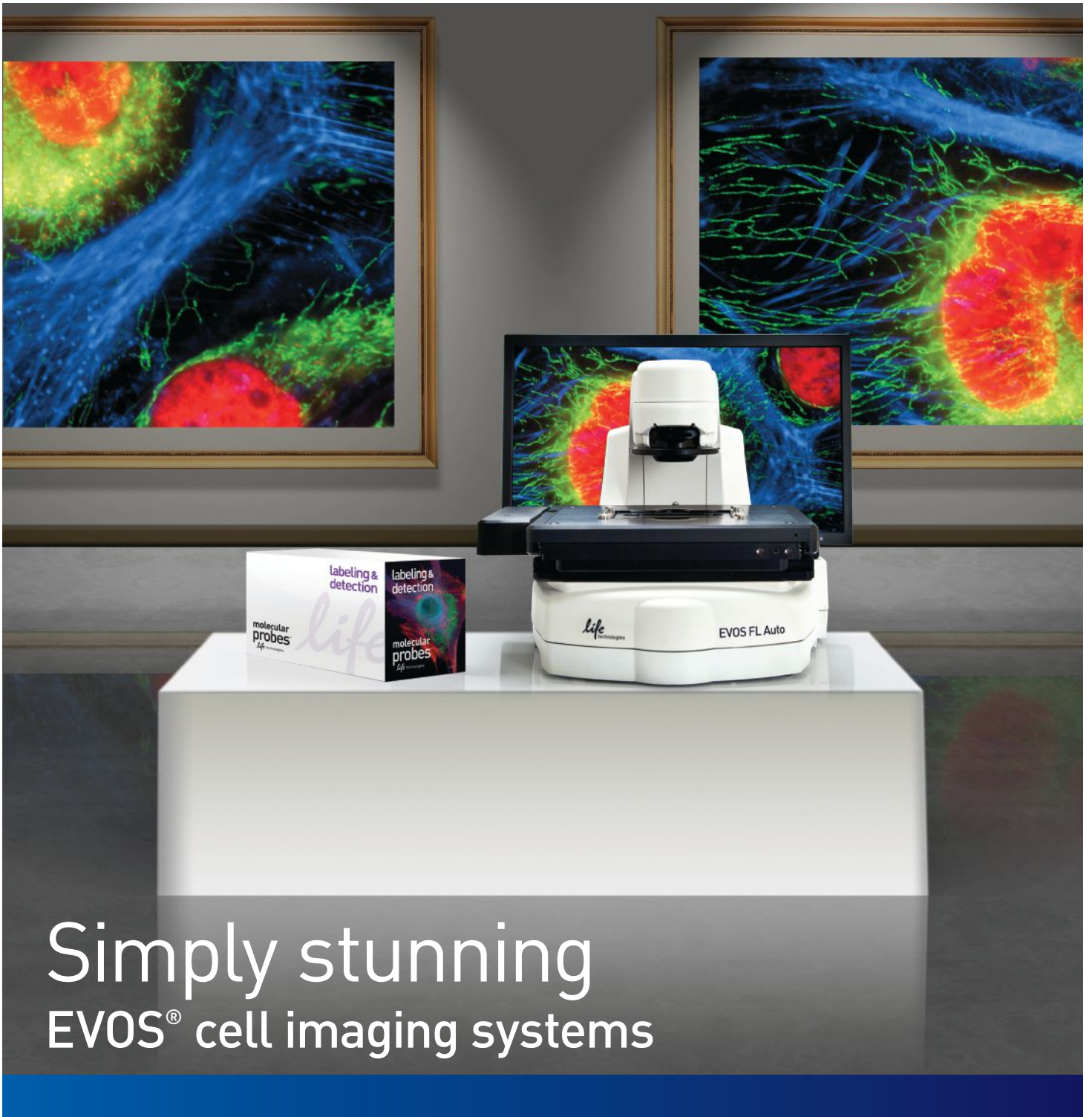
Visit www.transomic.com/pooledscreening/neuron for more details and to place your order.

Find shRNA, cDNA and ORFs for
your gene of interest using

 **FETCH my gene**

www.transomic.com

 **transOMIC**
technologies



Simply stunning EVOS® cell imaging systems

Minimize the complexities of microscopy without compromising performance
Smarter systems | Easier cell imaging | Faster results

Compare systems at lifetechnologies.com/simplystunning



For Research Use Only. Not for use in diagnostic procedures. © 2014 Thermo Fisher Scientific Inc. All rights reserved.
All trademarks are the property of Thermo Fisher Scientific and its subsidiaries unless otherwise specified. C0012666 1114

A Thermo Fisher Scientific Brand

Ruled by Ubiquitylation: A New Order for Polycomb Recruitment

Yuri B. Schwartz^{1,*} and Vincenzo Pirrotta^{2,*}

¹Department of Molecular Biology, Umeå University, Byggnad 6L, NUS, 901 87 Umeå, Sweden

²Department of Molecular Biology and Biochemistry, Rutgers University, 604 Allison Road, Piscataway, NJ 08854, USA

*Correspondence: yuri.schwartz@molbiol.umu.se (Y.B.S.), pirrotta@dls.rutgers.edu (V.P.)

<http://dx.doi.org/10.1016/j.celrep.2014.07.001>

This is an open access article under the CC BY-NC-ND license (<http://creativecommons.org/licenses/by-nc-nd/3.0/>).

Polycomb complexes are found in most cells, but they must be targeted to specific genes in specific cell types in order to regulate pluripotency and differentiation. The recruitment of Polycomb complexes to specific targets has been widely thought to occur in two steps: first, one complex, PRC2, produces histone H3 lysine 27 (H3K27) trimethylation at a specific gene, and then the PRC1 complex is recruited by its ability to bind to H3K27me3. Now, three new articles turn this model upside-down by showing that binding of a variant PRC1 complex and subsequent H2A ubiquitylation of surrounding chromatin is sufficient to trigger the recruitment of PRC2 and H3K27 trimethylation. These studies also show that ubiquitylated H2A is directly sensed by PRC2 and that ablation of PRC1-mediated H2A ubiquitylation impairs genome-wide PRC2 binding and disrupts mouse development.

Biological problems often reach a cusp at which several laboratories with different approaches converge to provide unexpected solutions to longstanding questions. In the present case, the problem is how a major epigenetic mechanism, Polycomb silencing, is targeted to specific genes in the appropriate cells at the appropriate moment in lineage differentiation. Three new papers combine to upend widely held assumptions and open new ways of thinking about the way in which Polycomb complexes regulate genes in development and disease (Blackledge et al., 2014; Cooper et al., 2014; Kalb et al., 2014).

Polycomb group (PcG) proteins constitute a major epigenetic mechanism for controlling gene expression during the development of higher eukaryotes. To a large degree, this is done through repression of the key developmental genes, and the question of how PcG complexes are specifically recruited to these genes has been a major research problem. The recruitment mechanism is likely to be subtle, given that PcG components are present in the nuclei of most cells, but whether or not they are targeted to a given locus depends on its chromatin state. In general, transcriptionally active genes are not targeted, but genes that are not strongly transcribed are susceptible to PcG repression. Conversely, high levels of activators can override PcG silencing of a given gene, resulting in derepression. Some intermediate states are also possible, of which the bivalent domains found in pluripotent stem cells are the best known example. Once established, the repressed state of a gene tends to be transmitted through mitosis to progeny cells.

Polycomb Complexes

PcG proteins act as large multisubunit complexes of the two principal classes: PRC1 and PRC2. Each class comprises

several alternative variants (Figure 1). PRC1 complexes form around RING2 (or the closely related RING1) subunit to which one of the six alternative PcG RING finger (PCGF) proteins binds. The RING-PCGF heterodimers constitute a minimal core that can transfer a single ubiquitin group to lysine 119 of histone H2A (H2AK119). The identity of the PCGF subunits determines additional components and therefore some of the specific biochemical properties of the variant complexes (for a comprehensive discussion of the subject, see Schwartz and Pirrotta, 2013). In brief, the heterodimers between RING2/RING1 and MEL18 (also known as PCGF2) or BMI1 (also known as PCGF4) are incorporated in the so-called canonical PRC1 variants (also known as PRC1.2 and PRC1.4). The canonical variants have characteristic polyhomeotic (PHC) and chromobox-containing protein (CBX) subunits and can specifically recognize histone H3 trimethylated at lysine 27 (H3K27me3) via the chromodomain of the CBX subunit. All RING-PCGF heterodimers can also form noncanonical PRC1 complexes. These contain RING and YY1 binding protein (RYBP) instead of CBX and PHC. Noncanonical PRC1 complexes cannot recognize the H3K27me3 but have much higher H2A ubiquitylating activity because of the specific interaction of RYBP with H2AK119 (see below). The variant noncanonical complexes differ substantially in additional subunits (Schwartz and Pirrotta, 2013). Important for this discussion, the PCGF1-containing complexes (also known as PRC1.1) incorporate the KDM2B protein, a histone H3K36 demethylase whose CXXC domain confers the ability to bind unmethylated CpG-rich DNA (Farcas et al., 2012). The H3K36 demethylase activity, which removes what is considered to be a repressive histone mark, is apparently not necessary for Polycomb mechanisms (He et al., 2013).

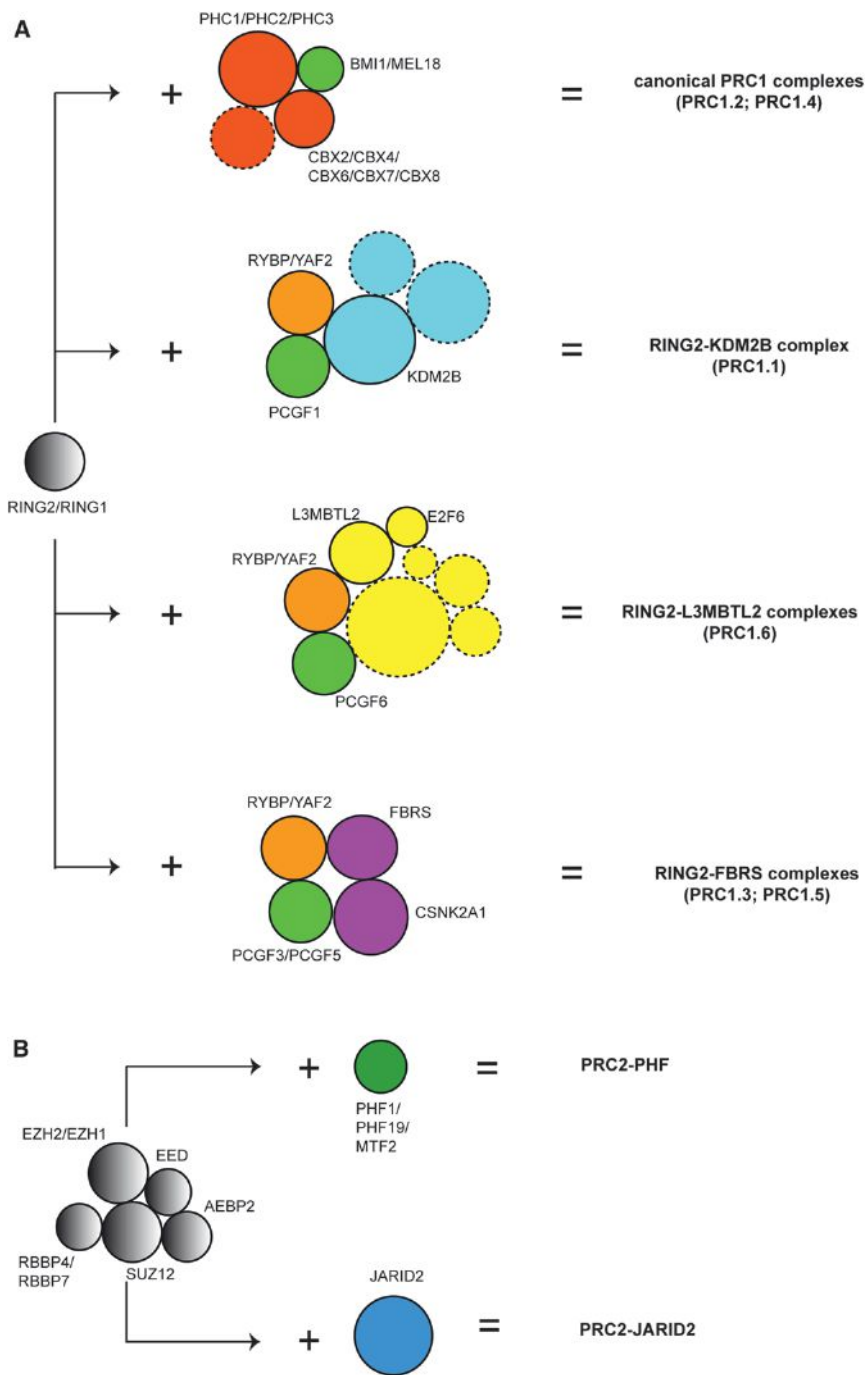


Figure 1. Varieties of PRC1 and PRC2 Complexes

(A) PRC1 complexes are built around the RING2 (or RING1) component. RING forms a heterodimer with one of six different PCGF proteins (green circles). Canonical PRC1 contains BMI1/PCGF2 or MEL18/PCGF4 as well as one of five CBX components. A variant PRC1 contains PCGF1 and KDM2B and the proteins RYBP or YAF2 (orange circles) instead of a CBX component. Variant PRC1 complexes containing RYBP or YAF2 are active H2AK119 ubiquityl transferases, whereas canonical PRC1 complexes have little activity.

(B) PRC2 complexes contain a core with the H3K27 methyltransferase activity stabilized by AEBP2. Associated factors such as JARID2 (blue circle) or PHF (green circle) modulate activity and binding specificities.

The Problem of Recruitment

How the recruitment of PRC1 and PRC2 complexes is targeted and coordinated is not clear, given that none of the PRC1 or PRC2 subunits can bind DNA in a sequence-specific fashion. The conspicuous ability of canonical PRC1 complexes to recognize H3K27me3 led to the widely held idea that PRC2 is somehow recruited first and then trimethylates H3K27, and this, in turn, recruits PRC1. Although initially appealing, this hypothesis is at odds with observations that, in *Drosophila melanogaster*, the H3K27me3 produced by PRC2, forms a broad domain, whereas the binding of PRC1 is sharply localized at Polycomb response elements (PREs) and that, in mouse cells, not all H3K27me3 domains correspond to PRC1 binding sites. In any case, the binding of noncanonical PRC1 complexes would not be dependent on H3K27 methylation.

As mentioned above, in *Drosophila*, both PRC1 and PRC2 are recruited to specific target genes by PREs, ~1 kb DNA elements containing recognition sequences for DNA binding proteins. These DNA binding proteins are believed to combine their individually weak interactions with PcG proteins in order to yield

The known diversity of PRC2 complexes is less broad. All PRC2 variants contain a core of five proteins: EZH2 (or the closely related EZH1), EED, SUZ12, RBBP4 (or closely related RBBP7), and AEBP2. This core complex acts as a histone methyltransferase specific for H3K27. In addition to the core, PRC2 complexes incorporate either JARID2 or PHD finger protein (PHF) subunits. In mammals, insects, and worms, PRC2 complexes are the sole source of H3K27me2 and H3K27me3, and the latter is essential for PcG repression.

robust recruitment. The combinatorial nature of the PRE-mediated recruitment and the paradoxical ability of PREs to also recruit trithorax group proteins that help to counteract PcG repression provide the necessary plasticity to the *Drosophila* PcG-repressive system.

So far, the search for mammalian PRE-like elements has had limited success. Notable examples are a 1.5 kb DNA region from the mouse *MafB/Kreisler* locus that can recruit PRC1, but not PRC2 (Sing et al., 2009), and a 1.8 kb DNA element within

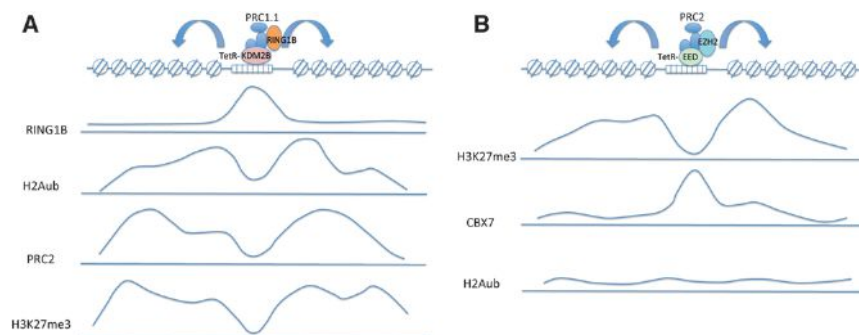


Figure 2. The Recruitment Hierarchy

(A) The top diagram represents the reporter constructs and results of Blackledge et al. (2014). At the center, an array of TetO sequences binds TetR fused to KDM2B and thus recruits the associated variant PRC1 complex with its RING2 component. The lower diagrams from top to bottom illustrate chromatin immunoprecipitation experiments with antibodies against RING2, H2AK119ub, PRC2, and H3K27me3. The complex containing RING2 is found only over the recruiting TetO array. The H2AK119ub is found over the neighboring nucleosomes, and the PRC2 complex coincides with it. The H3K27me3 produced spreads even further away from the TetO array.

(B) In this experiment, PRC2 is directly recruited to the TetO array by fusing TetR to the EED component. The PRC2 bound at the TetO produces H3K27me3 on flanking nucleosomes. Surprisingly, canonical PRC1 containing CBX7 is recruited not over the methylated region but over the TetO array, where PRC2 is bound. Canonical PRC1 has poor ubiquityl transferase activity, and little H2AK119ub is produced.

the human *HOXD* cluster that can recruit both PRC1 and PRC2 (Woo et al., 2010). In addition, several mouse promoter fragments containing binding sites for the RE1-silencing transcription factor or SNAIL proteins were reported to autonomously “recruit” PRC2 and possibly PRC1 (Arnold et al., 2013; Dietrich et al., 2012). The promoters of most PcG-regulated genes in mammals contain clusters of CpG dinucleotides, the CpG islands. Analysis in embryonic stem cells (ESCs) showed that, when CpG islands lack DNA methylation and are not associated with transcriptional activity, they bind PRC2 and contain H3K27me3 (Lynch et al., 2012; Mendenhall et al., 2010; Riising et al., 2014). The discovery of noncanonical PRC1 complexes containing KDM2B paved the way for understanding how such complexes might be recruited to CpG islands by the CXXC domain of KDM2B (Lagarou et al., 2008; Farcas et al., 2012; He et al., 2013; Wu et al., 2013). But how do we account for PRC2 recruitment?

A Link between PRC1 and PRC2

Two recent papers have studied how the full-fledged panoply of PcG complexes might be recruited to target genes or genomic regions. One paper (Blackledge et al., 2014) uses a specially constructed reporter region of 170 kb containing at its center a short array of Tet operator (TetO) binding sites for the bacterial TetR protein within a larger region devoid of other genes, enhancers, CpG islands, or elements that might recruit DNA methylation. Candidate components of PcG complexes can be targeted to the TetO array by fusion to the TetR DNA binding domain. The second paper (Cooper et al., 2014) exploits the fact that, in the absence of DNA methylation, CpG-containing regions in pericentric heterochromatin become targets for PcG complexes. In wild-type cells, these regions are DNA methylated, and proteins can be targeted to them by fusion with a 5mC binding methyl binding protein (MBP) domain, thus making the additional point that DNA methylation does not intrinsically prevent PRC2 complex binding or H3K27 methylation. Both approaches show that targeting the KDM2B protein recapitulates the recruitment of PRC2, H3K27me3, and CBX-containing PRC1 complexes. Therefore, the CpG binding KDM2B protein and its associated variant PRC1 complex can ultimately recruit both the PRC2 H3K27 methyltransferase complex and

the canonical CBX-containing PRC1. The key to this recruitment cascade is the RING1/RING2 protein, which forms the core of all PRC1-like complexes, and its ability to ubiquitylate histone H2A. Tethering a protein fragment that reconstructs the H2A ubiquitylating activity is sufficient to mimic the whole recruitment process. As a result of the RING1/RING2 activity, nucleosomes flanking the binding site become ubiquitylated. H2AK119ub now recruits PRC2, which in turn sets about trimethylating H3K27, which recruits canonical PRC1 complexes that include a chromodomain-containing CBX component.

This recruitment cascade implies that CpG islands must first bind variant PRC1 complexes that are ubiquitylation-competent in order to recruit PRC2, which recruits canonical PRC1 complexes, themselves poor ubiquityl transferases, but good at recognizing the H3K27me3 mark. Therefore, the initial step inverts the widely held notion that PRC2 is the initiator of the recruitment process, both clarifying and complicating the account as well as raising a number of interesting new questions.

That PRC2 really recognizes H2Aub, and not the ubiquitylation of some other chromatin protein such as Ring1/Ring2 itself, is shown by the distribution of PRC2 recruited at the reporter target site (Figure 2A). The recruiting variant PRC1 in this experiment binds to the TetO array, but the PRC2 is not found associated to the array but to the flanking regions that contain the H2Aub. Therefore, PRC2 is recruited to a broader region than that which bound the original variant PRC1 complex. PRC2 would then methylate H3K27 over an even broader region. The canonical PRC1 complex is then said to be recruited by virtue of its CBX component binding to H3K27me3. However, strangely, when PRC2 is targeted to the TetO array (by fusing TetR to the EED component of PRC2), the distribution of CBX7 over the recruiting region does not fit the expectation that it would coincide with the H3K27me3 mark. Instead, it appears to be centered squarely over the TetO array, which is depleted of nucleosomes and of H3K27me3. As the authors remark, this resembles the situation seen in *Drosophila* where the binding of the canonical PRC1 complex coincides with that of PRC2 at the PRE rather than the distribution of H3K27me3 (Figure 2B), arguing against the idea that H3K27me3 directly recruits PRC1 (Schwartz et al., 2006). Does PRC1 recruitment involve specific interactions with the PRC2 complex in addition to H3K27me3?

PRC2 Reads H2AK119ub

How does PRC2 recognize H2AK119ub? PRC2 has three core components, in addition to E(z), that are essential for its methyltransferase activity on nucleosomes. These subunits also confer ability to recognize the presence of H3K4me3 and H3K36me2/H3K36me3, which inhibit H3K27 methylation activity, and H3K27me3 and nucleosome density, which stimulate this activity (Schmitges et al., 2011; Margueron et al., 2009; Yuan et al., 2011, 2012). Two other components, AEBP2 and JARID2, enhance stability, activity, and target specificity (Li et al., 2010; Son et al., 2013; Ciferri et al., 2012). Ability to recognize and bind to H2Aub would add an additional capability to a very versatile protein complex.

Work from Kalb et al. (2014) now sheds light on this key interaction. The authors used oligonucleosomes to affinity purify interacting proteins, which were then identified by mass spectroscopy. They found that, when the nucleosomes contained H2AK119ub, they bound PRC2 components and, in particular, PRC2 enriched in AEBP2 and JARID2. Using reconstituted PRC2 complexes, they found that addition of AEBP2 and JARID2 greatly increased the methyltransferase activity on H2AK119ub-containing substrates. The presence of AEBP2 was essential for this differential activity, which was further stimulated when JARID2 was also present. They concluded that PRC2 complexes that included these two components interacted specifically with H2AK119ub-containing nucleosomes. It is not clear whether the increased enzymatic activity is accounted for by the increased binding or whether H2AK119ub also enhances catalytic activity. In addition, the authors point out that the H2AK119ub-affinity purification from extracts prepared from ESCs revealed that KDM2B-containing PRC1 complexes were also selected. This would then result in a self-reinforcing loop, whereby KDM2B first brings a ubiquitylation-competent PRC1 complex to unmethylated CpG islands, but the ubiquitylating activity then stimulates further binding of PRC1 as well as of PRC2, whose methyltransferase activity then recruits chromodomain-containing PRC1 complexes. Although the basic features of this recruitment pathway are clearly conserved between *Drosophila* and mammals, some aspects must be modified to some extent, given that *Drosophila* lacks CpG islands and that the recruitment occurs instead at specific PREs, most likely via a series of weak interactions with DNA binding proteins. Then, interaction of PRC2 with H2AK119ub would further reinforce this process.

Broader Considerations

There is much that remains to be accounted for. In particular, the distribution of H2AK119ub in the genome of flies or vertebrates remains poorly characterized. Recent work from Riising et al. (2014) indicates that blocking RNA Pol II transcription in mouse ESCs is sufficient to induce ectopic recruitment of PRC2 to CpG islands. The H2AK119ub-dependent recruitment model described above would imply that arrest of transcription immediately results in the binding of the KDM2B-containing complex and H2A ubiquitylation of CpG islands. Other complexes have been claimed to produce H2AK119 monoubiquitylation (histone H2A can also be ubiquitylated at other lysines that are not relevant to the present discussion). For example, BRCA1 has been said to ubiquitylate H2AK119 in order to silence satellite

sequences (Zhu et al., 2011) or at DNA damage sites (Wu et al., 2009). A PRC1 complex containing BMI1 has also been reported to be involved in H2A ubiquitylation at DNA damage sites (Ismail et al., 2010). Does DNA damage also recruit PRC2? Or is PRC2 recruitment prevented by the further ubiquitylation and phosphorylation events that target H2A upon DNA damage?

Why such a complicated recruitment? Which complex actually performs the transcriptional repression? We do not really know except that it seems to be linked to the ubiquityl transferase activity. H2AK119ub has been reported to interfere with the elongation of transcription by RNA Pol II (Zhou et al., 2008), but this does not exclude the possibility that other targets are ubiquitylated or that PRC1 complexes have additional repressive activities. Canonical PRC1 has been found to contribute little H2A ubiquitylation (Lagarou et al., 2008; Farcas et al., 2012; Wu et al., 2013), so why is it needed? One possibility is that it does, in fact, target some additional component important for transcription. An intriguing argument is that H2Aub generated by the initial noncanonical PRC1 complex is sufficient for transcriptional repression of nearby promoters, but the CBX-containing PRC1 is needed to mediate longer distance interactions through interaction with H3K27me3. Yet, recent evidence suggests that PRC2 is dispensable for repression in stem cells but necessary from the onset of their differentiation (Riising et al., 2014). Perhaps the best answer might be that the canonical PRC1, with its H3K27me3 recognition, might provide a more stable epigenetic maintenance function between cell cycles, which is particularly important for differentiating cells.

PcG recruitment by its nature cannot be hardwired but must remain flexible and dependent on the chromatin environment. The recruiting mechanism summarized here accounts for many of these features. KDM2B-dependent recruitment of PRC1 complexes is inhibited by transcriptional activity. Chromatin modifications associated with transcriptional activity modulate PRC2 enzymatic function (Margueron and Reinberg, 2011). In addition, transcriptional activity is associated with H3K27 acetylation both at enhancer sites and in the 5' region of active genes. Therefore, its presence would block H3K27 methylation. In contrast, the presence of pre-existent H3K27 methylation, as well as a high density of nucleosomes, promotes PRC2 methyltransferase activity (Margueron et al., 2009; Yuan et al., 2012). Therefore, the successful recruitment and maintenance of PcG repression would involve a complex interplay of these and probably other modulating circumstances. As a result, PcG mechanisms are better suited to maintaining a repressed state than turning off an active gene.

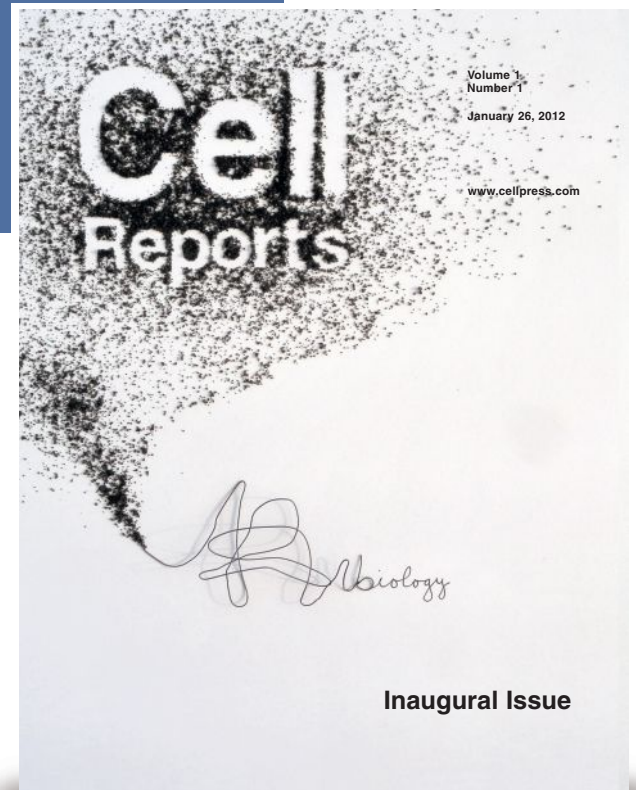
CpG methylation prevents the binding of KDM2B, and therefore the initiation of the entire recruitment cascade. This may avert the recruitment of PcG complexes to genes already silenced by the more long-term DNA methylation mechanism. It is possible that the KDM2B-based recruitment mechanism is particularly important in ESCs, where DNA methylation is relatively low and a large number of genes are kept in a bivalent state: neither silenced nor transcriptionally active but bearing both the H3K27me3 associated with repression and the H3K4me3 associated with transcriptional activation. In work that anticipated the approach of Blackledge et al. (2014), KDM2B was tethered at a reporter gene to demonstrate the

acquisition of H2AK119 ubiquitylation, but no recruitment of PRC2 and H3K27me3 was observed (Wu et al., 2013). The difference from the Blackledge et al. (2014) experiment is that Wu et al. (2013) used the differentiated HEK293T human cell line instead of mouse ESCs. It is very unlikely that such a fundamental recruiting difference is attributable to the difference between man and mouse but very possible that in differentiated cells PRC2 might become more selective. At later stages, when differentiating cell lineages are established, genomic regions that are not actively transcribed are likely to acquire DNA methylation, thus bypassing the PcG mode of transcriptional repression. Other recruitment mechanisms might become more important at specific sites or in specific cell lineages. A large number of noncoding RNAs have been said to bind PRC2 and, in some cases, PRC1 complexes and play a role in targeting them to specific genes (Khalil et al., 2009). PcG mechanisms are clearly highly versatile and nearly omnipresent. It would not be surprising if what was widely taken to be a well-understood mechanism revealed more new twists.

REFERENCES

- Arnold, P., Schöler, A., Pachkov, M., Balwiercz, P.J., Jørgensen, H., Stadler, M.B., van Nimwegen, E., and Schübeler, D. (2013). Modeling of epigenome dynamics identifies transcription factors that mediate Polycomb targeting. *Genome Res.* 23, 60–73.
- Blackledge, N.P., Farcas, A.M., Kondo, T., King, H.W., McGouran, J.F., Hanssen, L.L.P., Ito, S., Cooper, S., Kondo, K., Koseki, Y., et al. (2014). Variant PRC1 complex-dependent H2A ubiquitylation drives PRC2 recruitment and Polycomb domain formation. *Cell* 157, 1445–1459.
- Ciferri, C., Lander, G.C., Maiolica, A., Herzog, F., Aebbersold, R., and Nogales, E. (2012). Molecular architecture of human polycomb repressive complex 2. *Elife* 1, e00005.
- Cooper, S., Dienstbier, M., Hassan, R., Schermelleh, L., Sharif, J., Blackledge, N.P., De Marco, V., Elderkin, S., Koseki, H., Klose, R., et al. (2014). Targeting Polycomb to pericentric heterochromatin in embryonic stem cells reveals a role for H2AK119u1 in PRC2 recruitment. *Cell Rep* 7, 1456–1470.
- Dietrich, N., Lerdrup, M., Landt, E., Agrawal-Singh, S., Bak, M., Tommerup, N., Rappsilber, J., Södersten, E., and Hansen, K. (2012). REST-mediated recruitment of polycomb repressor complexes in mammalian cells. *PLoS Genet.* 8, e1002494.
- Farcas, A.M., Blackledge, N.P., Sudbery, I., Long, H.K., McGouran, J.F., Rose, N.R., Lee, S., Sims, D., Cerase, A., Sheahan, T.W., et al. (2012). KDM2B links the Polycomb Repressive Complex 1 (PRC1) to recognition of CpG islands. *Elife* 1, e00205.
- He, J., Shen, L., Wan, M., Taranova, O., Wu, H., and Zhang, Y. (2013). Kdm2b maintains murine embryonic stem cell status by recruiting PRC1 complex to CpG islands of developmental genes. *Nat. Cell Biol.* 15, 373–384.
- Ismail, I.H., Andrin, C., McDonald, D., and Hendzel, M.J. (2010). BMI1-mediated histone ubiquitylation promotes DNA double-strand break repair. *J. Cell Biol.* 191, 45–60.
- Kalb, R., Latwiel, S., Baymaz, H.I., Jansen, P.W.T.C., Müller, C.W., Vermeulen, M., and Müller, J. (2014). Histone H2A monoubiquitination promotes histone H3 methylation in Polycomb repression. *Nat. Struct. Mol. Biol.* 21, 569–571.
- Khalil, A.M., Guttman, M., Huarte, M., Garber, M., Raj, A., Rivea Morales, D., Thomas, K., Presser, A., Bernstein, B.E., van Oudenaarden, A., et al. (2009). Many human large intergenic noncoding RNAs associate with chromatin-modifying complexes and affect gene expression. *Proc. Natl. Acad. Sci. USA* 106, 11667–11672.
- Lagarou, A., Mohd-Sarip, A., Moshkin, Y.M., Chalkley, G.E., Bezstarosti, K., Demmers, J.A.A., and Verrijzer, C.P. (2008). dKDM2 couples histone H2A ubiquitylation to histone H3 demethylation during Polycomb group silencing. *Genes Dev.* 22, 2799–2810.
- Li, G., Margueron, R., Ku, M., Chambon, P., Bernstein, B.E., and Reinberg, D. (2010). Jarid2 and PRC2, partners in regulating gene expression. *Genes Dev.* 24, 368–380.
- Lynch, M.D., Smith, A.J.H., De Gobbi, M., Flenley, M., Hughes, J.R., Vernimmen, D., Ayyub, H., Sharpe, J.A., Sloane-Stanley, J.A., Sutherland, L., et al. (2012). An interspecies analysis reveals a key role for unmethylated CpG dinucleotides in vertebrate Polycomb complex recruitment. *EMBO J.* 31, 317–329.
- Margueron, R., and Reinberg, D. (2011). The Polycomb complex PRC2 and its mark in life. *Nature* 469, 343–349.
- Margueron, R., Justin, N., Ohno, K., Sharpe, M.L., Son, J., Drury, W.J., 3rd, Voigt, P., Martin, S.R., Taylor, W.R., De Marco, V., et al. (2009). Role of the polycomb protein EED in the propagation of repressive histone marks. *Nature* 461, 762–767.
- Mendenhall, E.M., Koche, R.P., Truong, T., Zhou, V.W., Issac, B., Chi, A.S., Ku, M., and Bernstein, B.E. (2010). GC-rich sequence elements recruit PRC2 in mammalian ES cells. *PLoS Genet.* 6, e1001244.
- Riising, E.M., Comet, I., Leblanc, B., Wu, X., Johansen, J.V., and Helin, K. (2014). Gene silencing triggers polycomb repressive complex 2 recruitment to cpG islands genome wide. *Mol. Cell* 55, Published online July 3, 2014. <http://dx.doi.org/10.1016/j.molcel.2014.06.005>.
- Schmitges, F.W., Prusty, A.B., Faty, M., Stützer, A., Lingaraju, G.M., Aiwazian, J., Sack, R., Hess, D., Li, L., Zhou, S., et al. (2011). Histone methylation by PRC2 is inhibited by active chromatin marks. *Mol. Cell* 42, 330–341.
- Schwartz, Y.B., and Pirrotta, V. (2013). A new world of Polycombs: unexpected partnerships and emerging functions. *Nat. Rev. Genet.* 14, 853–864.
- Schwartz, Y.B., Kahn, T.G., Nix, D.A., Li, X.-Y., Bourgon, R., Biggin, M., and Pirrotta, V. (2006). Genome-wide analysis of Polycomb targets in *Drosophila melanogaster*. *Nat. Genet.* 38, 700–705.
- Sing, A., Pannell, D., Karaiskakis, A., Sturgeon, K., Djabali, M., Ellis, J., Lipsitz, H.D., and Cordes, S.P. (2009). A vertebrate Polycomb response element governs segmentation of the posterior hindbrain. *Cell* 138, 885–897.
- Son, J., Shen, S.S., Margueron, R., and Reinberg, D. (2013). Nucleosome-binding activities within JARID2 and EZH1 regulate the function of PRC2 on chromatin. *Genes Dev.* 27, 2663–2677.
- Woo, C.J., Kharchenko, P.V., Daheron, L., Park, P.J., and Kingston, R.E. (2010). A region of the human HOXD cluster that confers polycomb-group responsiveness. *Cell* 140, 99–110.
- Wu, J., Huen, M.S.Y., Lu, L.-Y., Ye, L., Dou, Y., Ljungman, M., Chen, J., and Yu, X. (2009). Histone ubiquitination associates with BRCA1-dependent DNA damage response. *Mol. Cell. Biol.* 29, 849–860.
- Wu, X., Johansen, J.V., and Helin, K. (2013). Fbx10/Kdm2b recruits polycomb repressive complex 1 to CpG islands and regulates H2A ubiquitylation. *Mol. Cell* 49, 1134–1146.
- Yuan, W., Xu, M., Huang, C., Liu, N., Chen, S., and Zhu, B. (2011). H3K36 methylation antagonizes PRC2-mediated H3K27 methylation. *J. Biol. Chem.* 286, 7983–7989.
- Yuan, W., Wu, T., Fu, H., Dai, C., Wu, H., Liu, N., Li, X., Xu, M., Zhang, Z., Niu, T., et al. (2012). Dense chromatin activates Polycomb repressive complex 2 to regulate H3 lysine 27 methylation. *Science* 337, 971–975.
- Zhou, W., Zhu, P., Wang, J.K., Pascual, G., Ohgi, K.A., Lozach, J., Glass, C.K., and Rosenfeld, M.G. (2008). Histone H2A monoubiquitination represses transcription by inhibiting RNA polymerase II transcriptional elongation. *Mol. Cell* 29, 69–80.
- Zhu, Q., Pao, G.M., Huynh, A.M., Suh, H., Tonnu, N., Nederlof, P.M., Gage, F.H., and Verma, I.M. (2011). BRCA1 tumour suppression occurs via heterochromatin-mediated silencing. *Nature* 477, 179–184.

Discover high-quality, open-access research



Cell Reports features:

- High-quality, cutting-edge research
- A focus on short, single-point papers called Reports
- Broad scope covering all of biology
- Flexible open-access policy
- A highly engaged editorial board
- A distinguished advisory board
- New papers online weekly

cellreports.cell.com



The Fungal Aroma Gene *ATF1* Promotes Dispersal of Yeast Cells through Insect Vectors

Joaquin F. Christiaens,^{1,2,3,9} Luis M. Franco,^{3,4,5,9} Tanne L. Cools,^{1,2} Luc De Meester,⁶ Jan Michiels,¹ Tom Wenseleers,⁶ Bassem A. Hassan,^{3,4} Emre Yaksi,^{5,7,8,10,*} and Kevin J. Verstrepen^{1,2,10,*}

¹Laboratory for Genetics and Genomics, Centre of Microbial and Plant Genetics (CMPG), Department of Microbial and Molecular Systems, KU Leuven, Gaston Geenslaan 1, 3001 Leuven (Heverlee), Belgium

²VIB Laboratory of Systems Biology, Gaston Geenslaan 1, 3001 Leuven (Heverlee), Belgium

³Centre for Human Genetics, KU Leuven School of Medicine, Herestraat 49, 3000 Leuven, Belgium

⁴VIB Centre for the Biology of Disease, Herestraat 49, 3000 Leuven, Belgium

⁵Neuroelectronics Research Flanders (NERF), Kapeldreef 75, 3001 Leuven, Belgium

⁶Animal Ecology and Systematics Section, Department of Biology, KU Leuven, Charles Deberiotstraat 32, 3000 Leuven, Belgium

⁷VIB, Kapeldreef 75, 3001 Leuven, Belgium

⁸KU Leuven, Kapeldreef 75, 3001 Leuven, Belgium

⁹Co-first author

¹⁰Co-senior author

*Correspondence: emre.yaksi@nerf.be (E.Y.), kevin.verstrepen@biw.vib-kuleuven.be (K.J.V.)

<http://dx.doi.org/10.1016/j.celrep.2014.09.009>

This is an open access article under the CC BY-NC-ND license (<http://creativecommons.org/licenses/by-nc-nd/3.0/>).

SUMMARY

Yeast cells produce various volatile metabolites that are key contributors to the pleasing fruity and flowery aroma of fermented beverages. Several of these fruity metabolites, including isoamyl acetate and ethyl acetate, are produced by a dedicated enzyme, the alcohol acetyl transferase *Atf1*. However, despite much research, the physiological role of acetate ester formation in yeast remains unknown. Using a combination of molecular biology, neurobiology, and behavioral tests, we demonstrate that deletion of *ATF1* alters the olfactory response in the antennal lobe of fruit flies that feed on yeast cells. The flies are much less attracted to the mutant yeast cells, and this in turn results in reduced dispersal of the mutant yeast cells by the flies. Together, our results uncover the molecular details of an intriguing aroma-based communication and mutualism between microbes and their insect vectors. Similar mechanisms may exist in other microbes, including microbes on flowering plants and pathogens.

INTRODUCTION

Microbes produce many secondary metabolites, several of which have strong aromas and are central contributors to the flavor of fermented foods and beverages such as cheese, wine, chocolate, and beer (Styger et al., 2011; Swiegers et al., 2005). Flavor formation has been extensively studied in the common brewer's yeast *S. cerevisiae*, which produces several volatile acetate esters such as ethyl acetate (pear aroma), isoamyl acetate (banana aroma), and phenylethyl acetate (flowery aroma; Lambrechts and Pretorius, 2000; Nordström, 1966; Saerens

et al., 2008; Verstrepen et al., 2003a). These acetate esters are formed in a condensation reaction, catalyzed by an alcohol acetyl transferase (AAT), between acetyl-coenzyme A and various higher alcohols derived from the central carbon and amino acid metabolism. *S. cerevisiae* has two different genes coding for AATases, *ATF1* and *ATF2*, of which *ATF1* controls the bulk of the acetate ester formation (Lilly et al., 2000; Verstrepen et al., 2003b). Although many studies have focused on the optimization of aroma formation, the physiological role of these compounds remains elusive and highly debated (Mason and Dufour, 2000; Saerens et al., 2010). Some reports argue that some esters might help maintain plasma membrane fluidity in low-oxygen conditions where the synthesis of unsaturated fatty acids is impaired (Mason and Dufour, 2000). Other hypotheses suggest that ester synthesis may help tune the redox balance (Malcorps and Dufour, 1992) or that esterification of small organic acids may facilitate their removal from cells through diffusion through the plasma membrane (Nordström, 1964). However, no evidence has been found for any of these hypotheses, and deletion of *ATF1* does not reduce fitness under laboratory conditions (Saerens et al., 2010). Moreover, the most commonly used *S. cerevisiae* laboratory strains show significantly lower production of aroma compounds compared to their wild and industrial relatives (Verstrepen et al., 2003b), suggesting that the synthesis of these compounds has not been selected for under laboratory culture conditions and might rather be related to survival in complex natural environments.

In this study, we set out to investigate acetate ester production in the context of the well-established relationship between yeasts and their insect vectors (Fogleman et al., 1981; Giglioli, 1897; Phaff et al., 1956; Stefanini et al., 2012; Suh et al., 2005). Numerous studies have shown that, unlike fungi that disperse through air (Roper et al., 2010) or motile bacteria, sessile microbes like yeasts depend on animal and especially insect vectors for their dispersal (Francesca et al., 2012; Ganter et al., 1986; Goddard et al., 2010). In turn, microbes serve as a

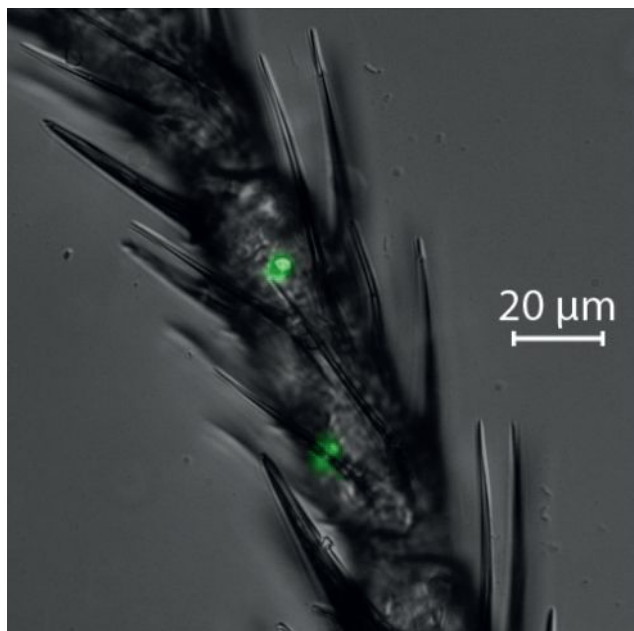


Figure 1. *Drosophila* Transport Yeast Cells in a Laboratory Setup

Yeast cells present on the front leg of a *Drosophila* fly. Sterile individual flies ($n = 11$) were allowed to roam a plate containing a single fluorescent yeast colony (Movie S1) for 1 hr. Afterward, flies were dissected and yeast cells on the various appendages were visualized using fluorescence microscopy. To quantify the number of cells that were transported, each part of the body was washed in a peptone buffer and the buffer was subsequently plated for cell counting (Table S1).

protein-rich food source for these insects and may even boost their immunocompetence (Anagnostou et al., 2010; Gibson and Hunter, 2010; Sang, 1956; Stamps et al., 2012). Previous studies have demonstrated that fermentation can increase the attractiveness of natural substrates toward *Drosophila* (Becher et al., 2012), even though there appears to be a variability in different yeast strains' ability to do so (Palanca et al., 2013). Additionally, multiple insect species are attracted to fruit and plant aroma mixtures that contain acetate esters (Boch et al., 1962; Galizia et al., 1999; Grosjean et al., 2011; Nojima et al., 2003). Finally, a few seminal studies have demonstrated that *Drosophila* antennae possess specific receptors for certain acetate esters (Elmore et al., 2003; Hallem and Carlson, 2006; Vosshall et al., 2000). Given this complex mutualism between microbes and insects, it seems likely that mechanisms evolved to facilitate these interactions. In this study, we show that a specific yeast gene, *ATF1*, produces acetate esters that change the neural representation of yeast odor in the *Drosophila* antennal lobe and help to attract insect vectors.

RESULTS

Yeast Strain Characterization

Experiments to investigate whether acetate esters help to attract insect vectors were carried out using two biological model systems: the fruit fly *Drosophila melanogaster* and the brewer's yeast *Saccharomyces cerevisiae*. To test the suitability of these

organisms for our research, we demonstrated that *Drosophila* do transport yeast cells in a laboratory setup and can indeed act as a vector (Figure 1; Movie S1; Table S1). However, the most commonly used *S. cerevisiae* lab strain, S288c, produces much less aroma compared to wild and industrial *S. cerevisiae* strains (Verstrepen et al., 2003b), making it a poor reference strain for this study. Hence, in order to select a suitable strain, we performed fermentations with 285 genetically diverse *Saccharomyces sensu lato* strains and analyzed their aroma profile (Figure S1). From this collection, we selected a representative diploid strain, coded Y182, for our experimental setup. This *S. cerevisiae* strain was isolated from a vineyard and has an average production of both isoamyl as well as ethyl acetate. Moreover, the strain also shows a relatively high efficiency for genetic transformation, which enabled us to use genetic engineering to create *ATF1* deletion mutants. We deleted both alleles of *ATF1* in this diploid strain and subsequently analyzed the concentration of aroma compounds in the fermentation products of the wild-type and null mutant strains, focusing on higher alcohols, acetate esters, and medium-chain fatty acid esters, as well as ethanol and acetic acid levels, compounds that have been proposed to attract *Drosophila* (Hallem and Carlson, 2006; Hallem et al., 2004). These analyses confirmed that the levels of various acetate esters were severely reduced or even completely abolished in the *atf1*⁻ mutant strain, whereas no significant differences in the concentration of other volatile compounds such as acetaldehyde or higher alcohols was observed (Table 1). The effect of the presence of *ATF1* on the yeast's fitness was investigated using an automated multimode plate reader as well as automated time-lapse microscopy. In keeping with previous studies (Saerens et al., 2010), no difference in the growth rate between the wild-type (WT) and *atf1*⁻ mutant was observed in liquid or on solid media (see Supplemental Information for more information).

The Presence of *ATF1* Leads to Increased *D. melanogaster* Attraction

To evaluate whether changes in the yeast's aroma profile caused by the deletion of the *ATF1* gene lead *D. melanogaster* to prefer one strain over the other, we used an olfactory behavioral assay in a specially constructed arena (Figure 2). In this computer-controlled system, different airstreams can be released independently from each other out of the four corners of the isolated arena and cleared through a vacuum, applied in the center of the arena (Figure 2A). In this setup, the aromas from two different fermentations are delivered from opposing corners, whereas odorless air is streamed from the two remaining corners. For each olfactory behavioral assay, 50 flies were released in the arena and their positions were recorded with a camera placed above the arena. Subsequently, automated image analysis was used to quantify the number of flies in each of the four quadrants, before, during, and after odor delivery. Based on these numbers, a preference index was calculated for each input (see Figure 2 for details). During the first 2 min of each experiment, odorless air was delivered from all four corners of the arena. During this period, flies did not show preference for any specific quadrant. However, as soon as the airflow was switched so that two out of four corners contained the aroma of WT and *atf1*⁻ mutants

Table 1. Aroma Production by WT and *ATF1*⁻ Strain

Compound (ppm)	WT-Y182	SD	<i>atf1</i> ⁻	SD	p Value
Acetaldehyde	8.98	2.73	9.67	2.89	0.74
Ethyl acetate	14.54	1.53	6.45	0.43	5.20 × 10^{-5a}
Ethyl propionate	0.08	0.01	0.09	0.01	0.19
Ethyl isobutyrate	0.02	0.00	0.02	0.00	0.90
Propyl acetate	0.03	0.01	ND	ND	^a
Isobutyl acetate	0.09	0.03	ND	ND	^a
Ethyl butyrate	20.24	3.26	20.40	2.23	0.94
Isobutanol	13.38	2.57	13.31	1.60	0.96
Isoamyl acetate	0.82	0.20	0.13	0.06	5.68 × 10^{-4a}
Butanol	55.45	2.21	57.67	5.22	0.53
Isoamyl alcohol	37.71	5.69	41.54	3.92	0.31
Ethyl hexanoate	0.13	0.03	0.18	0.01	0.04
Ethyl octanoate	1.08	0.23	1.14	0.13	0.66
Phenyl ethyl acetate	0.10	0.02	ND	ND	^a
Phenyl ethanol	0.13	0.06	0.08	0.03	0.16
Ethanol (% v/v)	6.50	0.05	6.46	0.02	0.14
Acetate (g/l)	24.75	6.25	22.15	3.69	0.32

Concentrations of aroma compounds (in parts per million) produced by the diploid WT Y182 strain and the isogenic *ATF1* double-deletion mutant during fermentation (see Figure S1 for more information on Y182). For each strain, four fermentations were performed and each was analyzed in four technical replicates. Acetate esters are displayed in bold. These results demonstrate that the only compounds significantly affected by the *ATF1*⁻ deletion are acetate esters (ND, not detected). Production of these aroma compounds by non-*Saccharomyces* strains may be found in Table S2.

^aSignificant difference between the WT and deletion strain ($p < 0.05$).

(each in one opposing corner), the flies significantly preferred the quadrant with the WT aroma over the aroma of *atf1*⁻ mutants (p value $< 1 \times 10^{-4}$). Afterward, when the airstream at all corners was switched back to odorless control, the flies no longer preferred a specific quadrant and were once again distributed randomly (Figure 2; Movies S2 and S3).

These results indicate that *Atf1* activity has a significant effect on the attraction of *Drosophila* by the yeast cells. To verify whether the observed behavioral differences are indeed due to the lower acetate ester levels produced by the *atf1*⁻ mutant, we supplemented the *atf1*⁻ fermentation medium with phenylethyl acetate, isoamyl acetate, and ethyl acetate (the three important acetate esters most affected by the *ATF1* deletion), so that the final concentration of each ester was equal to that in the WT fermentation medium. We then repeated the olfactory preference tests with this supplemented medium pitted against the fruity WT medium, and no significant difference in preference for either medium was observed, clearly illustrating the central role of phenylethyl, isoamyl, and ethyl acetate in the altered attraction phenotype (Figures 2C and 2D). To further tease apart the specific contribution of each ester, we supplemented the *atf1*⁻ medium with each ester separately and tested these against the WT medium. These experiments revealed that ethyl acetate is the most important compound, because addition of this ester is sufficient to

make the *atf1*⁻ medium as attractive as the WT medium in our olfactory behavioral assay. Addition of isoamyl acetate resulted in increased attraction compared to the unsupplemented *atf1*⁻ medium, but the WT attraction was not fully restored. Finally, phenylethyl acetate did not significantly affect *Drosophila* behavior.

To further confirm the role of the yeast *ATF1* gene in *Drosophila* attraction, we set up a second series of preference experiments, this time in larger cages (30 × 30 × 20 cm), allowing flies more freedom of movement in three dimensions, which has been implicated to alter their behavior compared to setups where their movement is more restricted (Becher et al., 2010; Lebreton et al., 2012). Analogous with the olfactory assay in the smaller arena, we placed traps containing either WT or *atf1*⁻ mutant fermentation medium in opposing corners of the larger cages and two traps containing only water in the two remaining corners. To account for position effects, the traps were switched across different repeats. Our results further confirmed a clear preference of *D. melanogaster* for the WT strain, attracting 2-fold more flies than the *atf1*⁻ strain (see Figure S2 for details).

WT and *atf1*⁻ Aromas Are Perceived Differently by *Drosophila*

To further evaluate the effect of isoamyl and ethyl acetate on the *Saccharomyces-Drosophila* interaction, we used *in vivo* calcium imaging to measure the neuronal responses to *atf1*⁻ and WT yeast aroma in the antennal lobe of a γ Gal4-*GH146/UAS-GCaMP6m*; *Drosophila* strain expressing the transgenic calcium indicator GCaMP6m in its projection neurons (Figures 3A and S3A; Chen et al., 2013). These measurements show a clear alteration in the response of projection neurons, which receive direct olfactory input from olfactory sensory neurons, to the mutant yeast strain compared to the WT strain (Figure 3B). To quantify the differences in the olfactory representation of the different yeast strains, we compared the odor-induced neuronal responses using pairwise Pearson's correlations (Figure 3C). Moreover, we further analyzed these activity maps by comparing the autocorrelation of the repetition of the WT yeast odor across different trials to the cross correlation of the odor representations of WT yeast against *atf1*⁻ yeast and *atf1*⁻ yeast supplemented with the missing esters (Figure S3E). Both analyses revealed that the WT and *atf1*⁻ yeast odor are represented by significantly different activity patterns in the fly antennal lobe. Moreover, we observed that the addition of each ester in physiological concentrations to the *atf1*⁻ mutant yeast medium shifts the evoked antennal lobe activity more toward the WT activity pattern, as evident by the significant increase in correlations between WT and *atf1*⁻ yeast odors when esters are supplemented. Furthermore, the principal component analysis of the antennal lobe odor responses shows that supplementing *atf1*⁻ with esters shifts the representation of *atf1*⁻ yeast odor toward WT yeast odor (Figure 3F). In summary, all these analyses confirm that *atf1*⁻ yeast odor and the WT yeast odor are represented differently in the *D. melanogaster* antennal lobe and the odor representations of *atf1*⁻ yeast become more similar to WT yeast when each ester is supplemented to the same levels as found in the WT medium.

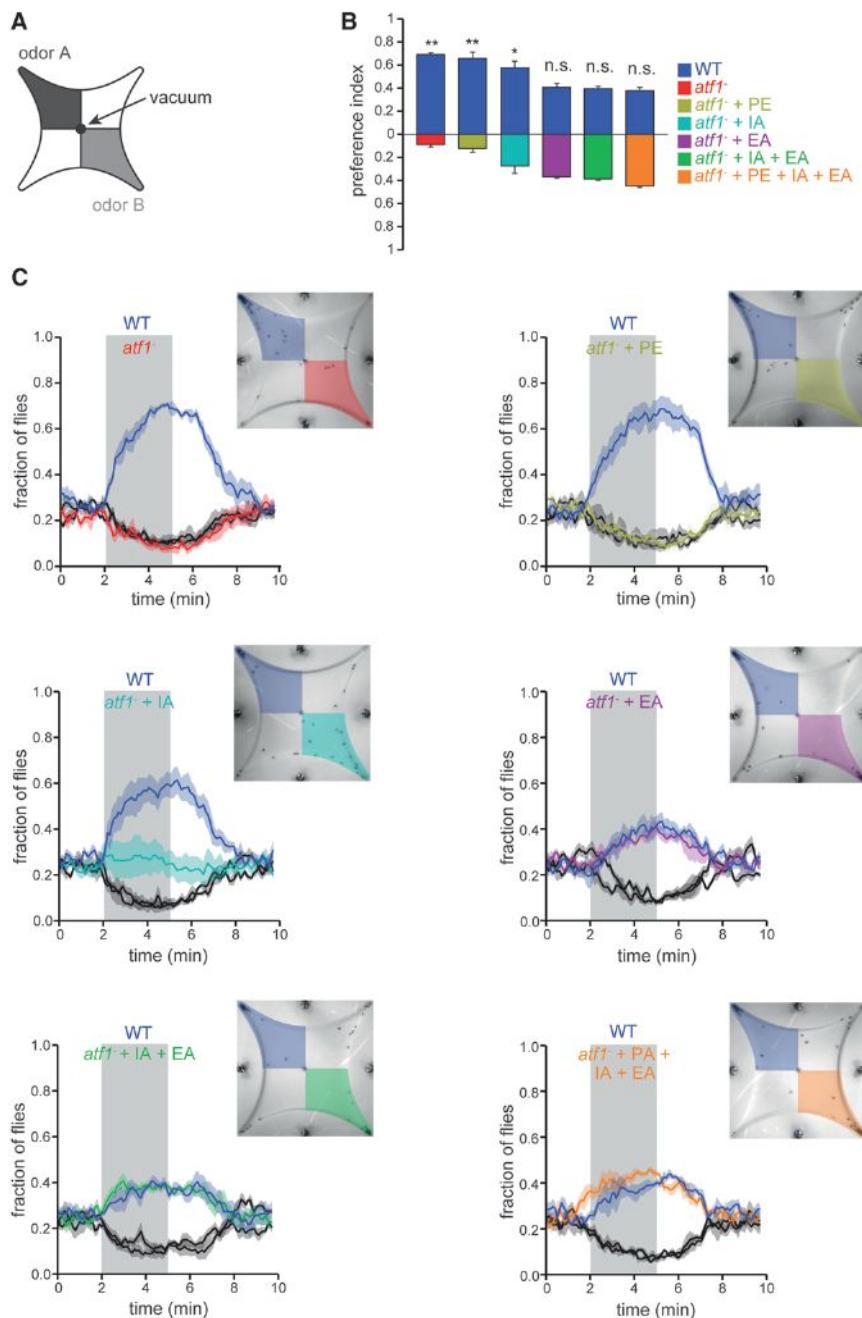


Figure 2. Volatile Acetate Ester Production Affects the Attractiveness of Yeast Cells for *Drosophila melanogaster*

(A) Experimental arena populated with fifty 20 hr-starved *D. melanogaster* CS10 flies. Air is blown from the four corners of the arena, with a common outlet in the center, generating four quadrants that each have their own air profile. Fly movements were recorded during 10 min experiments (odorless air for 2 min from each of the four corners, odors for 3 min from two opposing corners, and odorless air from the other two corners, and finally 5 min of odorless air from all four corners; see also main text for details and Movies S2 and S3).

(B) Preference index defined by the fraction of flies being present in the corresponding odorized quadrant during the last minute of odor exposure. The odors of WT yeast and *atf1*⁻ yeast supplemented with ethyl acetate (EA) and isoamyl acetate (IA) (at concentrations that match the levels present in the WT yeast) exhibit a higher preference index than *atf1*⁻ yeast odor whereas *atf1*⁻ supplemented with phenylethyl acetate (PA) does not (paired t test; **p* < 0.02; ***p* < 0.001). No significant difference was found when WT yeast odor was competed against *atf1*⁻ yeast odor supplemented with all three esters or with ethyl acetate and isoamyl acetate or with ethyl acetate. The error bars represent SEM. n.s., not significant.

(C) Temporal course of number of flies per quadrant for the different experimental conditions. Colors correspond to the respective media (air shown in black/gray). Shadowed traces represent SEM for the number of flies (*n* = 200 flies; four experimental sessions; three trials/odor/session). The gray rectangle indicates the time of odor exposure. Inset figures correspond to snapshots taken at the end of the odor delivery period (5th min). For the large cage setup, see Figure S2.

Expression of *ATF1* Results in Increased Yeast Dispersal

The previous experiments revealed that the *ATF1*-mediated production of acetate esters has a significant impact on the attractiveness of yeast cells toward *D. melanogaster*. However, this does not necessarily imply a benefit for the yeast, because increased attraction of flies might merely result in more yeast cells being consumed by the flies. However, we hypothesized that increased fly attraction might also result in increased dispersal of the yeast cells through their insect vectors. To study whether expression of *ATF1* affects yeast dispersal by fruit flies, both the WT and *atf1*⁻ mutant strain were fluorescently labeled

by overexpressing either *yEcitrine* or *mCherry*. These labeled strains were inoculated on one of two designated spots on a specially constructed YPD plate, equidistant from the center of the plate (Figure S4). For each strain, the inoculum contained 1×10^6 cells, corresponding to the amount of *Saccharomyces* cells that may be found on infected grapes (Mortimer and Polsinelli, 1999). Subsequently, a fly was allowed to roam around the test environment overnight in complete darkness, after which it was removed.

Then, the spots containing the initial inocula were removed as well so that only dispersed yeast cells remained and the plates were incubated to allow growth of these cells. After 48 hr, the plates were washed and the relative presence of each strain was quantified using a flow cytometer. Because there is no growth difference between the WT and mutant strains (Supplemental Information), the relative presence of each strain indicates the ratio in which the two strains were transported by the fly. Analysis of 100 independent experiments revealed that the fruity WT

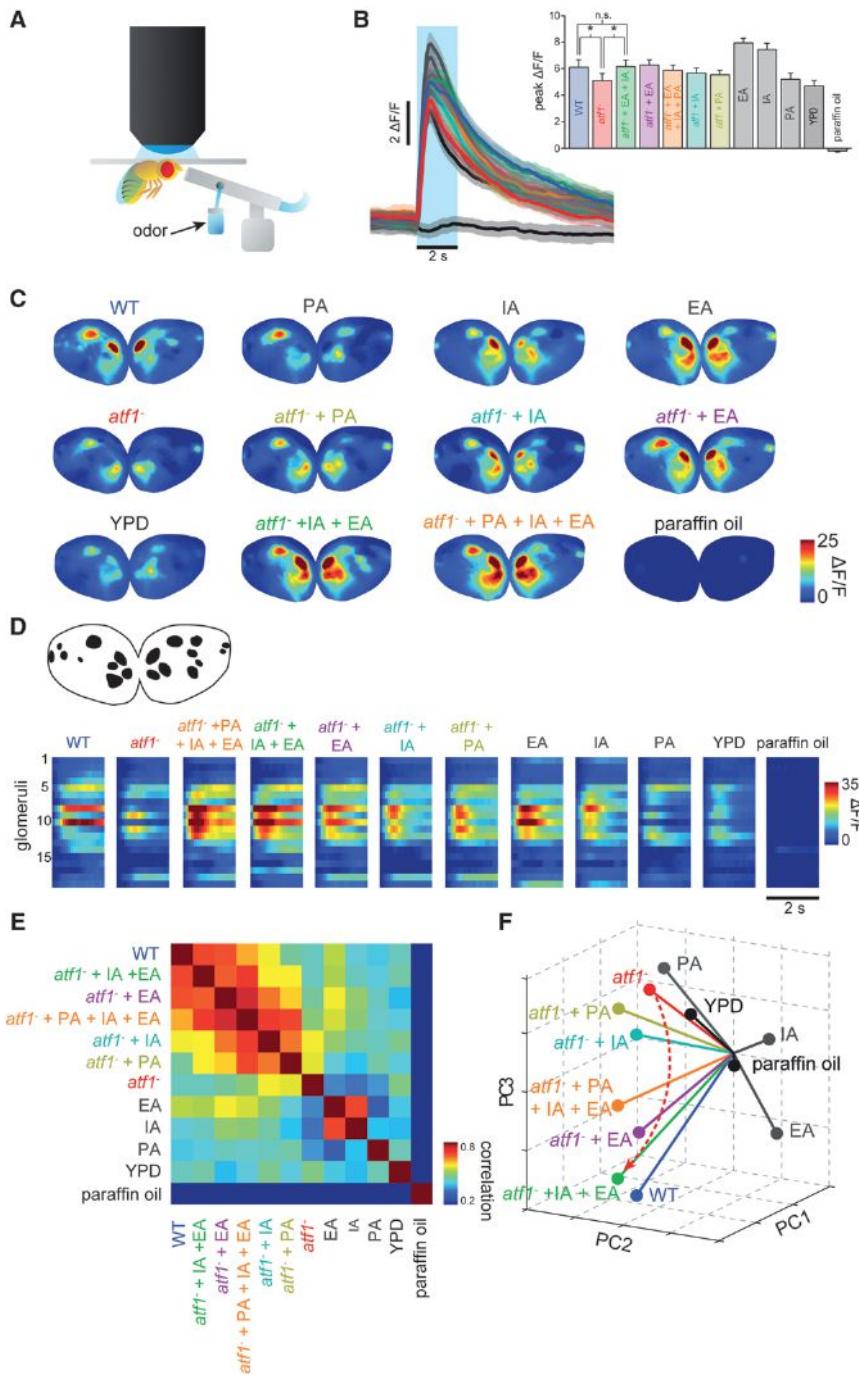


Figure 3. WT and *atf1*⁻ Yeast Odors Are Represented Differently in the Antennal Lobe of *Drosophila melanogaster*

(A) Experimental setup depicting a fly expressing the transgenic calcium indicator GCaMP6 in projection neurons. Briefly, the fly is fixed to an aluminum chamber with wax and the cuticle above the antennal lobes is removed, which allows imaging of the antennal lobes from the dorsal side. A tube is placed in front of its antennae for odors to be delivered (carrier stream flow rate = 2,000 ml/min).

(B) Temporal course of the average fluorescence signal in response to different odors in the entire antennal lobe. Shaded traces represent SEM for the change in fluorescence. The blue rectangle depicts the 2 s time window after response onset, used for quantitative analyses. Inset bar plot shows that pure *atf1*⁻ yeast odor and *atf1*⁻ odor supplemented with PA elicit significantly weaker responses than WT yeast odor and *atf1*⁻ yeast odor supplemented with EA and IA, respectively (n = 14 flies; *p < 0.02; paired t test).

(C) Representative antennal lobe activity maps corresponding to different yeast and ester odors as well as paraffin oil as control, respectively. Calcium responses were averaged during the 2 s window shown in (B).

(D) Regions of interest manually assigned to each responsive glomerulus based on activity maps for the fly shown in (C). On the right, the corresponding glomerulus-based response profiles for the different odors and control are shown. Profiles were constructed for the 2 s window shown in (B).

(E) Correlation matrix representing the pairwise similarities for the different odor response profiles (n = 14 flies). Note that *atf1*⁻ yeast odors supplemented with esters are more correlated to WT yeast odor than *atf1*⁻ yeast odor alone.

(F) Principal component analysis of the odor response profiles. The first three components are shown (total variances explained by first three principle components [PCs] = 79.6%; PC1 = 59.4%; PC2 = 12.8%; PC3 = 7.4%). Upon addition of more esters, the *atf1*⁻ yeast odor representations are progressively pushed in the direction of the representations of the WT yeast odor, indicating a more-similar response. Additional analyses are in Figure S3.

strain was on average transported four times more than the *atf1*⁻ mutant (Figure 4). A separate mirror experiment (n = 100) demonstrated that the nature of the fluorescent tag did not influence the dispersal of either strain (Supplemental Information).

DISCUSSION

Together, these results demonstrate that expression of the fungal alcohol acetyl transferase gene *ATF1* promotes attraction

of *D. melanogaster*, which in turn promotes dispersal of the yeast cells by the insect vector. Using a combination of molecular, behavioral, and neurobiological tests, we show that acetate esters produced by yeasts change the antennal lobe odor representations of *Drosophila melanogaster* and greatly increase its attraction to yeast. Moreover, we identify two acetate esters, ethyl acetate and isoamyl acetate, as the main signaling molecules associated with this phenotype.

It is interesting to note that compounds like ethyl acetate and isoamyl acetate render ripening fruits their typical aroma (Vermeir et al., 2009). It is therefore tempting to speculate that yeasts

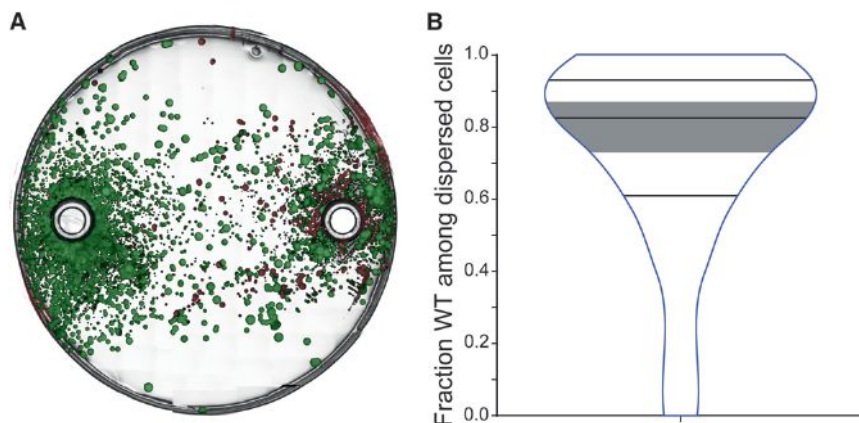


Figure 4. Fruity Yeast Strains Get Dispersed More by *D. melanogaster*

Two fluorescently labeled strains (green or red) were plated equidistantly from the center of a YPD agar plate (black circles; see also Figure S4 for details). A 20 hr-starved CS10 fly was introduced to the plate, which was closed and placed in a container, shielded from external light. After 14 hr, the fly was sedated and removed from the plate, after which the plate was incubated for 48 hr at 30°C to allow growth of dispersed yeast cells. Then, the spots from the initial inoculum were removed and the remaining cells were washed off the plate and analyzed using a flow cytometer.

(A) Image of a representative plate after 48 hr of incubation, before washing. The WT strain is yECitrine-labeled (green-yellow) and the *atf1*⁻

strain mCherry-labeled (red). The image clearly shows that the *atf1*⁻ (red) strain shows reduced dispersal by the flies.

(B) Violin plot of the fraction of dispersed WT cells ($n = 95$, excluding five samples where no cells were dispersed); black lines indicate quartiles and median. Fruity WT cells were dispersed significantly more than *atf1*⁻ cells, shown by the fact that the estimated fraction (gray band = 95% confidence interval) is significantly higher than the 50% expected if dispersal was equal for both (binomial mixed model; p value $< 1 \times 10^{-10}$; details in Experimental Procedures).

have evolved the capacity to synthesize these esters to mimic this aroma in order to attract flies. However, it is difficult to show that the yeast *ATF1* gene specifically evolved to stimulate the production of aroma compounds with the aim of attracting insects. Nonetheless, there are compelling arguments for this hypothesis, because several reports demonstrate the intricate mutualism between yeasts and flying insects like fruit flies (Ganter et al., 1986; Giglioli, 1897; Gilliam et al., 1974; Phaff et al., 1956; Reuter et al., 2007; Starmer et al., 1986; Stefanini et al., 2012). For the yeast, dispersal is essential to reach new niches, especially when nutrient levels are running low. Under these conditions, the center of yeast colonies is expected to be a hypoxic environment (Cáp et al., 2012) and hypoxic conditions may increase *ATF1* expression (Fujii et al., 1997), which in turn results in increased acetate ester formation (Lilly et al., 2000; Malcorps and Dufour, 1992; Verstrepen et al., 2003b). Hence, the production of aroma compounds like isoamyl acetate could help alert flies to the presence of yeast cells, a vital component of their diet. Whereas some of the yeast cells are consumed by the insects, a fraction of cells will stick to the fly body and get dispersed to a different environment. Furthermore, yeasts might reap more benefits from this interaction than mere dispersal. Low nutrient levels trigger the formation of spores that can survive passage through the fly gut and promote outbreeding and thus genetic variability (Freese et al., 1982; Reuter et al., 2007). Additionally, it has been demonstrated that certain insects, such as wasps, act as a reservoir for yeasts when environmental conditions are harsh, for example, during a cold winter (Stefanini et al., 2012).

A last important question is whether aroma-based attraction of insects is limited to *S. cerevisiae*. In a first preliminary assay, we observed that many different yeasts can be isolated from the body of *Drosophila* isolated from natural environments and that the vast majority of these yeasts produced aroma-active esters (Table S2). Moreover, we also isolated several strong aroma-producing yeasts from flowers. These preliminary results suggest that aroma production is not restricted to *S. cerevisiae* and may be a much more general theme in microbe-insect inter-

actions. This is further supported by other studies that reported the isolation of many different yeast species from various insects and the discovery that receptors for acetate esters are widespread in insects (Galizia et al., 1999; Phaff et al., 1956). The formation of fungal aroma compounds may even play a role in mimicry and the relation between plants and their pollinators (Dentinger and Roy, 2010; Stökl et al., 2010).

Lastly, our study also highlights the limitations of using standard laboratory conditions with pure single-species cultures. Clearly, studying model organisms in a more complex ecological context will increase our understanding of physiology and may help to reduce the number of genes with unknown functions.

EXPERIMENTAL PROCEDURES

Strains

Both *ATF1* alleles in the Y182 strain were deleted using deletion cassettes based on pUG6, conferring resistance to either Hygromycin B or G-418 disulfate. Both markers were removed through the Cre/LoxP technique using pSH65. Deletions as well as marker removal were confirmed through (lack of) growth on selective media, as well as PCR (primers in Table S3). Fermentations performed with WT and mutant strains were analyzed using a head-space-gas chromatography-flame ionization detector system; ethanol and acetate levels were determined using enzymatic kits. Growth rates in liquid YPD were measured in an automated multimode plate reader, whereas growth rates on solid media were determined using automated time-lapse microscopy (New et al., 2014). Differences between strains were analyzed using Mann-Whitney U tests.

Olfactory Preference Assays

Prior to testing, 50 CS10 flies were starved for 20 hr at ~25°C in scintillation vials containing a wet filter paper and then placed in the four-input arena. A camera placed above the arena filmed each trial, each lasting 10 min (2 min, odorless air; 3 min, odor exposure; 5 min, odorless air); each set of 50 flies was tested three times. The number of flies in each quadrant was detected by an automated MATLAB algorithm, based on binarized images. Paired t tests were used for statistical comparisons. For the assays in large cages, 20 CS10 flies were starved for 20 hr at 25°C in vials containing 2% agarose. Tests lasted 5 hr, after which all flies were sedated and the number of flies in each trap was counted. Statistical analyses were performed using a generalized linear mixed model (GLMM), available in R-package lme4. For the calcium

imaging experiments (Yaksi and Wilson, 2010), principle-component analyses and Pearson's correlations were calculated on the antennal lobe images obtained during 2 s after response onset windows. For statistical analyses, paired t tests were performed on antennal lobe peak responses and Mann-Whitney for correlation coefficients comparisons.

Dispersal Experiments

Flies were starved for 20 hr at 25°C in vials containing 2% agarose. Dispersal experiments were performed with custom-made plates (see Figure S4) filled with YPD-2% agar. Statistical analyses of the dispersal of both strains were performed using a GLMM, available in R-package lme4. Significance of deviation from 50:50 was tested using a Wald z test, also available in lme4.

SUPPLEMENTAL INFORMATION

Supplemental Information includes Supplemental Experimental Procedures, four figures, three tables, and three movies and can be found with this article online at <http://dx.doi.org/10.1016/j.celrep.2014.09.009>.

AUTHOR CONTRIBUTIONS

J.F.C. and L.M.F. designed, performed, and analyzed experiments and wrote the manuscript. T.L.C. performed experiments. L.D.M., J.M., T.W., and B.A.H. helped with design and interpretation of results and wrote the manuscript. K.J.V. conceived the study, and E.Y. and K.J.V. designed and interpreted experiments and wrote the manuscript.

ACKNOWLEDGMENTS

The authors thank Zeynep Okray; Ine Maes; and all K.J.V., E.Y., and B.A.H. lab members as well as CMPG members for their valuable help and suggestions. Research in B.A.H. lab is supported by VIB; the WiBrain Interuniversity Attraction Pole (BELSPO IUAP) network; and Fonds Wetenschappelijke Onderzoeks (FWO) grants G.0543.08, G.0680.10, G.0681.10, and G.0503.12. Research in the lab of E.Y. is supported by ERC Starting Grant 335561, FWO, VIB, and NERF funding. Research in the lab of K.J.V. is supported by ERC Starting Grant 241426, HFSP program grant RGP0050/2013, VIB, EMBO YIP program, FWO, and IWT.

Received: April 7, 2014

Revised: July 23, 2014

Accepted: September 3, 2014

Published: October 9, 2014

REFERENCES

- Anagnostou, C., LeGrand, E., and Rohlfis, M. (2010). Friendly food for fitter flies? Influence of dietary microbial species on food choice and parasitoid resistance in *Drosophila*. *Oikos* 119, 533–541.
- Becher, P.G., Bengtsson, M., Hansson, B.S., and Witzgall, P. (2010). Flying the fly: long-range flight behavior of *Drosophila melanogaster* to attractive odors. *J. Chem. Ecol.* 36, 599–607.
- Becher, P.G., Flick, G., Rozpędowska, E., Schmidt, A., Hagman, A., Lebreton, S., Larsson, M.C., Hansson, B.S., Piškur, J., Witzgall, P., et al. (2012). Yeast, not fruit volatiles mediate *Drosophila melanogaster* attraction, oviposition and development. *Funct. Ecol.* 26, 822–828.
- Boch, R., Shearer, D.A., and Stone, B.C. (1962). Identification of isoamyl acetate as an active component in the sting pheromone of the honey bee. *Nature* 195, 1018–1020.
- Čáp, M., Stěpánek, L., Harant, K., Váchová, L., and Palková, Z. (2012). Cell differentiation within a yeast colony: metabolic and regulatory parallels with a tumor-affected organism. *Mol. Cell* 46, 436–448.
- Chen, T.W., Wardill, T.J., Sun, Y., Pulver, S.R., Renninger, S.L., Baohan, A., Schreiter, E.R., Kerr, R.A., Orger, M.B., Jayaraman, V., et al. (2013). Ultrasensitive fluorescent proteins for imaging neuronal activity. *Nature* 499, 295–300.
- Dentinger, B.T.M., and Roy, B.A. (2010). A mushroom by any other name would smell as sweet: *Dracula* orchids. *Mcllvainea* 19, 1–13.
- Elmore, T., Ignell, R., Carlson, J.R., and Smith, D.P. (2003). Targeted mutation of a *Drosophila* odor receptor defines receptor requirement in a novel class of sensillum. *J. Neurosci.* 23, 9906–9912.
- Fogleman, J.C., Starmer, W.T., and Heed, W.B. (1981). Larval selectivity for yeast species by *Drosophila mojavensis* in natural substrates. *Proc. Natl. Acad. Sci. USA* 78, 4435–4439.
- Francesca, N., Canale, D.E., Settanni, L., and Moschetti, G. (2012). Dissemination of wine-related yeasts by migratory birds. *Environ. Microbiol. Rep.* 4, 105–112.
- Freese, E.B., Chu, M.I., and Freese, E. (1982). Initiation of yeast sporulation of partial carbon, nitrogen, or phosphate deprivation. *J. Bacteriol.* 149, 840–851.
- Fujii, T., Kobayashi, O., Yoshimoto, H., Furukawa, S., and Tamai, Y. (1997). Effect of aeration and unsaturated fatty acids on expression of the *Saccharomyces cerevisiae* alcohol acetyltransferase gene. *Appl. Environ. Microbiol.* 63, 910–915.
- Galizia, C.G., Sachse, S., Rappert, A., and Menzel, R. (1999). The glomerular code for odor representation is species specific in the honeybee *Apis mellifera*. *Nat. Neurosci.* 2, 473–478.
- Ganter, P.F., Starmer, W.T., Lachance, M.-A., and Phaff, H.J. (1986). Yeast communities from host plants and associated *Drosophila* in southern Arizona: new isolations and analysis of the relative importance of hosts and vectors on community composition. *Oecologia* 70, 386–392.
- Gibson, C.M., and Hunter, M.S. (2010). Extraordinarily widespread and fantastically complex: comparative biology of endosymbiotic bacterial and fungal mutualists of insects. *Ecol. Lett.* 13, 223–234.
- Giglioli, I. (1897). Insects and yeasts. *Nature* 56, 575–577.
- Gilliam, M., Wickerham, L.J., Morton, H.L., and Martin, R.D. (1974). Yeasts isolated from honey bees, *Apis mellifera*, fed 2,4-D and antibiotics. *J. Invertebr. Pathol.* 24, 349–356.
- Goddard, M.R., Anfang, N., Tang, R., Gardner, R.C., and Jun, C. (2010). A distinct population of *Saccharomyces cerevisiae* in New Zealand: evidence for local dispersal by insects and human-aided global dispersal in oak barrels. *Environ. Microbiol.* 12, 63–73.
- Grosjean, Y., Rytz, R., Farine, J.P., Abuin, L., Cortot, J., Jefferis, G.S., and Benton, R. (2011). An olfactory receptor for food-derived odours promotes male courtship in *Drosophila*. *Nature* 478, 236–240.
- Hallem, E.A., and Carlson, J.R. (2006). Coding of odors by a receptor repertoire. *Cell* 125, 143–160.
- Hallem, E.A., Ho, M.G., and Carlson, J.R. (2004). The molecular basis of odor coding in the *Drosophila* antenna. *Cell* 117, 965–979.
- Lambrechts, M.G., and Pretorius, I.S. (2000). Yeast and its importance to wine aroma: A review. *S. Afr. J. Enol. Vitic.* 21, 97–129.
- Lebreton, S., Becher, P.G., Hansson, B.S., and Witzgall, P. (2012). Attraction of *Drosophila melanogaster* males to food-related and fly odors. *J. Insect Physiol.* 58, 125–129.
- Lilly, M., Lambrechts, M.G., and Pretorius, I.S. (2000). Effect of increased yeast alcohol acetyltransferase activity on flavor profiles of wine and distillates. *Appl. Environ. Microbiol.* 66, 744–753.
- Malcorns, P., and Dufour, J.P. (1992). Short-chain and medium-chain aliphatic-ester synthesis in *Saccharomyces cerevisiae*. *Eur. J. Biochem.* 210, 1015–1022.
- Mason, A.B., and Dufour, J.P. (2000). Alcohol acetyltransferases and the significance of ester synthesis in yeast. *Yeast* 16, 1287–1298.
- Mortimer, R., and Polsinelli, M. (1999). On the origins of wine yeast. *Res. Microbiol.* 150, 199–204.
- New, A.M., Cerulus, B., Govers, S.K., Perez-Samper, G., Zhu, B., Boogmans, S., Xavier, J.B., and Verstrepen, K.J. (2014). Different levels of catabolite repression optimize growth in stable and variable environments. *PLoS Biol.* 12, e1001764.

- Nojima, S., Linn, C., Jr., and Roelofs, W. (2003). Identification of host fruit volatiles from flowering dogwood (*Cornus florida*) attractive to dogwood-origin *Rhagoletis pomonella* flies. *J. Chem. Ecol.* **29**, 2347–2357.
- Nordström, K. (1964). Formation of esters from acids by brewer's yeast. IV. Effect of higher fatty acids and toxicity of lower fatty acids. *Jnl. Institute Brewing* **68**, 398–407.
- Nordström, K. (1966). Formation of esters from acids by Brewer's yeast: formation from unsaturated acids. *Nature* **210**, 99–100.
- Palanca, L., Gaskett, A.C., Günther, C.S., Newcomb, R.D., and Goddard, M.R. (2013). Quantifying variation in the ability of yeasts to attract *Drosophila melanogaster*. *PLoS ONE* **8**, e75332.
- Phaff, H.J., Miller, M.W., and Shifrine, M. (1956). The taxonomy of yeasts isolated from *Drosophila* in the Yosemite region of California. *Antonie van Leeuwenhoek* **22**, 145–161.
- Reuter, M., Bell, G., and Greig, D. (2007). Increased outbreeding in yeast in response to dispersal by an insect vector. *Curr. Biol.* **17**, R81–R83.
- Roper, M., Seminara, A., Bandi, M.M., Cobb, A., Dillard, H.R., and Pringle, A. (2010). Dispersal of fungal spores on a cooperatively generated wind. *Proc. Natl. Acad. Sci. USA* **107**, 17474–17479.
- Saerens, S.M., Delvaux, F., Verstrepen, K.J., Van Dijck, P., Thevelein, J.M., and Delvaux, F.R. (2008). Parameters affecting ethyl ester production by *Saccharomyces cerevisiae* during fermentation. *Appl. Environ. Microbiol.* **74**, 454–461.
- Saerens, S.M., Delvaux, F.R., Verstrepen, K.J., and Thevelein, J.M. (2010). Production and biological function of volatile esters in *Saccharomyces cerevisiae*. *Microb. Biotechnol.* **3**, 165–177.
- Sang, J.H. (1956). The quantitative nutritional requirements of *Drosophila melanogaster*. *J. Exp. Biol.* **33**, 45–72.
- Stamps, J.A., Yang, L.H., Morales, V.M., and Boundy-Mills, K.L. (2012). *Drosophila* regulate yeast density and increase yeast community similarity in a natural substrate. *PLoS ONE* **7**, e42238.
- Starmer, W.T., Barker, J.S., Phaff, H.J., and Fogleman, J.C. (1986). Adaptations of *Drosophila* and yeasts: their interactions with the volatile 2-propanol in the cactus-microorganism-*Drosophila* model system. *Aust. J. Biol. Sci.* **39**, 69–77.
- Stefanini, I., Dapporto, L., Legras, J.L., Calabretta, A., Di Paola, M., De Filippo, C., Viola, R., Capretti, P., Polsinelli, M., Turillazzi, S., and Cavalieri, D. (2012). Role of social wasps in *Saccharomyces cerevisiae* ecology and evolution. *Proc. Natl. Acad. Sci. USA* **109**, 13398–13403.
- Stöckl, J., Strutz, A., Dafni, A., Svatos, A., Doubtsky, J., Knaden, M., Sachse, S., Hansson, B.S., and Stensmyr, M.C. (2010). A deceptive pollination system targeting drosophilids through olfactory mimicry of yeast. *Curr. Biol.* **20**, 1846–1852.
- Styger, G., Prior, B., and Bauer, F.F. (2011). Wine flavor and aroma. *J. Ind. Microbiol. Biotechnol.* **38**, 1145–1159.
- Suh, S.O., McHugh, J.V., Pollock, D.D., and Blackwell, M. (2005). The beetle gut: a hyperdiverse source of novel yeasts. *Mycol. Res.* **109**, 261–265.
- Swiegers, J.H., Bartowsky, E.J., Henschke, P.A., and Pretorius, I.S. (2005). Yeast and bacterial modulation of wine aroma and flavour. *Aust. J. Grape Wine Res.* **11**, 139–173.
- Vermeir, S., Hertog, M.L.A.T.M., Vankerschaver, K., Swennen, R., Nicolai, B.M., and Lammertyn, J. (2009). Instrumental based flavour characterisation of banana fruit. *LWT - Food Sci. Technol.* **42**, 1647–1653.
- Verstrepen, K.J., Derdelinckx, G., Dufour, J.P., Winderickx, J., Thevelein, J.M., Pretorius, I.S., and Delvaux, F.R. (2003a). Flavor-active esters: adding fruitiness to beer. *J. Biosci. Bioeng.* **96**, 110–118.
- Verstrepen, K.J., Van Laere, S.D., Vanderhaegen, B.M., Derdelinckx, G., Dufour, J.P., Pretorius, I.S., Winderickx, J., Thevelein, J.M., and Delvaux, F.R. (2003b). Expression levels of the yeast alcohol acetyltransferase genes ATF1, Lg-ATF1, and ATF2 control the formation of a broad range of volatile esters. *Appl. Environ. Microbiol.* **69**, 5228–5237.
- Vosshall, L.B., Wong, A.M., and Axel, R. (2000). An olfactory sensory map in the fly brain. *Cell* **102**, 147–159.
- Yaksi, E., and Wilson, R.I. (2010). Electrical coupling between olfactory glomeruli. *Neuron* **67**, 1034–1047.

The Cytosolic DNA Sensor cGAS Forms an Oligomeric Complex with DNA and Undergoes Switch-like Conformational Changes in the Activation Loop

Xu Zhang,^{1,*} Jiayi Wu,¹ Fenghe Du,^{1,2} Hui Xu,¹ Lijun Sun,^{1,2} Zhe Chen,³ Chad A. Brautigam,³ Xuewu Zhang,⁴ and Zhijian J. Chen^{1,2,*}

¹Department of Molecular Biology, University of Texas Southwestern Medical Center, Dallas, TX 75390-9148, USA

²Howard Hughes Medical Institute, University of Texas Southwestern Medical Center, Dallas, TX 75390-9148, USA

³Department of Biophysics, University of Texas Southwestern Medical Center, Dallas, TX 75390-9148, USA

⁴Department of Pharmacology, University of Texas Southwestern Medical Center, Dallas, TX 75390-9148, USA

*Correspondence: xu.zhang@utsouthwestern.edu (X.Z.), zhijian.chen@utsouthwestern.edu (Z.J.C.)

<http://dx.doi.org/10.1016/j.celrep.2014.01.003>

This is an open-access article distributed under the terms of the Creative Commons Attribution License, which permits unrestricted use, distribution, and reproduction in any medium, provided the original author and source are credited.

SUMMARY

The presence of DNA in the cytoplasm is a danger signal that triggers immune and inflammatory responses. Cytosolic DNA binds to and activates cyclic GMP-AMP (cGAMP) synthase (cGAS), which produces the second messenger cGAMP. cGAMP binds to the adaptor protein STING and activates a signaling cascade that leads to the production of type I interferons and other cytokines. Here, we report the crystal structures of human cGAS in its apo form, representing its autoinhibited conformation as well as in its cGAMP- and sulfate-bound forms. These structures reveal switch-like conformational changes of an activation loop that result in the rearrangement of the catalytic site. The structure of DNA-bound cGAS reveals a complex composed of dimeric cGAS bound to two molecules of DNA. Functional analyses of cGAS mutants demonstrate that both the protein-protein interface and the two DNA binding surfaces are critical for cGAS activation. These results provide insights into the mechanism of DNA sensing by cGAS.

INTRODUCTION

Infectious microorganisms contain and need nucleic acids in their life cycles. The innate immune system has evolved to recognize microbial DNA and RNA as an essential strategy for host defense (Takeuchi and Akira, 2010). Following endocytosis, microbial DNA and RNA can be detected in the endosome by the transmembrane Toll-like receptors, which then initiate signal transduction cascades in the cytoplasm that lead to activation of the transcription factors NF- κ B and interferon regulatory factors (IRFs; e.g. IRF3 and IRF7). These transcription factors then enter the nucleus to induce type I interferons (IFNs) and other antimicrobial molecules. For those

microbes that have succeeded in invading and replicating inside the host cells, the microbial DNA and RNA are detected in the cytoplasm by the innate immune systems. Viral RNA, which usually contains 5'-triphosphate and/or the double-stranded RNA (dsRNA) structure, is detected by the RIG-I family of receptors (Rehwinkel and Reis e Sousa, 2010; Yoneyama and Fujita, 2009). RIG-I then activates NF- κ B and IRFs through the mitochondrial adaptor protein MAVS (also known as IPS-1, VISA, or CARDIF).

We recently identified cyclic GMP-AMP synthase (cGAS) as the cytosolic DNA sensor that triggers type I IFN production (Sun et al., 2013; Wu et al., 2013). cGAS binds to microbial DNA as well as self DNA in a sequence-independent manner, which may allow this DNA sensor to detect any DNA that invades the cytoplasm. Upon DNA binding, cGAS is activated to catalyze the synthesis of a unique isomer of cyclic GMP-AMP (cGAMP) from ATP and GTP. This cGAMP isomer contains two phosphodiester bonds: one between 2'-OH of GMP and 5'-phosphate of AMP, and the other between 3'-OH of AMP and 5'-phosphate of GMP (Ablasser et al., 2013; Diner et al., 2013; Gao et al., 2013b; Zhang et al., 2013). This cGAMP, termed 2'3'-cGAMP, functions as a second messenger that binds to the endoplasmic reticulum membrane protein STING (also known as MITA, MPYS, or ERIS) (Barber, 2011; Wu et al., 2013; Zhang et al., 2013). This binding induces a conformational change of STING, which then recruits the kinases IKK and TBK1 to activate NF- κ B and IRF3, respectively (Ishikawa and Barber, 2008; Tanaka and Chen, 2012). Recent genetic studies have validated the essential role of cGAS in sensing cytosolic DNA in multiple cell types and in immune defense against DNA viruses in vivo (Li et al., 2013b). In addition, cGAS has been shown to be an innate immune sensor of retroviruses, including HIV (Gao et al., 2013a).

In this study, we investigated the mechanism by which cGAS is activated by DNA through crystallographic and biochemical approaches. We determined the human cGAS structures in their apo form, which represents the autoinhibited conformation, as well as in their 2'3'-cGAMP-bound and sulfate-bound forms, which are captured in a locally activated conformation, as compared with the mouse cGAS-DNA complex. On the basis

of these structures, we identified a conserved activation loop in cGAS, located near the primary DNA binding surface, that exhibits switch-like conformational changes after DNA binding. Surprisingly, in contrast to recent structural analyses, which focused on a cGAS-DNA complex that contains one molecule of cGAS and one molecule of DNA (Civril et al., 2013; Gao et al., 2013b; Kranzusch et al., 2013), we found that cGAS forms a 2:2 complex with DNA. Mutagenesis experiments demonstrated that the two DNA binding surfaces and the protein-protein interface of cGAS are important for IRF3 activation and IFN β induction.

RESULTS

Overall Structure of cGAS in the Apo Form

Human cGAS contains 522 amino acid residues, in which the N terminus containing approximately 160 residues is predicted to be unstructured and was previously shown to be dispensable for DNA-dependent cGAMP synthesis (Sun et al., 2013). We expressed a truncated human cGAS (residues 147–522) in *E. coli* as a SUMO fusion protein and purified it after removal of the SUMO tag. We determined the crystal structure of this human cGAS protein in its apo form at 2.45 Å using the selenomethionine derivative (Figures S1 and S2A; Table S1). Similarly to the recently reported structures of cGAS from different species (Civril et al., 2013; Gao et al., 2013b; Kranzusch et al., 2013), human cGAS adopts an overall fold of mixed α/β topology, which is composed of two lobes (Figure 1A, left and middle). The N-terminal lobe comprises a series of central-twisted β sheets (β 1– β 9) flanked by α 1– α 7 helices. The C-terminal lobe is a compact α -helix bundle (α 8– α 12), including a conserved zinc binding motif. The catalytic residues (Glu225, Asp227, and Asp319) are located on the central β sheet, the side chains of which point to the cleft between the N lobe and C lobe. Two residues (Gly212 and Ser213) are in a highly conserved loop region, connecting the first and second β strands (β 1 and β 2; Figure 1A, right). Mutations of Gly212 and Ser213 to alanine abolish the cGAS activity (Sun et al., 2013), underscoring the functional significance of this loop region. Herein, we refer to this loop (residues 210–220 in human cGAS; Figure S1) as the activation loop (see details below).

The Structure of cGAS in Complex with 2'3'-cGAMP

We attempted to cocrystallize human cGAS in complex with double-stranded DNA (dsDNA), but failed to obtain well-diffracting crystals. In the meantime, we were able to obtain well-diffracting crystals of cGAS (residues 161–522) bound to its product 2'3'-cGAMP. We determined the structure of this complex by molecular replacement (MR), using apo cGAS as the search model, and refined it to 2.44 Å with good R_{free} values and stereochemistry (Figure S2B; Table S1). A simulated annealing omit map and $2F_o - F_c$ electron density map revealed decent density for 2'3'-cGAMP (Figure 1B). 2'3'-cGAMP sits at the lower part of the cleft between the N lobe and C lobe (Figure 1C, left). The catalytic residues Asp227 and Asp319, in addition to Lys362, Arg376, and Ser434, interact with 2'3'-cGAMP through multiple polar contacts (Figure 1C, right). The base group of adenine moiety stacks against the aromatic residue Tyr436

(Figure 1D). The residues involved in 2'3'-cGAMP binding are identical to the corresponding residues identified in the recently determined structure of mouse cGAS that contains a 16-bp dsDNA in addition to 2'3'-cGAMP (Protein Data Bank ID code [PDB] 4K9B; Figure 1D; Gao et al., 2013b).

The Structure of cGAS in Complex with Sulfate Ions

We crystallized human cGAS (161–522) in the presence of 2 M $(\text{NH}_4)_2\text{SO}_4$ and refined the structure to 2.25 Å (Figure S2C; Table S1). During the structure refinement, two pieces of spherical electron density were observed in the cleft between the N lobe and C lobe (Figure 1E). They likely represent sulfate ions because of the crystallization condition. Sulfate ions are often utilized to mimic phosphate groups and interact with the phosphate binding site in order to trap specific conformations of kinase or nucleotide cyclase (Jeong et al., 2003; Tanaka et al., 2010). After fitting two sulfate ions in the cleft, we found that the first sulfate ion, in the upper part of the cleft, was well coordinated by the surrounding residues Ser213, Lys414, and Ser435 (Figure 1F). If the sulfate-bound cGAS structure is superimposed with the mouse-cGAS-DNA-linear-2'-GTP-GMP ternary complex (PDB 4K98), the first sulfate ion is located in a position similar to that of the γ -phosphate group in the GTP moiety, whereas the second ion sits near the α -phosphate group in the GMP moiety (Figure 1G). The structural similarity among cGAMP-bound human cGAS, sulfate-bound human cGAS, and DNA-bound mouse cGAS suggests that cGAS is trapped in a locally activated conformation in the presence of 2'3'-cGAMP or sulfate ions.

Conformational Changes in the Activation Loop of cGAS

A comparison of the activation loops in apo cGAS and the other two ligand-bound cGAS structures reveals that the loop undergoes significant conformational changes (Figure 2A). The activation loop is not involved in the crystal-packing interface (Figures S3A–S3C). The $2F_o - F_c$ electron density maps of the activation loops of apo cGAS and sulfate-bound cGAS are of decent quality (Figure 2B). The sulfate ion in the upper part of the cleft interacts directly with Ser213 in the activation loop (Figure 1F), resulting in a fixed loop orientation. However, the activation loop in the cGAMP-bound cGAS structure appears relatively more flexible (Figure 2A), probably because 2'3'-cGAMP binds to the lower part of the cleft and releases the activation loop to some extent (Figure 1C).

The conformational changes of the activation loop include not only an inward movement of the protruded loop (Gly212 and Ser213) but also an outward shift of Val218 and Lys219 in order to empty the pocket for the substrates (in this case, the sulfate ions that mimic the phosphate moieties of nucleotides; Figures 2C and 2D; Movie S1). Besides the rearrangement in the cleft of the active site, the N lobe also exhibits conformational shifts, especially in α 2, α 4, and the β sheet formed by β 5, β 6, β 7, and β 2 (Figures 2E and 2F; Movies S2 and S3). This region exhibits high B factors, suggesting relatively high mobility (Figure S3D).

The large conformational change of the activation loop from apo cGAS to sulfur-bound cGAS raises the question of how such conformational change is triggered. On the backside of the cleft, there is one positively charged patch, which was

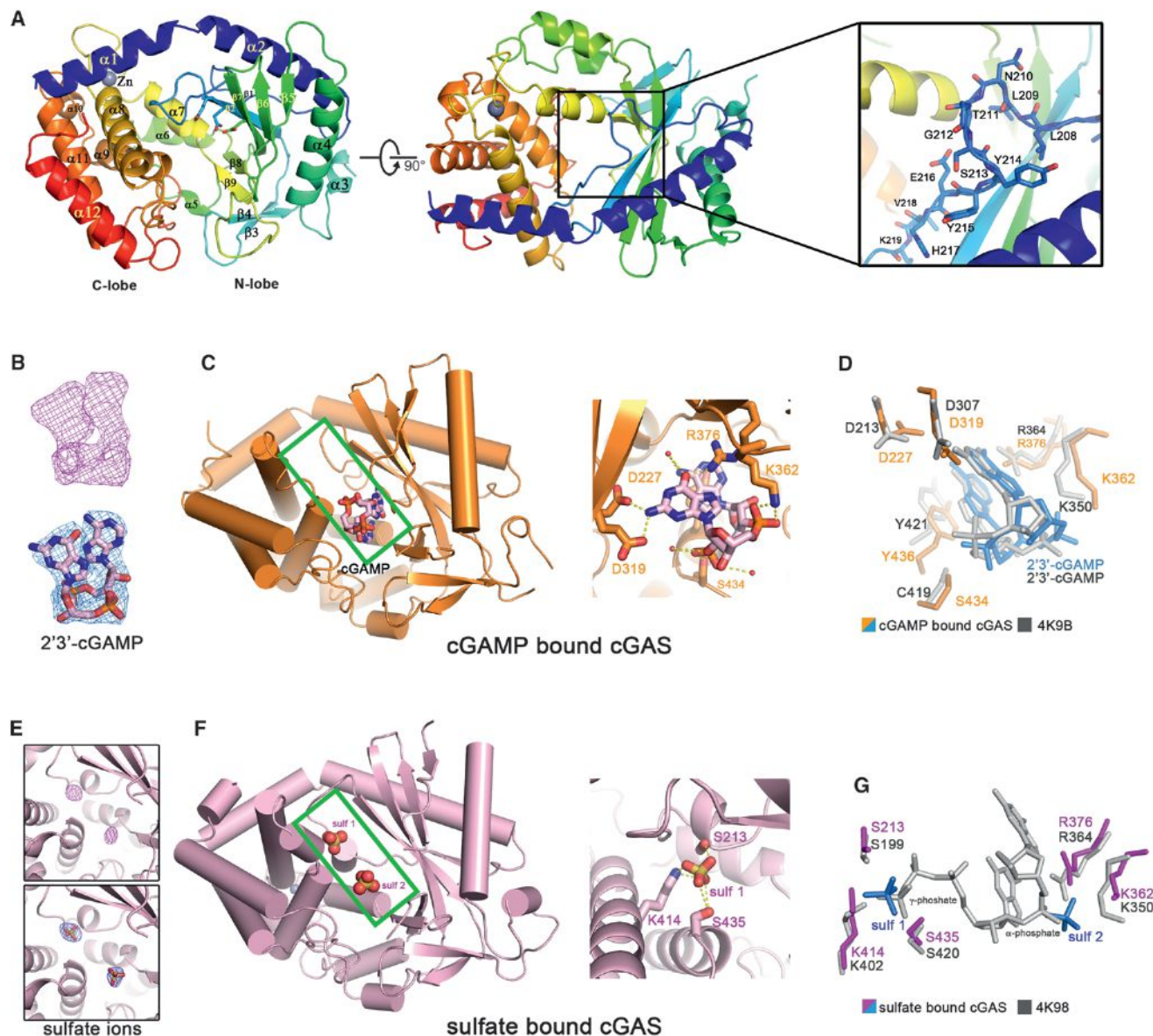


Figure 1. Overall Structures of Human cGAS in the apo Form or in Complex with 2'3'-cGAMP or Sulfate Ions

(A) Overall structure of human cGAS in the apo form. The catalytic residues are shown in sticks. Two perpendicular views and a close-up view of the conserved loop connecting the first and second β strands are shown. The residues in the loop are shown in sticks.

(B) The simulated annealing omit map (top) and the $2F_o - F_c$ electron density map (bottom) for 2'3'-cGAMP are contoured at 3.0σ and 1.0σ , respectively.

(C) Overall structure of cGAS in complex with 2'3'-cGAMP (left). The cleft between the N lobe and C lobe is highlighted by a green rectangle. 2'3'-cGAMP binds to cGAS by multiple polar contacts (right).

(D) Residues involved in 2'3'-cGAMP binding are identical to the ones in mouse-cGAS-DNA-2'3'-cGAMP ternary complex (PDB 4K9B).

(E) The simulated annealing omit map (top) and the $2F_o - F_c$ electron density map (bottom) for the sulfate ions are contoured at 4.0σ and 1.5σ , respectively.

(F) Overall structure of cGAS in complex with sulfate ions (left). The cleft between the N lobe and C lobe is highlighted by a green rectangle. Sulfate ion 1 is coordinated by several polar residues (right).

(G) Residues involved in sulfate ion binding are conserved in mouse-cGAS-DNA-linear-2'-GTP-GMP ternary complex (PDB 4K98). The position of sulfate ion 1 is similar to the γ -phosphate group of GTP moiety, whereas the position of sulfate ion 2 is similar to the α -phosphate group of GMP moiety. All of the structure figures were prepared in PyMol (DeLano, 2002).

See also Figures S1 and S2.

recently shown to bind DNA (Civril et al., 2013; Gao et al., 2013a; Kranzusch et al., 2013). Interestingly, the activation loop, pointing outward in apo cGAS, hinders the interaction between

human cGAS and DNA (Figure 3A). The sulfate ions trap a conformation that displays several positively charged patches and is able to accommodate the modeled dsDNA helix (Figure 3B).

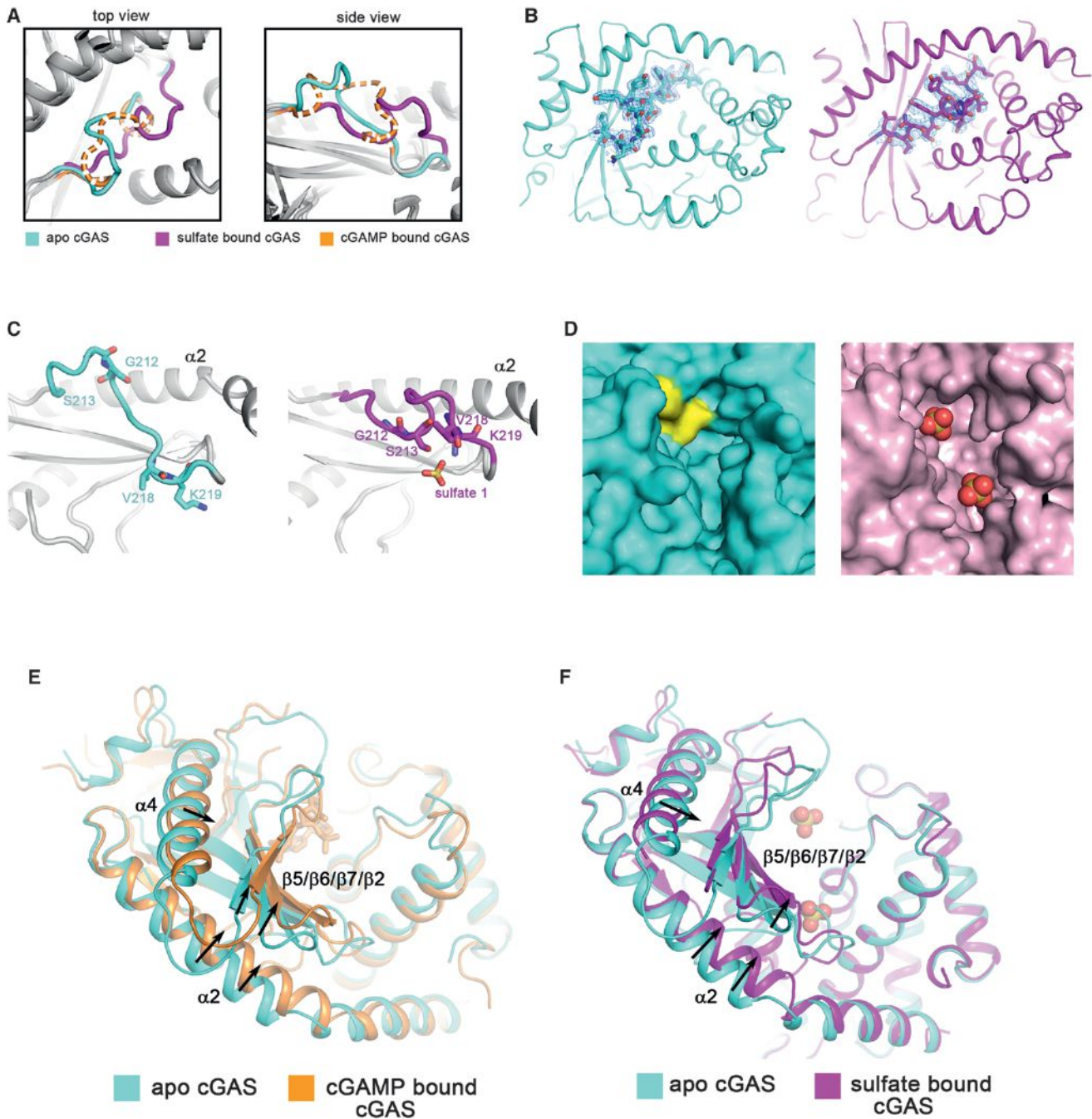


Figure 2. Ligand-Induced Conformational Changes of the Activation Loop and Active-Site Rearrangement of cGAS

(A) Comparison of the activation loops in apo cGAS (cyan), sulfate-bound cGAS (magenta), and cGAMP-bound cGAS (orange). The loop of cGAMP-bound cGAS is shown by a dashed line because of its high flexibility. Two perpendicular views are shown. The same color scheme is applied unless indicated otherwise.

(B) The $2F_o - F_c$ electron density maps of the activation loop in apo cGAS (left) or sulfate-bound cGAS (right), shown in blue mesh, are contoured at 0.8σ .

(C) The activation loop undergoes significant conformational changes in the presence of sulfate ions (right) compared with apo cGAS (left). $\alpha 2$ helix is used as the reference.

(D) Val218 and Lys219 (yellow) occupy a large part of the cleft between the N lobe and C lobe in apo cGAS. The sulfate ions are shown in red spheres in the right panel.

(E and F) The N lobe of cGAS exhibits distinguishable conformational shifts in the presence of 2'3'-cGAMP (E) or sulfate ions (F) as compared with the apo form. See also Figure S3 and Movies S1, S2, and S3.

We examined a series of conserved positively charged residues located on the potential DNA binding surface by mutagenesis. Expression plasmids encoding wild-type or mutant human cGAS were transfected into human embryonic kidney 293T (HEK293T) cells stably expressing STING and an IFN β -luciferase reporter. Luciferase activity and IRF3 dimerization assays show that Lys384, Lys407, and Lys411 are critical for cGAS function (Figure 3C). Lys407 and Lys411 are located on the preexisting positively charged patch, whereas Lys384 is near the activation loop and is exposed only in sulfate-bound cGAS (Figure 3D). Notably, mutations of several positively charged residues in the first and second α helices (R166A, K187A, and K198A) of cGAS did not abrogate its ability to induce IFN β or activate IRF3 (Figure 3C).

Modeling of the cGAS structures bound to the B-form dsDNA shows that the DNA binding clashes with the protruded activation loop, causing this loop to move inward and rearrange the active site (Figure 3E; Movie S1). In contrast, modeling using the A-form dsRNA shows that the activation loop inserts into the major groove of dsRNA without causing detectable conformational changes (Figure 3F), which may explain why cGAS cannot be activated by dsRNA.

cGAS Forms a 2:2 Functional Complex with DNA

To further understand how DNA binding activates cGAS, we solved the crystal structure of mouse cGAS in the presence of DNA. The same mouse cGAS protein and DNA were previously used to obtain the crystal structure of a cGAS-DNA complex, which was interpreted to contain one cGAS and one DNA (Gao et al., 2013b). However, we found that each asymmetric unit contains two cGAS molecules and two DNA molecules (Figure 4A). Besides the primary DNA binding surface (surface 1), which is identical to the ones reported previously (see also Figures 3B and 3D) (Civril et al., 2013; Gao et al., 2013b), cGAS has another surface area, composed of two positive patches, that interacts with DNA (Figure 4B).

Closer inspection of the apo- and sulfate-bound human cGAS also reveals a dimer in the crystal (Figures S4A and S4B). Interestingly, Lys394 within the zinc finger of human cGAS, corresponding to Lys382 in mouse cGAS, interacts with the carbonyl oxygen atoms of Asn389 and Gly391 (Figure 4C). Lys347 in human cGAS (Lys335 in mouse cGAS) not only mediates DNA binding (Figure 4B) but also interacts with Glu398 from the adjacent protomer (Figure 4C). The interaction area is about 678 Å² in total, suggesting a weak interaction, which may be reinforced by the binding of cGAS to DNA. Although it was not reported previously, the same dimer interface exists in the previously published crystal structures of apo- and DNA-bound cGAS proteins from different species and crystallized under different conditions (Figures S4C–S4F) (Civril et al., 2013; Gao et al., 2013a; Kranzusch et al., 2013), strongly suggesting that the formation of cGAS dimer is not a crystallographic artifact. Indeed, we found that Flag-cGAS and hemagglutinin (HA)-cGAS coimmunoprecipitated from HEK293T cells that expressed both of these proteins, suggesting that cGAS may form a dimer or oligomer in mammalian cells, perhaps in the presence of the transfected plasmid DNA (Figure S4G).

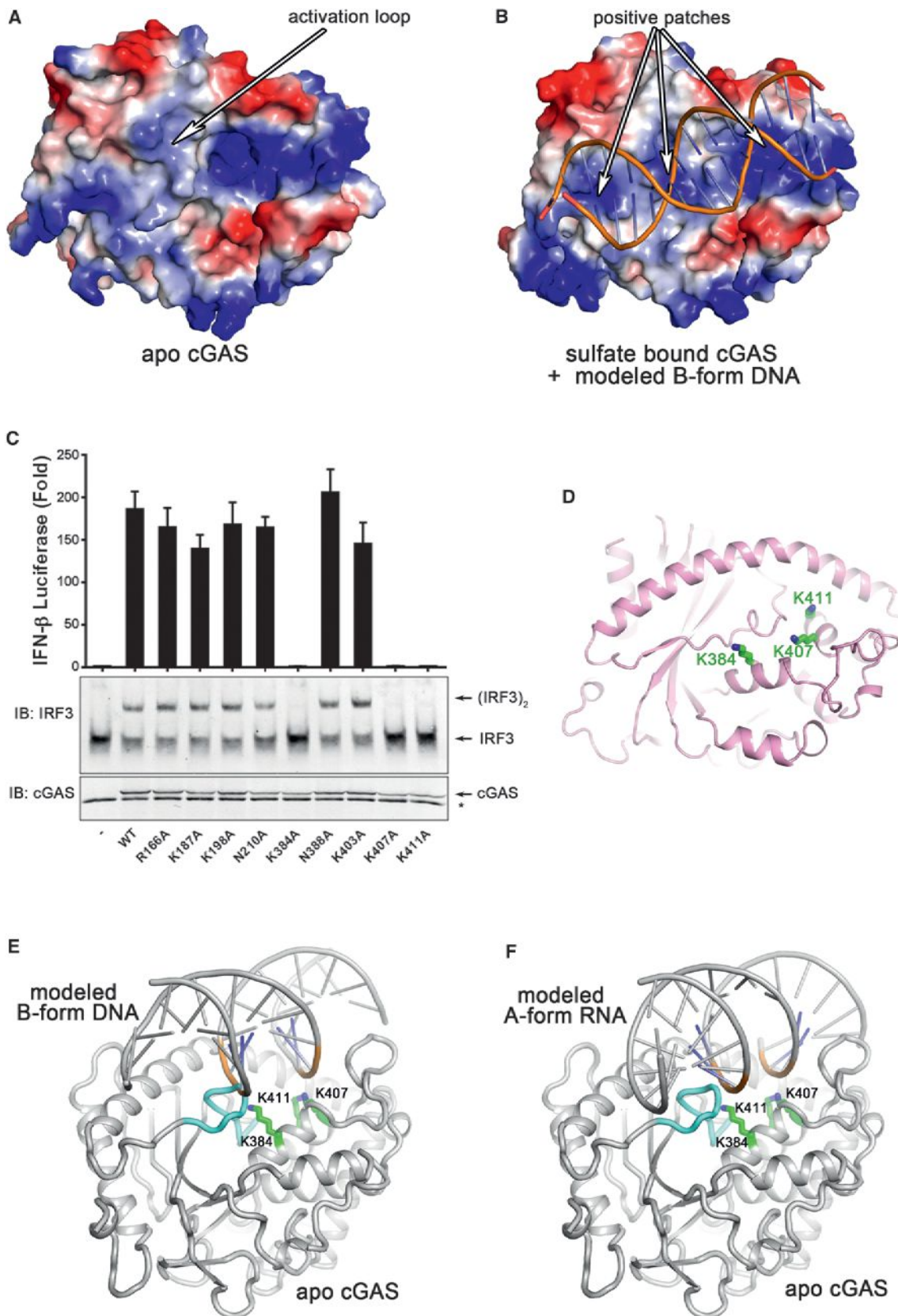
Analytical ultracentrifugation (AUC) sedimentation velocity (SV) experiments were performed to examine the hydrodynamic behavior of mouse cGAS (m-cGAS) in the absence and presence of DNA. Without DNA in solution, m-cGAS is a monomer that sediments at 3.2 S at all concentrations (0.8–80 μ M) studied (Figure S4H). Thus, the m-cGAS dimer observed in the crystal structures in the absence of DNA may be due to the very high concentrations of cGAS under the crystallographic conditions. However, in the presence of a 16-mer dsDNA, faster-sedimenting complexes are evident at 4.0 S, 5.3 S, and 6.5 S (Figure 4D). The latter peak is close to that expected for a 2:2 complex. A multisignal SV (Balbo et al., 2005; Padrick et al., 2010) analysis demonstrates that the molar ratio of protein:DNA in this peak is 0.9:1 (Figure S4I). Thus, the hydrodynamics and composition of this peak are consistent with the formation of the postulated 2:2 complex. The high concentrations needed to achieve this complex (80 μ M protein, 120 μ M DNA) reflect the apparently poor association constant of complex formation. The other fast-sedimenting peaks mentioned here are likely DNA and protein whose time-average sedimentation coefficients have been increased (resulting in “advanced species”) by brief residencies in complexes between the two.

The conclusion that the 6.5 S peak represents 2:2 complexes is further buttressed by parallel experiments carried out with the m-cGAS point mutant K335E (corresponding to K347 in human cGAS). As mentioned above, this residue mediates both cGAS-cGAS and cGAS-DNA interactions (Figure 4C). Under similar conditions (94 μ M protein, 120 μ M DNA), this mutant protein does not form fast-sedimenting complexes as efficiently as the wild-type m-cGAS (Figure 4D). Although this mutant efficiently binds DNA, its ability to form large complexes is greatly diminished, and thus the population of 2:2 complexes must be significantly smaller than that observed in the experiment with wild-type cGAS. It appears, therefore, that Lys335 is very important for the formation of the protein-protein interface, but its mutation does not disrupt DNA binding, likely because the intact DNA binding surface 1 and the other residues in the DNA binding surface 2 can still mediate DNA binding. The resolved peaks in this analysis likely consist of a combination of effective particles (Schuck, 2010) containing various populations of possible complexes and advanced species (Figure 4D, green curve).

In cell-based functional assays, point mutations of Lys347 (Lys335 in m-cGAS), Arg353, or Lys394 to Glu in the human cGAS completely abolished its ability to activate IRF3 and induce IFN β (Figure 4E). Although single mutations of Arg232, Lys254, and Lys327 to Glu only partially impaired the activity of cGAS, double (R236E/K254E and K254E/K327E) and triple (R236E/K354E/K327E) mutations abolished the activity. These results indicate that the second DNA binding site and the protein-protein interface in cGAS are important for activation of the type I IFN pathway (Figure S4J; Movie S4).

DISCUSSION

In this study, we determined the crystal structures of human cGAS in its apo form, 2′/3′-cGAMP-bound form, and sulfate-bound form. Structural alignment with the DNA-bound mouse cGAS shows that the ligand-bound human cGAS resembles



(legend on next page)

the activated conformation induced by DNA binding. In apo cGAS, the activation loop points to the outside. Once cGAS encounters cytosolic B-form DNA, the preexisting positively charged patch (Lys407, Lys411, and other DNA binding residues on $\alpha 1$ and $\alpha 2$ helices) “grabs” the DNA. The steric clash between the DNA and the activation loop “switches on” dramatic conformational changes in the loop region such that new positively charged patches are formed, including the exposure of Lys384, allowing further DNA binding (Figure 3E; Movie S1). The DNA binding causes the activation loop to move inward, thus rearranging the active site to catalyze cGAMP formation (Movie S4).

While we were refining the cGAS structures, three groups published the crystal structures of cGAS (Civril et al., 2013; Gao et al., 2013b; Kranzusch et al., 2013). Gao et al. (2013b) and Civril et al. (2013) determined the crystal structures of mouse cGAS and porcine cGAS, respectively, in both the apo form and DNA-bound form. Both groups observed that the first and second helices bind to DNA and undergo conformational shifts. Although Gao et al. (2013b) showed that none of the single-point mutations of the positive residues on $\alpha 1$ and $\alpha 2$ helices abrogated the DNA-dependent activity of cGAS, Civril et al. (2013) found that the double mutant K173A/R176A on $\alpha 1$ helix of human cGAS had greatly reduced activity. More recently, Li et al. (2013a) showed that R158E of mouse cGAS (equivalent to K173 of human cGAS) was largely defective in cGAMP synthesis and IFN β induction. Thus, DNA binding to the first two α helices of cGAS likely contributes to its activation. However, this is not sufficient. Here we show that the switch-like movement of the activation loop, which is triggered in part by DNA binding to the positively charged residues (K384, K407, and K411) located in $\alpha 7$ and $\alpha 8$ surrounding the zinc finger, mediates cGAS activation. Contrary to our results, which showed that K384A or K407A mutation abolished cGAS activity, Gao et al. (2013b) found that mutations of the corresponding residues in mouse cGAS did not impair its activity. However, two recent reports presented evidence showing that point mutations of K384, K407, and K411 in human cGAS or the corresponding residues in mouse cGAS abolished its ability to induce IFN β (Kato et al., 2013; Li et al., 2013a).

Interestingly, mouse cGAS is able to tolerate G199A mutation, but G199P or G199A/S200A largely abolishes its activity (Sun et al., 2013; Gao et al., 2013b), suggesting a crucial role of the loop flexibility in the activation process. The S200A mutation has little effect on cGAS activity, presumably because it does not affect the loop flexibility, and the binding of the γ -phosphate group from the substrate (sulfate ion in our structure)

involves multiple polar contacts besides the interaction with S200 (S213 in human cGAS). Kranzusch et al. (2013) determined the crystal structure of human cGAS in its apo form. The activation loop in this structure also protrudes to the outside, even though the cGAS protein fragment and the crystallization conditions were distinct from what were used in our study, suggesting that the outward protrusion of the activation loop in human cGAS is reproducible in different crystals. Although the protrusion of the activation loop is less obvious in mouse cGAS, the significant ligand-induced conformational switch of the activation loop occurs in both human and mouse cGAS structures.

cGAS is not the only protein that possesses an activation loop. A conserved activation segment, starting with the DFG motif and ending with the APE motif, exists in all protein kinase families and is also crucial for catalytic activity (Endicott et al., 2012). The DFG loop has been shown to be an important drug target. The identification of the activation loop in cGAS reveals a mechanism of its activation by DNA and may assist in the development of cGAS inhibitors.

Surprisingly, we found that the cGAS structures we determined and those that were published previously all form an identical dimer in the crystal (Figures 4 and S4) (Civril et al., 2013; Gao et al., 2013a; Kranzusch et al., 2013). These findings indicate that cGAS itself may form a dimer. However, our AUC analysis shows that the mouse cGAS protein does not form a dimer in the absence of DNA at all concentrations tested. In the presence of DNA, cGAS forms a 2:2 complex with DNA in solution, consistent with the crystal structure. A significant amount of this complex was detectable only when both cGAS and DNA were present at high concentrations, suggesting that the complex has a poor association constant. This is consistent with the fact that very few residues, notably K347 and K394 in human cGAS, are involved in the protein-protein interface. Despite this weak interaction, point mutation of either K347 or K394 completely abolishes the ability of cGAS to induce IFN β , underscoring the functional importance of forming the oligomeric complex. While our paper was in revision, Li et al. (2013a) reported that DNA binding induces oligomerization of cGAS that is important for its activation. Consistent with our results, these authors showed that mutations of cGAS at residues on the second DNA binding surfaces and at the protein dimer interface abolish cGAMP synthesis and IFN β induction. Although both studies independently identified a common set of residues involved in protein-DNA and protein-protein interactions, we identified and validated additional key residues that are crucial for cGAS functions. For example, we show that K411 and R353 are critical

Figure 3. The Primary DNA Binding Surface of cGAS Is Essential for IFN β Induction

(A and B) Electrostatic representations of apo cGAS (A) and sulfate-bound cGAS (B). A series of positively charged patches in sulfate-bound cGAS indicate the potential primary DNA binding surface.

(C) Expression plasmids encoding wild-type (WT) and various mutants of human cGAS fragments (161–522) containing alanine substitutions of positively charged residues shown in (B) were transfected into HEK293T-STING-IFN β luciferase reporter cells followed by luciferase assays to measure IFN β induction. Aliquots of the cell extracts were immunoblotted with an IRF3 antibody following native gel electrophoresis (middle) or with a cGAS antibody following SDS-PAGE (bottom). The error bars represent variation ranges of duplicate experiments.

(D) Functionally important positively charged residues, shown in green sticks, are located in the center of the primary binding surface.

(E and F) Docking B-form DNA to apo cGAS (E) results in a steric clash between the activation loop and the DNA, which likely triggers the inward movement of the activation loop. However, docking A-form RNA to apo cGAS (F) does not reveal the steric clash or the movement of the activation loop. The activation loop is colored in cyan. Loss-of-function mutations on the primary DNA binding surface are shown in sticks and colored in green.

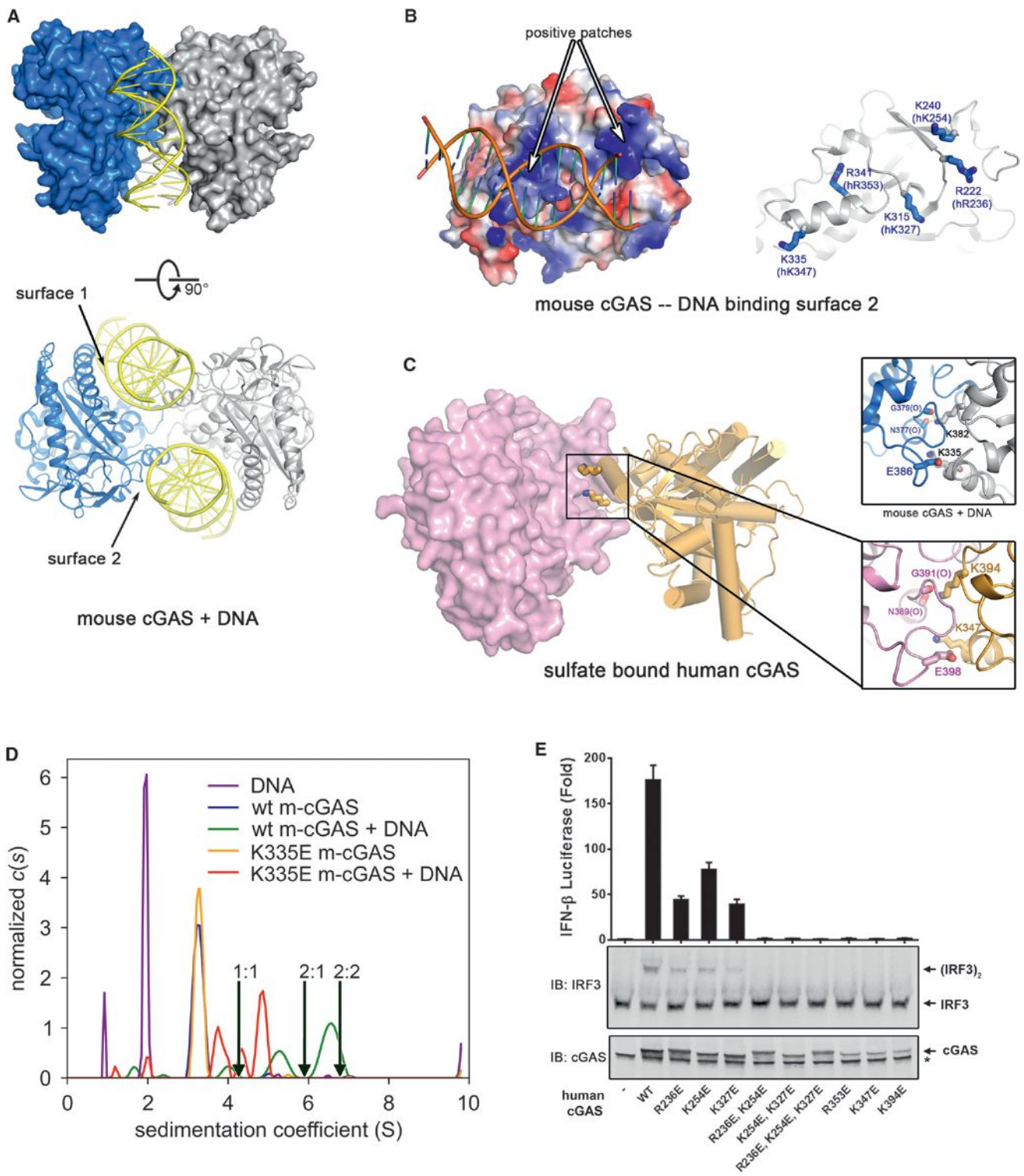


Figure 4. cGAS Forms a Functional 2:2 Complex with DNA

(A) Crystal structure of mouse cGAS in complex with a 16 bp dsDNA. Each asymmetric unit contains one 2:2 complex, composed of two protein molecules and two DNA molecules. Two perpendicular views are shown.

(B) Electrostatic representations of the DNA binding surface 2 of mouse cGAS (left). Conserved positively charged residues are shown on the right, with the corresponding residues in human cGAS shown in parentheses.

(legend continued on next page)

residues in DNA binding surfaces 1 and 2, respectively. In addition, our results reveal the activation loop of cGAS that is important for switching on the active-site rearrangement in response to DNA binding. Future studies should determine whether and how the formation of the cGAS oligomeric complex is regulated in cells to provide a sensitive and timely response to DNA that invades the cytoplasm.

EXPERIMENTAL PROCEDURES

Truncated human cGAS (147–522 in the apo form, and 161–522 in the 2′3′-cGAMP-bound form and sulfate-bound form) and mouse cGAS (147–507) were expressed in *E. coli* BL21 (DE3) pLysS as cleavable SUMO fusion proteins. The recombinant proteins were purified by Ni²⁺-nitrilotriacetate affinity resin (QIAGEN) followed by SUMO protease digestion at 4°C overnight. Further purification was applied on a Heparin column (GE Healthcare). The peak fractions of the protein were collected and concentrated to 6 mg/ml for crystallization trials. The selenomethionine-derivatized protein was purified similarly as described above. All of the crystals were grown at 20°C by the hanging-drop vapor diffusion method. The data were collected at 19-ID at the Advanced Photon Source (APS) or by using a Rigaku FR-E copper rotating-anode generator and an R-Axis IV²⁺ imaging-plate area detector (Rigaku Americas). The data were integrated and scaled with the HKL2000 package (Otwinowski and Minor, 1997). Initial phases were generated using anomalous differences of a 2.95 Å Se derivative data set by single-wavelength anomalous dispersion (SAD). The phase information was improved by MR-SAD using another 2.45 Å Se derivative data set. The initial model was built using the Autobuild suite aided by manual correction of the coordinates in COOT (Emsley et al., 2010). The cGAMP-bound cGAS and sulfate-bound cGAS structures were determined by MR using apo cGAS as the search model. The mouse cGAS DNA complex structure was solved by MR using 4K98 as the search model. AUC experiments were carried out using a Beckman Coulter Optima XL-I ultracentrifuge with samples in a buffer containing 25 mM Tris pH 8.0 and 25 mM NaCl. Data were acquired using both interference optics and absorbance optics. To test the IFN β -inducing ability of different cGAS mutants, expression plasmids were transfected into HEK293T-STING-IFN β luciferase reporter cells. After 24 hr of transfection, the lysate was used to measure firefly luciferase activity (Promega).

See the Supplemental Experimental Procedures for details.

ACCESSION NUMBERS

The coordinates of the structures of cGAS in its apo- and ligand-bound forms have been deposited in the RCSB PDB under the following accession numbers 4O68 (human cGAS alone), 4O69 (sulfate-bound human cGAS), 4O67 (2′3′-cGAMP-bound human cGAS), and 4O6A (DNA-bound mouse cGAS).

SUPPLEMENTAL INFORMATION

Supplemental Information includes Supplemental Experimental Procedures, four figures, one table, and four movies and can be found with this article online at <http://dx.doi.org/10.1016/j.celrep.2014.01.003>.

(C) Sulfate-bound human cGAS forms a dimer in the crystal (left); residues involved in the dimer interface of this structure (lower right) are identical to those in the mouse cGAS-DNA complex (upper right).

(D) AUC of m-cGAS and DNA. Shown are c(s) distributions for various combinations of WT or K335E m-cGAS in the presence or absence of DNA. A distribution for DNA alone is also shown. The following concentrations were used: DNA alone, 120 μ M; WT m-cGAS, 80 μ M; WT m-cGAS/DNA, 80 and 120 μ M, respectively; K335E m-cGAS, 94 μ M; and K335E m-cGAS/DNA, 94 μ M and 120 μ M, respectively. All of the distributions have been normalized by the total interference signal (in fringes) present in the respective experiments. The arrows show the theoretical sedimentation coefficients of 1:1, 2:1, and 2:2 protein/DNA complexes.

(E) The second DNA binding surface and the protein-protein interface are important for cGAS activity. Expression vectors encoding WT or mutant human cGAS proteins as indicated were transfected into HEK293T-STING-IFN β luciferase reporter cells, followed by measurement of luciferase activities (top). Aliquots of the cell extracts were immunoblotted with an IRF3 antibody following native gel electrophoresis (middle) or with a cGAS antibody following SDS-PAGE (bottom). The error bars represent variation ranges of duplicate experiments.

See also Figure S4 and Movie S4.

ACKNOWLEDGMENTS

We thank Drs. Diana Tomchick and Thomas Scheuermann at UT Southwestern Medical Center for assistance in crystallography and AUC experiments, respectively. Results shown in this report are derived from work performed at the Advanced Photon Source, Structural Biology Center at Argonne National Laboratory. Argonne is operated by University of Chicago Argonne, LLC, for the Office of Biological and Environmental Research, U.S. Department of Energy, under contract DE-AC02-06CH11357. This work was supported by an NIH grant (AI-093967) to Z.J.C. and an international graduate student fellowship from the Howard Hughes Medical Institute (HHMI) to J.W. Z.J.C. is an investigator of the HHMI.

Received: December 3, 2013

Revised: December 20, 2013

Accepted: January 2, 2014

Published: January 23, 2014

REFERENCES

- Ablasser, A., Goldeck, M., Cavlar, T., Deimling, T., Witte, G., Röhl, I., Hopfner, K.P., Ludwig, J., and Hornung, V. (2013). cGAS produces a 2′-5′-linked cyclic dinucleotide second messenger that activates STING. *Nature* 498, 380–384.
- Balbo, A., Minor, K.H., Velikovskiy, C.A., Mariuzza, R.A., Peterson, C.B., and Schuck, P. (2005). Studying multiprotein complexes by multisignal sedimentation velocity analytical ultracentrifugation. *Proc. Natl. Acad. Sci. USA* 102, 81–86.
- Barber, G.N. (2011). Cytoplasmic DNA innate immune pathways. *Immunol. Rev.* 243, 99–108.
- Civril, F., Deimling, T., de Oliveira Mann, C.C., Ablasser, A., Moldt, M., Witte, G., Hornung, V., and Hopfner, K.P. (2013). Structural mechanism of cytosolic DNA sensing by cGAS. *Nature* 498, 332–337.
- DeLano, W.L. (2002). The PyMOL Molecular Graphics System. <http://www.pymol.org>.
- Diner, E.J., Burdette, D.L., Wilson, S.C., Monroe, K.M., Kellenberger, C.A., Hyodo, M., Hayakawa, Y., Hammond, M.C., and Vance, R.E. (2013). The innate immune DNA sensor cGAS produces a noncanonical cyclic dinucleotide that activates human STING. *Cell Rep* 3, 1355–1361.
- Emsley, P., Lohkamp, B., Scott, W.G., and Cowtan, K. (2010). Features and development of Coot. *Acta Crystallogr. D Biol. Crystallogr.* 66, 486–501.
- Endicott, J.A., Noble, M.E., and Johnson, L.N. (2012). The structural basis for control of eukaryotic protein kinases. *Annu. Rev. Biochem.* 81, 587–613.
- Gao, D., Wu, J., Wu, Y.-T., Du, F., Aroh, C., Yan, N., Sun, L., and Chen, Z.J. (2013a). Cyclic GMP-AMP synthase is an innate immune sensor of HIV and other retroviruses. *Science* 341, 903–906.
- Gao, P., Ascano, M., Wu, Y., Barchet, W., Gaffney, B.L., Zillinger, T., Serganov, A.A., Liu, Y., Jones, R.A., Hartmann, G., et al. (2013b). Cyclic [G(2′,5′)ppA(3′,5′)p] is the metazoan second messenger produced by DNA-activated cyclic GMP-AMP synthase. *Cell* 153, 1094–1107.
- Ishikawa, H., and Barber, G.N. (2008). STING is an endoplasmic reticulum adaptor that facilitates innate immune signalling. *Nature* 455, 674–678.

- Jeong, S.Y., Kumagai, A., Lee, J., and Dunphy, W.G. (2003). Phosphorylated claspin interacts with a phosphate-binding site in the kinase domain of Chk1 during ATR-mediated activation. *J. Biol. Chem.* *278*, 46782–46788.
- Kato, K., Ishii, R., Goto, E., Ishitani, R., Tokunaga, F., and Nureki, O. (2013). Structural and functional analyses of DNA-sensing and immune activation by human cGAS. *PLoS ONE* *8*, e76983.
- Kranzusch, P.J., Lee, A.S., Berger, J.M., and Doudna, J.A. (2013). Structure of human cGAS reveals a conserved family of second-messenger enzymes in innate immunity. *Cell Rep* *3*, 1362–1368.
- Li, X., Shu, C., Yi, G., Chaton, C.T., Shelton, C.L., Diao, J., Zuo, X., Kao, C.C., Herr, A.B., and Li, P. (2013a). Cyclic GMP-AMP synthase is activated by double-stranded DNA-induced oligomerization. *Immunity* *39*, 1019–1031.
- Li, X.-D., Wu, J., Gao, D., Wang, H., Sun, L., and Chen, Z.J. (2013b). Pivotal roles of cGAS-cGAMP signaling in antiviral defense and immune adjuvant effects. *Science* *341*, 1390–1394.
- Otwinowski, Z., and Minor, W. (1997). Processing of X-ray diffraction data collected in oscillation mode. *Methods Enzymol.* *276*, 307–326.
- Padrick, S.B., Deka, R.K., Chuang, J.L., Wynn, R.M., Chuang, D.T., Norgard, M.V., Rosen, M.K., and Brautigam, C.A. (2010). Determination of protein complex stoichiometry through multisignal sedimentation velocity experiments. *Anal. Biochem.* *407*, 89–103.
- Rehwinkel, J., and Reis e Sousa, C. (2010). RIGorous detection: exposing virus through RNA sensing. *Science* *327*, 284–286.
- Schuck, P. (2010). Sedimentation patterns of rapidly reversible protein interactions. *Biophys. J.* *98*, 2005–2013.
- Sun, L., Wu, J., Du, F., Chen, X., and Chen, Z.J. (2013). Cyclic GMP-AMP synthase is a cytosolic DNA sensor that activates the type I interferon pathway. *Science* *339*, 786–791.
- Takeuchi, O., and Akira, S. (2010). Pattern recognition receptors and inflammation. *Cell* *140*, 805–820.
- Tanaka, Y., and Chen, Z.J. (2012). STING specifies IRF3 phosphorylation by TBK1 in the cytosolic DNA signaling pathway. *Sci. Signal.* *5*, ra20.
- Tanaka, N., Smith, P., and Shuman, S. (2010). Structure of the RNA 3'-phosphate cyclase-adenylate intermediate illuminates nucleotide specificity and covalent nucleotidyl transfer. *Structure* *18*, 449–457.
- Wu, J., Sun, L., Chen, X., Du, F., Shi, H., Chen, C., and Chen, Z.J. (2013). Cyclic GMP-AMP is an endogenous second messenger in innate immune signaling by cytosolic DNA. *Science* *339*, 826–830.
- Yoneyama, M., and Fujita, T. (2009). RNA recognition and signal transduction by RIG-I-like receptors. *Immunol. Rev.* *227*, 54–65.
- Zhang, X., Shi, H., Wu, J., Zhang, X., Sun, L., Chen, C., and Chen, Z.J. (2013). Cyclic GMP-AMP containing mixed phosphodiester linkages is an endogenous high-affinity ligand for STING. *Mol. Cell* *51*, 226–235.

Simple and Rapid In Vivo Generation of Chromosomal Rearrangements using CRISPR/Cas9 Technology

Rafael B. Blasco,^{1,4} Elif Karaca,^{1,4} Chiara Ambrogio,² Taek-Chin Cheong,¹ Emre Karayol,¹ Valerio G. Minero,³ Claudia Voena,^{1,3} and Roberto Chiarle^{1,3,*}

¹Department of Pathology, Boston Children's Hospital and Harvard Medical School, Boston, MA 02115, USA

²Molecular Oncology Program, Centro Nacional de Investigaciones Oncológicas, 28029 Madrid, Spain

³Department of Molecular Biotechnology and Health Sciences, University of Torino, 10126 Torino, Italy

⁴Co-first author

*Correspondence: roberto.chiarle@childrens.harvard.edu

<http://dx.doi.org/10.1016/j.celrep.2014.10.051>

This is an open access article under the CC BY-NC-ND license (<http://creativecommons.org/licenses/by-nc-nd/3.0/>).

SUMMARY

Generation of genetically engineered mouse models (GEMMs) for chromosomal translocations in the endogenous loci by a knockin strategy is lengthy and costly. The CRISPR/Cas9 system provides an innovative and flexible approach for genome engineering of genomic loci in vitro and in vivo. Here, we report the use of the CRISPR/Cas9 system for engineering a specific chromosomal translocation in adult mice in vivo. We designed CRISPR/Cas9 lentiviral vectors to induce cleavage of the murine endogenous *Eml4* and *Alk* loci in order to generate the *Eml4-Alk* gene rearrangement recurrently found in non-small-cell lung cancers (NSCLCs). Intratracheal or intrapulmonary inoculation of lentiviruses induced *Eml4-Alk* gene rearrangement in lung cells in vivo. Genomic and mRNA sequencing confirmed the genome editing and the production of the *Eml4-Alk* fusion transcript. All mice developed *Eml4-Alk*-rearranged lung tumors 2 months after the inoculation, demonstrating that the CRISPR/Cas9 system is a feasible and simple method for the generation of chromosomal rearrangements in vivo.

INTRODUCTION

Chromosomal rearrangements are key causative events in several types of human cancers (Gostissa et al., 2011; Mitelman et al., 2007). The generation of genetically engineered mouse models (GEMMs) that faithfully recapitulate chromosomal rearrangements have been instrumental to advance the understanding of the biology and therapy of cancer (Rabbitts et al., 2001). However, design and generation of GEMMs for chromosomal rearrangements targeted in the endogenous loci is expensive and time consuming. The bacterial type II clustered regularly interspaced short palindromic repeat (CRISPR)/CRISPR-associated (Cas) systems have recently shown great potential for RNA-

guided genome editing, including multiplexing genome engineering (Cong et al., 2013; Mali et al., 2013), homologous recombination and gene targeting (Wang et al., 2013; Yang et al., 2013), and regulation of transcription (Gilbert et al., 2013). CRISPR/Cas9 systems have been successfully used for precise genome editing in mouse embryonic stem cells (ESCs) and targeted biallelic mutagenesis in F0 zebrafish (Jao et al., 2013; Wang et al., 2013; Yang et al., 2013). Recently, CRISPR-Cas9 systems have been used to efficiently edit the genome of adult mice in vivo in liver and muscle (Long et al., 2014; Xue et al., 2014; Yin et al., 2014).

The RNA-guided Cas9 endonuclease induces sequence-specific DNA double-strand breaks (DSBs) that are repaired mostly by the classical and alternative nonhomologous end-joining pathways (c-NHEJ or AEJ) or by homology-directed repair (HDR) (Boboila et al., 2012). The DSB repair mediated by end-joining pathways can lead to insertion/deletion (indel) mutations, but it can also be inappropriately resolved into a chromosomal rearrangement (Alt et al., 2013; Chiarle et al., 2011; Klein et al., 2011). During the last few years, several studies demonstrated that DSBs generated by genome editing tools like zinc-finger nucleases (ZFNs) and transcription activator-like effector nucleases (TALENs) can be resolved into chromosomal rearrangements in human cell lines (Brunet et al., 2009; Lee et al., 2012; Piganeau et al., 2013) and zebrafish (Gupta et al., 2013; Xiao et al., 2013). Similarly, recent reports in cell lines in vitro demonstrated the potential application of the CRISPR/Cas9 system to induce, at high frequency, targeted cancer-associated chromosomal rearrangements in human cell lines, such as *EML4-ALK*, *CD74-ROS1*, *KIF5B-RET*, *EWSR1-FLI1*, and *AML1-ETO* rearrangements, by designing pairs of specific guide RNAs for the loci of interest (Choi and Meyerson, 2014; Torres et al., 2014).

EML4-ALK rearrangement is found in about 5%–7% of non-small-cell lung cancers (NSCLCs) and is one of the most frequent rearrangements in solid human cancers (Chiarle et al., 2008; Soda et al., 2007). In NSCLC, the *EML4-ALK* rearrangement is generated by an inversion of a chromosomal segment of ~12 Mb on human chromosome 2 with breakpoints in intron 19 of the human *ALK* gene and variable breakpoints in the *EML4* gene, the most frequent being in intron 13 (Mano, 2008). This chromosomal inversion generates an *EML4-ALK* fusion protein

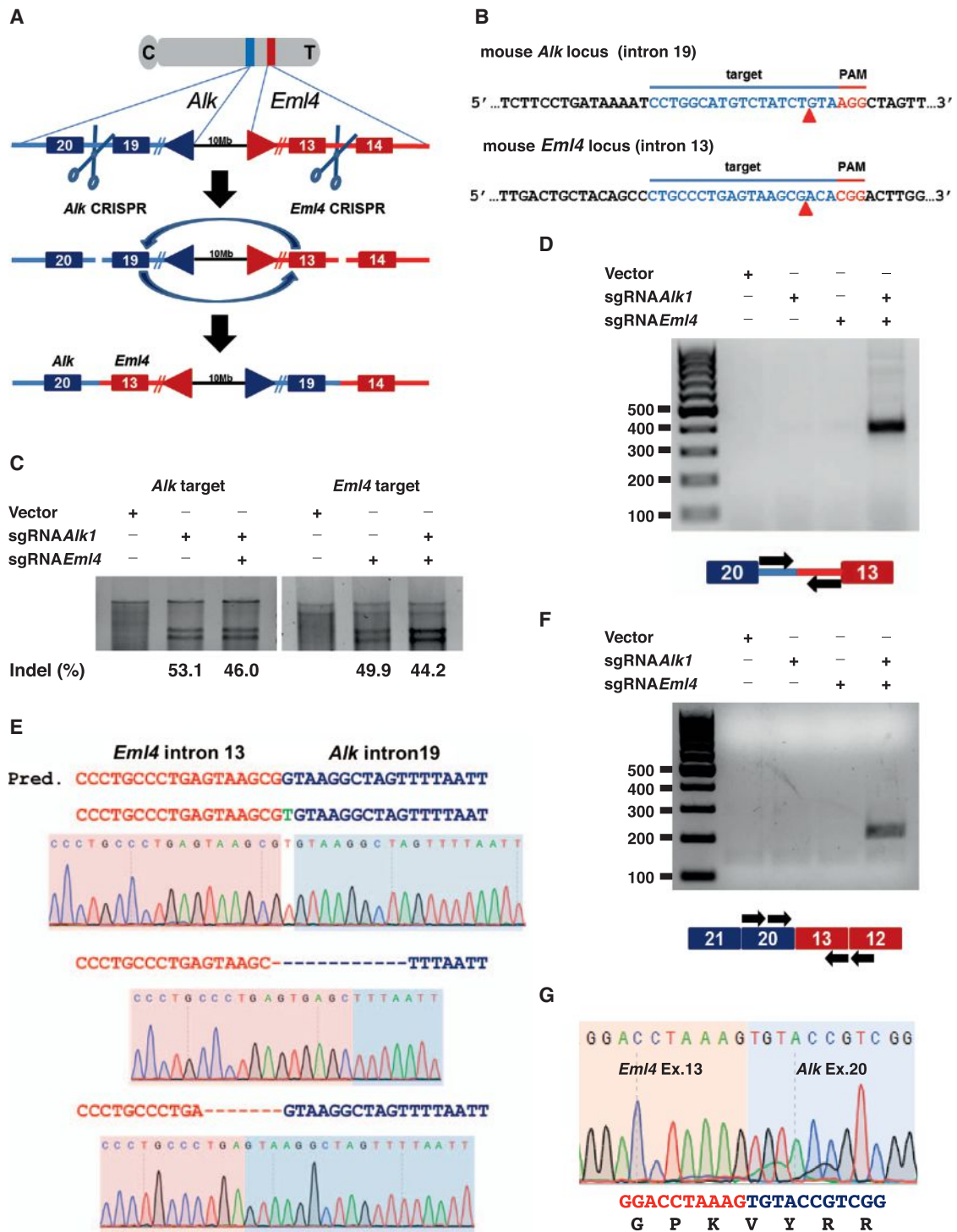


Figure 1. Generation of *Eml4-Alk* Rearrangements by the CRISPR/Cas9 System in Mouse Cells In Vitro

(A) Schematic representation of the CRISPR/Cas9-generated DSBs in the intron 19 of the *Alk* locus and in intron 13 of the *Eml4* locus. Simultaneous generation of DSBs induces a chromosomal inversion of ~10 Mb, leading to the generation of the *Eml4-Alk* chromosomal rearrangement.

(B) Schematic representation of base pairing between *Alk* and *Eml4* genomic loci and targeting sgRNAs. Red arrow indicates putative cleavage site.

(C) SURVEYOR assay for CRISPR/Cas9-mediated indels in the *Alk* and *Eml4* genomic loci.

(D) Detection of *Eml4-Alk* rearrangements by PCR on genomic DNA extracted from ASB-XIV lung cell line transduced with lentivirus expressing the Cas9 nuclease (vector) alone or together with *Eml4* or *Alk* sgRNA. Black arrows indicate PCR primers designed in intron 19 of the *Alk* locus and intron 13 of the *Eml4* locus.

(legend continued on next page)

that has constitutive tyrosine kinase activity that drives NSCLC growth (Chiarle et al., 2008; Shaw and Engelman, 2013).

In this study, we show the CRISPR/Cas9 system can be exploited to directly engineer *Eml4-Alk* rearrangements in vivo in adult mice. As a consequence of *Eml4-Alk* rearrangement induction, mice developed lung tumors within a short period of time. Therefore, this approach represents a simple and cost-effective method to model chromosomal rearrangements that could be used as an alternative to classical transgenic or knockin mice for a variety of biological and cancer studies.

RESULTS

Generation of *Eml4-Alk* Rearrangements and *Eml4-Alk* Fusion mRNA In Vitro by the CRISPR/Cas9 System

We engineered lentiviral vectors expressing Cas9 endonuclease and single-guide RNA (sgRNA) specific for either the *Eml4* or the *Alk* mouse genomic locus. As the mouse *Eml4* gene has a non-coding exon 1, which is lacking in human *EML4*, we designed sgRNAs to target intron 14 of the mouse *Eml4* gene, which is the equivalent of intron 13 of the human *EML4* gene. However, for parallelism with the human *EML4-ALK* rearrangement in NSCLC, in this paper, we will refer to this as intron 13. In the mouse *Alk* gene, the sgRNAs were designed to target intron 19 as in human *EML4-ALK* rearrangements, in order to generate DSBs in that position and eventually obtain a chromosomal breakpoint comparable to those found in human NSCLC (Figures 1A and 1B). Out of several independent sgRNAs, we selected the most efficient sequences by SURVEYOR assay for further use (Cong et al., 2013) (Figure 1C).

Next, we tested whether the combination of the two lentiviruses encoding *Eml4* and *Alk* sgRNAs would induce *Eml4-Alk* rearrangements at detectable frequency in murine cells. We transduced either murine immortalized tail fibroblasts or a murine lung carcinoma cell line (ASB-XIV) with single or both lentiviruses. Six days after transduction, the genomic product corresponding to the *Eml4-Alk* rearrangement was readily detectable in both cell types only when both *Eml4* and *Alk* sgRNA lentiviruses were used (Figures 1D and S1A). We Sanger sequenced several independent genomic breakpoint junctions to show that the CRISPR/Cas9 system can generate either precise genomic junctions originated by direct repair of the predicted DNA cleavage sites (three bases on the 5' end of the PAM sequence) or junctions with base insertions or deletions, a process consistent with editing by NHEJ (Alt et al., 2013) (Figure 1E). As predicted by the genomic breakpoint, such engineered *Eml4-Alk* rearrangements should produce in-frame fusion *Eml4-Alk* mRNA transcripts joining coding exons 1–13 of the *Eml4* gene and exons 20–29 of the *Alk* gene. Indeed, we detected in both cell lines mRNA fusion transcripts encoding for an in-frame *EML4-ALK* chimeric protein identical to that found in human NSCLC (Figures 1F, 1G, and S1B). Thus, the CRISPR/

Cas9 system can efficiently generate the desired chromosomal rearrangement by introducing DSBs in the targeted sites.

Other chromosomal events could be predicted as the result of the simultaneous activity of CRISPR/Cas9 on the *Eml4* and *Alk* loci located on the two alleles of chromosome 17. It is well known that DSBs generated by nucleases located in *cis* on the same chromosomal allele can result in deletions of the chromosome portion between the two DSBs in the immunoglobulin H (IgH) locus (Zarrin et al., 2007) as well as in other genomic loci (Gostissa et al., 2014). This general propensity of intrachromosomal DSBs to be frequently joined, even at long distances, could be the result of the nuclear architecture of chromosomal territories (Hakim et al., 2012; Zhang et al., 2012). Thus, we investigated whether intrachromosomal deletions were generated by the simultaneous activity of CRISPR/Cas9 on the *Eml4* and *Alk* genes (Figure S1C). Indeed, in both fibroblast and lung cells, we found genomic junctions that corresponded to a deletion of the 10 Mb region between the *Eml4* and *Alk* on chromosome 17 (Figure S2A). In addition to deletions, other complex chromosomal rearrangements could be also predicted, including the formation of dicentric or acentric chromosomes, when DSBs on both alleles of the *Eml4* or the *Alk* locus are joined (Figure S1C). However, we did not detect such rearrangements by PCR, indicating that they could be rare or alternatively be lost during cell replication because genetically unstable. Finally, we found genomic junctions between the intron 13 of *Eml4* and intron 19 of *Alk* (Figure S2B). These could be explained either as large 10 Mb deletion circles (Figure S1C) or as interchromosomal translocations with duplication of the 10 Mb region between the *Eml4* and the *Alk* loci (Figure S1C). Therefore, we concluded that engineering the genome with CRISPR/Cas9 system in two independent loci leads to several genomic rearrangements that can be predicted by the position of the targeted loci.

Generation of *Eml4-Alk* Rearrangements and *Eml4-Alk* Fusion mRNA In Vivo by the CRISPR/Cas9 System

Next, we tested whether *Eml4-Alk* rearrangements could be obtained in vivo in adult mice. Since *Eml4-Alk* rearrangements are mostly found in human NSCLC, we delivered lentiviral particles to lungs of adult mice either by intratracheal inoculation (Simpson et al., 2001) or by direct intrapulmonary injection (Onn et al., 2003) (Figure 2A). We inoculated mice with both lentiviruses expressing Cas9/*Alk* sgRNA and Cas9/*Eml4* sgRNA. As controls, we inoculated mice with lentiviruses expressing Cas9 without sgRNA or expressing *Eml4* sgRNA or *Alk* sgRNA alone. After 6 days of lentiviral inoculation, we took the lungs for DNA isolation in order to investigate the presence of *Eml4-Alk* rearrangements by PCR and sequencing. Following intratracheal inoculation or intrapulmonary injections, we detected *Eml4-Alk* rearrangements in mice injected with both *Eml4* and *Alk* sgRNAs, but not in controls (Figure 2B). The pattern of genomic junctions was similar to those obtained in cells in vitro, with perfect

(E) Examples of chromatograms showing a single base insertion, a microdeletion in the *Alk* intron, and a microdeletion in the *Eml4* intron. Red or blue dashes, deleted bases; green bases, insertions or mutations. Pred., sequence of the predicted genomic junction of *Eml4-Alk* rearrangement.

(F) Detection of *Eml4-Alk* fusion transcripts in ASB-XIV cell line transduced with lentiviral vectors as indicated in (D). RT-PCR shows a fusion transcript between exon13 of *Eml4* and exon 20 of *Alk* genes. Black arrows indicate the position of PCR primers.

(G) An example chromatogram showing the fusion transcripts producing an in-frame *EML4-ALK* chimeric protein.

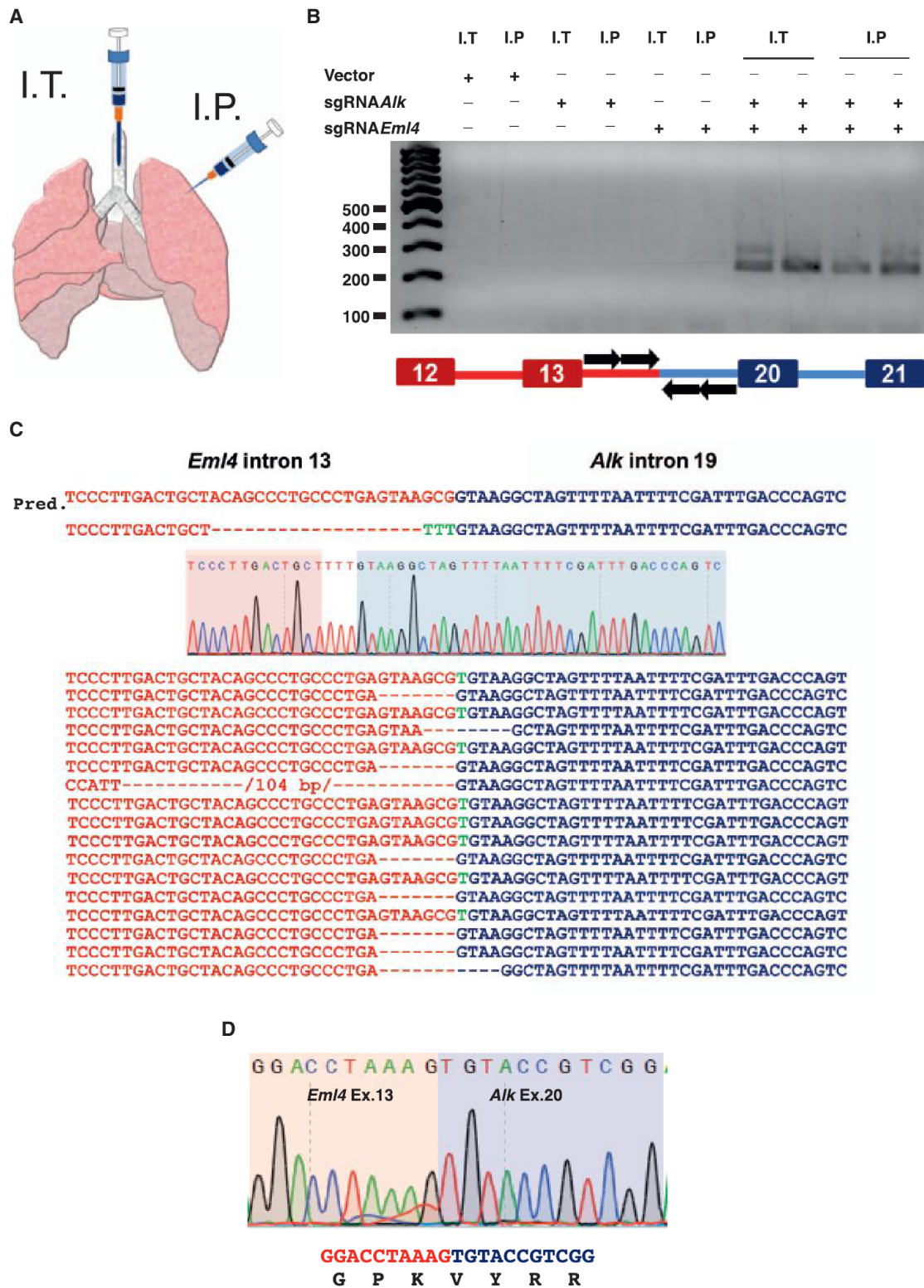


Figure 2. In Vivo Generation of *Eml4-Alk* Rearrangements in Mice

(A) Schematic diagrams showing intratracheal inoculations (I.T.) or intrapulmonary injections (I.P.) of CRISPR/Cas9 lentivirus and isolation of lung epithelial cells.

(legend continued on next page)

junctions or indels (Figure 2C). Remarkably, we also found in vivo genomic junctions corresponding to a 10 Mb deletion or to an interchromosomal translocation between the *Eml4* and *Alk* genomic loci (Figures S3A and S3B). To determine frequency of cells in vivo carrying the genomic *Eml4-Alk* rearrangement, or other genomic events such as 10 Mb deletions, after *Eml4* and *Alk* sgRNA lentiviral infection, we applied a technique previously used to determine the frequency in cell populations of chromosomal translocations such as IgH/c-*myc* in B lymphocytes (Chiarle et al., 2011). By this approach, in four independent mice, we found 17 *Eml4-Alk* rearrangements in 114 independent PCR reactions each from 10^5 cells. All the PCR products were sequenced and confirmed to have the expected genomic *Eml4-Alk* rearrangement. No *Eml4-Alk* rearrangements were found in 152 independent PCR reactions from control mice (i.e., in cells from mice infected with either empty or *Alk* sgRNA-only lentivirus). Thus, we calculated that the frequency of *Eml4-Alk* inversion in vivo was approximately 1.5 rearrangements/ 10^6 cells for the amount of lentivirus and the technique we used. When we studied the genomic product resulting from the 10 Mb deletion, we found and confirmed by sequencing PCR products corresponding to genomic deletion in 10 out of 38 independent PCR reactions from mice infected with both *Eml4* and *Alk* sgRNAs and in 0 out of 38 controls, giving an estimated frequency of 2.6 deletions/ 10^6 cells. Finally, by isolating mRNA, we found fusion transcripts coding for an in-frame EML4-ALK chimeric protein as predicted by the genomic breakpoint (Figure 2D). Thus, direct delivery of CRISPR/Cas9 elements to epithelial lung cells can efficiently generate DNA DSBs in vivo that are resolved into chromosomal rearrangements.

***Eml4-Alk* Inversion Induced by the CRISPR/Cas9 System Drives Tumor Development in Lungs**

A critical point was to determine whether the generation of *Eml4-Alk* rearrangements by the CRISPR/Cas9 system was sufficient to drive transformation of lung epithelial cells and therefore lung tumor formation. Transgenic expression of the human EML4-ALK cDNA under either a surfactant protein C (SPC) promoter (Soda et al., 2008) or under a bicistronic CC10-rTA doxycycline-inducible promoter (Chen et al., 2010) induces the formation of lung tumors. We also developed a GEMM with transgenic expression of human EML4-ALK under the SPC promoter and observed tumor formation with 100% penetrance. Tumor formation was further accelerated by heterozygous or homozygous deletion of *p53* (C.V. and R.C., unpublished data). Therefore, to investigate whether the generation of *Eml4-Alk* rearrangements was sufficient to induce lung tumor formation, we injected CRISPR/Cas9 lentivirus expressing *Eml4* and *Alk* sgRNAs in *p53^{+/-}* or *p53^{-/-}* mice. Mice were sacrificed 8 weeks after the injection, and lungs were analyzed for the presence of tumors by histology and immunohistochemistry. We found lung tumors in six out of six *p53^{-/-}* mice and in four out of four *p53^{+/-}* mice,

but not in control mice (zero out of three *p53^{-/-}* mice and zero out of three *p53^{+/-}* mice) (Figure 3A). Tumors were composed of atypical epithelial cells that showed a strong positivity for cytokeratin and a high proliferation index as determined by Ki-67 (Figure 3B). To investigate whether tumor expressed the EML4-ALK fusion protein, we performed immunohistochemistry (IHC) against ALK with an antibody that recognizes the mouse ALK protein. By this approach, we detected positive cells only in tumors from mice infected with *Eml4* and *Alk* sgRNAs, whereas normal lungs in control mice did not show detectable staining (Figure 3C). Next, we wanted to investigate whether such tumors indeed carried the engineered *Eml4-Alk* rearrangement at the genomic DNA. We first used laser capture microdissection (LCM) to dissect tumors and isolate genomic DNA for PCR analysis. As controls, we dissected similarly sized areas of lungs from control mice or from nontumoral areas adjacent to the tumors of mice injected with CRISPR/Cas9 lentivirus expressing *Eml4* and *Alk* sgRNAs. PCR amplification demonstrated the presence of the expected *Eml4-Alk* rearrangements only in the DNA extracted from tumors, but not in both types of controls (Figure 3E). Finally, sequencing of the genomic junction obtained from tumor DNA confirmed the expected *Eml4-Alk* rearrangement generated by DSBs initiated by CRISPR/Cas9 activity (Figure 3F).

DISCUSSION

We have described a simple, fast, and rather inexpensive technique to model oncogenic chromosomal rearrangements directly in adult mice and induce tumor formation. In principle, the CRISPR/Cas9 approach to engineer chromosomal rearrangements could be applied to most, if not all, chromosomal rearrangements as predicted by recent in vitro studies (Choi and Meyerson, 2014; Torres et al., 2014). This technique is embedded with great potential, but we showed that it is also associated with the formation of unwanted genomic rearrangements, such as genomic deletions and, possibly, duplications. Another caveat associated with the CRISPR/Cas9 system is the generation of undesired off-targeting, which appeared as an important concern in original in vitro studies, but it is probably less relevant in vivo (Duan et al., 2014; Hsu et al., 2013; Kuscu et al., 2014; Wu et al., 2014). Thus, all these elements must be carefully considered during the application of such technique to cancer studies.

We expect that this approach could be complementary or even replace time consuming approaches such as traditional knockin targeting of ESCs and lengthy crossing of GEMMs with different genetic backgrounds. Indeed, clear advantages implied by such approach are the possibility of using different cancer-relevant mouse genetic backgrounds for functional studies. To this end, we demonstrated the feasibility of engineering *Eml4-Alk* rearrangements in *p53^{-/-}* or *p53^{+/-}* mice, but virtually any viable mouse background could be used. We tested

(B) PCR assay 6 days after lentivirus injections demonstrates that *Eml4-Alk* rearrangements are detectable only in mice injected with CRISPR/Cas9 and *Eml4* and *Alk* sgRNA.

(C) An example chromatogram showing perfect *Eml4-Alk* genomic junction, as well as representative sequences of junctions identified from 17 out of 30 amplicons. Pred., sequence of the predicted genomic junction of *Eml4-Alk* rearrangement.

(D) Representative chromatogram of *Eml4-Alk* fusion transcripts obtained from mRNA extracted from lung cells in vivo.

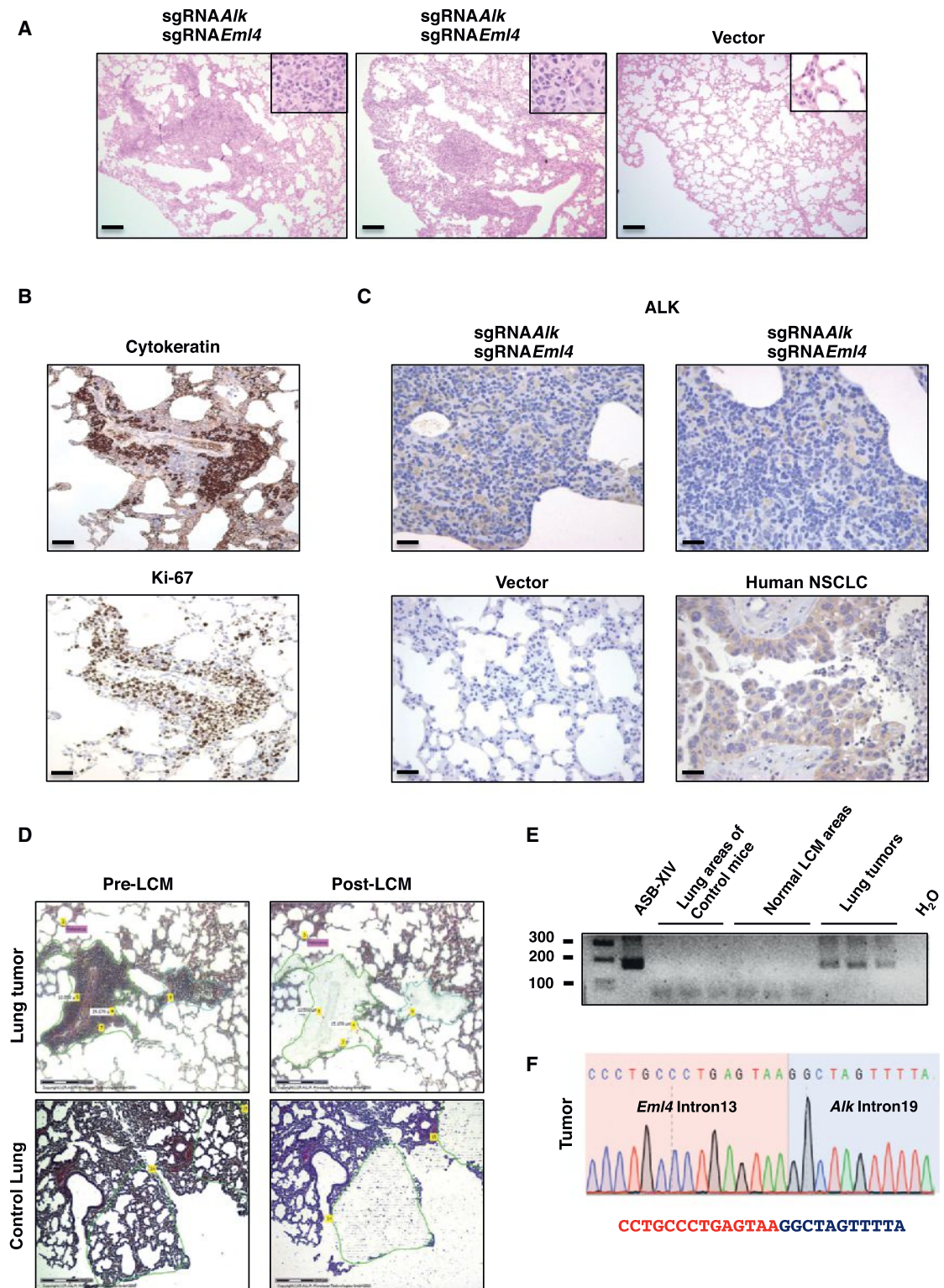


Figure 3. Lung Tumors Generated by CRISPR/Cas9-Induced *Em14-Alk* Rearrangements

(A) Representative histological sections of lung tumors in $p53^{+/-}$ mice after intrapulmonary injections with two CRISPR/Cas9 lentiviruses expressing the *Em14* and *Alk* sgRNAs. Control $p53^{+/-}$ mice were injected with a lentiviral vector expressing CRISPR/Cas9, but not sgRNAs. Objective magnification, 10 \times (inset, 40 \times). Scale bars represent 100 μ m.

(legend continued on next page)

wild-type (WT) mice, but at 8 weeks of age, we could only find small clusters of epithelial hyperplasia, possibly due to the slower tumor development in WT mice as compared to $p53^{-/-}$ or $p53^{+/-}$ mice. Thus, as compared to *Eml4-Alk* transgenic mice, in our system, CRISPR/Cas9-induced tumors were smaller and less frequent, possibly due to the lower expression levels of the *Eml4-Alk* fusion and the lower frequency of cells carrying the *Eml4-Alk* rearrangement. Recently, it has been shown that expressing both sgRNAs in one single adenoviral vector is efficient in inducing *Eml4-Alk* rearrangements and tumor development (Maddalo et al., 2014).

Additional applications could be envisioned as the possibility of combining several CRISPR/Cas9-mediated targeting for cancer studies. A recent work showed that in the liver of adult mice, the simultaneous disruption of *p53* and *PTEN* tumor suppressors induced tumor formation (Xue et al., 2014). Therefore, the possibility of combining CRISPR/Cas9-engineered chromosomal rearrangements with multiple targeted gene disruption of oncosuppressors or oncogenes could greatly facilitate and accelerate the study of the complexity of human cancers. The recent generation of a Cre-dependent Cas9 knockin combined with tissue-specific strains of Cre (Platt et al., 2014) could further expand the potential use of the CRISPR/Cas9 system in vivo, as several tissues such as nervous tissues or liver, skin, and bone marrow could be targeted by this technology. To this end, tissue-specific delivery methods to many organs could be easily adapted to the delivery of sgRNAs for the generation of a variety of tissue-specific genomic rearrangements.

EXPERIMENTAL PROCEDURES

Mice

All the animal experiments were approved by the Boston Children's Hospital (BCH) Institutional Animal Care and Use Committee. This review was conducted in accordance with the standards outlined in the National Research Council's *Guide for the Care and Use of Laboratory Animals* and BCH's PHS Assurance.

Cell Culture

Human embryonic kidney 293T (HEK293T) and ASB-XIV cell lines were grown in Dulbecco's modified Eagle's medium (DMEM) supplemented with 10% fetal bovine serum. Primary fibroblast cells were isolated from mouse tail, immortalized with SV40 and maintained in DMEM/Hank's solution.

CRISPR sgRNA Design and Cloning

Alk sgRNA and *Eml4* sgRNA targeted sites were designed manually and checked in silico. Oligomers were annealed and cloned in the BsmBI restriction site of pHKO5 in order to achieve stable expression (Ran et al., 2013). Sequences of *Alk* and *Eml4* sgRNAs are listed in Table S1.

Lentivirus Production and Purification

To produce the lentiviruses, HEK293T cells were seeded at ~70% confluence in 10 cm dishes the day before transfection in D10 media (DMEM supplemented with 10% fetal bovine serum). For each dish, 18 μ g of lentiCRISPR plasmid and 3.6 μ g of packaging plasmids (pVSV-G, REV, 8.74) were cotransfected into HEK293T cells using a calcium phosphate transfection kit (Clontech) following the manufacturer's recommended protocol. After 30 hr, viruses were harvested and concentrated by ultracentrifugation at 50,000 \times g for 2 hr at 4°C and resuspended with sterile 1X PBS. Aliquots were stored at -80°C. To evaluate the viral titers, we transduced ASB-XIV or mouse fibroblasts with increasing dilutions of the lentivirus and then selected cells with puromycin, as the lentiviral vectors express the puromycin resistance gene. Even if puromycin selection likely underestimates the number of infectious particles, by counting the numbers of puromycin-resistant cells, we calculated that our lentiviruses contained at least a titer of 1–2 \times 10⁶/ml infectious particles, with slight variations among different preparations. As we used 40 μ l of virus for each mouse inoculation, we estimated that we inoculated 4–8 \times 10⁴ infectious particles/mouse.

Cell Transduction, Puromycin Selection, and Surveyor Assays

For transduction of fibroblasts or ASB-XIV cells with CRISPR/Cas9 lentivirus, we seeded 2 \times 10⁴ fibroblasts or 8 \times 10⁴ ASB-XIV cells into six-well plates. After 24 hr, transduction was performed in fresh media supplemented with 8 μ g/ml polybrene (Sigma-Aldrich), and 48 hr later, optimal puromycin concentration was added for selection (6 μ g/ml for fibroblasts, 1 μ g/ml for ASB-XIV) until noninfected control group cells were completely dead. The SURVEYOR assay was performed as described previously (Cong et al., 2013). Primers used for PCR amplifications are indicated in Table S1.

In Vivo Lentiviral Transduction

Mice were inoculated with lentiviruses either by intratracheal inoculation (Simpson et al., 2001) or by direct intrapulmonary injection (Onn et al., 2003). Briefly, for intratracheal inoculation, a total volume of 40 μ l from the different lentiviral combinations was inoculated into 8-week-old BALB/c mice as previously described (Blasco et al., 2011). For intrapulmonary injections, 40 μ l volume was injected into the left lobule of 8-week-old mice as previously described (Onn et al., 2003). Mice were sacrificed 6 days after intratracheal inoculations or intrapulmonary injections for molecular studies and 8 weeks after intrapulmonary injections for tumor studies. DNA was obtained from the lungs of these mice following the classical phenol/chloroform extraction.

PCR and RT-PCR for *Eml4-Alk* Rearrangements

PCR reactions for the different types of genomic rearrangements were performed using DNA from transduced cell lines and lungs as indicated above. Primers used for PCR amplifications are indicated in Table S1. In vivo rearrangements were identified by nested PCR. In a first round of 18 cycles, 1 μ g of DNA was used for every reaction. In a second round of 25 cycles, 1 μ l of the previous round was used for every reaction. Primers used for PCR amplifications are indicated in Table S1.

For RT-PCR, cDNA synthesis was performed from extracted total RNA and nested PCR was performed for determining the mRNA fusion transcripts originating from the *Eml4-Alk* rearrangement. RT-PCR reactions were sequenced

(B) Immunohistochemical staining for cytokeratin AE1/AE3 (top) and the proliferation marker Ki-67 (bottom) of a representative lung tumor from a $p53^{+/-}$ mouse injected with two CRISPR/Cas9 lentiviruses expressing the *Eml4* and *Alk* sgRNAs.

(C) Immunohistochemical staining for ALK in two representative lung tumors from a $p53^{+/-}$ mouse injected with two CRISPR/Cas9 lentiviruses expressing the *Eml4* and *Alk* sgRNAs (top), healthy tissue from the same animals (bottom left), and a human ALK-rearranged NSCLC (bottom right).

(D) Representative tumor and healthy lung areas before (left) and after (right) LCM isolation. Scale bars represent 150 μ m.

(E) PCR assay on genomic DNA obtained from microdissected normal lung areas of mice injected with control CRISPR/Cas9 lentivirus (Lung areas of Control mice) or nontumoral areas and tumors from mice injected with CRISPR/Cas9 lentiviruses expressing both the *Eml4* and *Alk* sgRNAs (Normal LCM areas and Lung tumors) demonstrates the presence of *Eml4-Alk* rearrangements in lung tumors, but not in control samples. Gel depicts one representative experiment of LCM with three independent tumors out of four independent experiments. DNA from ASB-XIV cells infected with lentiviruses encoding both *Eml4* and *Alk* sgRNAs was used as a positive control for *Eml4-Alk* rearrangement.

(F) An example chromatogram showing an *Eml4-Alk* genomic junction in lung tumors from *Eml4/Alk* sgRNAs CRISPR/Cas9 lentivirus-injected mice.

to confirm the *Eml4-Alk* in frame fusion. Primers used for PCR amplifications are indicated in Table S1.

Immunohistochemistry and LCM

Formalin-fixed paraffin-embedded lung sections were stained with H&E and cytokeratin AE1/AE3 in order to unambiguously detect tumor cells. ALK immunostaining was performed using an anti-ALK rabbit monoclonal antibody (clone sp8, Abcam) and Ki-67 immunostaining with a rabbit monoclonal (clone SP6, Master Diagnostica). The consecutive sections were used for the LCM using a PALMMicroBeam System (Carl Zeiss) controlled with PALM Robosoftware. Approximately 300–500 microdissected cells per region (either tumor cells or normal lung) were captured into caps of 0.5 ml PCR tubes and stored at room temperature. DNA was extracted and processed for nested PCR. Primers used for PCR amplifications are indicated in Table S1.

SUPPLEMENTAL INFORMATION

Supplemental Information includes three figures and one table and can be found with this article online at <http://dx.doi.org/10.1016/j.celrep.2014.10.051>.

AUTHOR CONTRIBUTIONS

R.B.B. conceived the idea of using CRISPR/Cas9 for *Eml4-Alk* inversion in vivo, performed experiments, prepared the figures, and corrected the manuscript. E.K. provided ideas, performed experiments, and corrected the manuscript. C.A. performed the LCM experiment. T.C.C. contributed ideas. E.K., V.G.M., and C.V. helped with experiments. R.C. conceived, supported, and steered the project; provided ideas; and wrote the manuscript.

ACKNOWLEDGMENTS

We thank Feng Zhang and the members of his lab, Le Cong and Neville E. Sanjana, for sharing precious reagents and technical advice. We thank all the members of our lab for discussions and technical help. This work was supported by grants FP7 ERC-2009-StG (proposal 242965, “Lunely”), the Koch Institute-Dana-Farber/Harvard Cancer Center Bridge Project, Associazione Italiana per la Ricerca sul Cancro (AIRC) grant IG-12023, and International Association for Cancer Research (AICR) grant 12-0216. R.B.B. was supported by a fellowship from the Ramon Areces Foundation. C.A. is supported by a fellowship from the Asociación Española Contra el Cáncer (AECC).

Received: September 17, 2014

Revised: October 22, 2014

Accepted: October 24, 2014

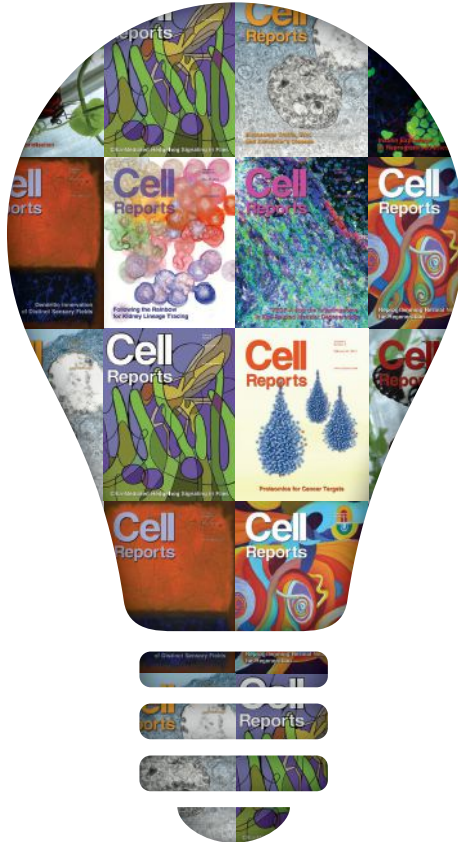
Published: November 13, 2014

REFERENCES

- Alt, F.W., Zhang, Y., Meng, F.L., Guo, C., and Schwer, B. (2013). Mechanisms of programmed DNA lesions and genomic instability in the immune system. *Cell* **152**, 417–429.
- Blasco, R.B., Francoz, S., Santamaría, D., Cañamero, M., Dubus, P., Charron, J., Baccarini, M., and Barbacid, M. (2011). c-Raf, but not B-Raf, is essential for development of K-Ras oncogene-driven non-small cell lung carcinoma. *Cancer Cell* **19**, 652–663.
- Boboila, C., Alt, F.W., and Schwer, B. (2012). Classical and alternative end-joining pathways for repair of lymphocyte-specific and general DNA double-strand breaks. *Adv. Immunol.* **116**, 1–49.
- Brunet, E., Simsek, D., Tomishima, M., DeKelver, R., Choi, V.M., Gregory, P., Urnov, F., Weinstock, D.M., and Jasin, M. (2009). Chromosomal translocations induced at specified loci in human stem cells. *Proc. Natl. Acad. Sci. USA* **106**, 10620–10625.
- Chen, Z., Sasaki, T., Tan, X., Carretero, J., Shimamura, T., Li, D., Xu, C., Wang, Y., Adelman, G.O., Capelletti, M., et al. (2010). Inhibition of ALK, PI3K/MEK, and HSP90 in murine lung adenocarcinoma induced by EML4-ALK fusion oncogene. *Cancer Res.* **70**, 9827–9836.
- Chiarle, R., Voena, C., Ambrogio, C., Piva, R., and Inghirami, G. (2008). The anaplastic lymphoma kinase in the pathogenesis of cancer. *Nat. Rev. Cancer* **8**, 11–23.
- Chiarle, R., Zhang, Y., Frock, R.L., Lewis, S.M., Molinie, B., Ho, Y.J., Myers, D.R., Choi, V.W., Compagno, M., Malkin, D.J., et al. (2011). Genome-wide translocation sequencing reveals mechanisms of chromosome breaks and rearrangements in B cells. *Cell* **147**, 107–119.
- Choi, P.S., and Meyerson, M. (2014). Targeted genomic rearrangements using CRISPR/Cas technology. *Nat Commun* **5**, 3728.
- Cong, L., Ran, F.A., Cox, D., Lin, S., Barretto, R., Habib, N., Hsu, P.D., Wu, X., Jiang, W., Marraffini, L.A., and Zhang, F. (2013). Multiplex genome engineering using CRISPR/Cas systems. *Science* **339**, 819–823.
- Duan, J., Lu, G., Xie, Z., Lou, M., Luo, J., Guo, L., and Zhang, Y. (2014). Genome-wide identification of CRISPR/Cas9 off-targets in human genome. *Cell Res.* **24**, 1009–1012.
- Gilbert, L.A., Larson, M.H., Morsut, L., Liu, Z., Brar, G.A., Torres, S.E., Stern-Ginossar, N., Brandman, O., Whitehead, E.H., Doudna, J.A., et al. (2013). CRISPR-mediated modular RNA-guided regulation of transcription in eukaryotes. *Cell* **154**, 442–451.
- Gostissa, M., Alt, F.W., and Chiarle, R. (2011). Mechanisms that promote and suppress chromosomal translocations in lymphocytes. *Annu. Rev. Immunol.* **29**, 319–350.
- Gostissa, M., Schwer, B., Chang, A., Dong, J., Meyers, R.M., Marecki, G.T., Choi, V.W., Chiarle, R., Zarrin, A.A., and Alt, F.W. (2014). IgH class switching exploits a general property of two DNA breaks to be joined incised over long chromosomal distances. *Proc. Natl. Acad. Sci. USA* **111**, 2644–2649.
- Gupta, A., Hall, V.L., Kok, F.O., Shin, M., McNulty, J.C., Lawson, N.D., and Wolfe, S.A. (2013). Targeted chromosomal deletions and inversions in zebrafish. *Genome Res.* **23**, 1008–1017.
- Hakim, O., Resch, W., Yamane, A., Klein, I., Kieffer-Kwon, K.R., Jankovic, M., Oliveira, T., Bothmer, A., Voss, T.C., Ansarah-Sobrinho, C., et al. (2012). DNA damage defines sites of recurrent chromosomal translocations in B lymphocytes. *Nature* **484**, 69–74.
- Hsu, P.D., Scott, D.A., Weinstein, J.A., Ran, F.A., Konermann, S., Agarwala, V., Li, Y., Fine, E.J., Wu, X., Shalem, O., et al. (2013). DNA targeting specificity of RNA-guided Cas9 nucleases. *Nat. Biotechnol.* **31**, 827–832.
- Jao, L.E., Wenthe, S.R., and Chen, W. (2013). Efficient multiplex biallelic zebrafish genome editing using a CRISPR nuclease system. *Proc. Natl. Acad. Sci. USA* **110**, 13904–13909.
- Klein, I.A., Resch, W., Jankovic, M., Oliveira, T., Yamane, A., Nakahashi, H., Di Virgilio, M., Bothmer, A., Nussenzweig, A., Robbiani, D.F., et al. (2011). Translocation-capture sequencing reveals the extent and nature of chromosomal rearrangements in B lymphocytes. *Cell* **147**, 95–106.
- Kuscu, C., Arslan, S., Singh, R., Thorpe, J., and Adli, M. (2014). Genome-wide analysis reveals characteristics of off-target sites bound by the Cas9 endonuclease. *Nat. Biotechnol.* **32**, 677–683.
- Lee, H.J., Kweon, J., Kim, E., Kim, S., and Kim, J.S. (2012). Targeted chromosomal duplications and inversions in the human genome using zinc finger nucleases. *Genome Res.* **22**, 539–548.
- Long, C., McAnally, J.R., Shelton, J.M., Mireault, A.A., Bassel-Duby, R., and Olson, E.N. (2014). Prevention of muscular dystrophy in mice by CRISPR/Cas9-mediated editing of germline DNA. *Science* **345**, 1184–1188.
- Maddalo, D., Machado, E., Concepcion, C.P., Bonetti, C., Vidigal, J.A., Han, Y.C., Ogdowski, P., Crippa, A., Rekhman, N., de Stanchina, E., et al. (2014). In vivo engineering of oncogenic chromosomal rearrangements with the CRISPR/Cas9 system. *Nature*, Published online October 22, 2014. <http://dx.doi.org/10.1038/nature13902>.
- Mali, P., Yang, L., Esvelt, K.M., Aach, J., Guell, M., DiCarlo, J.E., Norville, J.E., and Church, G.M. (2013). RNA-guided human genome engineering via Cas9. *Science* **339**, 823–826.
- Mano, H. (2008). Non-solid oncogenes in solid tumors: EML4-ALK fusion genes in lung cancer. *Cancer Sci.* **99**, 2349–2355.

- Mitelman, F., Johansson, B., and Mertens, F. (2007). The impact of translocations and gene fusions on cancer causation. *Nat. Rev. Cancer* 7, 233–245.
- Onn, A., Isobe, T., Itasaka, S., Wu, W., O'Reilly, M.S., Ki Hong, W., Fidler, I.J., and Herbst, R.S. (2003). Development of an orthotopic model to study the biology and therapy of primary human lung cancer in nude mice. *Clin. Cancer Res.* 9, 5532–5539.
- Piganeau, M., Ghezraoui, H., De Cian, A., Guittat, L., Tomishima, M., Perrouault, L., René, O., Katibah, G.E., Zhang, L., Holmes, M.C., et al. (2013). Cancer translocations in human cells induced by zinc finger and TALE nucleases. *Genome Res.* 23, 1182–1193.
- Platt, R.J., Chen, S., Zhou, Y., Yim, M.J., Swiech, L., Kempton, H.R., Dahlman, J.E., Parnas, O., Eisenhaure, T.M., Jovanovic, M., et al. (2014). CRISPR-Cas9 Knockin Mice for Genome Editing and Cancer Modeling. *Cell* 159, 440–455.
- Rabbitts, T.H., Appert, A., Chung, G., Collins, E.C., Drynan, L., Forster, A., Lobato, M.N., McCormack, M.P., Pannell, R., Spandidos, A., et al. (2001). Mouse models of human chromosomal translocations and approaches to cancer therapy. *Blood Cells Mol. Dis.* 27, 249–259.
- Ran, F.A., Hsu, P.D., Wright, J., Agarwala, V., Scott, D.A., and Zhang, F. (2013). Genome engineering using the CRISPR-Cas9 system. *Nat. Protoc.* 8, 2281–2308.
- Shaw, A.T., and Engelman, J.A. (2013). ALK in lung cancer: past, present, and future. *J. Clin. Oncol.* 31, 1105–1111.
- Simpson, A.J., Wallace, W.A., Marsden, M.E., Govan, J.R., Porteous, D.J., Haslett, C., and Sallenave, J.M. (2001). Adenoviral augmentation of elafin protects the lung against acute injury mediated by activated neutrophils and bacterial infection. *J. Immunol.* 167, 1778–1786.
- Soda, M., Choi, Y.L., Enomoto, M., Takada, S., Yamashita, Y., Ishikawa, S., Fujiwara, S., Watanabe, H., Kurashina, K., Hatanaka, H., et al. (2007). Identification of the transforming EML4-ALK fusion gene in non-small-cell lung cancer. *Nature* 448, 561–566.
- Soda, M., Takada, S., Takeuchi, K., Choi, Y.L., Enomoto, M., Ueno, T., Haruta, H., Hamada, T., Yamashita, Y., Ishikawa, Y., et al. (2008). A mouse model for EML4-ALK-positive lung cancer. *Proc. Natl. Acad. Sci. USA* 105, 19893–19897.
- Torres, R., Martin, M.C., Garcia, A., Cigudosa, J.C., Ramirez, J.C., and Rodriguez-Perales, S. (2014). Engineering human tumour-associated chromosomal translocations with the RNA-guided CRISPR-Cas9 system. *Nat Commun* 5, 3964.
- Wang, H., Yang, H., Shivalila, C.S., Dawlaty, M.M., Cheng, A.W., Zhang, F., and Jaenisch, R. (2013). One-step generation of mice carrying mutations in multiple genes by CRISPR/Cas-mediated genome engineering. *Cell* 153, 910–918.
- Wu, X., Scott, D.A., Kriz, A.J., Chiu, A.C., Hsu, P.D., Dadon, D.B., Cheng, A.W., Trevino, A.E., Konermann, S., Chen, S., et al. (2014). Genome-wide binding of the CRISPR endonuclease Cas9 in mammalian cells. *Nat. Biotechnol.* 32, 670–676.
- Xiao, A., Wang, Z., Hu, Y., Wu, Y., Luo, Z., Yang, Z., Zu, Y., Li, W., Huang, P., Tong, X., et al. (2013). Chromosomal deletions and inversions mediated by TALENs and CRISPR/Cas in zebrafish. *Nucleic Acids Res.* 41, e141.
- Xue, W., Chen, S., Yin, H., Tammela, T., Papagiannakopoulos, T., Joshi, N.S., Cai, W., Yang, G., Bronson, R., Crowley, D.G., et al. (2014). CRISPR-mediated direct mutation of cancer genes in the mouse liver. *Nature* 514, 380–384.
- Yang, H., Wang, H., Shivalila, C.S., Cheng, A.W., Shi, L., and Jaenisch, R. (2013). One-step generation of mice carrying reporter and conditional alleles by CRISPR/Cas-mediated genome engineering. *Cell* 154, 1370–1379.
- Yin, H., Xue, W., Chen, S., Bogorad, R.L., Benedetti, E., Grompe, M., Kotliansky, V., Sharp, P.A., Jacks, T., and Anderson, D.G. (2014). Genome editing with Cas9 in adult mice corrects a disease mutation and phenotype. *Nat. Biotechnol.* 32, 551–553.
- Zarrin, A.A., Del Vecchio, C., Tseng, E., Gleason, M., Zarin, P., Tian, M., and Alt, F.W. (2007). Antibody class switching mediated by yeast endonuclease-generated DNA breaks. *Science* 315, 377–381.
- Zhang, Y., McCord, R.P., Ho, Y.J., Lajoie, B.R., Hildebrand, D.G., Simon, A.C., Becker, M.S., Alt, F.W., and Dekker, J. (2012). Spatial organization of the mouse genome and its role in recurrent chromosomal translocations. *Cell* 148, 908–921.

Inspire your peers with Cell Reports



Breaking new ground? From molecular genetics to developmental neurobiology, *Cell Reports* publishes thought-provoking, cutting edge research spanning the spectrum of life sciences.

Cell Reports is an open access journal that offers the quality, rigor, and visibility you've come to expect from Cell Press.

Do you have a new biological insight? Submit your paper to *Cell Reports*.

For more information visit www.cell.com/cell-reports

An open access journal with impact.
From Cell Press.

Cell
Reports

Long-Term Health of Dopaminergic Neuron Transplants in Parkinson's Disease Patients

Penelope J. Hallett,¹ Oliver Cooper,¹ Damaso Sadi,² Harold Robertson,² Ivar Mendez,² and Ole Isacson^{1,*}

¹Neuroregeneration Research Institute, Harvard University and McLean Hospital, 115 Mill Street, Belmont, MA 02478, USA

²Division of Neurosurgery, Department of Anatomy and Neurobiology, and Department of Pharmacology, Dalhousie University and Queen Elizabeth II Health Sciences Centre, Halifax, NS B3H 3A7, Canada

*Correspondence: isacson@hms.harvard.edu

<http://dx.doi.org/10.1016/j.celrep.2014.05.027>

This is an open access article under the CC BY-NC-ND license (<http://creativecommons.org/licenses/by-nc-nd/3.0/>).

SUMMARY

To determine the long-term health and function of transplanted dopamine neurons in Parkinson's disease (PD) patients, the expression of dopamine transporters (DATs) and mitochondrial morphology were examined in human fetal midbrain cellular transplants. DAT was robustly expressed in transplanted dopamine neuron terminals in the reinnervated host putamen and caudate for at least 14 years after transplantation. The transplanted dopamine neurons showed a healthy and nonatrophied morphology at all time points. Labeling of the mitochondrial outer membrane protein Tom20 and α -synuclein showed a typical cellular pathology in the patients' own substantia nigra, which was not observed in transplanted dopamine neurons. These results show that the vast majority of transplanted neurons remain healthy for the long term in PD patients, consistent with clinical findings that fetal dopamine neuron transplants maintain function for up to 15–18 years in patients. These findings are critically important for the rational development of stem-cell-based dopamine neuronal replacement therapies for PD.

INTRODUCTION

There is a need to understand how transplanted neurons can survive despite ongoing disease processes in the brains of patients with Parkinson's disease (PD). Currently, there is some controversy surrounding the neural transplantation field and neuroscience research regarding interactions between potentially pathological toxic proteins as a cause of neurodegeneration, and the concept of "disease spread" from cell to cell (Desplats et al., 2009; Isacson and Mendez, 2010). The accumulation of Lewy-body-like inclusions in some transplanted fetal dopamine neurons after long-term survival (over a decade) in the PD brain has been described (Cooper et al., 2009; Kordower et al., 2008; Kurowska et al., 2011; Li et al., 2008). Such pathology is a rare occurrence, with only a very low frequency (~1%) of

grafted neuromelanin-containing neurons in cell suspension grafts exhibiting signs of α -synuclein pathology even 22 years after grafting (Kurowska et al., 2011). These isolated cell inclusions are not observed in all patients (Mendez et al., 2008) and are usually found in less than 1%–5% of transplanted neurons depending on the transplantation method used, and clinical and postmortem data indicate that this rare pathology does not affect overall graft function (Cooper et al., 2009; Isacson and Mendez, 2010). It has been suggested that such Lewy-body-like pathology is a product of protein transfer from the parkinsonian host brain to the transplanted fetal cells (Kurowska et al., 2011). However, α -synuclein pathology is not definitive for PD, and incidental α -synuclein pathology has also been reported in the normal aging brain, with frequencies of 8%–22.5% in normal aging and up to 34.8% in centenarians (Ding et al., 2006; Klos et al., 2006; Mikolaenko et al., 2005; Saito et al., 2004; Wakisaka et al., 2003). Experimental paradigms of oxidative stress (e.g., rotenone exposure) or neuroinflammation can also induce α -synuclein accumulation in dopamine neurons (Gao et al., 2008; Sherer et al., 2003).

Recent results from postmortem examinations of fetal ventral mesencephalic grafts in PD patients suggested that dopamine transporters (DATs) are downregulated in the transplanted dopamine neurons (Kordower et al., 2008; Kurowska et al., 2011), and that such changes (which also include reduction of the dopamine neuron phenotypic marker tyrosine hydroxylase [TH]) are indicative of neuronal dysfunction and PD pathophysiological changes in the transplanted neurons. Since a cell therapy approach holds considerable promise as a therapeutic strategy for PD (C.R. Freed et al., 2013, Soc. Neurosci., conference; Kefalopoulou et al., 2014; Ma et al., 2010; Mendez et al., 2005; Politis et al., 2010, 2012), it is important to address the status of transplanted fetal dopamine cells in more detail. In previous studies, we reported surgical, clinical, and histopathological data obtained in five patients with advanced idiopathic PD who had received intracerebral transplantation of fetal dopaminergic cell suspension grafts 4–14 years earlier (Cooper et al., 2009; Mendez et al., 2005, 2008). In those studies, therapeutic improvements were seen without clinical side effects, such as off-period dyskinesias. Postmortem examinations demonstrated that grafted dopaminergic neurons survived for up to 14 years posttransplantation. In the current study, we examined DAT expression as a measure of neuronal function, and the mitochondrial marker Tom20 (translocase of outer mitochondrial membrane 20 kDa)

to assess mitochondrial morphology, to further understand the long-term phenotypical characteristics of the transplanted dopamine neurons and potential effects of the aging of transplants.

RESULTS

Dopamine Transporter Localization and Expression in Transplanted Fetal Dopamine Neurons

In the present study, we assessed DAT immunostaining in 4- to 14-year-old grafts in five patients from our previously published series (Mendez et al., 2005, 2008) in order to further understand the long-term phenotypical characteristics of the transplanted dopamine neurons and potential effects of the aging of transplants.

We conducted immunofluorescence staining for DAT using a monoclonal antibody that recognizes the N terminus of DAT (Miller et al., 1997), and performed colabeling with a TH antibody to label dopaminergic neurons and fibers. A general assessment of the integrity of the grafted TH-immunoreactive neurons in all patients revealed cells with a healthy appearance, including a robust cell soma and absence of signs of atrophy (Figures 1A–1C, 1F–1H, 1K–1M, and 1P–1R). In two independent patients at 4 years posttransplantation (Figures 1A–1J), an examination of DAT/TH immunostaining at low magnification (Figures 1A and 1F) showed dense DAT and TH expression in the reinnervated putamen and caudate in areas both near to and farther away from the graft. Although DAT was also expressed in the grafted cell soma, the intense punctate staining pattern in the reinnervated areas was most striking (Figures 1B and 1G). This expression, consistent with that of synaptic proteins, was easily observed at high magnification (Figures 1C, 1D, 1H, and 1I) where DAT was localized along TH-immunoreactive fibers.

To determine whether DAT expression was maintained in the long term, we examined DAT immunolabeling in transplanted neurons at 9 years and 14 years posttransplantation (Figures 1K–1T). As also seen at the younger time points, a robust punctate expression in the reinnervated striatum was observed (Figures 1K–1M and 1P–1R) and higher-magnification imaging verified the coexpression of DAT puncta along TH-immunoreactive dopaminergic fibers (Figures 1N and 1S). The intensity of DAT immunofluorescence was quantified in the reinnervated putamen at 4–14 years after transplantation (Figure S1) and compared with DAT labeling intensity in the contralateral (non-transplanted) putamen from subject 2. As expected, very low levels of DAT labeling in the nontransplanted parkinsonian putamen were observed, consistent with the severe loss of DAT expression in the putamen in PD (Miller et al., 1997). In contrast, at 4, 9, and 14 years after transplantation, DAT expression was significantly increased within the grafted putamen.

Parallel control immunostainings in which the primary antibodies were omitted showed no immunoreactivity of DAT or TH (data not shown). To further confirm the specificity of the DAT labeling observed in the reinnervated putamen and caudate, we also examined DAT immunolabeling in adjacent anatomical regions on the same tissue sections (see Figure 1). As expected, in the lateral and medial globi pallidi, which are regions that receive comparatively little dopaminergic innervation

and normally exhibit little DAT expression in the human brain (Ciliax et al., 1999), we observed weak DAT immunolabeling and a sharp boundary from high to low DAT and TH expression (Figures 1E, 1J, 1O, and 1T).

Mitochondrial Localization and Expression in Transplanted Fetal Dopamine Neurons

Tom20 was used to label mitochondria in grafted neurons and also in the host substantia nigra and globus pallidus. In the remaining substantia nigra TH-immunoreactive neurons from PD patients (subjects 2, 5, and 6; Figures 2A, 2A', 2D, 2D', 2G, and 2G'), Tom20 labeling often appeared intensely labeled in the cell soma, with accumulation in the perinuclear area and little immunostaining in the axon and processes. In neurons costained with Tom20 and α -synuclein, the host patient's substantia nigra showed Lewy bodies and variable or reduced distribution of Tom20-stained mitochondria (Figure 3A). In grafted TH-immunoreactive neurons at 4 years posttransplantation (Figures 2B and 2B'), Tom 20 immunostaining was robust in the perikarya and neuronal processes, similar to what was observed in the normal brain. At 9 and 14 years posttransplantation, Tom20 labeling was generally less intense in the grafted TH-immunoreactive neurons (Figures 2E, 2E', 2H, and 2H') compared with the Tom20 staining pattern observed in subject 2 at 4 years posttransplantation; however, there was no abnormal accumulation of mitochondria in the cell soma as was observed in the host substantia nigra. The localization of Tom20 in neurons within the host medial globus pallidus (Figures 2C, 2F, and 2I) exhibited a homogeneous localization throughout the cell soma and processes, and showed no evidence of abnormal perinuclear accumulation as was observed in the patients' own substantia nigra. In neurons within the transplants costained with Tom20 and α -synuclein, a normal distribution of Tom20 staining was observed in the absence of Lewy bodies (Figures 3B–3D).

DISCUSSION

Efficacious fetal ventral mesencephalic grafts can reduce both PD motor symptoms and levodopa-induced dyskinesia for many years, and can reduce or negate the requirement for dopamine replacement therapy. Months to years are required for the newly replaced dopaminergic neurons to mature, integrate into the host brain, and function (Barker et al., 2013), and most fetal ventral mesencephalic cell transplants provide improvement in PD motor symptoms starting at ~1 year after transplantation (Evans et al., 2012). However, successful transplants can survive and function for many years. Recent studies by Kefalopoulou et al. (2014) and Politis et al. (2010, 2012) described two patients who were still improving (as shown by PET neuroimaging of dopamine uptake and reduction of the Unified Parkinson's Disease Rating Scale score) more than 18 years after they had undergone transplantation of fetal ventral mesencephalic cells.

The study presented here shows long-term graft survival in PD patients with maintained DAT localization along TH-immunoreactive axons in the reinnervated striatum, indicating functional dopaminergic neurons. Abnormalities in mitochondrial localization, as indicated by accumulation in the cell soma in dopaminergic neurons in the host substantia nigra, were not observed

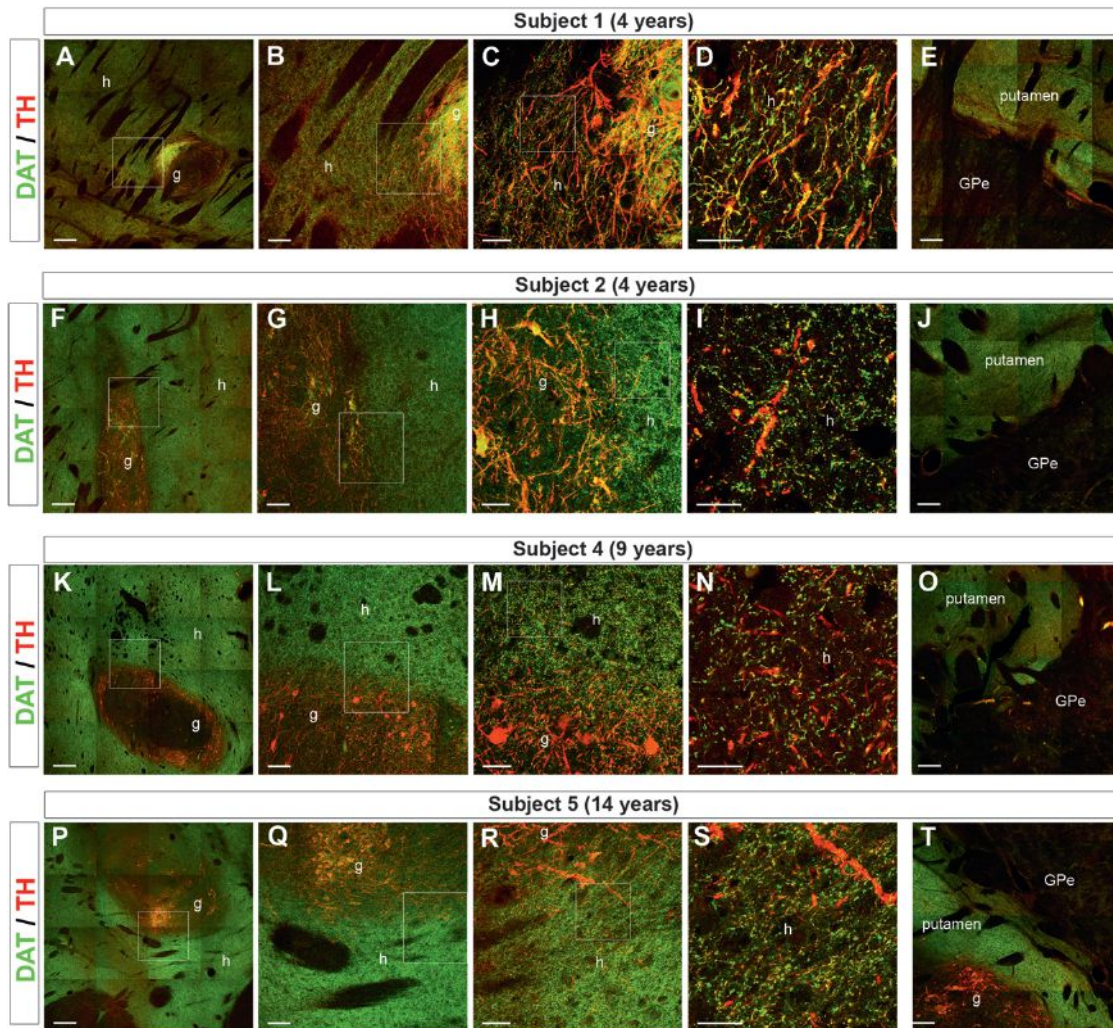


Figure 1. Dopamine Transporter Expression in the Reinnervated Putamen at 4–14 Years Posttransplantation

(A–T) Double immunolabeling for DAT (green) and TH (red) in subjects 1 (A–E; graft survival of 4 years), 2 (F–J; graft survival of 4 years), 4 (K–O; graft survival of 9 years), and 5 (P–T; graft survival of 14 years). Panels (A), (F), (K), and (P) show a low-magnification composite for each subject to illustrate the grafted cell bodies and adjacent reinnervated putamen. Successively higher-magnification images are illustrated in (B)–(D), (G)–(I), (L)–(N), and (Q)–(S). Boxed areas represent the image shown in the subsequent panel. Panels (E), (J), (O), and (T) show a low-magnification composite of the patient’s putamen and adjacent external segment of the globus pallidus. DAT immunostaining shows a robust punctate localization along dopaminergic (TH-immunoreactive) fibers in the reinnervated putamen and caudate in all grafts, even up to 14 years posttransplantation. In addition, the transplanted dopamine neurons show a healthy and nonatrophied morphology. Parallel control immunostainings in which the primary antibodies were omitted showed no immunoreactivity of DAT or TH (data not shown). To further confirm the specificity of the DAT labeling observed in the reinnervated putamen and caudate, we also examined DAT immunolabeling in adjacent anatomical regions on the same tissue sections. As expected, in the lateral and medial globus pallidi, which are regions that receive comparatively little dopaminergic innervation and normally exhibit little DAT expression in the human brain (Ciliax et al., 1999), we observed weak DAT immunolabeling and a sharp boundary from high to low DAT and TH expression (E, J, O, and T). We also performed immunostaining in the substantia nigra of each patient and confirmed the loss of both DAT and TH immunoreactivity (data not shown). g, graft; h, host; GPe, globus pallidus externa. Scale bars, 400 μ m in (A), (E), (F), (J), (K), (O), (P), and (T); 100 μ m in (B), (G), (L), and (Q); 50 μ m in (C), (H), (M), and (R); and 20 μ m in (D), (I), (N), and (S). See also Figure S1.

in grafted neurons. These data are consistent with clinical and neuroimaging data showing stable dopamine cell survival and function more than 18 years after surgery (Kefalopoulou et al., 2014; Politis et al., 2010, 2012).

DAT is a plasma membrane protein located on presynaptic dopamine nerve terminals, where it is responsible for the termination of dopamine transmission and reuptake of dopamine released into the synaptic cleft back into the presynaptic dopa-

mine neurons (Nirenberg et al., 1997). DAT is highly concentrated in the striatum in nigrostriatal dopaminergic projections and is localized to the plasma membranes of axonal varicosities and terminals containing synaptic vesicles (Nirenberg et al., 1997), consistent with its involvement in dopaminergic synaptic transmission in the striatum. Recent studies have suggested that in human PD patients, DAT expression in transplanted fetal dopamine ventral mesencephalic neurons is downregulated over

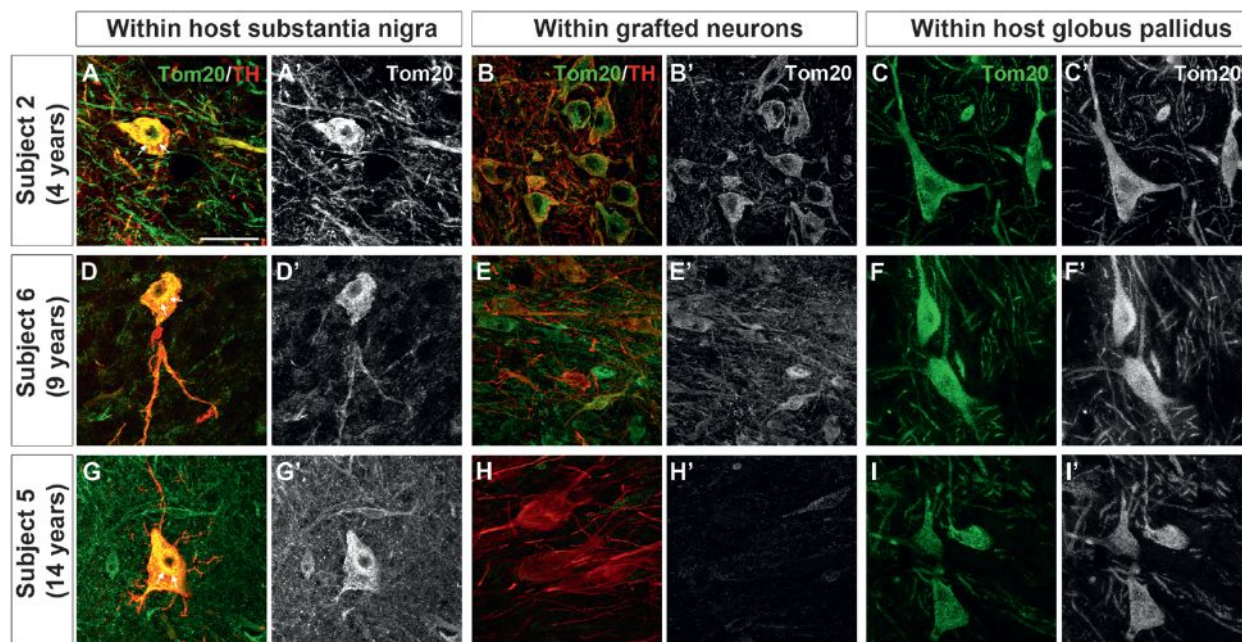


Figure 2. Mitochondrial Phenotype in Transplanted Fetal Dopamine Neurons at 4–14 Years Posttransplantation

(A–I') Double immunolabeling for translocase of outer mitochondrial membranes 20 kDa (Tom20, green) and TH (red) in the host substantia nigra (left panels), grafted dopamine neurons (middle panels), and host globus pallidus (right panels) in subject 2 (A, A', B, B', C, and C'; graft survival of 4 years), subject 6 (D, D', E, E', F, and F'; graft survival of 9 years), and subject 5 (G, G', H, H', I, and I'; graft survival of 14 years). Panels (A')–(I') show single-channel Tom20 labeling from corresponding panels (A)–(I). In dopamine (TH-immunoreactive) neurons from the patients' own substantia nigra, Tom20 labeling often appeared intensely labeled in the cell soma, with accumulation in the perinuclear area (arrows) and little immunostaining in the dopaminergic axons and processes (A, A', D, D', G, and G'). In grafted TH-immunoreactive neurons at 4 years posttransplantation, Tom20 labeling was robust in the perikarya and neuronal processes (B and B'). At 9 and 14 years posttransplantation, Tom20 labeling was generally less intense in the grafted TH-immunoreactive neurons (E, E', H, and H') compared with the Tom20 staining pattern observed in subject 2 at 4 years posttransplantation; however, there was no abnormal accumulation of mitochondria in the cell soma as was observed in the host substantia nigra. No perinuclear accumulation or fragmentation of Tom20-labeled mitochondria was observed in the host globus pallidus (C, C', F, F', I, and I'). Scale bar, 50 μ m.

time, and that this is indicative of PD processes within the graft and loss of function of the grafted dopamine neurons (Kordower et al., 2008; Kurowska et al., 2011). In these studies, the authors used immunolabeling for DAT and subsequent light microscopy. Surprisingly, in older grafts, these studies described only the expression of DAT in the grafted cell soma, with no reported analysis or discussion of the expression and localization of DAT in the dopamine neuron fibers reinnervating the putamen. In the current study, we also noted a qualitative reduction in the intensity of the DAT signal in the cell soma of the grafted dopamine neurons over time when we compared grafts at 4, 9, and 14 years posttransplantation, but it was striking to us that the punctate DAT expression in the reinnervated putamen and caudate was maintained, even over a decade posttransplantation. We previously showed that the extent of DAT labeling in the caudate and putamen of 1-methyl-4-phenyl-1,2,3,6-tetrahydropyridine (MPTP)-lesioned monkeys, as detected by [11 C]CFT PET neuroimaging, is congruent with the number of surviving dopaminergic fibers (Hantraye et al., 1992). DAT is a marker of mature dopamine synapse function, and thus our findings of robust DAT labeling in the putamen of patients analyzed in our series are indicative of the long-term, continued health and function of transplanted dopamine neurons. Therefore, based on DAT expression, we do not find evidence of PD pathophysiological

processes in grafted dopaminergic neurons. Clearly, using the current transplantation methodology, fetal grafts can result in dopamine neurons that are clinically functional for the long term (Barker et al., 2013; Mendez et al., 2005). A previous analysis of α -synuclein pathology in the same transplant cases described here (Cooper et al., 2009; Mendez et al., 2008) revealed only one Lewy body in a neuron of a fetal graft in one of these cases (Cooper et al., 2009). In fetal ventral mesencephalic transplant cases from other transplant-method series, in which we have also observed more frequent Lewy body and α -synuclein pathology (albeit still <5% of grafted neurons), the overall morphology in the vast majority of the surviving transplanted dopaminergic neurons was also unchanged (Cooper et al., 2009; Kordower et al., 2008). Indeed, it was also reported that there is no alteration in the expression of VMAT2, another marker of dopamine presynaptic nerve terminals, in grafted dopamine neurons over time (Kordower et al., 2008). The current study provides important additional evidence against the relevance of a postulated prion-like α -synuclein mechanism for disease propagation. Instead of the concept of α -synuclein spreading from host to graft to cause dysfunction, the opposite may be true, i.e., the healthy transplanted cells provide a clearance mechanism for exogenous unfolded proteins. Our present study unequivocally demonstrates positive markers of dopamine neuron

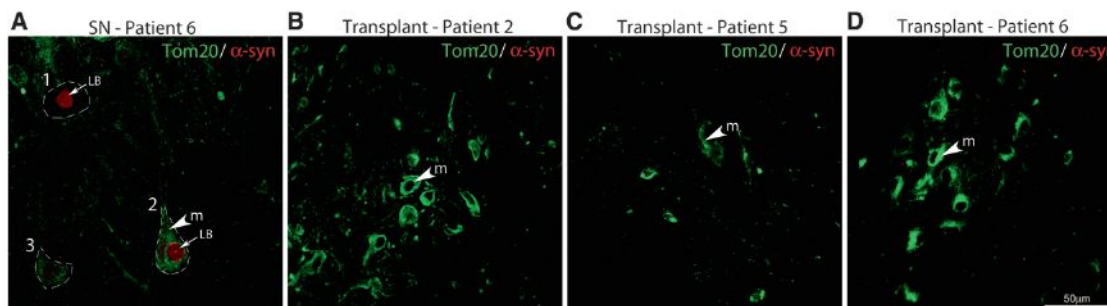


Figure 3. Mitochondria Abnormalities Occur Independently of Lewy Body Pathology in Host Neurons and Neither Lewy Body Pathology nor Mitochondrial Abnormalities Were Found in Transplanted Neurons

(A) Coimmunofluorescence labeling of α -synuclein (red) and the mitochondrial import receptor subunit Tom20 (green) was observed in neurons within the substantia nigra of PD patient 6. Mitochondria in neurons containing accumulated α -synuclein in the host were either diffusely distributed throughout the cytoplasm (cell 1) or were dense in appearance (cell 2). Mitochondria were also diffusely distributed in the cytoplasm of cells without Lewy bodies (cell 3). (B–D) No Lewy body pathology was found in the transplanted neurons of PD patients 2 (B), 5 (C), and 6 (D), and mitochondria were dense throughout the cytoplasm. m, mitochondria; LB, Lewy body. Scale bar, 50 μ m.

function and thus provides a further rationale for clinical cell therapy for PD using stem cell-derived dopamine neuron equivalents.

We also examined the localization and expression of mitochondria in grafted dopaminergic neurons as a possible indicator of increased aging and readout of neuronal function. Mitochondrial dynamics, including fission, fusion, and transport, are crucial for the maintenance of bioenergetic function and prevention of apoptosis (Detmer and Chan, 2007). Mitochondrial dysfunction is a prominent feature of PD and dopaminergic substantia nigra neurons are particularly vulnerable to mitochondrial dysfunction due to their dependence on a high metabolic rate (Exner et al., 2012). We frequently observed that the remaining dopaminergic neurons in the host substantia nigra pars compacta contained Tom20-labeled mitochondria that were accumulated in the cell soma, with very little staining or only a fragmented staining pattern in neurites. Such a redistribution of mitochondria has also been observed in pyramidal neurons in postmortem brains of patients with Alzheimer's disease, using antibodies against COX I and mitochondria fusion/fission proteins (Wang et al., 2009). Intracellular mitochondrial distribution is critical for the functioning of neurons and mitochondrial fragmentation, and a reduced localization of mitochondria in neurites may reflect disruptions in axonal transport and/or disrupted mitochondrial fusion/fission. In contrast, in grafted TH-immunoreactive neurons at 4 years posttransplantation, the Tom20-labeled mitochondria displayed a more uniform distribution throughout the cell soma and neurites, with no indication of fragmentation or accumulation in the cell soma. The overall reduced expression of Tom20-labeled mitochondria that we observed in grafted dopamine neurons at 9 and 14 years posttransplantation may reflect an overall reduced mitochondrial biogenesis or increased mitophagy as a function of accelerated aging in these neurons. By all current cell-biological accounts, the distribution of the mitochondrial network we describe is likely more informative than a total mitochondrial count, which is practically difficult (if not impossible) to obtain in regular postmortem material. Furthermore, even if such a method existed, a similar mitochondrial mass or number between populations of neurons would not

necessarily equate with physiologically functional mitochondria due to heteroplasmy (the coexistence of both faulty and functional mitochondria in the same cell) (Kraytsberg et al., 2006; Larsson, 2010; Sanders et al., 2014).

The observations of continued DAT expression and normal mitochondrial cellular distribution at 4–14 years posttransplantation are consistent with the clinical data and show that implanted dopamine neurons remain healthy and functional for decades (C.R. Freed et al., 2013, Soc. Neurosci., conference; Kefalopoulou et al., 2014; Politis et al., 2010, 2012). In summary, our postmortem examination of tissue from PD patients who had received fetal ventral mesencephalic cells transplanted as a cell suspension shows that following long-term graft survival, DAT localization along TH-immunoreactive axons and fibers is maintained in the reinnervated striatum, indicating functional dopaminergic neurons. Abnormalities in mitochondrial localization, as indicated by accumulation in the cell soma in dopaminergic neurons in the host substantia nigra, were not observed in grafted neurons. Our data are not consistent with the suggestion that these grafts degenerate over time, and instead show that there is no cell-biological evidence for such an assertion. These data support clinical and neuroimaging findings of the long-lasting functional benefit of dopamine neuron transplantation in PD patients (C.R. Freed et al., 2013, Soc. Neurosci., conference; Kefalopoulou et al., 2014; Ma et al., 2010; Mendez et al., 2005; Politis et al., 2010, 2012), and provide an important foundation for the development of future fetal and stem cell-derived dopamine replacement therapies for PD.

EXPERIMENTAL PROCEDURES

Patient Selection

Caudate putamen, globus pallidus, and substantia nigra tissues from five patients (referred to as subjects 1, 2, 4, 5, and 6) with advanced idiopathic PD who had undergone fetal tissue transplantation for 4–14 years were examined in this study. All protocols were approved by institutional review boards. We previously reported the surgical procedures, neuroimaging data, clinical outcome, and postmortem histological assessments of the phenotypical characteristics and PD pathophysiological markers in transplanted neurons in this series of patients (Cooper et al., 2009; Mendez et al., 2005, 2008).

Tissue Preparation

At postmortem examination (after a delay of 3–4 hr), the brains were infused with 2 l of cold 0.1 M phosphate buffer (pH 7.4), followed by 2 l of ice-cold 4% paraformaldehyde in 0.1 M phosphate buffer. The brains were subsequently blocked in the coronal plane in 3-cm-thick slabs. The slabs were cryoprotected in 30% sucrose in PBS at 4°C.

Immunohistochemistry

Sections (40 μm) were stained using immunofluorescence techniques. In order to maintain consistency of DAT or TOM20 labeling between subjects, immunostainings were performed at the same time and using identical reagents. DAT labeling was enhanced using a fluorescent streptavidin conjugate as described below. Sections were rinsed three times for 10 min in PBS, incubated in 10% normal donkey serum (Vector Laboratories) and 0.3% Triton X-100 in PBS for 60 min, and then incubated with gentle agitation for 48 hr at 4°C in primary antibody (rat anti-DAT, 1:200 [MAB369; Millipore]; sheep anti-TH, 1:300 [P60101-0, Pel-Freez]; rabbit anti-Tom20, 1:200 [sc-11415; Santa-Cruz]). For α-synuclein staining, the LB509 antibody (Invitrogen/Life Technologies) was used at 1:500 dilution. After an additional three 10 min rinses in PBS, the sections were incubated in fluorescent dye-conjugated secondary antibodies in PBS for 60 min at room temperature for detection of TH and Tom20 (Alexa Fluor donkey anti-rabbit/sheep 488/568; 1:500 [Molecular Probes]). For detection of DAT and α-synuclein, sections were incubated in a biotinylated secondary antibody (donkey anti-rat/mouse; 1:250; Vector Laboratories) in PBS for 60 min at room temperature, followed by three 10 min rinses in PBS, and incubation in streptavidin Alexa Fluor 488 (1:500, Molecular Probes) for 60 min. After rinsing in PBS (three times for 10 min), sections were mounted onto Superfrost Plus slides and an autofluorescence eliminator reagent was applied (Millipore) prior to coverslipping in Mowiol mounting media. The specificity of DAT, Tom20, TH, and α-synuclein labeling was confirmed using stainings in parallel tissue sections from each subject in which the primary antibody was omitted.

Confocal Microscopy

Immunofluorescence staining was examined with the use of a confocal microscope (LSM510 Meta; Carl Zeiss) at 10, 25, or 100× magnification. Single or z-stack images were acquired using a sequential scanning mode with a frame size of 1,024 × 1,024 pixels, and averaging of four frames. The laser intensity, confocal aperture, photomultiplier voltage, scan speed, image size, filter, and zoom were kept identical while all images were acquired. For quantification of DAT labeling, confocal images at 25× magnification (at least five per subject) were obtained in the reinnervated putamen or in the denervated, nontransplanted putamen. The average optical density of DAT immunofluorescence intensity in each subject was analyzed using ImageJ software (ImageJ 1.44i; National Institutes of Health).

SUPPLEMENTAL INFORMATION

Supplemental Information includes one figure and can be found with this article online at <http://dx.doi.org/10.1016/j.celrep.2014.05.027>.

AUTHOR CONTRIBUTIONS

P.J.H. designed and performed research, analyzed and interpreted data, and wrote the paper. O.C. designed research and analyzed data. D.S. performed research. H.R. evaluated data and wrote the paper. I.M. designed and performed research, evaluated data, and wrote the paper. O.I. designed and performed research, analyzed and interpreted data, and wrote the paper.

ACKNOWLEDGMENTS

We thank Dr. Gaynor Smith for helpful discussions, and Eduardo Perez-Torres and David Ahmadi for technical assistance. This work was supported by the National Institutes of Health/National Institute of Neurological Disorders and Stroke P50 (grant NS39793 to O.I.), the Harvard Stem Cell Institute Translational Neuroscience Fund (to O.I.), the Canadian Institute of Health Research,

Queen Elizabeth II Health Sciences Centre (to I.M.), The Consolidated Anti-Aging Foundation (to O.I.), The Poul Hansen Family (to O.I.), and the Harold and Ronna Cooper Family (to O.I.).

Received: April 12, 2013

Revised: April 1, 2014

Accepted: May 9, 2014

Published: June 5, 2014

REFERENCES

- Barker, R.A., Barrett, J., Mason, S.L., and Björklund, A. (2013). Fetal dopaminergic transplantation trials and the future of neural grafting in Parkinson's disease. *Lancet Neurol.* *12*, 84–91.
- Ciliax, B.J., Drash, G.W., Staley, J.K., Haber, S., Mobley, C.J., Miller, G.W., Mufson, E.J., Mash, D.C., and Levey, A.I. (1999). Immunocytochemical localization of the dopamine transporter in human brain. *J. Comp. Neurol.* *409*, 38–56.
- Cooper, O., Astradsson, A., Hallett, P., Robertson, H., Mendez, I., and Isacson, O. (2009). Lack of functional relevance of isolated cell damage in transplants of Parkinson's disease patients. *J. Neurol.* *256* (Suppl 3), 310–316.
- Desplats, P., Lee, H.J., Bae, E.J., Patrick, C., Rockenstein, E., Crews, L., Spencer, B., Masliah, E., and Lee, S.J. (2009). Inclusion formation and neuronal cell death through neuron-to-neuron transmission of alpha-synuclein. *Proc. Natl. Acad. Sci. USA* *106*, 13010–13015.
- Detmer, S.A., and Chan, D.C. (2007). Functions and dysfunctions of mitochondrial dynamics. *Nat. Rev. Mol. Cell Biol.* *8*, 870–879.
- Ding, Z.T., Wang, Y., Jiang, Y.P., Hashizume, Y., Yoshida, M., Mimuro, M., Inagaki, T., and Iwase, T. (2006). Characteristics of alpha-synucleinopathy in centenarians. *Acta Neuropathol.* *111*, 450–458.
- Evans, J.R., Mason, S.L., and Barker, R.A. (2012). Current status of clinical trials of neural transplantation in Parkinson's disease. *Prog. Brain Res.* *200*, 169–198.
- Exner, N., Lutz, A.K., Haass, C., and Winklhofer, K.F. (2012). Mitochondrial dysfunction in Parkinson's disease: molecular mechanisms and pathophysiological consequences. *EMBO J.* *31*, 3038–3062.
- Gao, H.M., Kotzbauer, P.T., Uryu, K., Leight, S., Trojanowski, J.Q., and Lee, V.M. (2008). Neuroinflammation and oxidation/nitration of alpha-synuclein linked to dopaminergic neurodegeneration. *J. Neurosci.* *28*, 7687–7698.
- Hantraye, P., Brownell, A.L., Elmaleh, D., Speelman, R.D., Wüllner, U., Brownell, G.L., Madras, B.K., and Isacson, O. (1992). Dopamine fiber detection by [¹¹C]-CFT and PET in a primate model of parkinsonism. *Neuroreport* *3*, 265–268.
- Isacson, O., and Mendez, I. (2010). Being too inclusive about synuclein inclusions. *Nat. Med.* *16*, 960–961, author reply 961.
- Kefalopoulou, Z., Politis, M., Piccini, P., Mencacci, N., Bhatia, K., Jahanshahi, M., Widner, H., Rehncrona, S., Brundin, P., Björklund, A., et al. (2014). Long-term clinical outcome of fetal cell transplantation for Parkinson disease: two case reports. *JAMA Neurol.* *71*, 83–87.
- Klos, K.J., Ahlskog, J.E., Josephs, K.A., Apaydin, H., Parisi, J.E., Boeve, B.F., DeLucia, M.W., and Dickson, D.W. (2006). Alpha-synuclein pathology in the spinal cords of neurologically asymptomatic aged individuals. *Neurology* *66*, 1100–1102.
- Kordower, J.H., Chu, Y., Hauser, R.A., Freeman, T.B., and Olanow, C.W. (2008). Lewy body-like pathology in long-term embryonic nigral transplants in Parkinson's disease. *Nat. Med.* *14*, 504–506.
- Kraytsberg, Y., Kudryavtseva, E., McKee, A.C., Geula, C., Kowall, N.W., and Khrapko, K. (2006). Mitochondrial DNA deletions are abundant and cause functional impairment in aged human substantia nigra neurons. *Nat. Genet.* *38*, 518–520.
- Kurowska, Z., Englund, E., Widner, H., Lindvall, O., Li, J.-Y., and Brundin, P. (2011). Signs of degeneration in 12–22-year old grafts of mesencephalic dopamine neurons in patients with Parkinson's disease. *J. Parkinsons Dis.* *1*, 83–92.

- Larsson, N.G. (2010). Somatic mitochondrial DNA mutations in mammalian aging. *Annu. Rev. Biochem.* 79, 683–706.
- Li, J.Y., Englund, E., Holton, J.L., Soulet, D., Hagell, P., Lees, A.J., Lashley, T., Quinn, N.P., Rehnrcrona, S., Björklund, A., et al. (2008). Lewy bodies in grafted neurons in subjects with Parkinson's disease suggest host-to-graft disease propagation. *Nat. Med.* 14, 501–503.
- Ma, Y., Tang, C., Chaly, T., Greene, P., Breeze, R., Fahn, S., Freed, C., Dhanwan, V., and Eidelberg, D. (2010). Dopamine cell implantation in Parkinson's disease: long-term clinical and (18)F-FDOPA PET outcomes. *J. Nucl. Med.* 51, 7–15.
- Mendez, I., Sanchez-Pernaute, R., Cooper, O., Viñuela, A., Ferrari, D., Björklund, L., Dagher, A., and Isacson, O. (2005). Cell type analysis of functional fetal dopamine cell suspension transplants in the striatum and substantia nigra of patients with Parkinson's disease. *Brain* 128, 1498–1510.
- Mendez, I., Viñuela, A., Astradsson, A., Mukhida, K., Hallett, P., Robertson, H., Tierney, T., Holness, R., Dagher, A., Trojanowski, J.Q., and Isacson, O. (2008). Dopamine neurons implanted into people with Parkinson's disease survive without pathology for 14 years. *Nat. Med.* 14, 507–509.
- Mikolaenko, I., Pletnikova, O., Kawas, C.H., O'Brien, R., Resnick, S.M., Crain, B., and Troncoso, J.C. (2005). Alpha-synuclein lesions in normal aging, Parkinson disease, and Alzheimer disease: evidence from the Baltimore Longitudinal Study of Aging (BLSA). *J. Neuropathol. Exp. Neurol.* 64, 156–162.
- Miller, G.W., Staley, J.K., Heilman, C.J., Perez, J.T., Mash, D.C., Rye, D.B., and Levey, A.I. (1997). Immunohistochemical analysis of dopamine transporter protein in Parkinson's disease. *Ann. Neurol.* 41, 530–539.
- Nirenberg, M.J., Chan, J., Vaughan, R.A., Uhl, G.R., Kuhar, M.J., and Pickel, V.M. (1997). Immunogold localization of the dopamine transporter: an ultrastructural study of the rat ventral tegmental area. *J. Neurosci.* 17, 5255–5262.
- Politis, M., Wu, K., Loane, C., Quinn, N.P., Brooks, D.J., Rehnrcrona, S., Björklund, A., Lindvall, O., and Piccini, P. (2010). Serotonergic neurons mediate dyskinesia side effects in Parkinson's patients with neural transplants. *Sci. Transl. Med.* 2, 38ra46.
- Politis, M., Wu, K., Loane, C., Quinn, N.P., Brooks, D.J., Oertel, W.H., Björklund, A., Lindvall, O., and Piccini, P. (2012). Serotonin neuron loss and non-motor symptoms continue in Parkinson's patients treated with dopamine grafts. *Sci. Transl. Med.* 4, 128ra141.
- Saito, Y., Ruberu, N.N., Sawabe, M., Arai, T., Kazama, H., Hosoi, T., Yamanouchi, H., and Murayama, S. (2004). Lewy body-related alpha-synucleinopathy in aging. *J. Neuropathol. Exp. Neurol.* 63, 742–749.
- Sanders, L.H., Laganière, J., Cooper, O., Mak, S.K., Vu, B.J., Huang, Y.A., Paschon, D.E., Vangipuram, M., Sundararajan, R., Urnov, F.D., et al. (2014). LRRK2 mutations cause mitochondrial DNA damage in iPSC-derived neural cells from Parkinson's disease patients: reversal by gene correction. *Neurobiol. Dis.* 62, 381–386.
- Sherer, T.B., Kim, J.H., Betarbet, R., and Greenamyre, J.T. (2003). Subcutaneous rotenone exposure causes highly selective dopaminergic degeneration and alpha-synuclein aggregation. *Exp. Neurol.* 179, 9–16.
- Wakisaka, Y., Furuta, A., Tanizaki, Y., Kiyohara, Y., Iida, M., and Iwaki, T. (2003). Age-associated prevalence and risk factors of Lewy body pathology in a general population: the Hisayama study. *Acta Neuropathol.* 106, 374–382.
- Wang, X., Su, B., Zheng, L., Perry, G., Smith, M.A., and Zhu, X. (2009). The role of abnormal mitochondrial dynamics in the pathogenesis of Alzheimer's disease. *J. Neurochem.* 109 (Suppl 1), 153–159.

Introducing the China Gateway

The home for Chinese scientists



The new Cell Press China Gateway is the ultimate destination for Chinese scientists. Now highlights of the latest research, regional events, and featured content from Cell Press are accessible online, on a single webpage.

The Cell Press China Gateway was designed with you in mind. We hope you'll make yourself at home.

Visit us at www.cell.com/china

CellPress

The Role of the Endocrine System in Feeding-Induced Tissue-Specific Circadian Entrainment

Miho Sato,¹ Mariko Murakami,¹ Koichi Node,² Ritsuko Matsumura,¹ and Makoto Akashi^{1,*}

¹The Research Institute for Time Studies, Yamaguchi University, 1677-1 Yoshida, Yamaguchi 753-8511, Japan

²Department of Cardiovascular Medicine, Saga University, 5-1-1 Nabeshima, Saga 849-8501, Japan

*Correspondence: akashima@yamaguchi-u.ac.jp

<http://dx.doi.org/10.1016/j.celrep.2014.06.015>

This is an open access article under the CC BY license (<http://creativecommons.org/licenses/by/3.0/>).

SUMMARY

The circadian clock is entrained to environmental cycles by external cue-mediated phase adjustment. Although the light input pathway has been well defined, the mechanism of feeding-induced phase resetting remains unclear. The tissue-specific sensitivity of peripheral entrainment to feeding suggests the involvement of multiple pathways, including humoral and neuronal signals. Previous *in vitro* studies with cultured cells indicate that endocrine factors may function as entrainment cues for peripheral clocks. However, blood-borne factors that are well characterized in actual feeding-induced resetting have yet to be identified. Here, we report that insulin may be involved in feeding-induced tissue-type-dependent entrainment *in vivo*. In *ex vivo* culture experiments, insulin-induced phase shift in peripheral clocks was dependent on tissue type, which was consistent with tissue-specific insulin sensitivity, and peripheral entrainment in insulin-sensitive tissues involved PI3K- and MAPK-mediated signaling pathways. These results suggest that insulin may be an immediate early factor in feeding-mediated tissue-specific entrainment.

INTRODUCTION

The circadian clock is driven by cell-autonomous clock gene expression rhythms in almost all organisms (Reppert and Weaver, 2002; Rosbash et al., 2007). The core circadian transcriptional feedback loop generates circadian expression of a wide range of numerous genes, which in turn leads to circadian oscillation in diverse physiological processes (Doherty and Kay, 2010; Mohawk et al., 2012). The circadian clock enables maximum expression of genes at appropriate times of the day, allowing organisms to adapt to earth rotation. It has been reported that chronic desynchronization between physiological and environmental rhythms carries a significant risk of diverse disorders, ranging from sleep disorders to diabetes, cardiovas-

cular diseases, and cancer (Sahar and Sassone-Corsi, 2012; Wijnen and Young, 2006). Thus, a thorough understanding of the mechanism of the circadian input pathway is critically important to the prevention of diseases. The circadian input consists of two major pathways. The first is the light input pathway via the hypothalamic suprachiasmatic nuclei (SCN), known as the circadian pacemaker. Details of this mechanism have been elucidated at the molecular level by a substantial number of studies (Doyle and Menaker, 2007). The second is the feeding input pathway (Damiola et al., 2000; Stokkan et al., 2001), for which a factor has yet to be identified and characterized *in vivo*. Temporal feeding restriction changes the phase of circadian gene expression in peripheral tissues without affecting the phase in the SCN, and food-induced phase resetting proceeds much faster in the liver than in the kidney, heart, or pancreas (Damiola et al., 2000). The tissue-specific sensitivity of peripheral entrainment to feeding suggests the involvement of multiple pathways, including humoral and neuronal signals.

The circadian clock is cell-autonomous (Nagoshi et al., 2004; Yamazaki et al., 2000), and much can therefore be learned from studies using cultured cells. Indeed, cell line-based experiments to elucidate the entrainment mechanism have been performed. A number of endogenous factors are reported to act on cell-autonomous circadian gene expression in cultured cell lines, including growth factors, calcium, glucose, angiotensin II, retinoic acid, and nitric oxide (Akashi and Nishida, 2000; Balsalobre et al., 2000; Hirota et al., 2002; McNamara et al., 2001; Nonaka et al., 2001). In addition, insulin, a humoral factor that regulates blood glucose levels, also has effects on clock gene expression in cultured cell lines (Balsalobre et al., 2000; Yamajuku et al., 2012). With regard to *in vivo* relevance, mice carrying pharmacologically damaged beta cells show altered expression of clock genes in peripheral tissues (Kuriyama et al., 2004; Oishi et al., 2004), indicating the presence of *in vivo* interaction between the circadian clock and insulin signaling. However, the physiological role of insulin in the circadian clock remains to be determined.

The pancreas secretes insulin in response to feeding. We speculated that insulin acts as an endogenous molecule required for feeding-induced tissue-specific phase resetting of peripheral clocks. To help elucidate the *in vivo* roles of insulin in feeding-induced circadian entrainment, we used *in vivo* imaging experiments to examine expression levels of *Per2* in

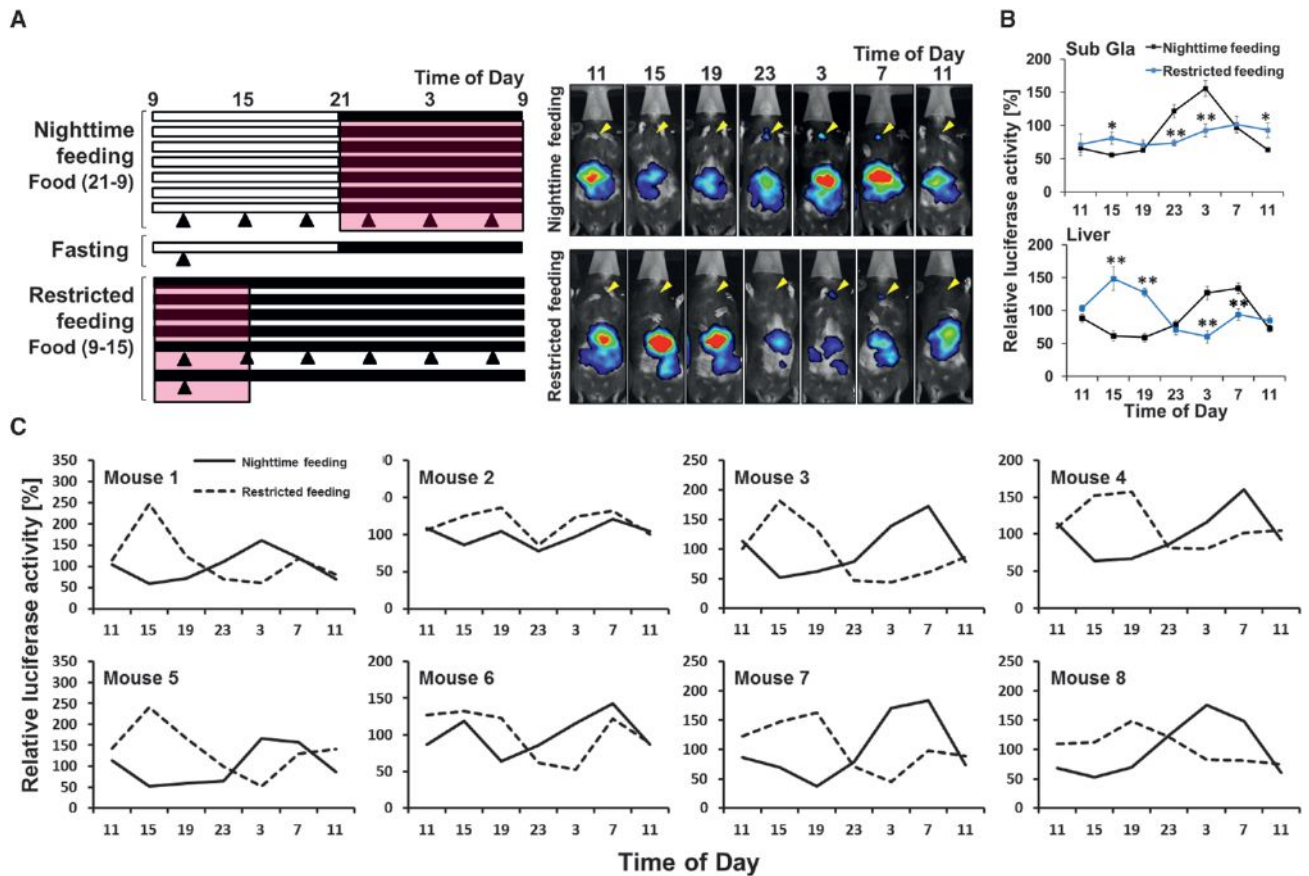


Figure 1. In Vivo Monitoring of Peripheral Tissues from Individual Animals during Restricted Feeding

(A–C) *Per2-luciferase* (*Per2^{Luc}*) mice during the restricted feeding schedule were monitored with an in vivo imaging system. Feeding schedule (A, left). *Per2^{Luc}* mice received food during the nighttime (21:00–9:00; light on at 9:00 and off at 21:00) for 1 week and then had restricted food access for 6 hr (9:00–15:00) under continuous dark conditions. Black-and-white bars represent light-dark (LD) conditions. Pink shadow represents feeding time. Images were taken at the time indicated by the black triangles. Right, representative in vivo images from the ventral aspect. Yellow arrowheads denote the submandibular gland (Sub Glia). (B) Averaged quantitative data of Sub Glia and the liver from (A). Rhythmic expression of *Per2* in the liver was entrained to restricted feeding, although not in the Sub Glia. * $p < 0.05$, ** $p < 0.01$ versus corresponding nighttime. The data represent the mean \pm SE ($n = 8$). (C) Individual quantitative data of liver from (A).

individual animals around the clock in the presence of a highly specific competitive peptide inhibitor of insulin. To exclude the possibility that the results were affected by secondary effects of the inhibitor, we used ex vivo approaches. We therefore conducted ex vivo tissue culture experiments to examine whether insulin-induced phase shift in peripheral clocks depends on tissue type, consistent with the tissue-specific sensitivity of insulin.

RESULTS AND DISCUSSION

Evaluation of peripheral clocks requires the preparation of a large number of animals, harvesting of tissues every few hours, and examination of clock gene expression levels using purified RNA. These experimental procedures are arduous, but provide no information about sequential changes in clock gene expression in individual animals. Rather, the data only show average expression levels from several dead animals. In contrast, a recent in vivo imaging technique enables detection of sequential changes in clock gene expression levels in individual animals

without killing them (Tahara et al., 2012). Hence, using in vivo imaging of individual *Per2-luciferase* knockin mice (Yoo et al., 2004), we investigated temporal changes in *Per2* expression rhythms in peripheral tissues of individual animals (Figure 1A, top). About 10 min after subcutaneous injection of luciferin, strong luminescence was detected in the liver and submandibular gland. We were then able to confirm circadian gene expression of *Per2* in these tissues by time course measurement around the clock. Furthermore, to observe feeding-induced phase shift of circadian gene expression, we changed the feeding schedule from ZT12-24 to ZT0-6, and 5 days later observed antiphase expression of *Per2* in the liver (Figure 1A, right). In contrast, this phase shift was subtle in the submandibular gland (Figures 1A and 1B), suggesting that there are significant differences among peripheral tissues in the rate of feeding-induced phase shift. The phase change in individual animals is shown in Figure 1C. While *Per2* expression in each animal's liver showed a similar and reproducible response to the restricted feeding, minor variation among individuals was

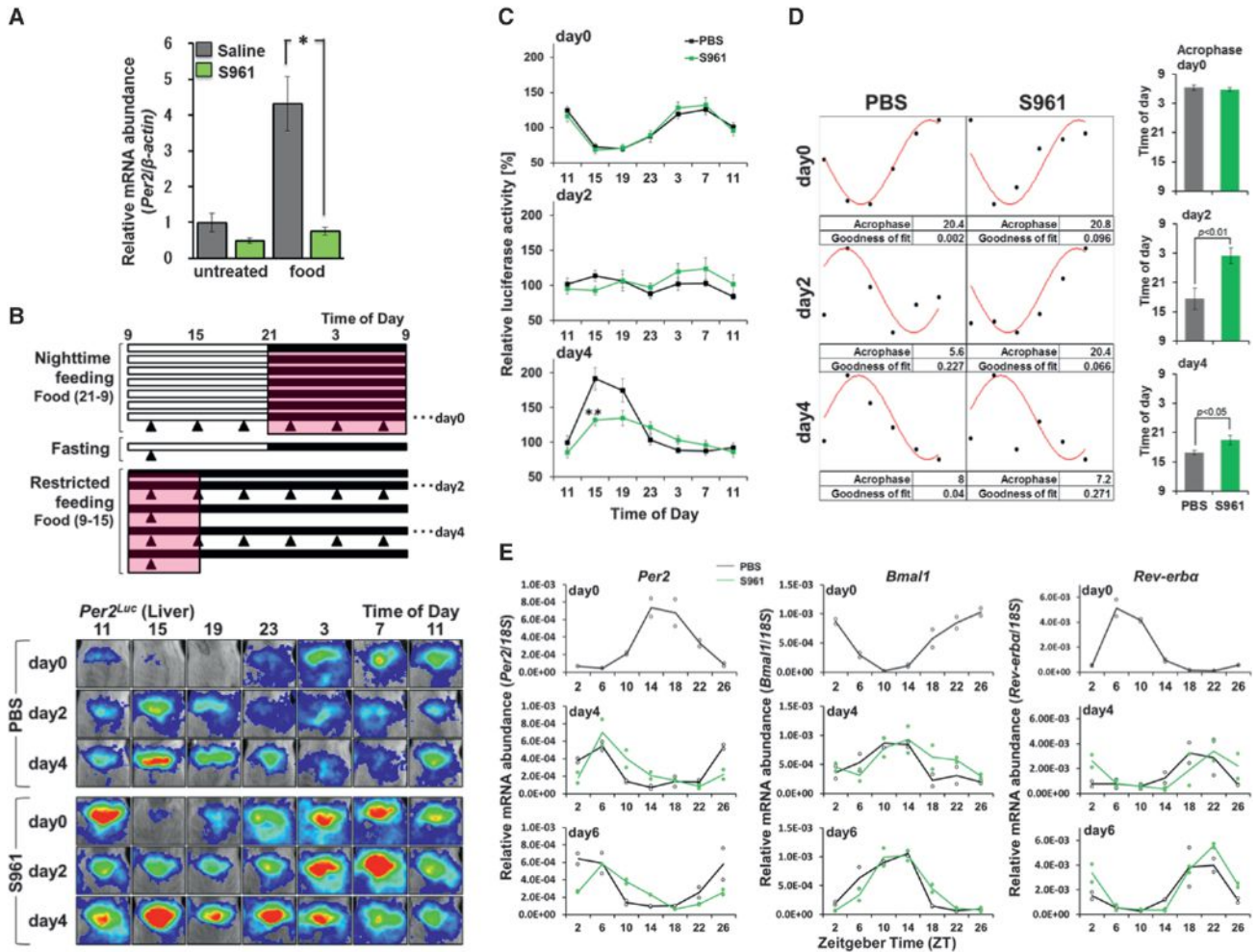


Figure 2. Involvement of Insulin in Feeding-Induced Circadian Phase Shift in the Liver

(A) Acute induction of *Per2* transcripts after feeding was blocked by S961. *Per2* mRNA expression levels in liver at ZT2 (60 min after feeding onset) were determined with RT-PCR. Each value was normalized with β -actin. The data represent the mean \pm SE (n = 3). *p < 0.05.

(B) Representative in vivo image of *Per2^{Luc}* mice liver injected with S961 30 min before the start of feeding every day during restricted feeding. S961 inhibited the entrainment of *Per2*.

(C) Quantitative data of bioluminescence in the liver from (B). The data represent the mean \pm SE (n = 8). **p < 0.01.

(D) Acrophases in a representative animal from (B) were calculated by a cosine curve fitting. The data at right represent the mean \pm SE (n = 8).

(E) Quantitative RT-PCR of *Per2*, *Bmal1*, and *Rev-erba* mRNA in the liver during RF (ZT1-7) in LD; n = 2. Black circles represent individual values of mice given PBS mice and green circles represent mice given S961. S961 was used at a concentration of 30 nmol/kg in all experiments.

apparent in the rate of the phase shift. The pancreas secretes insulin in response to feeding, and peripheral tissues show different sensitivity to insulin, indicating why the liver clock, but not the submandibular gland clock, was immediately phase-adjusted by restricted feeding. These results demonstrate that in vivo imaging technology is a powerful tool in investigating sequential and temporal changes in peripheral clocks in individuals.

It was reported that restricted feeding triggers a rapid transient induction of *Per2* transcription in the liver (Wu et al., 2010). The immediate early expression of *Per2* would likely affect the negative feedback loop in circadian transcription because *Per2* is a component of the negative limb. If insulin is indispensable to feeding-induced resetting, inhibition of insulin signaling should

result in attenuation of the *Per2* expression levels rapidly induced by restricted feeding (Figure 2A). To inhibit insulin action during feeding-induced phase shift without pharmacologically killing beta cells, mice received a subcutaneous injection of S961, a highly specific competitive peptide inhibitor of insulin, prior to feeding (Schäffer et al., 2008; Scherer et al., 2011; Vikram and Jena, 2010). S961-injected animals ate a similar amount of food as control animals. As expected, this pretreatment with S961 potentially inhibited the rapid transient induction of *Per2* by restricted feeding. Next, using an in vivo imaging system, we examined whether S961 suppresses the feeding-induced circadian phase shift of *Per2* expression rhythm in the liver of individual animals (Figure 2B). In the control animals, transition states of *Per2* expression rhythms were confirmed in each animal's liver

approximately 2 days after the inversion of feeding time. During the process of transition, individual differences in phase change were observed: some animals showed lower amplitudes of oscillation temporarily, whereas others had a second peak (Figure S1). Average transition states of eight animals are shown in Figure 2C. Compared with the control animals, animals pretreated with S961 showed a significant delay in phase shift on day 2, and phase adjustment was still not completed on day 4 (Figures 2B–2D). When we processed data from individual animals using a cosine curve fitting and calculated and quantified peak times (Figure 2D), we found that the shift speed of acrophase appeared to be attenuated in animals pretreated with S961.

A limitation of the present *in vivo* imaging approach is that it provides no information on expression levels of genes other than *Per2*. We therefore harvested the livers every 4 hours in the conventional manner and confirmed the effect of S961 on feeding-induced phase shift of clock gene oscillations with RT-PCR (Figure 2E). As is the case with the *in vivo* imaging data, circadian phase shift of the *Per2*, *Bmal1*, and *Rev-erb α* genes was significantly delayed compared with control animals. Sampling in this experiment was performed under light-dark conditions, but *Per2* expression results were similar to the *in vivo* imaging data obtained under dark-dark conditions (Figure 2B). Furthermore, the S961-treated mice weighed almost the same as the control mice throughout the experiment (Figure S2A). Because S961 treatment provoked transient hyperglycemia (Figure S2B), we used an *ex vivo* slice culture system to confirm that this hyperglycemia had no substantial influence on the effect of S961 on insulin-induced circadian phase shift (Figure S3).

These data illustrate that the inhibition of insulin signaling attenuates feeding-induced phase adjustment of the liver clock in individual animals. As mentioned above, S961 potentially inhibited the transient induction of *Per2* that was triggered by restricted feeding, whereas the phase shift of *Per2* expression rhythms was less strongly affected. This suggests that the transient induction may contribute to the phase shift, but is not absolutely required for it, and that other unknown endogenous factors are involved in the process.

There is no doubt that S961 treatment is a superior experimental approach for investigating the physiological role of insulin compared with methods using streptozotocin-treated, *ob/ob* or *db/db* mice. However, it is impossible to completely exclude the possibility that various secondary physiological events caused by S961-induced transient hyperglycemia may affect feeding-induced circadian phase shift. To exclude these secondary effects and examine the true contribution of insulin to the circadian phase shift, *ex vivo* or *in vitro* experimental approaches are required for further validation. We therefore conducted *ex vivo* culture experiments to investigate the effect of insulin on autonomous circadian gene expression. *Per2* expression rhythms in the liver were phase-shifted by the administration of insulin, and the effect was then almost completely inhibited in the presence of S961, suggesting that insulin acted on the liver clock in a receptor-specific manner (Figure 3A). Additionally, given the well-known decrease in insulin sensitivity in the fatty liver, we examined the effect of insulin on *Per2* expression rhythm in livers harvested from mice fed a high-fat diet (Figure 3B). As expected,

the insulin-induced phase shift in circadian gene expression was smaller in fatty livers than in healthy livers. We found a phase dependency in the insulin-mediated phase change of *Per2* expression rhythms in the liver (Figure 3C). Insulin caused a phase advance effect during the increasing phase of *Per2* expression, but a phase delay effect during the decreasing phase. Unexpectedly, the phase responsiveness observed on continuous administration of insulin was similar to that with 1 hr treatment with insulin (Figure 3C, right versus left), indicating the presence of a negative feedback mechanism for blocking continuous activation of the signaling pathway leading to the core clock. We constructed a dot-plot of phase responsiveness on administration of insulin at various circadian phases (Figure 3D). The data indicate that the direction of phase change of peripheral clocks depends on the feeding time of day. To confirm whether the phase shift by insulin is consistent with this tissue insulin sensitivity, we examined the tissue-specific effect of insulin on autonomous *Per2* expression rhythms *ex vivo* by performing slice culture of various peripheral tissues (Figure 3E). As expected, we confirmed a large phase shift of *Per2* oscillation not only in liver, but also in adipose tissue, both of which are insulin-sensitive. In contrast, insulin exerted no or only a subtle effect in insensitive tissues, including the lung, aorta, and submandibular gland.

On the assumption that the insulin-induced phase shift is in fact dependent on insulin receptor expression, we speculated that ectopic overexpression of the insulin receptor may confer a degree of insulin sensitivity to receptor-poor cells. To test this notion, we introduced an insulin receptor expression plasmid vector into NIH 3T3 fibroblasts, a receptor-poor cell line (Figure 4A). Insulin receptor overexpression was constitutively driven by the AG promoter. In cells transfected with the empty vector, insulin did not trigger a phase shift in *Bmal1* expression rhythm (here using a *Bmal1* promoter-driven *luciferase* expression vector), but did induce a phase shift in cells ectopically overexpressing the insulin receptor. Interestingly, we found a phase difference in insulin sensitivity in spite of constitutive overexpression of the receptor; insulin administration caused a phase advance during the decreasing phase of *Bmal1* (the increasing phase of *Per2*), as shown in the liver, versus a phase delay in the increasing phase (Figure 4B). This may indicate that phase-dependent insulin action might be explained in terms of the internal clock, independently of diurnal changes in receptor expression levels. On the other hand, we found that mRNA levels of the liver insulin receptor showed a clear circadian pattern with an opposite phase to *Per2* (Figure S4A), as indicated previously, which might have contributed not to the direction but rather to the intensity of the insulin-induced phase shift.

To examine whether transient activation of *Per2* transcription is sufficient to induce circadian phase shift in a phase-directed manner, we introduced an isopropyl- β -D-thiogalactopyranoside (IPTG)-inducible expression system to two cell lines, NIH 3T3 and U2OS (Figures 4C and 4D). In this culture system, whereas ectopic expression of *Per2* is suppressed by a lac repressor in the absence of IPTG, it can be rapidly activated by administration of IPTG without extracellular physiological stimuli and independently of any intracellular signaling pathways. A 1-hr administration of IPTG caused a 1.5-hr phase delay during the increasing

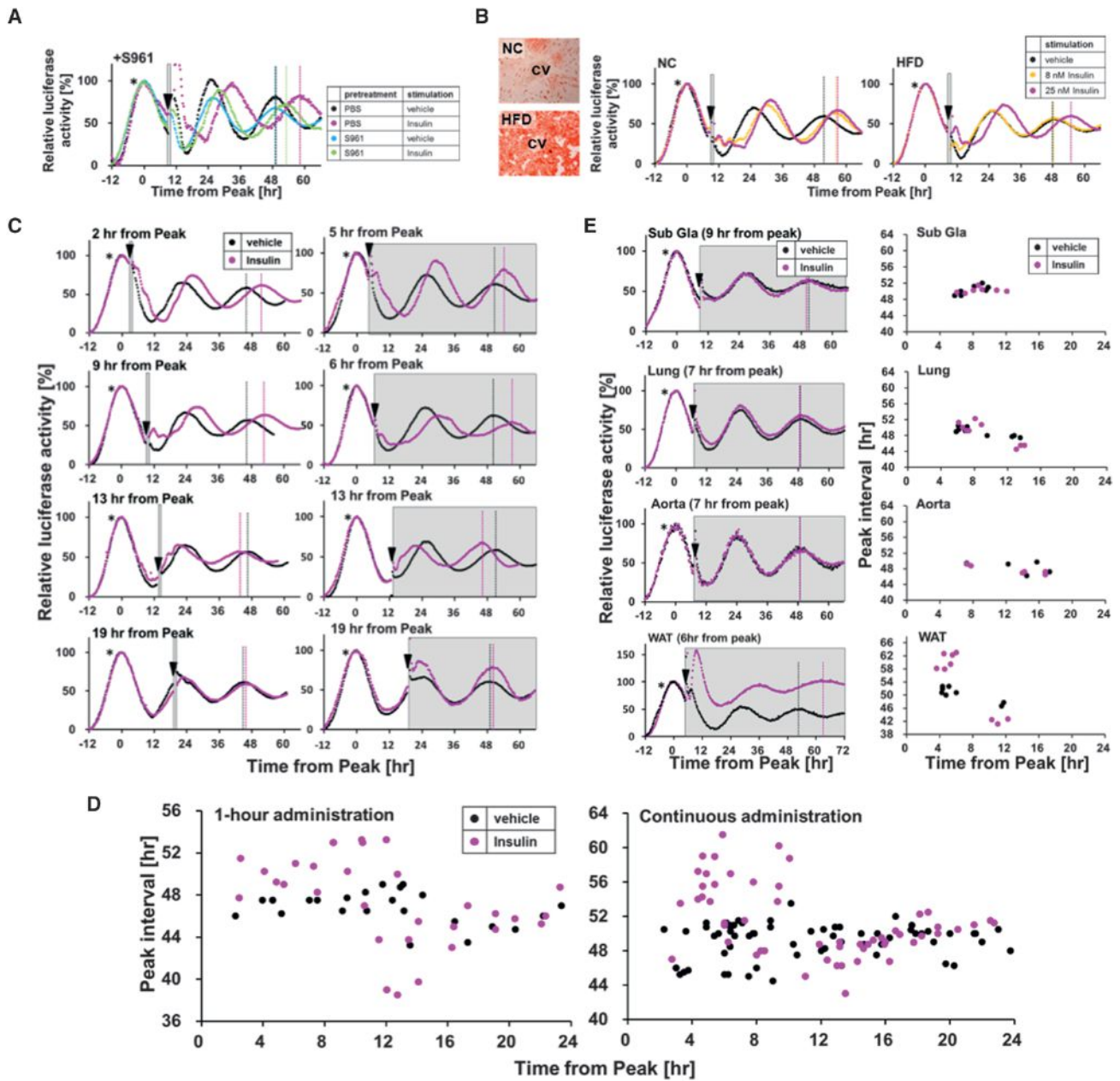


Figure 3. Insulin-Mediated Circadian Phase Shift of *Per2* Expression Rhythms in Insulin-Sensitive Tissues

(A–E) Explants derived from *Per2^{Luc}* mice were treated with insulin at specific phases. Bioluminescence was measured in real time.

(A) Representative data of liver explants pretreated with 200 nM S961 from 30 min before administration of insulin. Gray shadows represent the presence of insulin and S961 in culture media.

(B) Oil Red O staining and representative data of explants derived from high-fat diet (HFD)-fed *Per2^{Luc}* mice. Gray shadows represent the presence of insulin in culture media. CV, central vein; NC, normal control.

(C) Phase-dependent alteration of mice liver explants with insulin. Experiments with a transient treatment (1 hr) of insulin are shown on the left, and experiments with a continuous treatment at right. Gray shadows represent the presence of insulin in culture media. Representative data are shown.

(D) Phase response plot of time interval between peaks in liver from (C).

(E) Representative data and phase response plot of time interval between peaks of insulin-administered submandibular gland (Sub Gla), lung, aorta, and white adipose tissue (WAT). All explants were treated with dexamethasone (Dex) and the second peak after Dex treatment was defined as peak2 (*), and the next peak as peak3. Peak2-time was referred to as time = 0. Peak interval was calculated from the time difference between peak4 and peak2. Arrowheads indicate the time of administration. For the analysis of slices other than WAT, data were detrended by subtracting a 24 hr running average from raw data.

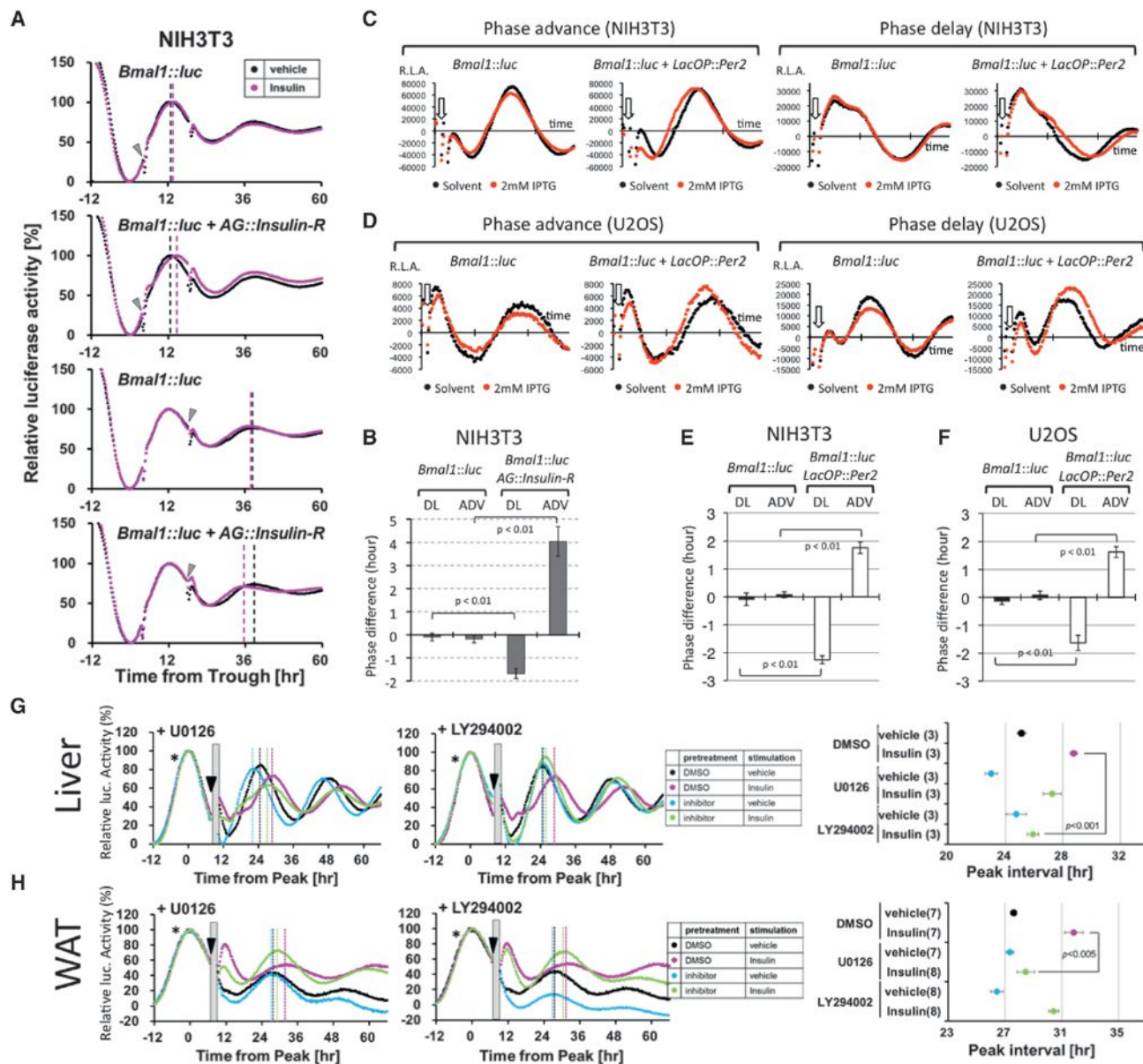


Figure 4. Acquisition of Insulin Sensitivity by Ectopic Receptor Expression and Phase-Dependent Circadian Phase Shift by Transient Induction of *Per2*

(A) NIH 3T3 fibroblasts were transfected with the *Bmal1*-driven luciferase and human insulin receptor α (*hIR* α) subunit expression vectors, and then stimulated with 60 nM insulin or vehicle. Arrowheads indicate the time of administration. To synchronize cellular clocks, the cells were treated with 50 nM dexamethasone more than 24 hr before insulin stimulation.

(B) Phase differences were calculated by comparing the first peak or trough after administration of insulin. DL, delay phase administration (increasing phase of *Bmal1* expression); ADV, advance phase administration (decreasing phase of *Bmal1* expression). Data are represented as the mean \pm SE for triplicate samples.

(C and D) NIH 3T3 and U2OS cells were transfected with the *Bmal1*-driven luciferase vector and a Lac repressor-expressing vector in the presence or absence of an IPTG-inducible *Per2* expression vector. The cells were treated with 50 nM dexamethasone (2 hr) to synchronize cellular clocks. *Bmal1* transcription was monitored in real-time using a cell culture-based luminescent monitoring system in the presence of luciferin. Approximately 18–20 hr (decreasing phase of *Bmal1* expression, for “phase advance” experiments) or 30–32 hr (increasing phase of *Bmal1* expression, for “phase delay” experiments) after the dexamethasone shock, 2 mM IPTG was added to the culture media to induce *Per2* for 1 hr. Arrows indicate the time of administration. One hour after the administration, IPTG was removed.

(E and F) Phase differences were calculated by comparing the first peak or trough after administration of IPTG. Data are represented as the mean \pm SE for triplicate samples. DL, delay phase administration (increasing phase of *Bmal1* expression); ADV, advance phase administration (decreasing phase of *Bmal1* expression).

(G and H) Liver and white adipose tissue (WAT) explants from *Per2*^{Luc} mice were pretreated with 50 μ M LY294002 (LY) or 20 μ M U0126 (U) before administration of insulin. Explants were incubated with insulin for 2 hr. The data represent the mean \pm SE. Gray shadows represent the presence of insulin and inhibitors in culture

(legend continued on next page)

phase of *Bmal1* (decreasing phase of *Per2*), versus a 1.5-hr phase advance in the decreasing phase, in both the cell lines (Figures 4E and 4F). Although the magnitude of phase shifts was not particularly large when compared with the insulin-induced phase shift in the liver, the direction of the phase shifts by insulin treatment was reproduced by simply inducing ectopic expression of *Per2*. These results support the possibility that the phase responsiveness is explained in terms of the internal clock, independently of any extracellular stimuli or intracellular signaling pathways.

Activation of the insulin receptor leads to cellular glucose uptake through the glucose transporter GLUT4, and activation of the phosphoinositide 3-kinase (PI3K) and mitogen-activated protein kinase (MAPK) signaling pathways. Previous reports suggest that these intracellular events may be involved in the resetting of clock gene expression in cultured cells. In Rat-1 fibroblasts, circadian gene expression is affected by treatment with a high concentration of glucose (Hirota et al., 2002). In H4IIE rat hepatoma cells treated with insulin, the MAPK and PI3K signaling pathways are involved in a rapid and transient induction of the *Per1* and *Per2* genes, respectively (Yamajuku et al., 2012). Although the insulin-independent glucose transporter GLUT2 is the main glucose transporter in the liver, we confirmed the ability of insulin to phase-shift circadian gene expression in the presence of cytochalasin B or D, an inhibitor of the glucose transporter GLUT4 (Figure S4B). As expected, cytochalasin treatment did not show any obvious effect on the insulin-mediated circadian phase shift. Next, we examined the effect of a PI3K inhibitor (LY294002) and a MEK inhibitor (U0126) on insulin-induced circadian phase shift in ex vivo-cultured liver (Figure 4G). Although U0126 showed no significant effect on insulin activity, inhibition of the PI3K pathway resulted in a significant attenuation of circadian phase shift. Unexpectedly, we also found that inhibition of the MAPK pathway, but not the PI3K pathway, led to an attenuation of circadian phase shift in white adipose tissue (Figure 4H), suggesting that the intracellular signaling pathways for insulin-mediated phase shift are tissue-specific. Our previous report indicated that the MAPK pathway is sufficient for resetting cell-autonomous circadian gene expression (Akashi and Nishida, 2000).

Together, these results indicate that not only the PI3K pathway, but also the MAPK pathway are involved in insulin-mediated circadian phase shift in insulin-sensitive tissues. Together, the data from our in vivo studies and ex vivo assays indicate that feeding causes circadian phase shift dependent on insulin via PI3K- and MAPK-mediated induction of *Per2* in a phase-specific manner (Figure S4C).

Peripheral clocks enable autonomous circadian gene expression in a tissue-specific manner. Just like radio-controlled clocks, the SCN functions as a standard clock, and then adjusts peripheral clocks to prevent internal desynchronization. In contrast, feeding acts on peripheral clocks as a zeitgeber, independently of the SCN. Our results indicate that insulin may be

one of the immediate early factors required for feeding-mediated entrainment. The internal clock in insulin-sensitive tissues is rapidly phase-shifted by feeding, and secondary factors such as intratissue communication then gradually adjust the clock phase of other peripheral tissues. However, the physiological significance of this stepwise entrainment of peripheral clocks remains undefined. In the SCN, the ventrolateral region is immediately entrained to a new light-dark cycle, whereas the dorsomedial region is gradually phase-adjusted by intercellular communication with the ventrolateral region (Nagano et al., 2003). The significance of the heterogeneity of the SCN is that it successfully combines the flexible response to the external environment with the robustness of the circadian system. The heterogeneous sensitivity to feeding among peripheral clocks might have a similar significance as the SCN. Furthermore, the present data might have clinical importance: in therapy for circadian disorders, they might provide valuable information for effective phase adjustment of the circadian clock by dietary manipulation. In addition, they suggest that the phase adjustment of peripheral clocks might not work well in patients with insulin resistance, and that medical staff might need to consider the side effect of insulin treatment on the circadian clock in diabetes care.

EXPERIMENTAL PROCEDURES

Feeding Schedule

After 1 week of nighttime feeding (ZT12-24; last day was termed day 0), mice were fasted for 1 day, followed by restricted feeding for 6 hr per day for 6 consecutive days (from day 1 to day 7). Food was restricted from 9:00 to 15:00 under constant dark conditions for in vivo monitoring and from 10:00 to 16:00 (ZT1-7) under light-dark conditions for RT-PCR. For injection of S961, the animals were injected with each solution subcutaneously on the dorsal neck at a dose of 30 nmol/kg at 30 min before the start of feeding every day during the restricted feeding. For feeding stimulus, male ICR mice were fasted for 24 hr and fed from ZT1 with a preinjection of saline or 100 nmol/kg of S961 on ZT0.5. All experiments were performed in accordance with the rules of the Yamaguchi University Animal Usage Committee.

In Vivo Monitoring

In vivo monitoring utilized a Lumazine CMS imaging system (NipponRoper). The animals were injected with D-luciferin potassium salt (Promega) subcutaneously on the back near the neck at a dose of 8.3 mg/kg (25 mg/10 ml, 0.1 ml/30 g body weight). Images were then taken at 8 min after luciferin injection with 1 min exposure from the ventral aspect while under anesthesia with isoflurane (DS Pharma Animal Health) inside a black box. Images were obtained seven times a day (ZT 2, 6, 10, 14, 18, 22, and 26). Mice were returned to their home cages after each imaging procedure and recovered quickly from anesthesia. The total time under anesthesia was approximately 20 min per experiment.

In Vivo Monitoring Data Analysis

The bioluminescence emitted from each organ (liver, submandibular gland) was calculated using the Metamorph (NipponRoper). For individual organs, the region of interest was set to the same shape and size for the same organ throughout all experiments. The averaged photon/sec value of the data from the seven time points for days 0–1 was designated as 100%, and the

media. For synchronization of cellular clocks, all explants were treated with 100 nM dexamethasone (Dex). The second peak after Dex treatment was defined as peak2 (*) and the next peak as peak3. Peak2-time was referred to as time = 0. Peak interval was calculated from the time difference between peak3 and peak2. Arrowheads indicate the time of administration. For the analysis of slices other than WAT, data were detrended by subtracting a 24 hr running average from raw data.

bioluminescence rhythm for the entire day was expressed as a percentage of each set of seven time points for the individual organs. The peak phase and amplitude of this normalized percentage data were determined with the single cosinor procedure program (Acro.exe, version 3.5; designed by Dr. Refinetti). Lower goodness of fit scores indicate stable states of circadian oscillation, whereas higher scores indicate transition states.

Preparation of Slice

Per2^{Luc} knockin mice were killed and used to make 300- μ m thick slices from liver, lung, and submaxillary gland with a McILWAIN tissue chopper, and white adipose tissue was prepared from epididymal tissue and aorta with a stainless steel surgical blade #11 (Feather) in ice-cold Hank's balanced salt solution (#14025, Life Technologies) with 10 mM HEPES (#H0887, Sigma-Aldrich). Each slice was cultured with millicell (#PICMORG, Merckmillipore) in Dulbecco's modified Eagle's medium (DMEM; #D2902, Sigma-Aldrich) with 0.035% sodium bicarbonate (S8761, Sigma-Aldrich), 10 mM HEPES (#H0887, Sigma-Aldrich), 4.5 g/l D-glucose (#G8769, Sigma-Aldrich), 1.0% penicillin-streptomycin (#15070-063, Life Technologies), 10% FBS (#04-001-1A, Biological Industries), and 0.1 mM D-luciferin (Promega). Note that DMEM (#D2902) basically includes 1.0 g/l of glucose, and a total of 4.5 g/l of D-glucose. For low-glucose culture, slices were cultured in no-glucose DMEM (#D5030, Sigma-Aldrich) with 0.035% sodium bicarbonate (S8761), 10 mM HEPES (#H0887), 1.0% penicillin-streptomycin (#15070-063), 1 mM sodium pyruvate (#S8636, Sigma-Aldrich), 4 mM L-glutamine (#16948-04, Nakalai Tesque), 10% FBS (#04-001-1A), and 0.1 mM D-luciferin (Promega). All explants were treated with 100 nM dexamethasone (Dex) for 60–90 min at 24–48 hr after preparation. Biological luminescence was measured and integrated for 1 min at intervals of 15 min with a LM2400 (Hamamatsu Photonics). Peak2-time was considered as time = 0 and administration of insulin or vehicle was performed at a specific time. Pretreatment was started from 15 min before insulin.

Analysis for Slice

For the analysis of the slices other than white adipose tissue, the original data (1 min bins) were subtracted with 24 hr running average from the raw data. In the case of white adipose tissue, the analysis did not work successfully, due to the strong intensity and long duration of insulin-induced transient induction of the *Per2* gene. Peak interval was calculated from the time difference between peak4 and peak2. The value of peak2 was considered as 100 and value of trough time just before peak2 was set as 0.

NIH 3T3 Analysis

The *hBmal1* promoter regions were isolated and cloned into the pGL3-Basic vector (Promega; Akashi and Takumi, 2005). NIH 3T3 cells were cultured and transfected with a *Bmal1::Luciferase* (*Bmal1::Luc*) expression vector and with or without a *human insulin receptor alpha* (AG promoter::*hIRa*) expression vector, and incubated for 24 hr. Two hours after 50 nM dexamethasone treatment, the medium was replaced with normal culture medium. In the presence of 0.1 mM luciferin, light emission was measured and integrated for 1 min at intervals of 15 min with a photomultiplier tube LM2400 (Hamamatsu Photonics). Bioluminescence was processed through a 24 hr moving average and expressed as a percentage value, with the first peak value designated as 100.

Real-Time Monitoring of the Luciferase Activity in Living Cells

We used LacSwitch Inducible Mammalian Expression System (Stratagene) for inducible expression of *Per2*. To perform IPTG-induced expression, *Per2* was subcloned into the pOPI3CAT vector. NIH 3T3 and U2OS cells were transfected with the indicated combinations of expression vectors (*hBmal1* promoter-driven luciferase vector, pOPI3CAT vector for inducible expression of *Per2*, and p3'SS Lac-repressor-expression vector). The cells were treated with 50 nM dexamethasone (2 hr) to synchronize cellular clocks and moved into a photomultiplier tube assembly (LM2400, Hamamatsu). Light emissions were measured using a photomultiplier tube in the presence of 0.1 mM luciferin and integrated for 1 min at 15 min intervals. Just before *Per2* induction, a part of the medium was collected from every culture dish for use as dilution medium. *Per2* expression was induced by administration of 2 mM IPTG to

transfected cells. One hour after administration, IPTG-containing medium was replaced with dilution medium to terminate *Per2* induction.

Statistical Analysis

All data are presented as the mean \pm SEM. The significance of differences between groups at each time point was analyzed by 2-way ANOVA with repeated measures, followed by post hoc analysis with Tukey's test when statistical significance between groups was evident. For the significance of two groups, Student's *t* test was used.

SUPPLEMENTAL INFORMATION

Supplemental Information includes Supplemental Experimental Procedures and four figures and can be found with this article online at <http://dx.doi.org/10.1016/j.celrep.2014.06.015>.

AUTHOR CONTRIBUTIONS

M.A. conceived and supervised the project, performed the experiments, analyzed the data, and wrote the manuscript. M.S. performed the experiments, analyzed the data, and wrote the manuscript. M.M. and R.M. performed experiments. K.N. provided critical reagents and samples, and gave conceptual advice.

ACKNOWLEDGMENTS

We thank Akihiko Okamoto, Yugo Muranaka, Rie Ichiyama, Kumiko Sato, Rie Tashiro, Junko Sumino, Kentaro Higashi, and Takezo Okamoto for their expert technical assistance. We express our great appreciation to Yu Tahara, Shigenobu Shibata, Tsuyoshi Kadamatsu, and Shin Yamazaki for their technical advice. *Period2-Luciferase* knockin mice, the *insulin receptor* expression vector, and S961 were kind gifts from Joseph Takahashi, Yosuke Ebina, and Lauge Schäfer, respectively. This study was supported by fellowships from the Japan Society for the Promotion of Science.

Received: June 10, 2013

Revised: May 7, 2014

Accepted: June 11, 2014

Published: July 10, 2014

REFERENCES

- Akashi, M., and Nishida, E. (2000). Involvement of the MAP kinase cascade in resetting of the mammalian circadian clock. *Genes Dev.* *14*, 645–649.
- Akashi, M., and Takumi, T. (2005). The orphan nuclear receptor RORalpha regulates circadian transcription of the mammalian core-clock *Bmal1*. *Nat. Struct. Mol. Biol.* *12*, 441–448.
- Balsalobre, A., Marcacci, L., and Schibler, U. (2000). Multiple signaling pathways elicit circadian gene expression in cultured Rat-1 fibroblasts. *Curr. Biol.* *10*, 1291–1294.
- Damiola, F., Le Minh, N., Preitner, N., Kornmann, B., Fleury-Olela, F., and Schibler, U. (2000). Restricted feeding uncouples circadian oscillators in peripheral tissues from the central pacemaker in the suprachiasmatic nucleus. *Genes Dev.* *14*, 2950–2961.
- Doherty, C.J., and Kay, S.A. (2010). Circadian control of global gene expression patterns. *Annu. Rev. Genet.* *44*, 419–444.
- Doyle, S., and Menaker, M. (2007). Circadian photoreception in vertebrates. *Cold Spring Harb. Symp. Quant. Biol.* *72*, 499–508.
- Hirota, T., Okano, T., Kokame, K., Shirota-Ikejima, H., Miyata, T., and Fukada, Y. (2002). Glucose down-regulates *Per1* and *Per2* mRNA levels and induces circadian gene expression in cultured Rat-1 fibroblasts. *J. Biol. Chem.* *277*, 44244–44251.
- Kuriyama, K., Sasahara, K., Kudo, T., and Shibata, S. (2004). Daily injection of insulin attenuated impairment of liver circadian clock oscillation in the streptozotocin-treated diabetic mouse. *FEBS Lett.* *572*, 206–210.

- McNamara, P., Seo, S.B., Rudic, R.D., Sehgal, A., Chakravarti, D., and FitzGerald, G.A. (2001). Regulation of CLOCK and MOP4 by nuclear hormone receptors in the vasculature: a humoral mechanism to reset a peripheral clock. *Cell* 105, 877–889.
- Mohawk, J.A., Green, C.B., and Takahashi, J.S. (2012). Central and peripheral circadian clocks in mammals. *Annu. Rev. Neurosci.* 35, 445–462.
- Nagano, M., Adachi, A., Nakahama, K., Nakamura, T., Tamada, M., Meyer-Bernstein, E., Sehgal, A., and Shigeyoshi, Y. (2003). An abrupt shift in the day/night cycle causes desynchrony in the mammalian circadian center. *J. Neurosci.* 23, 6141–6151.
- Nagoshi, E., Saini, C., Bauer, C., Laroche, T., Naef, F., and Schibler, U. (2004). Circadian gene expression in individual fibroblasts: cell-autonomous and self-sustained oscillators pass time to daughter cells. *Cell* 119, 693–705.
- Nonaka, H., Emoto, N., Ikeda, K., Fukuya, H., Rohman, M.S., Raharjo, S.B., Yagita, K., Okamura, H., and Yokoyama, M. (2001). Angiotensin II induces circadian gene expression of clock genes in cultured vascular smooth muscle cells. *Circulation* 104, 1746–1748.
- Oishi, K., Kasamatsu, M., and Ishida, N. (2004). Gene- and tissue-specific alterations of circadian clock gene expression in streptozotocin-induced diabetic mice under restricted feeding. *Biochem. Biophys. Res. Commun.* 317, 330–334.
- Reppert, S.M., and Weaver, D.R. (2002). Coordination of circadian timing in mammals. *Nature* 418, 935–941.
- Rosbash, M., Bradley, S., Kadener, S., Li, Y., Luo, W., Menet, J.S., Nagoshi, E., Palm, K., Schoer, R., Shang, Y., and Tang, C.H. (2007). Transcriptional feedback and definition of the circadian pacemaker in *Drosophila* and animals. *Cold Spring Harb. Symp. Quant. Biol.* 72, 75–83.
- Sahar, S., and Sassone-Corsi, P. (2012). Regulation of metabolism: the circadian clock dictates the time. *Trends Endocrinol. Metab.* 23, 1–8.
- Schäffer, L., Brand, C.L., Hansen, B.F., Ribbel, U., Shaw, A.C., Slaaby, R., and Sturis, J. (2008). A novel high-affinity peptide antagonist to the insulin receptor. *Biochem. Biophys. Res. Commun.* 376, 380–383.
- Scherer, T., O'Hare, J., Diggs-Andrews, K., Schweiger, M., Cheng, B., Lindtner, C., Zielinski, E., Vempati, P., Su, K., Dighe, S., et al. (2011). Brain insulin controls adipose tissue lipolysis and lipogenesis. *Cell Metab.* 13, 183–194.
- Stokkan, K.A., Yamazaki, S., Tei, H., Sakaki, Y., and Menaker, M. (2001). Entrainment of the circadian clock in the liver by feeding. *Science* 291, 490–493.
- Tahara, Y., Kuroda, H., Saito, K., Nakajima, Y., Kubo, Y., Ohnishi, N., Seo, Y., Otsuka, M., Fuse, Y., Ohura, Y., et al. (2012). In vivo monitoring of peripheral circadian clocks in the mouse. *Curr. Biol.* 22, 1029–1034.
- Vikram, A., and Jena, G. (2010). S961, an insulin receptor antagonist causes hyperinsulinemia, insulin-resistance and depletion of energy stores in rats. *Biochem. Biophys. Res. Commun.* 398, 260–265.
- Wijnen, H., and Young, M.W. (2006). Interplay of circadian clocks and metabolic rhythms. *Annu. Rev. Genet.* 40, 409–448.
- Wu, T., Ni, Y., Kato, H., and Fu, Z. (2010). Feeding-induced rapid resetting of the hepatic circadian clock is associated with acute induction of *Per2* and *Dec1* transcription in rats. *Chronobiol. Int.* 27, 1–18.
- Yamajuku, D., Inagaki, T., Haruma, T., Okubo, S., Kataoka, Y., Kobayashi, S., Ikegami, K., Laurent, T., Kojima, T., Noutomi, K., et al. (2012). Real-time monitoring in three-dimensional hepatocytes reveals that insulin acts as a synchronizer for liver clock. *Sci Rep* 2, 439.
- Yamazaki, S., Numano, R., Abe, M., Hida, A., Takahashi, R., Ueda, M., Block, G.D., Sakaki, Y., Menaker, M., and Tei, H. (2000). Resetting central and peripheral circadian oscillators in transgenic rats. *Science* 288, 682–685.
- Yoo, S.H., Yamazaki, S., Lowrey, P.L., Shimomura, K., Ko, C.H., Buhr, E.D., Siepack, S.M., Hong, H.K., Oh, W.J., Yoo, O.J., et al. (2004). PERIOD2: LUCIFERASE real-time reporting of circadian dynamics reveals persistent circadian oscillations in mouse peripheral tissues. *Proc. Natl. Acad. Sci. USA* 101, 5339–5346.

Inference of Tumor Evolution during Chemotherapy by Computational Modeling and In Situ Analysis of Genetic and Phenotypic Cellular Diversity

Vanessa Almendro,^{1,2,3,4} Yu-Kang Cheng,^{5,6} Amanda Randles,^{5,6,7} Shalev Itzkovitz,^{8,9} Andriy Marusyk,^{1,2,3} Elisabet Ametller,⁴ Xavier Gonzalez-Farre,⁴ Montse Muñoz,⁴ Hege G. Russnes,^{10,11,12} Åslaug Helland,^{10,13,14} Inga H. Rye,^{10,11} Anne-Lise Borresen-Dale,^{10,11} Reo Maruyama,^{1,2,3} Alexander van Oudenaarden,^{8,15} Mitchell Dowsett,¹⁶ Robin L. Jones,^{16,17} Jorge Reis-Filho,^{16,18} Pere Gascon,⁴ Mithat Gönen,¹⁹ Franziska Michor,^{5,6,*} and Kornelia Polyak^{1,2,3,20,21,*}

¹Department of Medical Oncology, Dana-Farber Cancer Institute, Boston, MA 02215, USA

²Department of Medicine, Brigham and Women's Hospital, Boston, MA 02115, USA

³Department of Medicine, Harvard Medical School, Boston, MA 02115, USA

⁴Department of Medical Oncology, Hospital Clinic, Institut d'Investigacions Biomediques August Pi i Sunyer, Barcelona 08036, Spain

⁵Department of Biostatistics and Computational Biology, Dana-Farber Cancer Institute, Boston, MA 02215, USA

⁶Department of Biostatistics, Harvard School of Public Health, Boston, MA 02115, USA

⁷Center for Applied Scientific Computing, Lawrence Livermore National Laboratory, Livermore, CA 94550, USA

⁸Departments of Physics and Biology and Koch Institute for Integrative Cancer Research, Massachusetts Institute of Technology, Cambridge, MA 02139, USA

⁹Department of Molecular Cell Biology, Weizmann Institute of Science, Rehovot 76100, Israel

¹⁰Department of Genetics, Institute for Cancer Research, Oslo University Hospital Radiumhospitalet, Oslo 0424, Norway

¹¹K.G. Jebsen Center for Breast Cancer Research, Institute for Clinical Medicine, Faculty of Medicine, University of Oslo, Oslo 0316, Norway

¹²Department of Pathology, Oslo University Hospital, Oslo 0424, Norway

¹³Department of Oncology, Oslo University Hospital, Oslo 0424, Norway

¹⁴Institute for Clinical Medicine, Faculty of Medicine, University of Oslo, Oslo 0316, Norway

¹⁵Hubrecht Institute, Royal Netherlands Academy of Arts and Sciences and University Medical Center Utrecht, Uppsalalaan 8, 3584 CT, Utrecht, the Netherlands

¹⁶The Royal Marsden Hospital, The Breakthrough Breast Cancer Research Centre, Institute of Cancer Research, London SW3 6JJ, UK

¹⁷Seattle Cancer Care Alliance, Seattle, WA 98109-1023, USA

¹⁸Department of Pathology, Memorial Sloan-Kettering Cancer Center, New York, NY 10065, USA

¹⁹Department of Epidemiology and Biostatistics, Memorial Sloan-Kettering Cancer Center, New York, NY 10065, USA

²⁰Harvard Stem Cell Institute, Cambridge, MA 02138, USA

²¹Broad Institute, Cambridge, MA 02142, USA

*Correspondence: michor@jimmy.harvard.edu (F.M.), kornelia_polyak@dfci.harvard.edu (K.P.)

<http://dx.doi.org/10.1016/j.celrep.2013.12.041>

This is an open-access article distributed under the terms of the Creative Commons Attribution-NonCommercial-No Derivative Works License, which permits non-commercial use, distribution, and reproduction in any medium, provided the original author and source are credited.

SUMMARY

Cancer therapy exerts a strong selection pressure that shapes tumor evolution, yet our knowledge of how tumors change during treatment is limited. Here, we report the analysis of cellular heterogeneity for genetic and phenotypic features and their spatial distribution in breast tumors pre- and post-neoadjuvant chemotherapy. We found that intratumor genetic diversity was tumor-subtype specific, and it did not change during treatment in tumors with partial or no response. However, lower pretreatment genetic diversity was significantly associated with pathologic complete response. In contrast, phenotypic diversity was different between pre- and post-treatment samples. We also observed significant changes in the spatial distribution of cells with

distinct genetic and phenotypic features. We used these experimental data to develop a stochastic computational model to infer tumor growth patterns and evolutionary dynamics. Our results highlight the importance of integrated analysis of genotypes and phenotypes of single cells in intact tissues to predict tumor evolution.

INTRODUCTION

Intratumor phenotypic heterogeneity is a defining characteristic of human tumors. Cancer cells within a tumor can display differences in many measurable traits, such as proliferative and metastatic capacity and therapeutic resistance (Almendro et al., 2013; Fidler, 1978; Heppner and Miller, 1983; Maley et al., 2006; Marusyk et al., 2012; Yap et al., 2012). Multiple mechanisms underlie intratumor heterogeneity, including both

heritable and nonheritable determinants (Fidler, 1978; Heppner and Miller, 1983; Maley et al., 2006; Marusyk et al., 2012; Marusyk and Polyak, 2010; Yap et al., 2012). In addition, cellular genetic diversity was observed within populations of tumor cells that is distinct from clonal diversity because it combines inputs from both clonal architecture and lower-scale differences arising from genomic instability that are not amplified by selection (Maley et al., 2006; Merlo et al., 2006). The study and treatment of cancer are complicated by this heterogeneity because small tissue samples, typically obtained by biopsy, may not be representative of the whole tumor (Gerlinger et al., 2012), and a treatment that targets one tumor cell population may not be effective against another (Turner and Reis-Filho, 2012; Yap et al., 2012).

Quantitative measures of intratumor heterogeneity might aid in the clinical management of patients with cancer including identifying those at a high risk of progression and recurrence. For example, a larger extent of intratumor clonal heterogeneity is associated with a higher risk of invasive progression in Barrett's esophagus (Maley et al., 2006; Merlo et al., 2010), and higher genetic heterogeneity in head and neck squamous carcinomas is related to worse outcome (Mroz et al., 2013). The presence of multiple cellular clones with distinct genetic alterations has also been implicated in therapeutic resistance (Engelman et al., 2007; Mroz et al., 2013; Nazarian et al., 2010; Sakai et al., 2008) and in metastatic progression (Fidler, 1978).

Cancer therapy exerts a strong selection pressure that shapes tumor evolution (Merlo et al., 2006). Thus, residual tumors after treatment are likely to have different, frequently less-favorable characteristics and composition than those of the diagnostic sample. Despite the importance of these treatment-induced changes for the success of subsequent therapy, tumors have been rarely resampled and reanalyzed, with the exception of hematopoietic malignancies (Ding et al., 2012; Landau et al., 2013). Thus, our understanding of how treatment impacts intratumor heterogeneity and cellular diversity in solid tumors, which then in turn determines the effectiveness of treatment, is very limited.

The most informative approach to uncover intratumor heterogeneity in clinical samples is the definition of the overall clonal architecture within a tumor. However, this level of resolution is not practically feasible. A lower-resolution view of clonal architecture can be outlined based on computational inferences from allele frequencies of whole-genome sequencing of bulk tumors (Ding et al., 2012) or by low-resolution sequencing of single cancer cells (Navin et al., 2011). Unfortunately, both of these approaches have many technical caveats and are prohibitively expensive to apply for large patient cohorts.

An alternative to the whole-genome studies is to study genetic diversity using a single or a few genomic loci. Although this approach cannot reveal the clonal architecture within a tumor, it is more feasible due to minimal sample requirements and low cost. Importantly, diversity indices calculated based on a limited number of loci (even selectively neutral ones) have been shown to predict clinical outcome (Maley et al., 2006; Merlo et al., 2010). Cellular heterogeneity reflects both clonal heterogeneity and genetic instability; thus, it can be impacted by anticancer therapy on several levels. First, the new selective pressures are expected to favor relatively treatment-resistant clonal subpopulations over sensitive ones, therefore limiting clonal

diversity. Second, genotoxic treatments may elevate genomic instability, thereby potentially increasing cellular genetic diversity. Despite its clinical importance, the potential impact of cancer therapy on cellular genetic heterogeneity is largely unknown. Here, we report the effects of neoadjuvant chemotherapy on the extent of genetic and phenotypic cellular diversity within breast tumors and the associations between intratumor genetic heterogeneity and therapeutic outcomes.

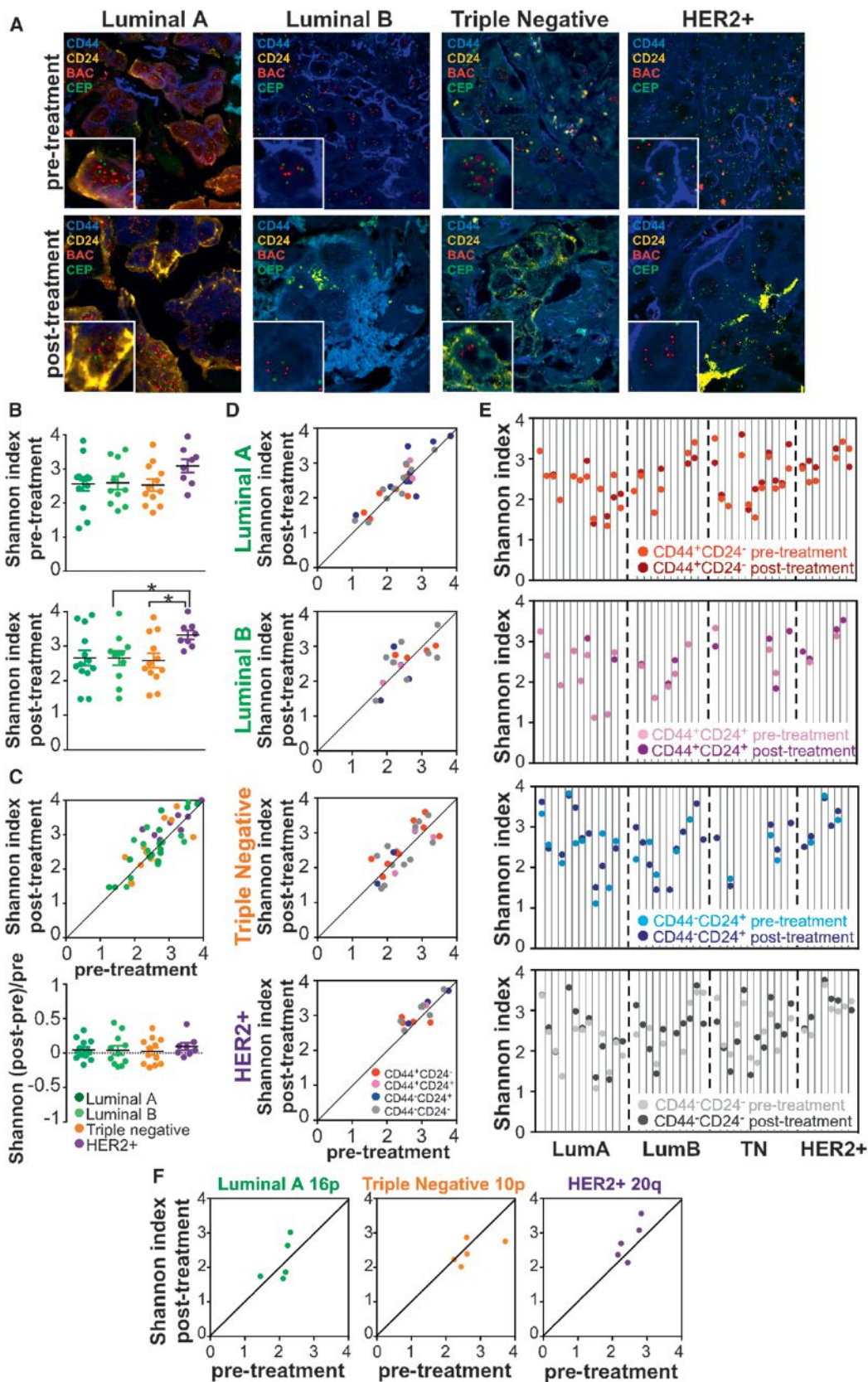
RESULTS

Tumor-Subtype- and Cancer Cell-Type-Specific Differences in Genetic Diversity

To investigate relationships between intratumor heterogeneity and cancer therapy, we analyzed pre- and posttreatment tumor biopsies from 47 patients with breast cancer undergoing neoadjuvant chemotherapy (Table S1). These included 13 luminal A, 11 luminal B, 11 HER2+, and 12 TNBC (triple-negative breast cancer) tumors representing each of the major breast tumor subtypes (Perou et al., 2000). Four patients showed pathologic complete response (pCR) to treatment; thus, in these cases, posttreatment samples could not be analyzed.

Genetic heterogeneity was assessed based on immunofluorescence in situ hybridization (iFISH) using BAC (bacterial artificial chromosome) probes for 8q24.3, 10p13, 16p13.3, and 20q13.31 and the corresponding centromeric probes (CEPs) to distinguish between gain of whole chromosomes versus specific chromosomal regions. These genomic loci were selected because they are the most commonly amplified chromosomal regions in breast cancer regardless of tumor subtype (e.g., 8q24) or within a specific tumor subtype (Nikolsky et al., 2008). Phenotypic heterogeneity was assessed by staining for CD44 and CD24 (Figure 1A) because prior studies from our and other laboratories demonstrated that these cell surface markers identify cancer cells with distinct molecular and biological properties (Al-Hajj et al., 2003; Bloussaint-Qimron et al., 2008; Li et al., 2008; Liu et al., 2007; Shipitsin et al., 2007), including genetic heterogeneity both between and within CD44⁺ and CD24⁺ breast cancer cell populations (Park et al., 2010a; Shipitsin et al., 2007). The neoplastic nature of the cells was confirmed by examining cellular and nuclear morphology using adjacent hematoxylin and eosin-stained slides and in the majority of cases by the presence of chromosomal copy number gain.

The 8q24 BAC and chromosome 8 (chr8) CEP signals were counted in about 100 individual cells for each of the four phenotypically distinct tumor cell populations (i.e., CD44⁺CD24⁻, CD44⁺CD24⁺, CD44⁻CD24⁺, and CD44⁻CD24⁻ cells). Diversity was evaluated based on Shannon and Simpson indices (Magurran, 2004) that were calculated in four different ways based on measures of (1) copy number of 8q24 (BAC probe), (2) copy number of chr8 centromeric region (CEP), (3) ratio of BAC/CEP counts, and (4) individual copy number of both BAC and CEP probes in each cell (unique counts). Overall, each of the four different calculations displayed similar relative differences among tumors and matched pre- and posttreatment samples, but diversity indices were the highest based on unique counts (Table S2). Thus, owing to its more accurate prediction of genetic



(legend on next page)

diversity, we subsequently used unique counts for all analyses unless otherwise indicated.

First, we investigated whether pre- and posttreatment genetic diversity for 8q24 is different in distinct breast tumor subtypes. HER2+ tumors had significantly higher diversity after treatment compared to luminal B and TNBC tumors (Figure 1B; Table S2). However, there was no significant difference in overall genetic diversity in any of the tumors between pre- and post-treatment samples (Figure 1C). Next, we investigated potential changes in genetic diversity in phenotypically distinct tumor cell subpopulations. We required cell subpopulations for analysis to represent at least 5% of all cancer cells within a tumor in order to avoid a counting bias; thus, not all four phenotypic types were analyzed in all samples. In some tumors, we observed significant differences in the relative distribution of copy number for BAC or CEP probes or BAC/CEP ratios in specific cell subpopulations when comparing pre- and post-treatment data (Figure S1A). We also observed changes in cell populations and unique cancer cells based on kernel density estimates and Whittaker plots (Figures S1B and S1C). However, pairwise analysis of pre- and posttreatment differences in genetic diversity in each of the four phenotypic subpopulations across all tumors did not reveal significant changes (Figure 1D); cell-type-specific genetic diversity was significantly higher after treatment only in a few cases (Figure 1E; Table S2).

To ensure that our results were not due to the inaccurate reflection of overall genomic diversity based on 8q24 counts, we also analyzed three additional loci commonly amplified in luminal (16p13), TNBC (10p13), and HER2+ (20q13) tumors. Similar to 8q24, these additional loci also failed to demonstrate significant changes in genetic diversity (Figure 1F). Our data suggest that genetic diversity is an intrinsic tumor trait that remains relatively stable during treatment.

Changes in Phenotypic Heterogeneity Highlight Biologic Differences among Cell Types

To determine potential changes in cellular phenotypes due to treatment, we analyzed the relative frequency of the four distinct cell subpopulations within tumors. We observed a significant increase in the frequency of CD44⁻CD24⁺ cells in luminal A, luminal B, and TNBC tumors after treatment, and residual TNBC tumors were also enriched for CD44⁻CD24⁻ cells (Figures 2A and 2B). Concomitantly, there were fewer CD44⁺CD24⁻ cells in luminal A and triple-negative tumors after treatment, whereas HER2+ tumors displayed very few changes in the distribution of cell subpopulations. Next, we estimated the degree of pheno-

typic diversity based on the Shannon index and found that phenotypic diversity for CD44 and CD24 markers tends to decrease in luminal tumors, whereas it increases in TNBC tumors (Figure S2).

Because chemotherapy is thought to target proliferative cells (Collecchi et al., 1998), the observed changes in the relative frequencies of the four cell subpopulations could be due to cell-type-specific differences in proliferation. Thus, we assessed the frequency of cells positive for the Ki67 proliferation marker within each of the four cell types before and after treatment. The fraction of Ki67⁺ cells was lower in all cell types in all tumors after treatment, with only a few exceptions (Figure S3A). We also observed significant differences in the proportion of Ki67⁺ cells before treatment between CD44⁺CD24⁻ and CD44⁻CD24⁺ cell populations, which were the most and least proliferative, respectively (Figures 2C and 2D). Spearman correlation analysis of associations between changes in the frequency of Ki67⁺ cells and cell subpopulations revealed a significant positive correlation in CD44⁺CD24⁻ cells ($p = 0.007$) and a significant negative correlation in CD44⁻CD24⁺ cells ($p < 0.001$) (Figure 2E). These results imply that the increase in the relative frequency of CD24⁺ compared to CD44⁺ cells after treatment might be due to the preferential elimination of the more proliferative CD44⁺ cells by chemotherapy. Thus, if a tumor remains highly proliferative after treatment, it has a higher CD44⁺CD24⁻-to-CD44⁻CD24⁺ cell ratio. However, the possibility of conversion from CD44⁺ to CD24⁺ cellular phenotypes or a change in the expression of these markers due to the cell-cycle phase or as a direct effect of treatment cannot be excluded. These results are in agreement with previous findings that treatment selects for slow-growing CD24⁺ cancer cells in lung cancer (Sharma et al., 2010) and in melanoma (Roesch et al., 2013).

Differences in cellular proliferation could also be related to differences in genetic diversity because faster-growing cells may have a larger population size and might therefore be more likely to accumulate genetic abnormalities. Thus, we also analyzed potential associations between the proliferation rate of each cell type and its genetic diversity index. Spearman correlation analysis demonstrated significant associations between Ki67 levels and the Shannon index of genetic diversity in CD44⁻CD24⁺ ($p = 0.007$) and CD44⁺CD24⁺ ($p = 0.027$) cells before treatment, suggesting that the observed genetic diversity in these cell subpopulations could be influenced by their lower proliferation rates (Figure S3B). In contrast, after treatment, Ki67 levels and Shannon indices showed a significant ($p = 0.04$) correlation only in CD44⁺CD24⁻ cells. We failed to observe

Figure 1. Genetic Diversity in Breast Cancer According to Tumor Subtype and Treatment

- (A) Representative images of iFISH in four tumors of the indicated subtypes before and after treatment.
- (B) Shannon index of diversity in each tumor subtype before and after treatment calculated based on unique BAC and CEP counts for each cell. Each dot represents an individual tumor, black line shows mean \pm SEM, and colors indicate luminal A (dark green), luminal B (light green), triple-negative (orange), and HER2+ (violet) tumor subtypes. Asterisks mark significant differences between subtypes: * $p \leq 0.05$ and ** $p \leq 0.01$, by Wilcoxon rank sum test.
- (C) Correlations between Shannon indices in each tumor before and after treatment and the relative change in diversity in each tumor. Black line shows mean \pm SEM.
- (D) Correlations between pre- and posttreatment Shannon indices in the indicated cell subpopulations and tumor subtypes. Not all cell subpopulations are present in all tumors.
- (E) Shannon index in phenotypically distinct subpopulations in individual tumors before and after treatment. Each vertical line separates individual cases. LumA, luminal A; LumB, luminal B; TN, triple negative.
- (F) Correlations between Shannon indices in each tumor before and after treatment for the indicated loci.
- See also Figure S1 and Tables S1 and S2.

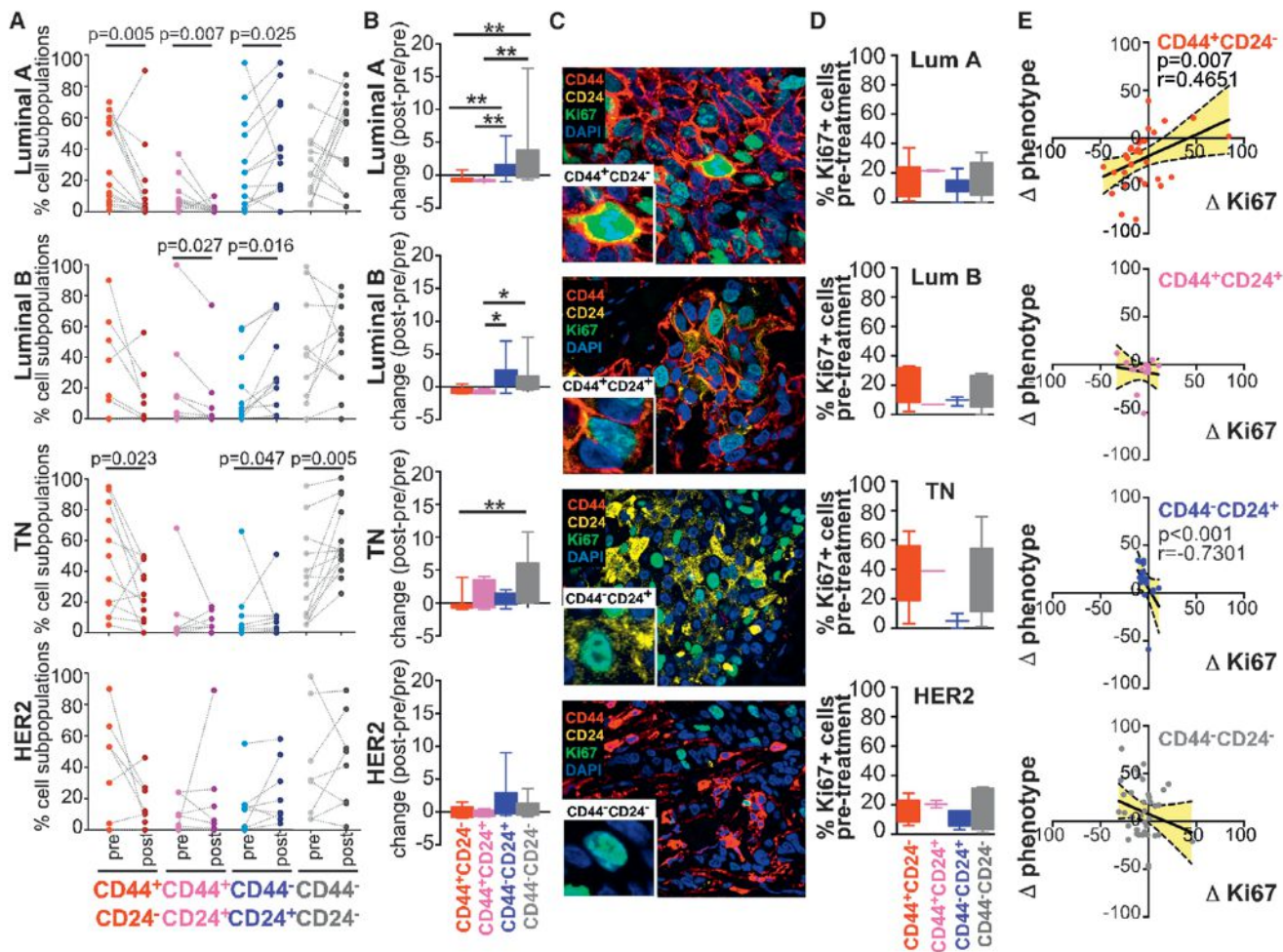


Figure 2. Changes in Phenotypic Heterogeneity and Cell-Type-Specific Variations in Proliferation Rates

(A) Changes in the frequency of the indicated cell subpopulations in the different tumor subtypes. Dotted line connects values for each cell subpopulation before and after treatment. Significant p values by two-sided Wilcoxon matched-pairs signed rank test are shown.

(B) Box plot depicts relative changes in the frequency of each of the four cell subpopulations. Boxes correspond to 25th–75th percentile, whereas whiskers mark maximum and minimum values. Asterisks indicate statistically significant differences by two-sided Wilcoxon matched-pairs signed rank test: *p < 0.05 and **p < 0.01.

(C) Representative immunofluorescence images of Ki67 staining in specific cell subpopulations.

(D) Frequency of Ki67⁺ cells before treatment. Boxes correspond to 25th–75th percentile, whereas whiskers mark maximum and minimum values.

(E) Correlation between differences (Δ denotes posttreatment minus pretreatment values) in the frequency of cell subpopulations and percentage (%) of Ki67⁺ cells after treatment. Negative values indicate a decrease of each variable after treatment. A 95% confidence interval is indicated in yellow.

See also Figures S2 and S3.

any associations between changes in diversity and changes in the fraction of Ki67⁺ cells during treatment (Figure S3C), suggesting that although differences in proliferation could be associated with differences in diversity in some cell subpopulations before treatment, changes in proliferation were not generally associated with differences in diversity after treatment.

Topology Maps to Explore Changes of Cellular Heterogeneity in Spatially Explicit Context

The previous analyses focused on population-level genotypic and phenotypic diversity. However, intermixing of tumor cells is substantially restricted in solid tumors by tissue architecture. Furthermore, heterogeneity of intratumor microenvironments, including differences in extracellular matrix and vascularization,

is expected to impact selective pressures and differentiation cues, thereby translating into differences in genotypes and phenotypes. Therefore, we decided to address whether accounting for spatially explicit tissue organization can reveal therapy-induced changes in cellular heterogeneity missed by population-based analyses. To investigate this issue, we created tumor topology maps by analyzing the distribution of cancer cells with distinct genotypes and phenotypes in three physically distinct regions in 15 tumors (5 of each of the 3 major subtypes) before and after treatment. These cases were selected based on the presence of sufficiently large cell numbers after treatment to allow cell-to-cell interaction analyses. For each cell, we recorded copy numbers of 8q24 BAC and chr8 CEP probes and cellular phenotype. Representative examples of such topology maps

are depicted in Figures 3A–3C (Patient 1, Luminal A tumor) and S4 (patient 20, TNBC, and patient 30, HER2+ tumor). The tumor of patient 1 showed a marked increase in both 8q24 BAC and chr8 CEP copy numbers and in the frequency of CD44⁻CD24⁺ cells after treatment (Figures 3A–3C). In patient 20, there was a clear decrease in both 8q24 BAC and chr8 CEP copy numbers, but no substantial changes in the frequencies of cellular phenotypes (Figures S4A–S4C). In contrast, in patient 30, there was a dramatic increase in 8q24 BAC copy numbers with a concomitant decrease in chr8 CEP counts but essentially no changes in cellular phenotypes (Figures S4D–S4F). Therefore, at least some tumors display substantial phenotypic and genotypic differences pre- and posttreatment. Despite these changes, pre- and posttreatment genetic diversity indices in the three topologically distinct areas of each tumor were not significantly different (Table S3; Figure S5), with the exception of two cases (patients 1 and 3, both with partial response to treatment). These results imply that the analysis of even one region might be sufficient to assess overall genetic diversity of a tumor. However, because the distant regions we compared were still within one section and one biopsy, the possibility cannot be excluded that biopsies taken from distant parts of the tumor may show more pronounced differences. Furthermore, the lack of significant differences in genetic diversity in different regions of the same tumor does not mean that tumor cells located in distinct areas are genetically identical. It rather implies that diversity is an inherent feature of the tumors that is less subjective to sampling bias than the measurement of a specific trait.

Effect of Treatment on the Distribution of Genetic Heterogeneity within Topology Maps

We then employed the topology maps to assess the effects of treatment on spatial distribution of genetic heterogeneity by measuring genetic distances between the adjacent and all cancer cells within tumors using the copy number differences for both 8q24 BAC and chr8 CEP. We observed that in most cases, the distribution of the differences in copy number was significantly different after treatment compared to before treatment, both when considering the differences only in adjacent cells or in all cells (Figures 3D and 4A). However, in some cases, the distribution of the differences in adjacent cells was not significantly different (Figure 4B), indicating the differential topologic distribution of cells with similar copy number. We observed that in several tumors, the genetic distance for both 8q24 BAC and chr8 CEP probes changed in the same direction after treatment, whereas in a few cases, the divergence for the 8q24 BAC probe decreased with a concomitant increase in variability for chr8 CEP (Figures 3D and 4A–4C). Overall, in the 15 tumors analyzed, the cell-to-cell variability for 8q24 BAC and chr8 CEP counts was significantly higher after treatment in eight cases, lower for chr8 CEP copy number in five patients, and decreased for 8q24 in three cases (Figure 4C). Therefore, incorporation of spatially explicit context into analysis of genetic diversity has revealed differences missed by population-wide analysis. However, the causes of the observed differences are difficult to interpret because increase in copy number differences between adjacent cells after chemotherapy could be due to an increase in genetic instability, the selection for slowly proliferating cells

that are more likely to be phylogenetically distinct, or increased cell migration.

We then sought to obtain further insight by analyzing changes in genetic divergence within cells with similar phenotype focusing on the four phenotypically distinct cellular subpopulations defined by expression of CD24 and CD44. We found significant cell-type-specific differences in the degree of genetic variability between all cells and all adjacent cells of the same phenotype within individual tumors. For example, in a luminal tumor (patient 1), the increase in cell-to-cell variability for 8q24 and chr8 CEP copy numbers was significant in CD44⁻CD24⁺ and CD44⁻CD24⁻ cells when considering all cells, whereas in adjacent cells, only the CD44⁻CD24⁺ fraction showed a significant increase for both BAC and CEP probes (Figure 3E). In this tumor, we could not detect any CD44⁺CD24⁻ and CD44⁺CD24⁺ cells after treatment. Thus, it is possible that the increased genetic heterogeneity of the CD44⁻CD24⁺ and CD44⁻CD24⁻ fractions was due to phenotypic switch of the CD44⁺ cell populations due to treatment.

Similarly, in a TNBC (patient 20), variability for 8q24 and chr8 CEP counts decreased in all CD44⁺CD24⁻ and CD44⁻CD24⁻ cells (adjacent or not), but in CD44⁺CD24⁺ cells, the variability for 8q24 only decreased in adjacent cells (Figures 5A and 5B). Similar differences were observed in other cases for changes in genetic variability between adjacent cells compared to all cells within the tumor, like in a HER2+ tumor (patient 30) (Figures 5B and 5C).

The increased genetic variability in adjacent cells of the same phenotype together with the significant changes in the relative frequency of distinct cell subpopulations due to treatment suggests either selection for distinct phenotypes based on their differential sensitivity to the treatment or increased rates of genomic instability resulting from the treatment. Interestingly, in all 15 tumors analyzed, the frequency of homotypic-phenotypic clustering was significantly higher compared to the heterotypic one both before and after treatment (Figure 3F). Thus, tumor cells tend to cluster more based on their phenotype than on their genotype. The results of these topology analyses highlight the insights afforded by analyzing tumors at the single-cell level and in situ because the spatial organization of the cells with distinct genotypes and phenotypes is lost when analyzing bulk tissues or dissociated cells.

Computational Modeling Allows an Investigation of Tumor Growth Patterns and Evolution during Treatment

To better understand the forces that could give rise to the observed patterns of spatial clustering of cells with the same phenotype, we next developed a stochastic computational model of cellular proliferation and death utilizing our tumor topology and Ki67 data (see Supplemental Experimental Procedures for details). This model is based on a stochastic process of cell growth and death in a 2D cross-section of a tumor, implemented as a patient-specific computer simulation informed by parameters measured in a patient-specific manner. This model was used to investigate the growth patterns and evolutionary dynamics of tumor cells during chemotherapy and also enabled us to determine the extent to which proliferation alone could explain the detected clustering of phenotypes.

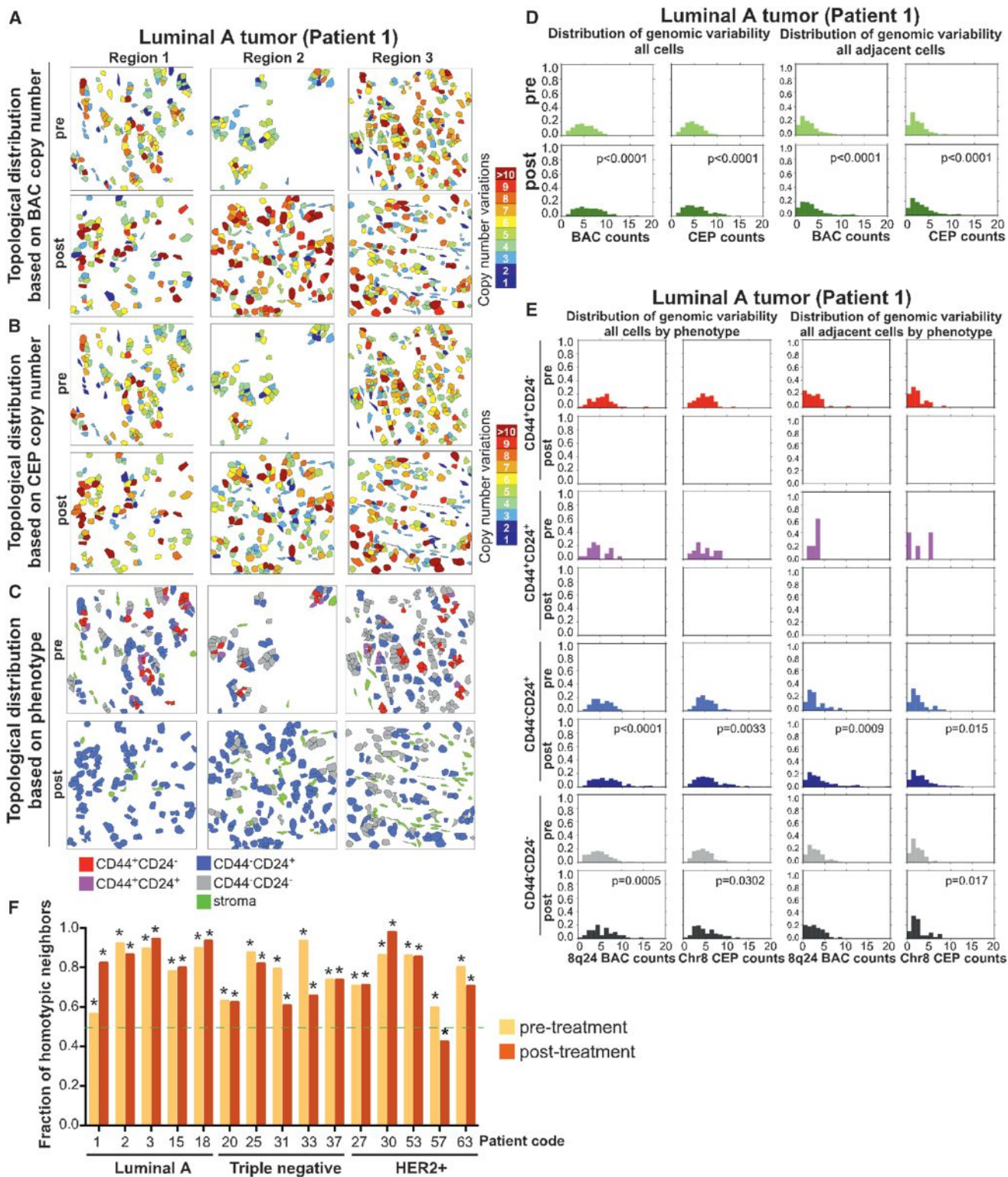


Figure 3. Analysis of Tumor Topology

(A–C) Maps showing topologic differences in the distribution of genetically distinct tumor cells based on copy number for 8q24 BAC (A), chr8 CEP (B), and cellular phenotype (C) in three different regions of a luminal A tumor (Patient 1).

(D) Histograms depicting absolute differences in copy numbers for BAC and CEP probe counts regardless of phenotype in all cells or in adjacent cells before and after treatment.

(legend continued on next page)

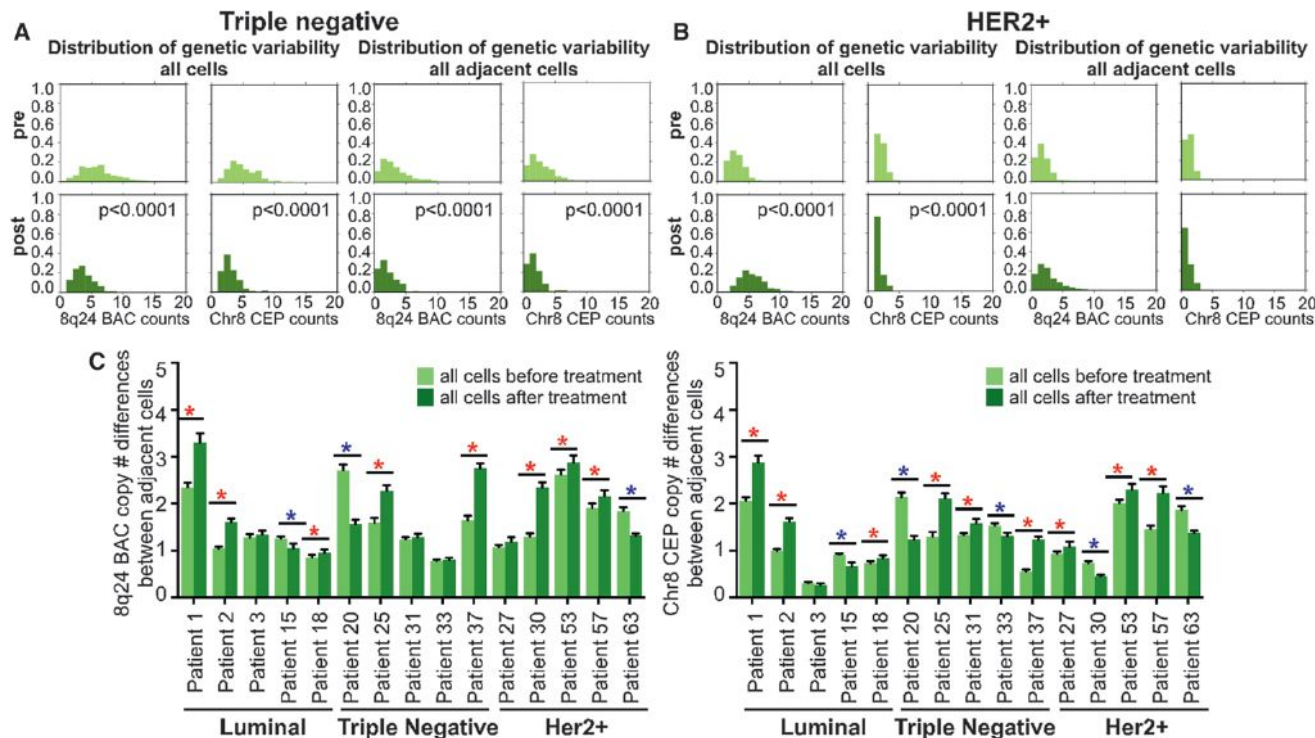


Figure 4. Genotype of All Cells and Adjacent Cells within Tumors

(A and B) Histograms depicting variability for 8q24 BAC and chr8 CEP probe counts regardless of phenotype in all cells (left panel) or in adjacent cells (right panel) before and after treatment in a triple-negative tumor (patient 20) (A) and in a HER2+ tumor (patient 30) (B).

(C) Summary of differences for 8q24 BAC or chr8 CEP probe counts in all cells before and after treatment in the 15 tumors analyzed. Asterisks mark significant differences, and red and blue color indicates increase and decrease in differences, respectively. Data are presented as mean \pm SEM.

The initialization state for the simulation for each patient consisted of the cell coordinates for each cell in the pretreatment samples, an estimation of the age of each cell based on its size, and the cellular phenotypes. We considered the average length of the cell cycle across all cellular phenotypes and all patients to be comparable to the average cell-cycle time determined by cell line experiments (Schiffer et al., 1979), and then varied individual cell-cycle times based on the corresponding Ki67 values. Initially, we assumed that daughter cells maintained the same phenotype as the mother cell, thus neglecting the possibility of phenotypic switching or migration; this assumption was later relaxed.

Each patient-specific simulation was performed for three phases of proliferation. The first phase consisted of the period of time between biopsy and start of chemotherapy. Cell proliferation occurred at the rates determined by the pretreatment Ki67 data. The probability of cell death per unit time for each phenotype was selected to maintain a roughly constant population size. We chose these values for cell death because rates of apoptosis correlate well with proliferation, and the montage of visualized cells did not consist of cells crowded together as

would be consistent with high growth rates. During treatment, we lowered proliferation by 5% and adjusted the rate of cell death accordingly. This choice of treatment effect was selected by fitting the number of cells at the end of the simulation to the number of cells observed in the posttreatment samples, and due to evidence of a decrease in proliferation with anthracyclines with a corresponding decrease in apoptotic index (Burcombe et al., 2006). The last phase consisted of the period of time between the end of chemotherapy and surgery. Cell proliferation in this phase occurred at the rates determined by the post-treatment Ki67 data (Figure 6). These three time periods were obtained individually for each patient and implemented in the patient-specific simulations.

Using this model, we found that the level of clustering detected in our posttreatment samples was less than what would be expected in a model without cellular motility or phenotypic switching (Figure 6; Table S4; Movie S1). Therefore, we sought to determine rates of phenotypic switching that would fit the distribution of cell types found in our posttreatment samples. We identified a lower requirement for phenotypic switching or motility among the luminal tumors, whereas we observed both

(E) Histograms depicting absolute differences in copy numbers for BAC and CEP probe counts in all cells of the same phenotype or in adjacent cells of the same phenotype before and after treatment. CD44⁺CD24⁻ and CD44⁺CD24⁺ cell subpopulations are not present after treatment.

(F) Fraction of adjacent cells with the same phenotype before and after treatment. Asterisks indicate significant changes. Significance of differences was determined by calculating the homotypic fraction for 100,000 iterations of permutation testing over randomized cellular phenotypes.

See also Figures S4 and S5 and Table S3.

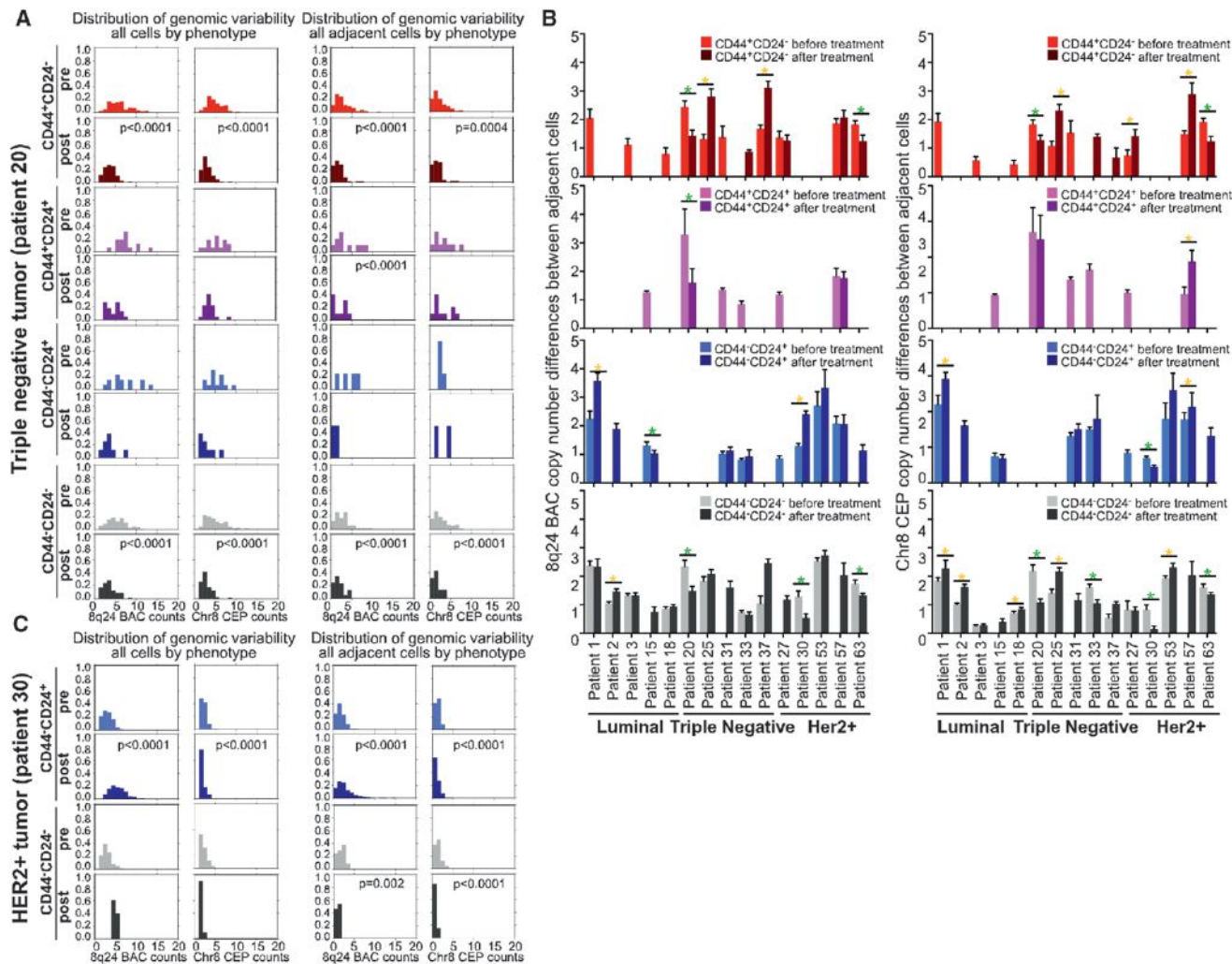


Figure 5. Genetic and Phenotypic Differences between All Cells and Adjacent Cells

(A) Histograms depicting variability for 8q24 BAC and chr8 probe counts in all cells of the same phenotype (left panel) or in adjacent cells of the same phenotype (right panel) before and after treatment in a triple-negative tumor (patient 20).

(B) Plots depicting differences in 8q24 BAC and chr8 CEP copy number in all adjacent cells and in adjacent cells of the same phenotype. Asterisks indicate significant differences, and yellow and green color indicates increase and decrease in differences, respectively. Data are presented as mean \pm SEM.

(C) Similar as (A), histograms for a HER2+ tumor (patient 30).

low and high rates for patients with HER2+ and triple-negative tumors (see Supplemental Experimental Procedures for more details). The inclusion of migration in this model, based on intravital imaging of metastatic breast cancer cells (Kedrin et al., 2008), led to increases in the rates of phenotypic switching necessary to recapitulate the posttreatment data but did not change the relative ordering of the breast tumor subtypes with regard to this rate. Migration was assumed to occur in a nondirected manner (i.e., in random directions) and was considered to be higher for CD44⁺CD24⁻ and CD44⁺CD24⁺ cells as compared to CD44⁻CD24⁺ and CD44⁻CD24⁻ cells. This model provides a proof of principle of feasibility of the prediction of therapy-induced phenotypic changes in tumor based on the detailed characterization of tissue samples at the single-cell level before and after treatment.

The Impact of Intratumor Diversity on Therapeutic Responses

To explore the potential impact of intratumor diversity on therapeutic resistance, we compared genetic and phenotypic diversity among tumors classified as pCR and pathological partial response (pPR) or stable disease. Interestingly, tumors with pCR had the lowest pretreatment genetic diversity using measures that incorporated 8q24 copy number, whereas tumors with partial response or stable disease were not significantly different from each other, neither before nor after treatment (Figures 7 and S6A; Table S5).

Age at diagnosis affects both breast tumor subtype and the success of chemotherapy within a subtype (Hess et al., 2006). TNBC is more common in younger women, and chemotherapy also tends to be more effective in younger patients (Silver

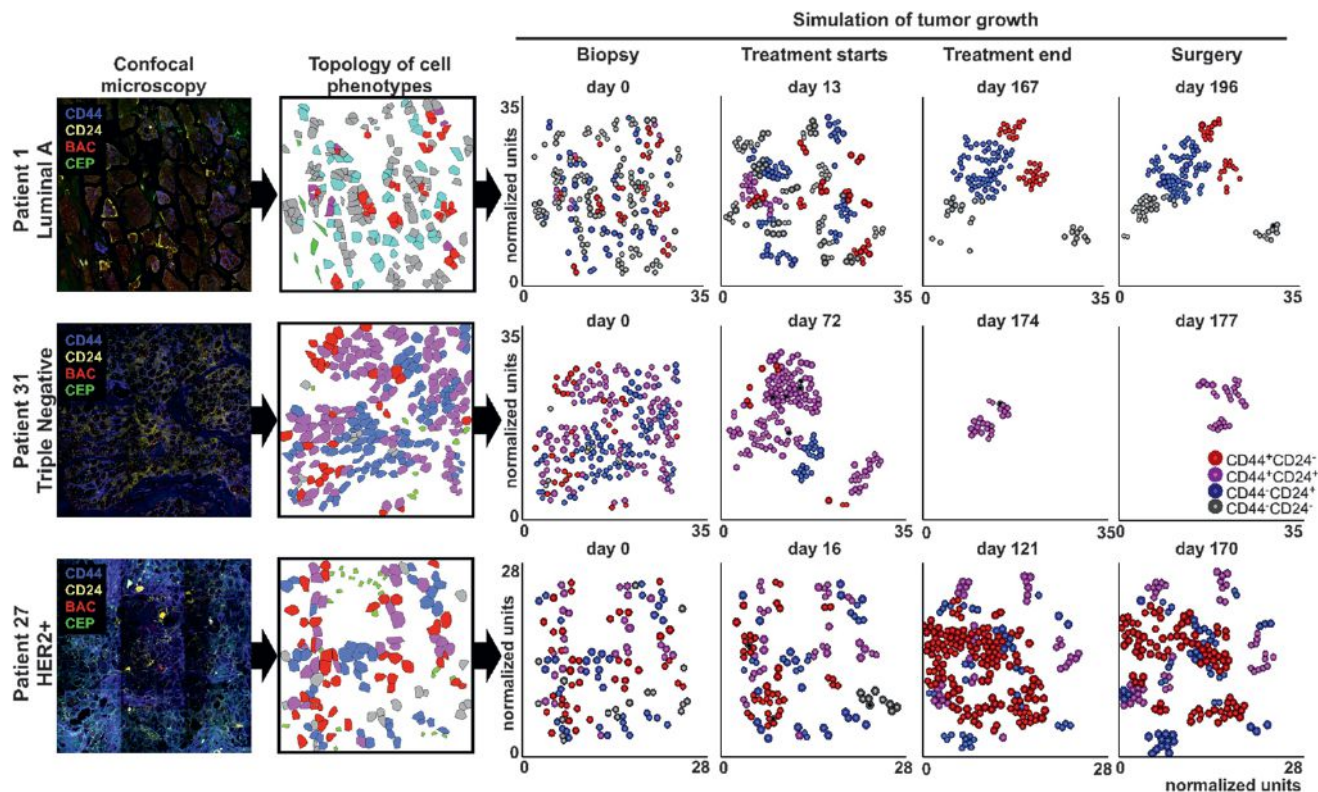


Figure 6. Examples of Snapshots of Computer-Simulated Tumor Growth during Treatment

Representative images depicting changes in tumor topology and cellular composition during treatment based on simulations. Modeling was built based on actual data obtained from cases analyzed for topology. Confocal images were converted into topology maps for the distribution of cell phenotypes that served as time zero for the mathematical simulations of tumor growth. See also Table S4 and Movie S1.

et al., 2010). These epidemiological data suggest that tumors of different subtypes may have different evolutionary paths and growth kinetics such as the length of time from tumor initiation to diagnosis, which may influence both treatment responses and intratumor heterogeneity. Thus, we analyzed potential associations between the age at diagnosis and the Shannon diversity index of each tumor. We found that the extent of pre-treatment diversity did not display a significant correlation with patient age (Figure S6B). However, older age at diagnosis was significantly correlated with a decrease in genetic diversity during treatment in TNBC ($p = 0.025$) and an increase in genetic diversity in HER2+ tumors ($p = 0.038$; Figure S6C). These results suggest that TNBC in older women may have a dominant, slowly proliferating subpopulation that is resistant to treatment, whereas HER2+ tumors in older women might be more genetically unstable.

It is possible that treatment-induced changes in genetic diversity might be masked by rediversification during the time interval between the end of treatment and posttreatment sample collection (i.e., surgery). Similarly, the duration of the treatment (i.e., length of selective pressure) might affect intratumor genetic diversity. Thus, we analyzed potential associations between these clinical variables and changes in genetic diversity but did not detect any significant associations (Figures S6D and S6E). These results suggest that the observed lack of changes in ge-

netic diversity during neoadjuvant chemotherapy is not likely to be affected by the lengths of treatment and time between the last dose of chemotherapy and the surgical removal of residual tumors.

DISCUSSION

Here, we describe a single-cell-based analysis of intratumor genetic and phenotypic diversity and topology in a cohort of breast tumors prior to and after neoadjuvant chemotherapy. Although inter- and intratumor heterogeneity has been described and well characterized in breast cancer (Cancer Genome Atlas Network, 2012; Geyer et al., 2010; Hernandez et al., 2012; Polyak, 2011; Stephens et al., 2012; Yap et al., 2012), our knowledge of how intratumor heterogeneity may change during therapeutic interventions in distinct subtypes of breast cancers is very limited.

Neoadjuvant (i.e., preoperative) chemotherapy is a well-established standard treatment option for patients diagnosed with locally advanced disease or patients with large potentially operable tumors (Kaufmann et al., 2006). In addition to its effectiveness in reducing the size of the primary tumor, allowing for less-extensive surgery, neoadjuvant chemotherapy also improves long-term clinical outcome, presumably by eliminating micrometastatic disease (Fisher et al., 1998). Moreover,

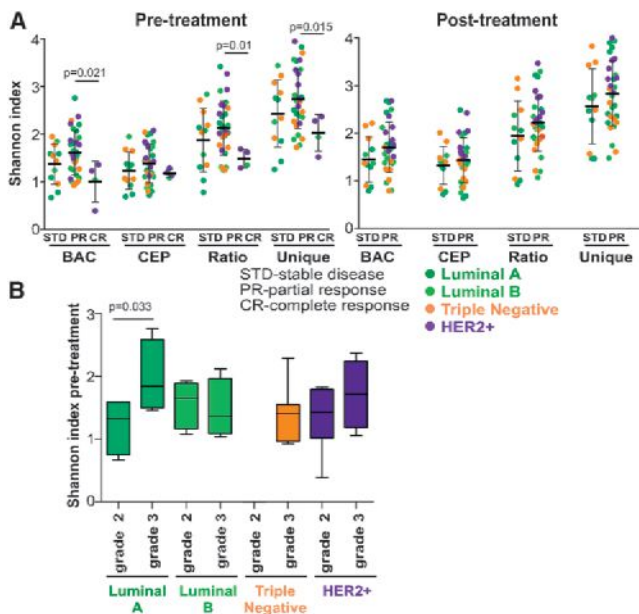


Figure 7. Associations between Intratumor Diversity and Pathologic Response to Treatment

(A) Shannon index of diversity before and after treatment in tumors with different response to treatment. Significant p values between groups by the Wilcoxon rank sum test are indicated. Black lines show the mean \pm SEM. Tumors with lower pretreatment diversity are more likely to have pCR regardless of tumor subtype. Tumors with pCR were only analyzed prior to treatment because there was no tumor tissue left at the time of surgery.

(B) Shannon index of diversity before and after treatment in tumors with different grade. Boxes correspond to 25th–75th percentile, whereas whiskers mark maximum and minimum values. Significant p values by two-sided Wilcoxon matched-pairs signed rank test are shown. See also Figure S6 and Table S5.

a pCR to neoadjuvant treatment is a strong predictor of long-term disease-free survival (Esserman et al., 2012), particularly in estrogen receptor (ER)-negative cancers. Despite widespread use of neoadjuvant therapies, our knowledge of their influence on the subsequent evolution of the tumors is very limited.

The success of chemotherapy is influenced by breast tumor subtype, with luminal tumors in general being less responsive than HER2+ and TNBC (Houssami et al., 2012). Because chemotherapy is thought to target proliferating cells, associations between tumor proliferation (measured by the Ki67 index) and treatment response have been extensively characterized, with conflicting results. A recent study found that the relative change in the fraction of Ki67⁺ cells, but not the absolute pre- and post-treatment levels of Ki67⁺ cells, is an independent predictor of treatment outcomes after neoadjuvant chemotherapy in luminal B, HER2+, and TNBC subtypes (Matsubara et al., 2013). Changes in hormone receptors and HER2 due to neoadjuvant therapy have also been analyzed with inconclusive results (van de Ven et al., 2011).

More recently, intratumor heterogeneity for cellular phenotypes, mainly focusing on stem cell-like and more differentiated cell features, has been explored as a potential predictor of the

success of neoadjuvant chemotherapy. The frequency of CD44⁺ stem cell-like and CD24⁺ more-differentiated breast cancer cells varies within tumors according to subtype, with CD44⁺ cells being more common in TNBCs than in luminal cancers (Honeth et al., 2008; Park et al., 2010b). The relative frequency of these cells within tumors also changes during neoadjuvant chemotherapy. A study analyzing pre- and posttreatment samples by fluorescence-activated cell sorting (FACS) found an increase in CD44⁺CD24⁻ cells; however, the neoplastic nature of these cells was not confirmed (Li et al., 2008). Another report found that whereas an increased frequency of CD44⁺CD24⁻ cells after neoadjuvant chemotherapy was a poor prognostic factor, tumors that had a high fraction of these cells were more likely to have a pCR (Lee et al., 2011).

Here, we showed that whereas overall intratumor cellular genetic diversity for 8q24, 16p13, 10p13, and 20q does not change during treatment in tumors with a partial or no response, there are significant changes in phenotypically distinct tumor cell subpopulations within tumors and in the relative localization of these populations of cells. Some of these changes might be explained by the observed differences in the proliferation rates among cell types, with CD44⁺CD24⁻ cells being more proliferative and thus more likely to be eliminated. Our data, however, also imply potential changes in cellular phenotypes and selection for cells with more differentiated luminal features due to lower sensitivity to the therapy stemming from lower proliferation capacity. Moreover, our findings provide a potential explanation for the apparent paradox between the presumed resistance of CD44⁺ stem cell-like breast cancer cells (i.e., cancer stem cells) (Dave et al., 2012) and our data demonstrating a relative decrease in this cell population due to treatment. Based on our data, CD44⁺CD24⁻ cells are more proliferative than CD44⁻CD24⁺ cells, and thus, they might be preferentially eliminated by chemotherapy. If a tumor does not respond to treatment due to inherent resistance, which is independent of stem cell-like or epithelial phenotype, then there is an apparent increase in the relative frequency of CD44⁺CD24⁻ cells due to their higher proliferation.

Our observation that in some cases adjacent cells within a tumor are more likely to be genetically divergent yet phenotypically similar implies that homotypic cell-cell interactions might favor treatment resistance and also that chemotherapy might increase genetic instability or select for cells with higher chromosomal instability.

Our computational model of tumor cell proliferation provides a tool with which we can predict changes in the distribution of cell phenotypes in a patient-specific fashion. These variations can manifest themselves in spatial coordinates and clustering of cells, or they can be the result of changing population dynamics over periods of time with and without therapy. Here, we found that the clustering of cellular phenotypes could not have occurred solely due to cell division placing daughter cells closer to the parent cell but must require some level of phenotypic plasticity. We tested varying levels of phenotypic switching and found that no single rate of switching could account for the divergence between simulation and biopsy samples: instead, rates of switch may vary at the subtype or individual patient level. We

also investigated the effects of migration on the predicted levels of phenotypic switching and found that migration increases the rate of phenotype switching necessary to explain the patient data. This effect might arise because migration scatters cells more widely throughout the tumor, and hence, phenotype switching is needed to return the patterns of cells to those observed in patient samples.

In summary, our data provide an integrated view of how the genotype (measured by 8q24 copy number), phenotype (CD24 and CD44 expression and proliferation state), and topology (distribution of cancer cells with defined genotype and phenotype within tumors) change in response to neoadjuvant chemotherapy in breast cancer. Because phenotypic diversity in combination with selection pressure by local microenvironmental signals is the driver of tumor evolution, our results highlight the importance of using an integrated approach. Finally, our *in silico* simulation of tumor growth using models built on the patient-specific characterization of tumors at the single-cell level *in situ* prior to and after chemotherapy illustrates the feasibility of predicting the evolution of tumors during treatment—knowledge that could be used for the design of more effective treatment strategies.

EXPERIMENTAL PROCEDURES

For further details, see the Supplemental Experimental Procedures.

ImmunofISH

The use and collection of the human tissue samples were performed following protocols approved by the institutional review boards of the hospitals participating in this study. Formalin-fixed paraffin-embedded breast tumor samples were dewaxed in xylene and hydrated in a series of ethanol. Heat-induced antigen retrieval was performed in citrate buffer (pH 6), following by pepsin digestion. The immunostaining for CD44 and CD24 was performed at room temperature, followed by the hybridization with BAC and CEP probes and incubation for 20 hr at 37°C. After several washes with different stringent SCC buffers, the slides were air-dried and protected for long storage with ProLong Gold. Different immunofluorescence images from multiple areas of each sample were acquired with a Nikon Ti microscope attached to a Yokogawa spinning-disk confocal unit, 60× plan apo objective, and OrcaER camera controlled by Andor iQ software.

Immunofluorescence Analysis of Cellular Phenotypes and Proliferation

Multicolor immunofluorescence for CD44, CD24, and Ki67 was performed using whole sections of formalin-fixed paraffin-embedded breast tumor samples by sequential staining after antigen retrieval in citrate buffer (pH 6). Different immunofluorescence images were acquired as described before, and the frequency of each cell phenotype was calculated by counting an average of 300 cells in each sample.

Statistical Analyses

Genetic diversity was determined as described by Park et al. (2010a). Statistical differences in genetic diversity were analyzed by bootstrapping and comparing the mean count of each bootstrap repetition against the mean count of the smaller cell population. Correlations were assessed using Spearman's rank-based coefficient. The association between diversity indices and clinical variables was assessed using the Wilcoxon test for categorical clinical variables (such as response) and a permutation test based on Spearman's rank correlation for continuous clinical variables (such as size). Statistical differences in pre- and posttreatment BAC and CEP counts were evaluated using the achieved significance level (ASL) method of Efron and Tibshirani (1993).

SUPPLEMENTAL INFORMATION

Supplemental Information includes Supplemental Experimental Procedures, six figures, five tables, and one movie and can be found with this article online at <http://dx.doi.org/10.1016/j.celrep.2013.12.041>.

ACKNOWLEDGMENTS

We thank members of our laboratories for their critical reading of this manuscript and useful discussions. We thank Lisa Cameron in the DFCI Confocal Microscopy for her technical support. This work was supported by the National Cancer Institute Physical Sciences Oncology Center U54CA143874 (to A.v.O.) and U54CA143798 (to F.M.), the Susan G. Komen Foundation (to R.M.), Cellex Foundation (to V.A.), by Redes Temáticas de Investigación en Cáncer (RD12/0036/0055 to P.G. and E.A.), and the Breast Cancer Research Foundation (to K.P.). Part of this work was performed under the auspices of the U.S. Department of Energy by Lawrence Livermore National Laboratory under Contract DE-AC52-07NA27344.

Received: June 14, 2013

Revised: November 14, 2013

Accepted: December 30, 2013

Published: January 23, 2014

REFERENCES

- Al-Hajj, M., Wicha, M.S., Benito-Hernandez, A., Morrison, S.J., and Clarke, M.F. (2003). Prospective identification of tumorigenic breast cancer cells. *Proc. Natl. Acad. Sci. USA* *100*, 3983–3988.
- Almendro, V., Marusyk, A., and Polyak, K. (2013). Cellular heterogeneity and molecular evolution in cancer. *Annu. Rev. Pathol.* *8*, 277–302.
- Blouhstain-Qimron, N., Yao, J., Snyder, E.L., Shipitsin, M., Campbell, L.L., Mani, S.A., Hu, M., Chen, H., Ustyansky, V., Antosiewicz, J.E., et al. (2008). Cell type-specific DNA methylation patterns in the human breast. *Proc. Natl. Acad. Sci. USA* *105*, 14076–14081.
- Burcombe, R., Wilson, G.D., Dowsett, M., Khan, I., Richman, P.I., Daley, F., Detre, S., and Makris, A. (2006). Evaluation of Ki-67 proliferation and apoptotic index before, during and after neoadjuvant chemotherapy for primary breast cancer. *Breast Cancer Res.* *8*, R31.
- Cancer Genome Atlas Network (2012). Comprehensive molecular portraits of human breast tumours. *Nature* *490*, 61–70.
- Collecchi, P., Baldini, E., Giannessi, P., Naccarato, A.G., Passoni, A., Gardin, G., Roncella, M., Evangelista, G., Bevilacqua, G., and Conte, P.F. (1998). Primary chemotherapy in locally advanced breast cancer (LABC): effects on tumour proliferative activity, bcl-2 expression and the relationship between tumour regression and biological markers. *Eur. J. Cancer* *34*, 1701–1704.
- Dave, B., Mittal, V., Tan, N.M., and Chang, J.C. (2012). Epithelial-mesenchymal transition, cancer stem cells and treatment resistance. *Breast Cancer Res.* *14*, 202.
- Ding, L., Ley, T.J., Larson, D.E., Miller, C.A., Koboldt, D.C., Welch, J.S., Ritchey, J.K., Young, M.A., Lamprecht, T., McLellan, M.D., et al. (2012). Clonal evolution in relapsed acute myeloid leukaemia revealed by whole-genome sequencing. *Nature* *481*, 506–510.
- Efron, B., and Tibshirani, R.J. (1993). *An Introduction to the Bootstrap* (London: Chapman & Hall).
- Engelman, J.A., Zejnullahu, K., Mitsudomi, T., Song, Y., Hyland, C., Park, J.O., Lindeman, N., Gale, C.M., Zhao, X., Christensen, J., et al. (2007). MET amplification leads to gefitinib resistance in lung cancer by activating ERBB3 signaling. *Science* *316*, 1039–1043.
- Esserman, L.J., Berry, D.A., DeMichele, A., Carey, L., Davis, S.E., Buxton, M., Hudis, C., Gray, J.W., Perou, C., Yau, C., et al. (2012). Pathologic complete response predicts recurrence-free survival more effectively by cancer subset: results from the I-SPY 1 TRIAL—CALGB 150007/150012, ACRIN 6657. *J. Clin. Oncol.* *30*, 3242–3249.

- Fidler, I.J. (1978). Tumor heterogeneity and the biology of cancer invasion and metastasis. *Cancer Res.* 38, 2651–2660.
- Fisher, B., Bryant, J., Wolmark, N., Mamounas, E., Brown, A., Fisher, E.R., Wickerham, D.L., Begovic, M., DeCillis, A., Robidoux, A., et al. (1998). Effect of preoperative chemotherapy on the outcome of women with operable breast cancer. *J. Clin. Oncol.* 16, 2672–2685.
- Gerlinger, M., Rowan, A.J., Horswell, S., Larkin, J., Endesfelder, D., Gronroos, E., Martinez, P., Matthews, N., Stewart, A., Tarpey, P., et al. (2012). Intratumor heterogeneity and branched evolution revealed by multiregion sequencing. *N. Engl. J. Med.* 366, 883–892.
- Geyer, F.C., Weigelt, B., Natrajan, R., Lambros, M.B., de Biase, D., Vatcheva, R., Savage, K., Mackay, A., Ashworth, A., and Reis-Filho, J.S. (2010). Molecular analysis reveals a genetic basis for the phenotypic diversity of metaplastic breast carcinomas. *J. Pathol.* 220, 562–573.
- Heppner, G.H., and Miller, B.E. (1983). Tumor heterogeneity: biological implications and therapeutic consequences. *Cancer Metastasis Rev.* 2, 5–23.
- Hernandez, L., Wilkerson, P.M., Lambros, M.B., Campion-Flora, A., Rodrigues, D.N., Gauthier, A., Cabral, C., Pawar, V., Mackay, A., A'hern, R., et al. (2012). Genomic and mutational profiling of ductal carcinomas in situ and matched adjacent invasive breast cancers reveals intra-tumour genetic heterogeneity and clonal selection. *J. Pathol.* 227, 42–52.
- Hess, K.R., Anderson, K., Symmans, W.F., Valero, V., Ibrahim, N., Mejia, J.A., Booser, D., Theriault, R.L., Buzdar, A.U., Dempsey, P.J., et al. (2006). Pharmacogenomic predictor of sensitivity to preoperative chemotherapy with paclitaxel and fluorouracil, doxorubicin, and cyclophosphamide in breast cancer. *J. Clin. Oncol.* 24, 4236–4244.
- Honeth, G., Bendahl, P.O., Ringnér, M., Saal, L.H., Gruvberger-Saal, S.K., Lövgren, K., Grabau, D., Fernö, M., Borg, A., and Hegardt, C. (2008). The CD44+/CD24- phenotype is enriched in basal-like breast tumors. *Breast Cancer Res.* 10, R53.
- Houssami, N., Macaskill, P., von Minckwitz, G., Marinovich, M.L., and Mamounas, E. (2012). Meta-analysis of the association of breast cancer subtype and pathologic complete response to neoadjuvant chemotherapy. *Eur. J. Cancer* 48, 3342–3354.
- Kaufmann, M., Hortobagyi, G.N., Goldhirsch, A., Scholl, S., Makris, A., Valagussa, P., Blohmer, J.U., Eiermann, W., Jackesz, R., Jonat, W., et al. (2006). Recommendations from an international expert panel on the use of neoadjuvant (primary) systemic treatment of operable breast cancer: an update. *J. Clin. Oncol.* 24, 1940–1949.
- Kedrin, D., Gligorijevic, B., Wyckoff, J., Verkhusha, V.V., Condeelis, J., Segall, J.E., and van Rhee, J. (2008). Intravital imaging of metastatic behavior through a mammary imaging window. *Nat. Methods* 5, 1019–1021.
- Landau, D.A., Carter, S.L., Getz, G., and Wu, C.J. (2013). Clonal evolution in hematological malignancies and therapeutic implications. *Leukemia*. Published online August 27, 2013. <http://dx.doi.org/10.1038/leu.2013.248>.
- Lee, H.E., Kim, J.H., Kim, Y.J., Choi, S.Y., Kim, S.W., Kang, E., Chung, I.Y., Kim, I.A., Kim, E.J., Choi, Y., et al. (2011). An increase in cancer stem cell population after primary systemic therapy is a poor prognostic factor in breast cancer. *Br. J. Cancer* 104, 1730–1738.
- Li, X., Lewis, M.T., Huang, J., Gutierrez, C., Osborne, C.K., Wu, M.F., Hilsenbeck, S.G., Pavlick, A., Zhang, X., Chamness, G.C., et al. (2008). Intrinsic resistance of tumorigenic breast cancer cells to chemotherapy. *J. Natl. Cancer Inst.* 100, 672–679.
- Liu, R., Wang, X., Chen, G.Y., Dalerba, P., Gurney, A., Hoey, T., Sherlock, G., Lewicki, J., Shedden, K., and Clarke, M.F. (2007). The prognostic role of a gene signature from tumorigenic breast-cancer cells. *N. Engl. J. Med.* 356, 217–226.
- Magurran, A.E. (2004). *Measuring Biological Diversity* (Malden: Blackwell).
- Maley, C.C., Galipeau, P.C., Finley, J.C., Wongsurawat, V.J., Li, X., Sanchez, C.A., Paulson, T.G., Blount, P.L., Risques, R.A., Rabinovitch, P.S., and Reid, B.J. (2006). Genetic clonal diversity predicts progression to esophageal adenocarcinoma. *Nat. Genet.* 38, 468–473.
- Marusyk, A., and Polyak, K. (2010). Tumor heterogeneity: causes and consequences. *Biochim. Biophys. Acta* 1805, 105–117.
- Marusyk, A., Almendro, V., and Polyak, K. (2012). Intra-tumour heterogeneity: a looking glass for cancer? *Nat. Rev. Cancer* 12, 323–334.
- Matsubara, N., Mukai, H., Fujii, S., and Wada, N. (2013). Different prognostic significance of Ki-67 change between pre- and post-neoadjuvant chemotherapy in various subtypes of breast cancer. *Breast Cancer Res. Treat.* 137, 203–212.
- Merlo, L.M., Pepper, J.W., Reid, B.J., and Maley, C.C. (2006). Cancer as an evolutionary and ecological process. *Nat. Rev. Cancer* 6, 924–935.
- Merlo, L.M., Shah, N.A., Li, X., Blount, P.L., Vaughan, T.L., Reid, B.J., and Maley, C.C. (2010). A comprehensive survey of clonal diversity measures in Barrett's esophagus as biomarkers of progression to esophageal adenocarcinoma. *Cancer Prev. Res. (Phila.)* 3, 1388–1397.
- Mroz, E.A., Tward, A.D., Pickering, C.R., Myers, J.N., Ferris, R.L., and Rocco, J.W. (2013). High intratumor genetic heterogeneity is related to worse outcome in patients with head and neck squamous cell carcinoma. *Cancer* 119, 3034–3042.
- Navin, N., Kendall, J., Troge, J., Andrews, P., Rodgers, L., McIndoo, J., Cook, K., Stepansky, A., Levy, D., Esposito, D., et al. (2011). Tumour evolution inferred by single-cell sequencing. *Nature* 472, 90–94.
- Nazarian, R., Shi, H., Wang, Q., Kong, X., Koya, R.C., Lee, H., Chen, Z., Lee, M.K., Attar, N., Sazegar, H., et al. (2010). Melanomas acquire resistance to B-RAF(V600E) inhibition by RTK or N-RAS upregulation. *Nature* 468, 973–977.
- Nikolsky, Y., Sviridov, E., Yao, J., Dosymbekov, D., Ustyansky, V., Kaznacheev, V., Dezzo, Z., Mulvey, L., Macconail, L.E., Winckler, W., et al. (2008). Genome-wide functional synergy between amplified and mutated genes in human breast cancer. *Cancer Res.* 68, 9532–9540.
- Park, S.Y., Gönen, M., Kim, H.J., Michor, F., and Polyak, K. (2010a). Cellular and genetic diversity in the progression of in situ human breast carcinomas to an invasive phenotype. *J. Clin. Invest.* 120, 636–644.
- Park, S.Y., Lee, H.E., Li, H., Shipitsin, M., Gelman, R., and Polyak, K. (2010b). Heterogeneity for stem cell-related markers according to tumor subtype and histologic stage in breast cancer. *Clin. Cancer Res.* 16, 876–887.
- Perou, C.M., Sørlie, T., Eisen, M.B., van de Rijn, M., Jeffrey, S.S., Rees, C.A., Pollack, J.R., Ross, D.T., Johnsen, H., Akslen, L.A., et al. (2000). Molecular portraits of human breast tumours. *Nature* 406, 747–752.
- Polyak, K. (2011). Heterogeneity in breast cancer. *J. Clin. Invest.* 121, 3786–3788.
- Roesch, A., Vultur, A., Bogeski, I., Wang, H., Zimmermann, K.M., Speicher, D., Körbel, C., Laschke, M.W., Gimotty, P.A., Philipp, S.E., et al. (2013). Overcoming intrinsic multidrug resistance in melanoma by blocking the mitochondrial respiratory chain of slow-cycling JARID1B(high) cells. *Cancer Cell* 23, 811–825.
- Sakai, W., Swisher, E.M., Karlan, B.Y., Agarwal, M.K., Higgins, J., Friedman, C., Villegas, E., Jacquemont, C., Farrugia, D.J., Couch, F.J., et al. (2008). Secondary mutations as a mechanism of cisplatin resistance in BRCA2-mutated cancers. *Nature* 451, 1116–1120.
- Schiffer, L.M., Braunschweiger, P.G., Stragand, J.J., and Poulakos, L. (1979). The cell kinetics of human mammary cancers. *Cancer* 43, 1707–1719.
- Sharma, S.V., Lee, D.Y., Li, B., Quinlan, M.P., Takahashi, F., Maheswaran, S., McDermott, U., Azizian, N., Zou, L., Fischbach, M.A., et al. (2010). A chromatin-mediated reversible drug-tolerant state in cancer cell subpopulations. *Cell* 141, 69–80.
- Shipitsin, M., Campbell, L.L., Argani, P., Weremowicz, S., Bloushtain-Qimron, N., Yao, J., Nikolskaya, T., Serebryiskaya, T., Beroukhim, R., Hu, M., et al. (2007). Molecular definition of breast tumor heterogeneity. *Cancer Cell* 11, 259–273.
- Silver, D.P., Richardson, A.L., Eklund, A.C., Wang, Z.C., Szallasi, Z., Li, Q., Juul, N., Leong, C.O., Calogrias, D., Buraimoh, A., et al. (2010). Efficacy of neoadjuvant Cisplatin in triple-negative breast cancer. *J. Clin. Oncol.* 28, 1145–1153.

Stephens, P.J., Tarpey, P.S., Davies, H., Van Loo, P., Greenman, C., Wedge, D.C., Nik-Zainal, S., Martin, S., Varela, I., Bignell, G.R., et al.; Oslo Breast Cancer Consortium (OSBREAC) (2012). The landscape of cancer genes and mutational processes in breast cancer. *Nature* 486, 400–404.

Turner, N.C., and Reis-Filho, J.S. (2012). Genetic heterogeneity and cancer drug resistance. *Lancet Oncol.* 13, e178–e185.

van de Ven, S., Smit, V.T., Dekker, T.J., Nortier, J.W., and Kroep, J.R. (2011). Discordances in ER, PR and HER2 receptors after neoadjuvant chemotherapy in breast cancer. *Cancer Treat. Rev.* 37, 422–430.

Yap, T.A., Gerlinger, M., Futreal, P.A., Pusztai, L., and Swanton, C. (2012). Intratumor heterogeneity: seeing the wood for the trees. *Sci. Transl. Med.* 4, 127ps110.

Gli Protein Activity Is Controlled by Multisite Phosphorylation in Vertebrate Hedgehog Signaling

Pawel Niewiadomski,^{1,2,5,*} Jennifer H. Kong,^{4,7} Robert Ahrends,^{3,6,7} Yan Ma,^{1,2} Eric W. Humke,^{1,2,8} Sohini Khan,^{1,2} Mary N. Teruel,³ Bennett G. Novitch,⁴ and Rajat Rohatgi^{1,2,*}

¹Department of Medicine, Stanford University School of Medicine, Stanford, CA 94305, USA

²Department of Biochemistry, Stanford University School of Medicine, Stanford, CA 94305, USA

³Department of Chemical and Systems Biology, Stanford University School of Medicine, Stanford, CA 94305, USA

⁴Department of Neurobiology, Eli and Edythe Broad Stem Cell Research Center, David Geffen School of Medicine at UCLA, Los Angeles, CA 90095, USA

⁵Department of Cell Biology, Nencki Institute of Experimental Biology, 02-093 Warsaw, Poland

⁶Laboratory of Quantitative Systems Analysis, Leibniz-Institute for Analytical Sciences (ISAS) e.V., 44227 Dortmund, Germany

⁷These authors contributed equally to this work

⁸Present address: Genentech, Inc., Early Clinical Development, 1 DNA Way, M/S 442, South San Francisco, CA 94080, USA

*Correspondence: p.niewiadomski@nencki.gov.pl (P.N.), rrohathgi@stanford.edu (R.R.)

<http://dx.doi.org/10.1016/j.celrep.2013.12.003>

This is an open-access article distributed under the terms of the Creative Commons Attribution-NonCommercial-No Derivative Works License, which permits non-commercial use, distribution, and reproduction in any medium, provided the original author and source are credited.

SUMMARY

Gli proteins are transcriptional effectors of the Hedgehog (Hh) pathway in both normal development and cancer. We describe a program of multisite phosphorylation that regulates the conversion of Gli proteins into transcriptional activators. In the absence of Hh ligands, Gli activity is restrained by the direct phosphorylation of six conserved serine residues by protein kinase A (PKA), a master negative regulator of the Hh pathway. Activation of signaling leads to a global remodeling of the Gli phosphorylation landscape: the PKA target sites become dephosphorylated, while a second cluster of sites undergoes phosphorylation. The pattern of Gli phosphorylation can regulate Gli transcriptional activity in a graded fashion, suggesting a phosphorylation-based mechanism for how a gradient of Hh signaling in a morphogenetic field can be converted into a gradient of transcriptional activity.

INTRODUCTION

The Hedgehog (Hh) pathway is an evolutionarily conserved signaling system that plays a central role in embryogenesis and adult tissue homeostasis. Its misregulation leads to developmental defects and to cancers of the skin and the brain (Briscoe and Théron, 2013; Hahn et al., 1996). The Gli (*Glioblastoma*) transcription factors in vertebrates control the Hh gene expression program (Hui and Angers, 2011). Despite the importance of Gli proteins in development, regeneration, and cancer, the mechanism by which they acquire the ability to activate target genes has remained enigmatic.

Among the three mammalian Gli proteins, Gli2 and Gli3 are the first responders to the Hh signal. Once activated, Gli2/3 then induce the expression of Gli1, which acts as an amplifier of the response. Gli2/3 can perform two opposing functions at target promoters (Figure 1A; reviewed in Hui and Angers, 2011). When the pathway is off, Gli2/3 proteins are converted into truncated repressor forms (hereafter abbreviated GliR), which inhibit target gene transcription. When the Hh ligand is received, GliR production is blocked and Gli2/3 proteins are converted into transcriptional activators (hereafter abbreviated GliA). In the nucleus, the balance between GliR and GliA shapes the Hh response. Between these two extremes, a substantial fraction of Gli2/3 remains in the cytoplasm in a transcriptionally inactive state (Humke et al., 2010). Quantitative changes in the GliR/GliA ratio can lead to developmental defects in humans, underscoring the point that the precise level of Gli activity is often critical for the sophisticated patterning events regulated by Hh signaling during development (Hill et al., 2007; Kang et al., 1997; Wang et al., 2000).

GliR and GliA production are both controlled by the seven-transmembrane protein Smoothed (Smo; Figure 1A). Upon Hh ligand reception by Patched (Ptc), Smo accumulates in a microtubule-based protrusion of the cell membrane known as the primary cilium (Corbit et al., 2005). Through an unknown mechanism, ciliary Smo inhibits GliR formation and induces the transport of Gli proteins to the tips of cilia (Kim et al., 2009; Wen et al., 2010), where they dissociate from the negative regulator Suppressor of Fused (SuFu; Humke et al., 2010; Tukachinsky et al., 2010). Thereupon, Glis translocate into the nucleus and activate target genes. Nuclear Gli proteins are characterized by a short half-life and reduced mobility on SDS-PAGE gels caused by a distinct phosphorylation event, hereafter referred to as “hyperphosphorylation” (Humke et al., 2010).

The mechanistic details of the interaction between Smo and Gli proteins are not understood. Several lines of evidence point to protein kinase A (PKA) as a key regulator of the Hh signal

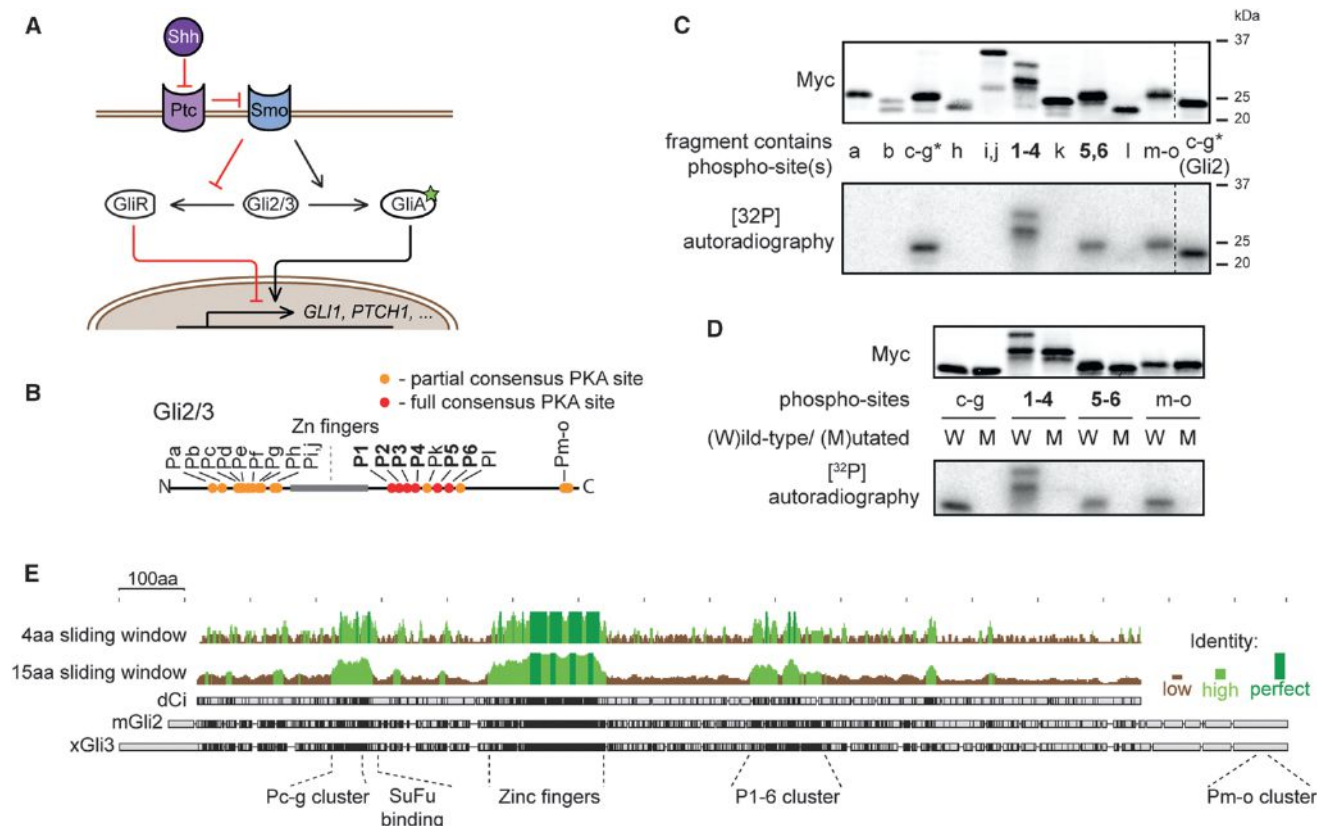


Figure 1. PKA Phosphorylates Both Full and Partial Consensus Sites on Gli2/3 In Vitro

(A) Schematic representation of Gli2/3 regulation by Hh signaling. Active Smo induces the formation of GliA and suppresses the production of the truncated GliR. (B) Location of the full (red dots; P1–6) and partial consensus (orange dots; Pa–o) PKA target sites that are conserved in both mouse and human Gli2 and Gli3. (C) In vitro PKA phosphorylation of Myc-tagged Gli3 fragments containing the indicated target sites. An anti-myc immunoblot (top) shows total protein levels of each fragment in the assay and the autoradiogram (bottom) shows ³²P incorporation. The Pc-g (*) fragment was tested for both Gli3 and Gli2 since only the former contains an additional PKA consensus target sequence. (D) S/T residues presumed to be PKA targets were mutated in Gli3 fragments containing sites Pc-g, P1–4, P5,6, and Pm-o. Wild-type (W) or mutant (M) fragments were subjected to in vitro phosphorylation as in (C). (E) Protein sequences of *Drosophila* Ci, mouse Gli2, and *Xenopus* Gli3 were aligned using the Geneious algorithm and the degree of conservation of protein sequences was plotted for either a 4-amino-acid or 15-amino-acid sliding window.

downstream of Smo (Fan et al., 1995; Hammerschmidt et al., 1996; Hynes et al., 1995; Jiang and Struhl, 1995; Lepage et al., 1995; Li et al., 1995; Niewiadomski et al., 2013; Pan and Rubin, 1995; Strutt et al., 1995; Tuson et al., 2011). Pharmacological activation of PKA completely blocks Hh signaling, even in the presence of the Hh ligand or a Smo agonist. Conversely, genetic ablation of PKA shifts the GliR/GliA balance strongly in favor of GliA. This leads to full ligand-independent activation of Hh target genes, manifested as complete ventralization of the embryonic neural tube in mutant mice (Tuson et al., 2011). These data clearly identify PKA as a negative regulator of Gli function, but on a molecular level, our understanding of how Gli proteins are influenced by PKA remains incomplete.

The mechanism by which PKA promotes GliR has been elucidated in detail, guided by studies of the *Drosophila* Gli homolog *cubitus interruptus* (Ci; Aza-Blanc et al., 1997; Méthot and Basler, 1999; Price and Kalderon, 1999; Wang et al., 1999). PKA can phosphorylate Gli2/3 at six conserved serine residues (P1–6) located on

the carboxyterminal side of the DNA binding Zn-finger domain (Figure 1B; Wang et al., 2000). The phosphorylation of the first four of these residues (P1–4) by PKA initiates a pathway that leads to the partial processing of full-length Glis into GliR fragments by the proteasome (Pan et al., 2009; Wang et al., 1999); the function of the last two phosphorylation sites (P5,6) is unknown.

PKA plays an equally important but much less well-understood role in suppressing Gli2/3A. Loss of phosphorylation at sites P1–4, which regulates GliR production, does not seem to be sufficient for this activation step. Transgenic mice harboring nonphosphorylatable serine-to-alanine mutations in P1–4 of Gli2 do not show the developmental phenotypes expected if Gli2 was fully activated (Pan et al., 2009). Importantly, the neural tube of these animals, in contrast to animals lacking PKA activity, is not strongly ventralized. Thus, PKA must inhibit Gli2 activation by phosphorylating sites other than P1–4.

Here, we elucidate the mechanism by which PKA inhibits the production of GliA. PKA uses distinct phosphorylation patterns

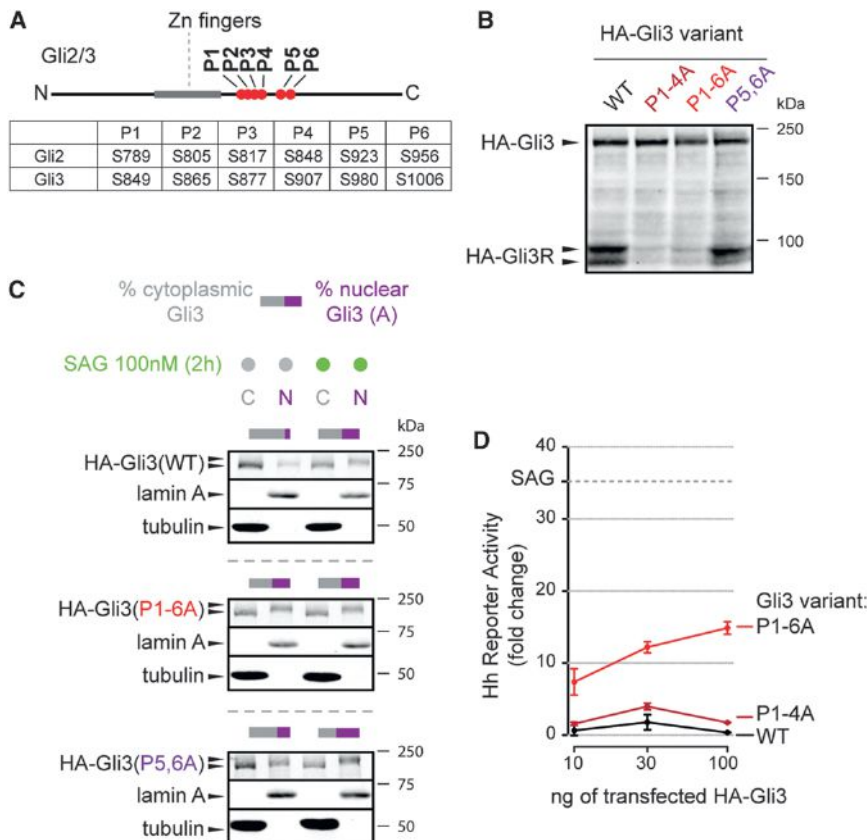


Figure 2. The P1-6 Cluster Regulates the Balance between Gli3 Activator and Gli3 Repressor

(A) Location of sites P1-6 on mouse Gli2 and Gli3. (B) An anti-HA immunoblot reveals the relative levels of full-length and repressor Gli3 in whole-cell extracts from NIH/3T3 Flp-In cells stably expressing HA-tagged Gli3 variants.

(C) Distribution of full-length HA-Gli3 variants in the nuclear (N) and cytoplasmic (C) fractions of NIH/3T3 Flp-In cells left untreated or treated with SAG (100 nM, 2 hr). In this and subsequent figures, lamin A and tubulin serve as control nuclear and cytoplasmic proteins to assess the quality of the fractionation and bars above each blot represent the relative abundance of HA-Gli3 in the cytoplasmic (gray) and nuclear (purple) fractions as determined by quantitative immunoblotting. Figure S2B compiles data from five repeats of such an experiment.

(D) Activation of a luciferase-based Hh reporter gene in NIH/3T3 cells (untreated with any Hh agonists) transiently transfected with the reporter construct in combination with the indicated Gli3 variants. Values were normalized to reporter induction seen with an empty plasmid (control). Dashed gray line shows the level of reporter activation seen with SAG (100 nM; 24 hr) in cells transfected with a control vector. See also Figure S2C. Error bars indicate SD from three independent transfections.

to regulate GliR and GliA; phosphorylation of P1-4 is sufficient for GliR production, while the inhibition of GliA formation is dependent on all six sites from the P1-6 cluster. Smo activation reduces phosphorylation of P1-6, showing that Hh signaling wields direct control over phosphorylation at these sites. We also find that P1-6 dephosphorylation allows the phosphorylation of Gli2 at a distinct cluster of sites, which plays a positive role in Hh signaling. We propose that remodeling of the phosphorylation landscape of Gli2/3 proteins controls the transcriptional output of Hh signaling and discuss the implications of this model for the role of Hh as a morphogen in development.

RESULTS

PKA Phosphorylates Gli2/3 at Multiple Sites In Vitro

Previous work has implicated PKA both in GliR formation and in GliA inhibition (Hammerschmidt et al., 1996; Pan et al., 2009; Tuson et al., 2011; Wang et al., 1999, 2000), but the biochemical mechanism by which PKA blocks GliA formation was unknown. We hypothesized that PKA suppresses the formation of GliA by direct phosphorylation of Gli2/3. In order to identify putative inhibitory PKA target sites on Gli2/3, we looked for full consensus sites (R or K present at positions -2 and -3 from the S or T) and partial consensus sites (R or K only present at either position -2 or position -3 from the S or T) that were conserved among human and mouse Gli2 and Gli3 and were located outside the DNA-binding zinc finger domain (Figure S1A). In addition to the

full consensus sites (P1-6) described previously (Pan et al., 2009; Price and Kalderon, 1999; Wang et al., 2000), we identified 15 partial consensus sites (hereafter called Pa-o; Figures 1B and S1B). Myc-tagged fragments of Gli3 containing various subsets of these sites were tested as PKA substrates using an in vitro kinase assay. Four fragments containing sites P1-4, P5,6, Pc-g, and Pm-o could be phosphorylated by PKA (Figures 1C and 1D). Interestingly, both the P1-6 and the Pc-g clusters are located in regions of Gli2/3 that are strongly conserved among the *Drosophila*, *Xenopus*, and mouse proteins (Figure 1E).

PKA Target Sites P1-6 Regulate Gli3 Repressor and Activator Functions

We first analyzed the six sites in the P1-6 cluster, which had previously been identified as PKA targets (Riobó et al., 2006; Wang et al., 2000; Figure 2A). We decided to study P1-6 in the context of both Gli3 and Gli2, since Gli3 is the major repressor (Gli3R) and Gli2 the major activator (Gli2A) in most tissues. To understand the role of specific sites within the P1-6 cluster in regulating the GliR/GliA balance, we made nonphosphorylatable alanine mutants of P1-4 (P1-4A), P5 and P6 (P5,6A), or of the entire P1-6 cluster (P1-6A) in Gli2 and Gli3. Since Gli proteins fail to be regulated by Hh signaling when overproduced in cells (Humke et al., 2010), we sought to evaluate these Gli mutants under endogenous expression levels. To that end, we stably expressed hemagglutinin (HA)-tagged Gli2/3 (HA-Gli2/3) mutants in NIH/3T3 fibroblasts using the Flp-In system, in which an expression

construct is introduced as a single-copy insertion into a defined locus in the genome by Flp-mediated recombination (Torres et al., 2009; Zhou et al., 2010). The Flp-In system allowed us to rapidly generate stable cell lines expressing Gli protein variants at near-endogenous (Figure S2A) and roughly equal (Figure 2B) levels.

Starting with Gli3, we verified that a wild-type (WT) HA-Gli3 behaved like its endogenous counterpart. Indeed, HA-Gli3(WT) could be processed into a HA-GliR fragment when expressed using the Flp-In system (Figure 2B). Consistent with previous reports (Pan et al., 2006, 2009; Tempé et al., 2006; Wang and Li, 2006), mutation of sites P1–4 into alanine was sufficient to block Gli3R formation, as neither Gli3(P1–4A) nor Gli3(P1–6A) was converted into Gli3R. In contrast, Gli3(P5,6A) readily formed Gli3R in unstimulated cells (Figure 2B). Prior reports have implicated all six sites in the P1–6 cluster in GliR formation (Wang et al., 2000), but these studies were based on transient Gli3 overexpression and required stimulation with high doses of forskolin for prolonged periods of time to produce Gli3R. Using experimental conditions that faithfully reflect endogenous Gli3 processing in untreated cells, we find that sites P5 and P6 are not involved in the PKA-dependent truncation of Gli3 into a repressor fragment.

The formation of Hh-induced Gli3A can be experimentally followed by two biochemical events: activated Gli3 translocates into the nucleus and undergoes hyperphosphorylation, which appears as a shift in the apparent molecular weight of Gli proteins on SDS-PAGE gels (Humke et al., 2010). As we have previously described for endogenous Gli3, treatment of cells with the Smo agonist SAG led to the redistribution of HA-Gli3(WT) into the nuclear fraction; nuclear HA-Gli3 also showed the characteristic reduction in electrophoretic mobility indicative of hyperphosphorylation (Figure 2C, top panel, and Figure S2B). In contrast, when all six of the P1–6 sites were simultaneously mutated to alanines, Gli3 accumulated to high levels in the nucleus even in the absence of Hh signaling (Figure 2C, middle panel, and Figure S2B). Saturating concentrations of SAG did not further increase the nuclear accumulation of HA-Gli3(P1–6A), showing that the mutation of these six residues makes Gli3 unresponsive to upstream Hh signals. Alanine mutations only in sites P5 and P6 increased levels of Gli3 in the nucleus seen in the absence of signaling but did not result in maximal nuclear accumulation; HA-Gli3(P5,6A) still moved to the nucleus in response to SAG (Figure 2C, bottom panel, and Figure S2B).

To measure transcriptional activity of the Gli3 mutants, we transiently transfected constructs encoding each protein and measured the activation of an Hh-dependent firefly luciferase reporter gene (Sasaki et al., 1997). Consistent with prior characterization of Gli3 as a weak transcriptional activator (Sasaki et al., 1997), both HA-Gli3(WT) and HA-Gli3(P1–4A) failed to substantially increase Hh-dependent luciferase expression. On the other hand, HA-Gli3(P1–6A) could activate the reporter gene (Figure 2D), confirming the role of P5 and P6 in limiting the ability of Gli3 to activate transcription. Neither HA-Gli3(P1–4A) nor HA-Gli3(P1–6A) could be processed to Gli3R (Figure 2B), and so differences in their ability to activate transcription cannot be attributed differences in Gli3R levels. All six sites in the P1–6 cluster play a role in tuning Gli3 activity, since HA-Gli3(P5,6A)

also demonstrated low levels of transcriptional activity, analogous to that of HA-Gli3(P1–4A) (Figure S2C).

These results suggest that Gli3 may be regulated by graded dephosphorylation. Loss of P1–4 phosphorylation blocks Gli3R repressor formation but is insufficient for the full activation of Gli3. The additional loss of P5,6 phosphorylation is required to achieve complete transformation of Gli3 into Gli3A.

Sites P1–6 Determine the Transcriptional Activity of Gli2

Since Gli2 is the major transcriptional activator of Hh target genes in most tissues, we made a similar series of mutations in the P1–6 sites of Gli2. While WT HA-Gli2 can activate the Hh reporter in transient overexpression assays (Figure 3A; Sasaki et al., 1999), the Gli2(P1–6A) mutant was significantly more active at all doses tested. The P1–4A and P5,6A mutants of Gli2 showed an intermediate capacity to activate the reporter. Mutation of either P5 or P6 individually in combination with P1–4 also increased activity of Gli2, suggesting that P5 and P6 may be partially redundant (Figure S2D). Conversely, mutation of both sites P5 and P6 to aspartate (P5,6D), a phospho-mimetic mutation, substantially reduced the activating potential of Gli2 (Figure S2D). These results are consistent with an inhibitory role of P1–6 phosphorylation in the activation of Gli2.

To examine Gli2 regulation under physiological expression levels, we turned to Flp-In stable lines carrying HA-tagged Gli2 mutants (Figure S2A). Similar to its effect on Gli3, the P1–6A mutation in HA-Gli2 caused constitutive Hh-independent accumulation in the nucleus, consistent with Gli2(P1–6A) being a fully active molecule (Figure 3B). In order to correlate nuclear accumulation with transcriptional activity, we measured the expression of endogenous *Gli1*, a Hh target gene commonly used as a metric for pathway activity, in these same stable cell lines. In the absence of Hh signaling, Gli1 levels were not elevated in the line expressing HA-Gli2(WT), confirming that this exogenous protein is properly regulated (Figure S2E). To account for differences in expression levels of the HA-Gli2 variants (Figure 3C), we compared their specific activities, calculated as the level of Gli1 induction divided by the protein level of the corresponding HA-Gli2 variant. The specific activities of the mutants fell along a gradient: the HA-Gli2(P1–4A) and HA-Gli2(P5,6A) mutants demonstrated ~3- to 4-fold higher specific activity and the HA-Gli2(P1–6A) mutant displayed ~13-fold higher specific activity compared to HA-Gli2(WT) (Figure 3C). The high level of Gli1 in cells carrying Gli2(P1–6A) was resistant to inhibition by two Smo antagonists, cyclopamine and SANT-1 (Figures 3D and S2F), demonstrating that the activity of this mutant protein was independent of Smo. Importantly, all the stable cell lines (which also contain endogenous Gli2) were able to produce equivalent levels of Gli1 when stimulated with SAG, showing that they did not differ in their intrinsic capacity to activate Hh targets (Figure 3C). Since the Flp-In lines also expressed endogenous Gli2, the *Gli1* induction in response to SAG (Figure 3C) could not be used to infer the Hh-responsiveness of the HA-Gli2 variants expressed in these lines.

To analyze the ability of upstream Hh signaling to regulate the HA-Gli2 mutants in our Flp-In cell lines, we selectively depleted endogenous Gli2 with a small interfering RNA (siRNA) directed against its 3' UTR (Figures 3E and S2G). Under these conditions,

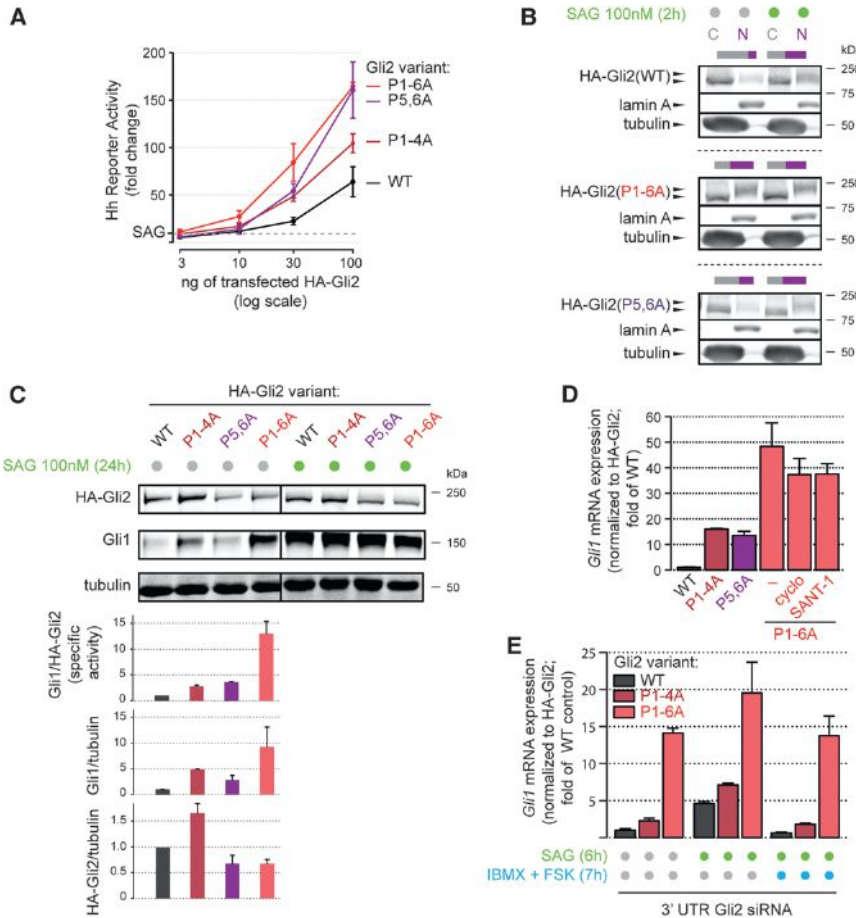


Figure 3. The P1-6 Cluster Regulates the Activation of Gli2

(A) Luciferase reporter activity in NIH/3T3 cells (untreated with any Hh agonists) transiently transfected with the indicated Gli2 variants. The dashed line shows levels of reporter induction seen when cells transfected with a control vector are exposed to SAG (100 nM). Error bars denote SD from three independent transfections.

(B) Distribution of full-length HA-Gli2 in NIH/3T3 Flp-In cells stably expressing the indicated variants.

(C) Levels of the Hh target gene *Gli1* and HA-Gli2, measured using anti-Gli1 and anti-HA immunoblots respectively, in NIH/3T3 Flp-In stable cell lines expressing the indicated Gli2 variants. Cells were left untreated or treated with SAG (100 nM, 24 hr). Bar charts underneath show quantitation of the *Gli1* and HA-Gli2 proteins (normalized to tubulin) in each cell line and the specific activity of each variant (top chart), expressed as the ratio of the intensities of the *Gli1* band to the HA band. Bars denote the mean (\pm SD) from two independent experiments.

(D) *Gli1* mRNA level, measured by quantitative RT-PCR, in Flp-In stable cell lines expressing the indicated HA-Gli2 variants. HA-Gli2(P1-6A) cells were left untreated or treated with the Smo inhibitors cycloamine (5 μ M) or SANT-1 (100 nM). The *Gli1* mRNA level was normalized to the HA-Gli2 protein level as in (C) to adjust for differences in expression level of the Gli variants. Bars denote the mean (\pm SD) from two independent samples.

(E) *Gli1* mRNA level in the indicated stable cell lines treated with SAG (100 nM) in the presence or absence of the PKA activators IBMX (100 μ M) and FSK (0.1 μ M). In all cells, expression of endogenous Gli2 was reduced by a siRNA directed

against the 3' UTR to examine signaling through the HA-Gli2 variants. The *Gli1* mRNA level was normalized to HA-Gli2 protein measured as in (C) and (D); graphs depicting data without the HA-Gli2 protein normalization are shown in Figures S2F and S2G. Bars denote the mean (\pm SD) from two independent samples.

the SAG initiated signal should be largely transduced through our HA-tagged Gli2 variants. In the absence of endogenous Gli2, SAG could significantly increase *Gli1* expression in either HA-Gli2(WT) or HA-Gli2(P1-4A) cells. In the same cell lines, PKA activation, accomplished with the drugs isobutylmethylxanthine (IBMX) and forskolin (FSK) antagonized the effect of SAG (Figure 3E). In contrast, the high baseline expression of *Gli1* in the HA-Gli2(P1-6A) line was largely insensitive to regulation by either SAG or IBMX/FSK (Figures 3E and S2G). This is further evidence that Gli2(P1-6A) corresponds to a maximally active form of Gli2, which cannot be regulated by either Smo or PKA. Gli2(P1-4A) remains SAG and PKA sensitive, perhaps through phosphoregulation at the P5 and P6 sites. We conclude that only after losing all phosphates at sites P1-6 does Gli2 become a bona fide GliA. These data explain why the previously studied Gli2(P1-4A) mutant of Gli2 failed to fully activate Hh responses during development (Pan et al., 2009).

P1-6 Mutants of Gli2 Ectopically Specify Ventral Cell Types in the Developing Spinal Cord

Encouraged by these results, we tested the ability of Gli2(P1-6A) to drive Hh-regulated cell fate decisions in vivo in a cell-autono-

mous manner. In the ventral neural tube, Shh acts as a graded signal that specifies the dorsal-ventral pattern of progenitor subtypes (Figure 4A). This precise spatial patterning is established by a gradient of Gli activity (Bai et al., 2004; Lei et al., 2004; Stamatiki et al., 2005), making the neural tube an ideal place to test the activities of our Gli2(P1-4A) and Gli2(P1-6A) mutants. Using in ovo electroporation techniques, we expressed the Gli2 mutants under the control of a weak SV40 early promoter in one-half of the neural tube of Hamburger-Hamilton (HH) stage 10-12 chicken embryos and examined the expression of various progenitor markers 48 hr later. Ectopic expression of Gli2(WT) did not alter the spatial arrangement of neuronal progenitors (Figures 4B-4D, top row, and Figure S3C) and also did not induce expression of *PTCH1*, a direct Hh target gene (Figure 4E, top row).

In contrast, overexpression of Gli2(P1-6A) at any position along the dorsoventral axis led to the ectopic specification of ventral cells, identified by the ventral-most progenitor domain (pFP/p3) marker FOXA2 and the p3 marker NKX2.2, both of which depend on the highest levels of Hh/Gli signaling (Figure 4B, bottom row, and Figure S3C). Gli2(P1-6A) could also induce NKX6.1, which labels the pFP, p3, pMN, and p2 progenitor

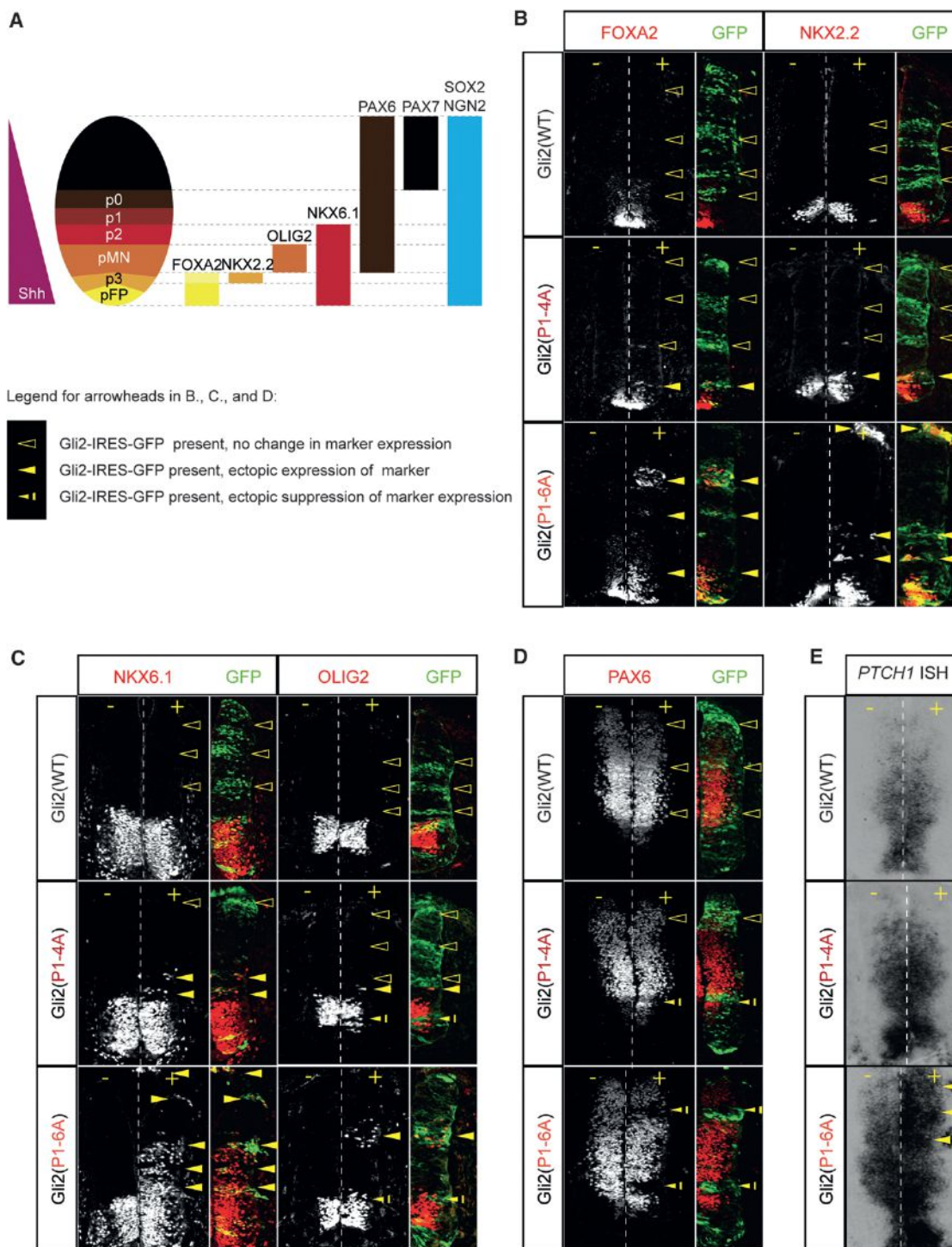
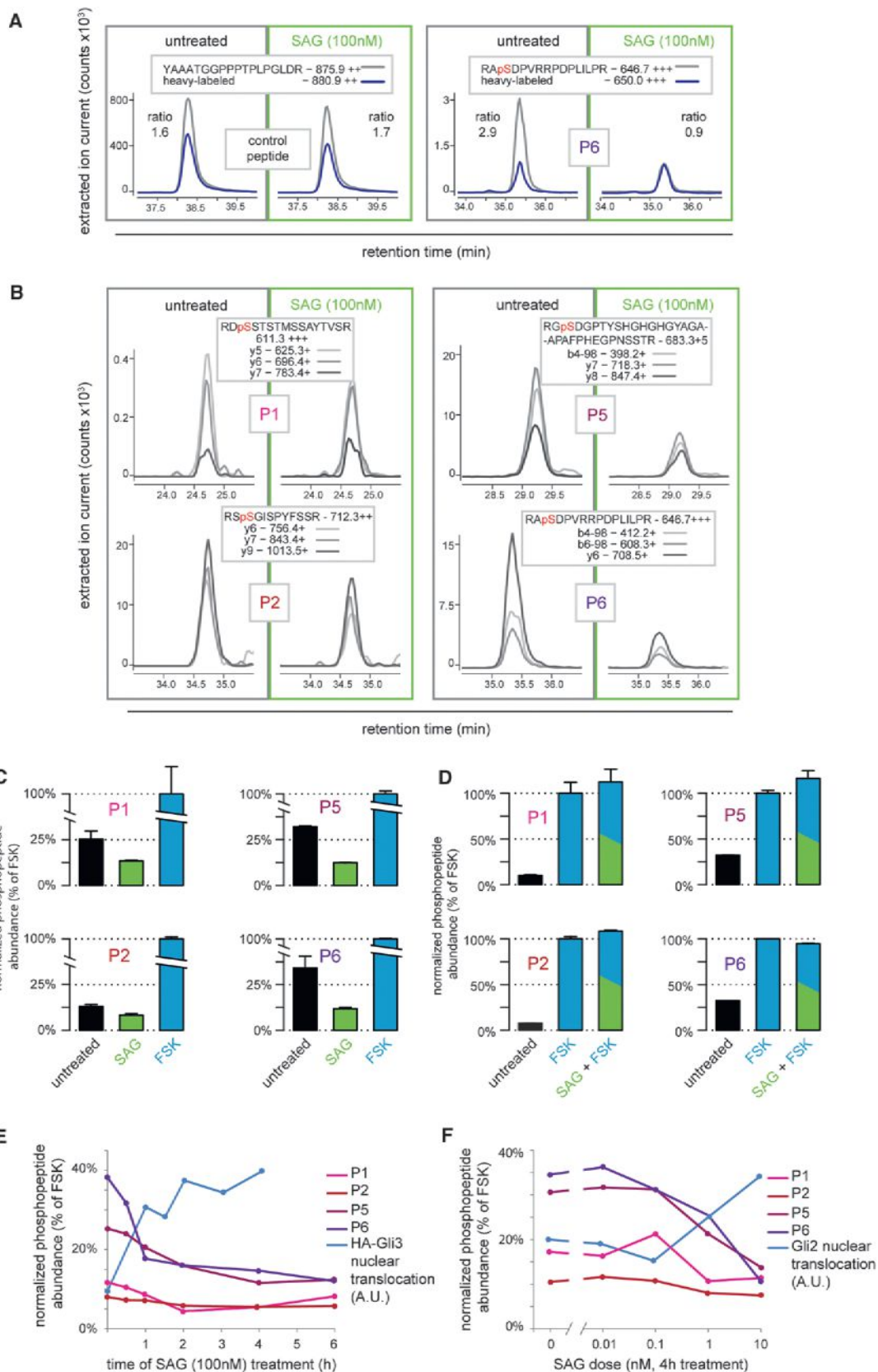


Figure 4. Gli2(P1-6A) Can Induce Ventral Cell Fates in the Developing Spinal Cord

(A) A schematic illustrating the relationship between marker proteins and progenitor cell populations in the embryonic neural tube (adapted from Stamatakis et al., 2005). pFP, floor plate progenitors; pMN, motor neuron progenitors; p0, p1, p2, p3, ventral interneuron progenitors.

(B–D) Constructs encoding Gli2 variants (green) were electroporated into developing spinal cords of chicken embryos. Expression of the indicated progenitor population markers (red) was detected by immunofluorescence 48 hr later. Black and white panels show marker expression in both sides of the spinal cord (“+” indicates the electroporated side, “–” the unelectroporated side). Overlay panels show the electroporated side only. See also Figure S3C.

(E) In situ hybridization for *PTCH1* mRNA in sections of spinal cord electroporated with the indicated Gli2 constructs. The right side of each section was electroporated.



(legend on next page)

domains. OLIG2, a marker of motor neuron progenitors (pMN), which are specified by intermediate levels of Hh signaling, was induced mostly in cells expressing lower levels of Gli2(P1–6A) but often suppressed in strongly Gli2(P1–6A)-positive cells, most likely reflecting the cross-repressive interaction between NKX2.2 and OLIG2 in the neural tube (Novitsch et al., 2001). Moreover, Gli2(P1–6A) suppressed the expression PAX6, a dorsal marker known to be negatively regulated by Hh signaling. Consistent with this ability to specify cell fates that depend on high levels of Hh ligand, Gli2(P1–6A) induced the robust expression of *PTCH1*, a direct Hh target gene, throughout the neural tube. The ability Gli2(P1–6A) to induce the ventral and suppress the dorsal markers was resistant to coexpression of a constitutively active mutant of Patched, Ptch^{Δloop2} (Briscoe et al., 2001), confirming that the P1–6A mutant of Gli2 escapes regulation by the upstream elements of the Hh pathway (Figure S3A).

Gli2(P1–4A) demonstrated intermediate activity: it induced FOXA2, NKX2.2, and NKX6.1 when expressed immediately adjacent to their normal domains but not when expressed in more dorsal regions of the neural tube (Figures 4B–4D, middle row, and Figure S3C). This expansion of the ventral domains suggests that Gli2(P1–4A) sensitized cells to Shh, such that the same level of Shh exposure is translated to more ventral cell fates. Even though our Gli2 variants induced ectopic FOXA2, they did not drive SHH expression (Figure S3B), suggesting that the effects we describe in Figure 4 were not due to non-cell-autonomous effects of ectopic floor plate induction in the electroporated spinal cords. These data are consistent with previous reports showing that activated Smo and Gli proteins expressed in the HH12 stage neural tube can promote ventral character while at the same time inhibiting the formation of floor-plate cells (Lei et al., 2004; Ribes et al., 2010). Neither Gli2 mutant affected the expression of Hh-independent progenitor markers SOX2 and NGN2, suggesting that the total number of neuronal progenitors is unchanged by the expression of these constructs (Figure S3B).

Taken together, these data suggest that there is a fundamental difference between blocking phosphorylation at sites P1–4 only and blocking it throughout the P1–6 cluster. Because both the P1–4A and P1–6A mutations block repressor formation (Figure 2B), the marked differences in the activities of Gli2(P1–4A) and Gli2(P1–6A), both in cultured cells and in the developing neural tube, must be attributed to the role of P5 and P6 in the

formation of Gli2A. Dephosphorylation of these sites in response to Hh ligands appears to be necessary to unleash the full activation potential of Gli2. P6 phosphorylation has been previously implicated in the interaction of Glis with 14-3-3 proteins (Asaoka et al., 2010), but in our system, this interaction did not appear to be required for the inhibitory function of P6 in GliA formation (see Supplemental Discussion and associated Figures S6B and S6C).

Hh Signaling Reduces Phosphorylation of P1–6

Our mutagenesis studies suggested that loss of phosphorylation on the serine residues at P1–6 is a regulatory step in the activation of Gli proteins. Hence, we sought to monitor changes in the phosphorylation status of these sites on endogenous Gli2 in response to signaling. We were unable to raise phospho-specific antibodies that recognized multiple sites on endogenous Gli2 in a quantitative fashion. Instead, we developed a mass spectrometry (MS)-based selected reaction monitoring (SRM) assay to quantitatively assess phosphate occupancy at P1, P2, P5, and P6 (Cox et al., 2005; Gerber et al., 2003; Mayya et al., 2006). Endogenous Gli2, isolated by immunoaffinity purification, was digested with trypsin, and the phosphorylated versions of the tryptic peptides encompassing sites P1, P2, P5, and P6 were quantified by triple-quadrupole MS (Figure 5A).

Activation of Hh signaling by SAG reduced the abundance of phosphorylated peptides containing sites P1, P2, P5, and P6 (Figures 5B and 5C), with changes at P5 and P6 being more marked than those in sites P1 and P2. The phosphorylation of sites P5 and P6 was sensitive to both the concentration of SAG and the duration of SAG treatment (Figures 5E and 5F). In both cases, reduction in phosphorylation correlated with the amount of Gli in the nucleus. The changes in Gli2 phosphorylation were not due to differences in protein stability, since all measurements were conducted on cells pretreated with the proteasome inhibitor bortezomib and results obtained in the absence and presence of this drug were similar (Figures 5C and S4A). In addition, no changes were observed after SAG addition in the abundance of a control, nonphosphorylatable peptide from a different region of Gli2 (Figure 5A). A caveat with measuring dephosphorylation by quantitative MS is that the observed reduction in the abundance of a phosphopeptide might reflect a change in phosphate occupancy of nearby sites rather than actual dephosphorylation of the site of interest. To address this concern, we also monitored the nonphosphorylated

Figure 5. Phosphorylation of the P1–6 Sites Declines with Hh Signaling

(A) Measurement of phosphopeptide abundance using SRM. Peptides were monitored in tryptic digests of immunoprecipitated Gli2 either in untreated NIH/3T3 Flip-In cells or in cells treated for 4 hr with 100 nM SAG, both in the presence of the proteasome inhibitor bortezomib (1 μ M). The intensity of the “strongest” transition for two peptides, a nonphosphorylatable peptide used as a loading control (left) and a phospho-P6-containing peptide (right), was plotted versus retention time (XIC, extracted ion current; gray trace). Blue traces are XICs of the corresponding heavy isotope-labeled standard peptide spiked into the tryptic digest before the run. For each condition, the normalized abundance of a peptide was calculated as the ratio of the area under the curve (AUC) for the light (endogenous) peptide to the AUC for the heavy peptide.

(B) XIC versus retention time plots showing three SRM transitions for each of the endogenous (light) phosphorylated peptides containing sites P1, P2, P5, and P6. (C and D) Normalized abundance of phosphopeptides (calculated using an SRM assays of the kind shown in A) containing the P1, P2, P5, and P6 sites derived from tryptic digests of immunopurified Gli2 isolated from NIH/3T3 cells treated (4 hr) with SAG (100 nM) or IBMX (100 μ M) + FSK (100 nM). Phosphopeptide abundance measured in cells after PKA activation with IBMX + FSK was taken as maximal (100%) phosphorylation. Bars denote means (\pm SD) of two to three independent MS runs.

(E and F) Phosphopeptide abundance was monitored as a function of time after SAG treatment (E) and as a function of SAG concentration (F) and compared to the levels of Gli3 (E) or Gli2 (F) in the nucleus (blue line). Percent of total Gli in the nucleus was calculated based on subcellular fractionation experiments as shown in Figure 2C (Humke et al., 2010).

peptide encompassing site P6 (dephospho-P6) by SRM and observed that its abundance rose with SAG treatment and declined with IBMX and FSK (reciprocal to the pattern seen with phospho-P6; Figure S4B), suggesting that the changes in phospho-P6 were due to bona fide dephosphorylation of the P6 site.

Stimulation of PKA activity with IBMX and FSK strongly increased phosphate occupancy at all sites within the P1–6 cluster and also prevented SAG from decreasing phosphorylation (Figure 5D). This result is consistent with the model that PKA negatively regulates Hh signaling by phosphorylating P1–6. It also suggests that even in resting cells, Gli proteins are not fully phosphorylated at the P1–6 sites. The reason why these partially dephosphorylated Glis do not become transcriptionally active is unknown but may be related to the dynamics of the phosphate turnover on individual sites within the cluster. For instance, there may be some redundancy between individual sites in the P1–4 and P5,6 clusters.

A Cluster of Serine/Threonine Sites Is Important for Gli2/3 Activation

Since phosphorylation of the P1–6 cluster seemed sufficient for the inhibition of GliA formation, we were curious to determine how the two remaining clusters of putative PKA target sites (Pc–g, Pm–o; Figures 1B and 1C) affected Gli function. Alanine mutations in Pm–o cluster did not have a discernable effect (Figure S5A) in our assays, so we focused on the Pc–g cluster. To explore the role of Pc–g phosphorylation in the regulation of Gli2, we made both nonphosphorylatable and phosphomimetic mutations of this cluster in Gli2, replacing the serine and threonine residues with alanine or glutamate [hereafter called Gli2(Pc–gA) and Gli2(Pc–gE)]. In Hh reporter assays, HA-Gli2(Pc–gE) was significantly more active than the WT protein (Figure 6A) and Gli2(Pc–gA) was approximately 40% less active than the WT protein (Figure 6B). We also generated cell lines stably expressing HA-Gli2(Pc–gE) using the Flp-In system. Gli2(Pc–gE) protein levels were lower than Gli2 (WT), suggesting that the mutant protein was less stable (Figure S5B). The higher specific activity of HA-Gli2(Pc–gE) (Figure 6C) supported the model that Pc–g phosphorylation, in contrast to P1–6 phosphorylation, plays a positive role in Gli2 activity. Gli2(Pc–gE) also showed other hallmarks of activation, including reduced mobility on a gel and higher levels in the nucleus (Figure 6D).

Hh Signaling Promotes and PKA Antagonizes Phosphorylation on Pg

The characterization of Pc–g phosphorylation as playing a positive role in Gli activity was inconsistent with our initial identification of these sites as *in vitro* targets for PKA (Figure 1), a kinase that has an inhibitory effect on Hh signaling in vertebrates (Epstein et al., 1996; Humke et al., 2010; Tukachinsky et al., 2010; Tuson et al., 2011). To monitor Pc–g phosphorylation in the context of endogenous Gli2 in cells, we established an SRM assay to measure levels of a phosphorylated tryptic peptide that encompassed Pg, the only site in the Pc–g cluster whose phosphorylation could be easily monitored by MS (Table S1). Surprisingly, in cells treated with FSK and IBMX to activate PKA, Pg phosphorylation was reduced (Figure 6E), demon-

strating that the Pg site is not a bona fide PKA target in cells. Instead, we observed a 5-fold increase in the abundance of phosphorylated Pg upon SAG treatment (Figure 6E), supporting the mutational data pointing to a positive role for Pc–g phosphorylation in Gli2 activity. As for P6, we also monitored the abundance of a nonphosphorylated tryptic peptide encompassing site Pg (dephospho-Pg; Figure S5C). As expected, dephospho-Pg abundance dropped with SAG treatment and increased with IBMX + FSK treatment, providing further evidence for the positive regulation of Pc–g phosphorylation by the Shh signal. Experiments performed in the presence and absence of a proteasome inhibitor gave qualitatively similar results (Figure S5D).

Interestingly, both the temporal dynamics and SAG dose-sensitivity of Pc–g phosphorylation (Figures 6F and 6G) mirrored those of P1–6 dephosphorylation (Figures 5E and 5F). PKA activation had opposite effects on the phosphorylation of the Pc–g and P1–6 clusters, suppressing the former while promoting the latter (Figures 6E and 5D). A parsimonious interpretation of these data is that PKA prevents Pc–g phosphorylation and Gli activation by directly phosphorylating the P1–6 sites.

To dissect the hierarchy between the Pc–gE and P1–6 sites, we combined activating (Pc–gE) and inhibitory (Pc–gA) mutations in the Pc–g sites with either inactivating (P5,6D) or activating (P1–6A) mutations in the P1–6 sites (Figure 6H). In Hh reporter assays, the activities of the Gli2(Pc–gE/P5,6D) and Gli2(Pc–gE/P1–6A) combination mutants were very similar, demonstrating that activating modifications at Pc–g make the phosphorylation status of P1–6 irrelevant. Controls confirmed that the isolated P5,6D mutation is much less active than the P1–6A mutant. Conversely, introduction of the inactivating Pc–gA mutation into Gli2(P1–6A) caused a substantial drop in its constitutive activity both in transient transfection assays (Figure 6I) and in a stable cell line (Figure 6J). These results support the model that Pc–g phosphorylation is an activating event gated by PKA-regulated phosphorylation of the P1–6 sites.

DISCUSSION

Distinct Phospho-codes for Gli Activator and Gli Repressor Regulation

We show here that phosphorylation of Gli proteins at six PKA target sites (P1–6) is a central determinant of their transcriptional activity, controlling the production of both repressor (GliR) and activator (GliA) forms. Our data are most consistent with a model involving ordered changes of phosphate occupancy at sites located in two distinct serine/threonine clusters (Figure 7A). In resting cells, PKA phosphorylates sites P1–6 on Gli2/3, triggering proteasomal processing into GliR and blocking conversion into GliA. When Hh binds to Ptc, Smo inhibits P1–6 phosphorylation, initiating a pathway that ultimately leads to the production of GliA: Gli proteins undergo phosphorylation at the Pc–g cluster, enter the nucleus, and are converted to unstable transcriptional activator proteins. We propose that the full transcriptional activation of Gli proteins requires the loss of phosphates at the P1–6 cluster followed by the gain of phosphates at the Pc–g cluster. The relative ordering of these two events is demonstrated by the fact that PKA activation enhances P1–6 phosphorylation and blocks Pc–g phosphorylation

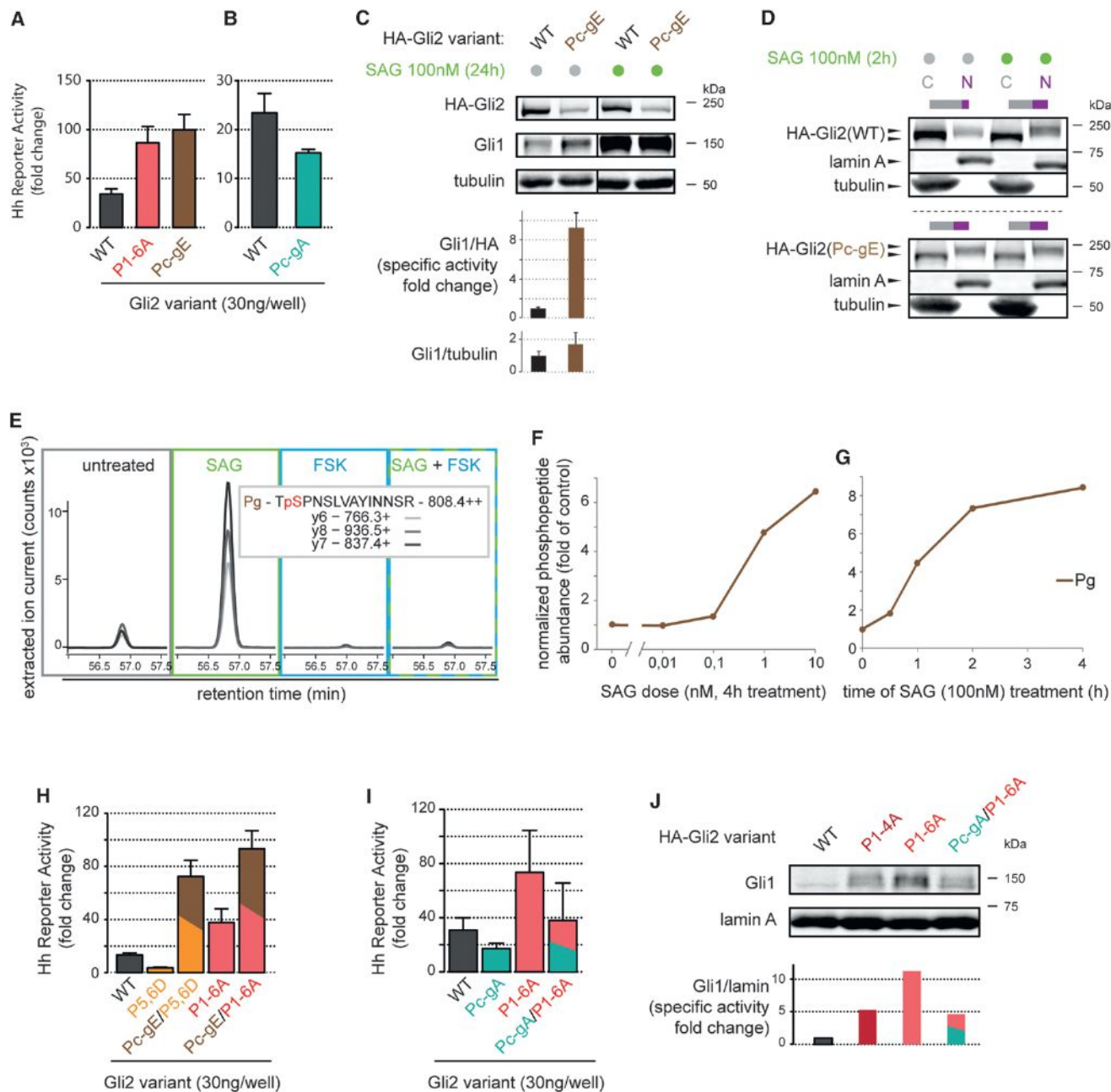


Figure 6. Pc-g Phosphorylation Positively Regulates Gli2 Activity

(A and B) Hh reporter activity in NIH/3T3 cells transiently transfected with Gli2(WT), Gli2(Pc-gA) or Gli2(Pc-gE). Bars are mean (\pm SD) of two independent transfections.

(C and D) NIH/3T3 Flp-In cell lines expressing HA-Gli2(WT) or HA-Gli2(Pc-gE) were used to evaluate the specific activity (C, analyzed as in Figure 3C) and subcellular distribution (D, analyzed as in Figure 2C) of the Gli2 variants. Bars are mean (\pm SD) of three independent experiments.

(E) XIC versus retention time traces for three SRM transitions derived from a Gli2 tryptic phosphopeptide containing the Pg residue. Phosphopeptide abundance is compared for Gli2 immunopurified from cells treated with the indicated drugs (4 hr).

(F and G) Pg phosphorylation abundance as a function of the concentration of SAG (F) or the duration of SAG exposure (G).

(H) Hh reporter activity in NIH/3T3 cells transiently transfected with Gli2(WT), Gli2(P5,6D), Gli2(P1-6A), and the combined mutants Gli2(Pc-gE/P1-6A) and Gli2(Pc-gE/P5,6D). Bars are mean (\pm SD) of three independent transfections.

(I) Hh reporter activity in NIH/3T3 cells transiently transfected with Gli2(WT), Gli2(Pc-gA), Gli2(P1-6A), and the combined mutant Gli2(Pc-gA/P1-6A). Bars denote mean \pm SD from two independent transfections.

(J) Level of the Hh target gene Gli1 measured using anti-Gli1 immunoblot in cell lines stably expressing near-endogenous levels of the indicated HA-Gli2 constructs. Bar chart shows quantitation of Gli1 protein normalized to lamin.

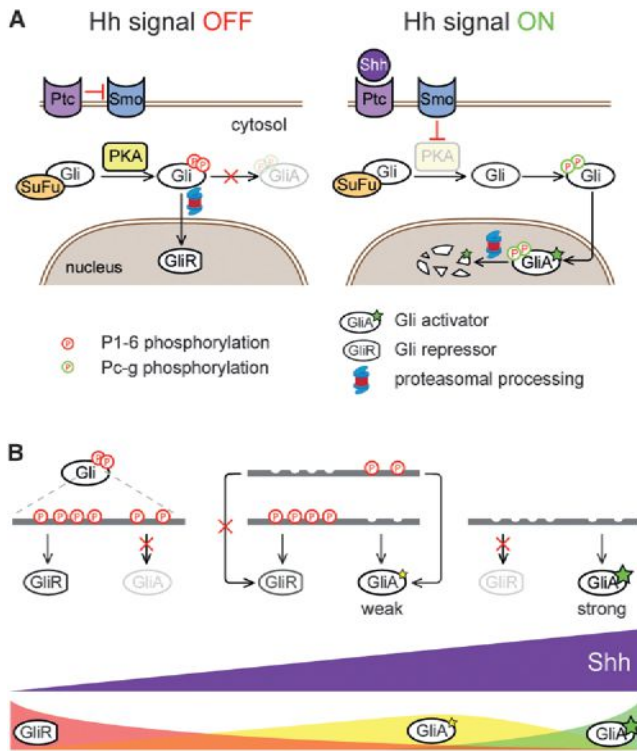


Figure 7. Our Model for the Phosphoregulation of Gli Proteins in Hh Signaling

(A) Diagram illustrating the multisite phosphorylation model of Gli2/3 regulation.

(B) Multiple states of Gli activity can be encoded by different patterns of Gli phosphorylation at the P1–6 cluster. Full phosphorylation of P1–6 (left) drives GliR formation and blocks GliA formation. Partially dephosphorylated Gli proteins (middle) function as weak activators and may be able to form GliR, depending on the pattern of phosphorylation. Fully dephosphorylated Gli proteins (right) cannot form GliR and function as strong transcriptional activators. See also Supplemental Discussion.

(Figure 6E). This regulatory motif, a gating dephosphorylation event coupled to nuclear translocation and an activating phosphorylation event at a distinct site, is reminiscent of the mechanism by which nuclear factor of activated T cells (NFAT) is regulated in response to T cell receptor engagement (Okamura et al., 2000). The concerted dephosphorylation of 13 phosphoserine residues by the phosphatase calcineurin triggers a conformational change in NFAT that drives nuclear localization. Like the Gli proteins, NFAT also requires an activating phosphorylation event at a separate site to acquire full transcriptional activity. Interestingly, in Gli1, which acts as a strong constitutive activator, the P1–6 cluster is poorly conserved (only sites P1, P2, and P6 show some degree of conservation). By contrast, four out of the five sites in the Pc-g cluster, including Pg, show remarkable sequence conservation among the three mammalian Gli proteins. This suggests that Pc-g phosphorylation may act as a universal activating signal for the Gli family.

Many signaling pathways, such as the NFAT pathway, regulate the conversion of a transcription factor from an inactive to an active state. The Hh pathway is different in that it controls

the balance between gene repression, mediated by GliR, and gene activation, mediated by GliA. For instance, in *Drosophila*, low levels of Hh signaling suppress the formation of CiR, but higher levels are required for the production of CiA (Méthot and Basler, 1999, 2001). Our analysis of the P1–6 cluster in Gli3 (Figure 2) suggests that repressor and activator functions of Gli proteins can be encoded by different patterns of phosphorylation: loss of phosphates at P1–4 is enough to block repressor formation, but loss of phosphates at all six P1–6 residues is needed for full nuclear translocation and transcriptional activity (Figure 7B). This provides a simple mechanism by which signaling can exert independent control over the repressor and activator functions of Gli2/3.

While repressors forms of the Gli proteins can be assayed directly due to their truncated length, a reliable biochemical mark for Gli activator formation has remained elusive. GliA formation has been inferred indirectly from changes in subcellular localization, such as nuclear translocation, or from target gene activation. This is a clinically relevant issue, since such a mark of Gli protein activity would be a valuable predictive biomarker for patients being considered for Hh antagonists, and could be used as a pharmacodynamic parameter to assess responses. Our SRM MS analysis suggests that Pg phosphorylation can serve as such a marker for Gli2 activity.

Graded Control of Gli Activity by Multisite Phosphorylation

Why might Gli proteins be regulated through such a complex phosphorylation scheme? Multisite phosphorylation is a commonly used regulatory module in diverse signaling systems (reviewed in Salazar and Höfer, 2009). It can be used to engineer an ultrasensitive ON/OFF switch or to encode a rheostat, allowing graded responses to varying signal strength. Examples of the latter include graded enhancement of p53 binding to CREB in response to genotoxic stress (Lee et al., 2010), graded binding of Ets-1 to DNA (Pufall et al., 2005), and graded regulation of the gating properties of the Kv2.1 potassium channel (Park et al., 2006). In fact, a theoretical model has shown that multisite phosphorylation may serve to refine such a rheostat by allowing multistability, the existence of multiple discrete activity states in the target protein or signaling module (Thomson and Gunawardena, 2009). A multistable rheostat would be well adapted to the function that Gli proteins serve during embryonic development. In developmental fields such as the limb, the inner ear, and the neural tube, Hh ligands function as classical morphogens, and a central task of signaling is to translate ligand exposure into discrete outputs, such as cell fate, at the level of transcription (Bai et al., 2004; Bok et al., 2007; Fuccillo et al., 2004; Stamatakis et al., 2005). Multisite phosphorylation might provide one mechanism by which differences in signal strength are converted into multiple discrete states of Gli activity (Figure 7B).

Indeed, our mutant analysis of the P1–6 cluster in Gli2 (Figures 3 and 4) is not consistent with a model in which Gli2 exists in either a fully inactive or fully active state. Particularly pertinent is the observation that both the P5,6A and the P1–4A mutants of Gli2 show an intermediate intrinsic capacity for transcriptional activation, which is higher than that of the WT protein but

significantly lower than that of the P1–6A mutant. Thus, Gli2 may occupy multiple states with differing activity, states that could represent different conformations of Gli2 that are stabilized by different patterns of phosphorylation at the P1–6 and Pc-g clusters. An important question going forward will be to ascertain how these changes in phosphate occupancy at the two conserved serine/threonine clusters affect the ability of Gli proteins to interact with other proteins in the cytoplasm, the cilium, and the nucleus and how these changes ultimately shape the Hh transcriptional program (also see Supplemental Discussion).

EXPERIMENTAL PROCEDURES

Cell Culture

293T cells, NIH/3T3 cells, and NIH/3T3 Flp-In cells (Life Technologies), including derivative stable clones, were cultured in media composed of Dulbecco's modified Eagle's medium (high glucose), 10% fetal bovine serum (FBS; Thermo Fisher Scientific), 1 × GlutaMAX, 1 × nonessential amino acids, 1 × sodium pyruvate, and 1 × penicillin/streptomycin (all from Life Technologies). Prior to harvesting, the cells were serum-starved in the same media but containing 0.5% FBS for 24–36 hr and treated with the indicated drugs/compounds. The 24 hr starvation was only used in assays where treatment time was 18–24 hr. For shorter treatment times (2–6 hr), a 36 hr starvation was preferred to induce a rapid response.

In Vitro Phosphorylation

Myc-tagged Gli2/3 fragments were cloned into pCS2 and overexpressed in HEK293T cells. In vitro phosphorylation was carried out on immunoprecipitated proteins in the PKA reaction buffer (Promega) in the presence of 0.5 mM ATP, 10 μ Ci of [γ - 32 P]ATP, and 21 U of PKA (NEB) for 30 min at 30°C. See Supplemental Experimental Procedures for more details.

Hedgehog Reporter Luciferase Assay

The Hedgehog reporter luciferase assay was performed as described by us before (Dorn et al., 2012). See Supplemental Experimental Procedures for more details. All plots are mean \pm SD.

Generation of Stable Cell Lines

Stable cell lines expressing low levels of HA-tagged Gli2 and Gli3 variants were generated using the Flp-In method exactly according to the manufacturer's recommendations (Life Technologies). Briefly, cells were cotransfected with pOG44 and the pEF5/FRT/V5-DEST vector containing the Gli2/3 construct of interest. After 2 days, the cells were reseeded at low density and the culture media was supplemented with hygromycin for stable integrant selection. Stable cell lines were reselected with hygromycin on every other passage to preserve selection pressure and prevent silencing of the transgene.

Subcellular Fractionation

The method for subcellular fractionation has been described by us in detail previously (Humke et al., 2010). Quantification of western blot bands was performed using ImageJ. Percent of the Gli2/3 variant present in the nuclear fractions was calculated for each sample by dividing the integrated band density for the nuclear fraction by the sum of densities for the cytoplasmic and nuclear fraction of the same sample.

In Ovo Electroporation and Immunohistochemistry/In Situ Hybridization of Chick tissue

HH stage 10–12 chick embryos were electroporated as previously described (Novitsch et al., 2001) and incubated for \sim 48 hr to HH stages 20–22. See Supplemental Experimental Procedures for detailed methods of tissue staining and a list of reagents used.

Selected Reaction Monitoring Mass Spectrometry

Cells from two to six confluent 150 mm tissue culture dishes were serum-starved for 36 hr and treated for indicated times with SAG and/or IBMX +

FSK. Bortezomib (1 μ M) was added 4 hr prior to harvesting unless indicated otherwise. The cell lysate was collected under denaturing conditions and then diluted in RIPA buffer for immunoprecipitation. Endogenous Gli2 was immunoprecipitated and the eluted protein was resolved using SDS-PAGE. The gel fragment containing Gli2 was excised and trypsinized. Tryptic fragments were extracted from the gel, purified using Oasis μ Elution columns, and loaded onto a nano high-performance liquid chromatography system for separation and MS analysis (Abell et al., 2011). See Supplemental Experimental Procedures for more details regarding protein harvesting, purification, and SRM.

SUPPLEMENTAL INFORMATION

Supplemental Information includes Supplemental Discussion, Supplemental Experimental Procedures, six figures, and one table and can be found with this article online at <http://dx.doi.org/10.1016/j.celrep.2013.12.003>.

ACKNOWLEDGMENTS

We would like to thank Siggie Nachtergaele, Andres Lebensohn, and Ganesh Pusapati for critical reading of the manuscript, Casey Hughes for technical assistance, and James Briscoe for insightful discussions. This work was supported by NIH grants R21NS074091 and R00CA129174 (to R.R.), R01NS072804 and R01NS053976 (to B.G.N.), and P50GM107615 (to M.T.) and by grants from the V Foundation (to R.R.), the Sontag Foundation (to R.R.), the German Research Foundation (grant AH 220/1-1, to R.A.), and the March of Dimes Foundation (grant 6-FY10-296, to B.G.N.).

Received: September 30, 2013

Revised: November 7, 2013

Accepted: December 3, 2013

Published: December 26, 2013

REFERENCES

- Abell, E., Ahrends, R., Bandara, S., Park, B.O., and Teruel, M.N. (2011). Parallel adaptive feedback enhances reliability of the Ca²⁺ signaling system. *Proc. Natl. Acad. Sci. USA* 108, 14485–14490.
- Asaoka, Y., Kanai, F., Ichimura, T., Tateishi, K., Tanaka, Y., Ohta, M., Seto, M., Tada, M., Ijichi, H., Ikenoue, T., et al. (2010). Identification of a suppressive mechanism for Hedgehog signaling through a novel interaction of Gli with 14-3-3. *J. Biol. Chem.* 285, 4185–4194.
- Bai, C.B., Stephen, D., and Joyner, A.L. (2004). All mouse ventral spinal cord patterning by hedgehog is Gli dependent and involves an activator function of Gli3. *Dev. Cell* 6, 103–115.
- Aza-Blanc, P., Ramirez-Weber, F.A., Laget, M.P., Schwartz, C., and Kornberg, T.B. (1997). Proteolysis that is inhibited by hedgehog targets Cubitus interruptus protein to the nucleus and converts it to a repressor. *Cell* 89, 1043–1053.
- Bok, J., Dolson, D.K., Hill, P., R  ther, U., Epstein, D.J., and Wu, D.K. (2007). Opposing gradients of Gli repressor and activators mediate Shh signaling along the dorsoventral axis of the inner ear. *Development* 134, 1713–1722.
- Briscoe, J., and Th  ron, P.P. (2013). The mechanisms of Hedgehog signaling and its roles in development and disease. *Nat. Rev. Mol. Cell Biol.* 14, 416–429.
- Briscoe, J., Chen, Y., Jessell, T.M., and Struhl, G. (2001). A hedgehog-insensitive form of patched provides evidence for direct long-range morphogen activity of sonic hedgehog in the neural tube. *Mol. Cell* 7, 1279–1291.
- Corbit, K.C., Aanstad, P., Singla, V., Norman, A.R., Stainier, D.Y.R., and Reiter, J.F. (2005). Vertebrate Smoothed functions at the primary cilium. *Nature* 437, 1018–1021.
- Cox, D.M., Zhong, F., Du, M., Duchoslav, E., Sakuma, T., and McDermott, J.C. (2005). Multiple reaction monitoring as a method for identifying protein post-translational modifications. *J. Biomol. Tech.* 16, 83–90.

- Dorn, K.V., Hughes, C.E., and Rohatgi, R. (2012). A Smoothened-Evc2 complex transduces the Hedgehog signal at primary cilia. *Dev. Cell* 23, 823–835.
- Epstein, D.J., Marti, E., Scott, M.P., and McMahon, A.P. (1996). Antagonizing cAMP-dependent protein kinase A in the dorsal CNS activates a conserved Sonic hedgehog signaling pathway. *Development* 122, 2885–2894.
- Fan, C.M., Porter, J.A., Chiang, C., Chang, D.T., Beachy, P.A., and Tessier-Lavigne, M. (1995). Long-range sclerotome induction by sonic hedgehog: direct role of the amino-terminal cleavage product and modulation by the cyclic AMP signaling pathway. *Cell* 81, 457–465.
- Fuccillo, M., Rallu, M., McMahon, A.P., and Fishell, G. (2004). Temporal requirement for hedgehog signaling in ventral telencephalic patterning. *Development* 131, 5031–5040.
- Gerber, S.A., Rush, J., Stemman, O., Kirschner, M.W., and Gygi, S.P. (2003). Absolute quantification of proteins and phosphoproteins from cell lysates by tandem MS. *Proc. Natl. Acad. Sci. USA* 100, 6940–6945.
- Hahn, H., Wicking, C., Zaphiropoulos, P.G., Gailani, M.R., Shanley, S., Chidambaram, A., Vorechovsky, I., Holmberg, E., Uden, A.B., Gillies, S., et al. (1996). Mutations of the human homolog of *Drosophila* patched in the nevus basal cell carcinoma syndrome. *Cell* 85, 841–851.
- Hammerschmidt, M., Bitgood, M.J., and McMahon, A.P. (1996). Protein kinase A is a common negative regulator of Hedgehog signaling in the vertebrate embryo. *Genes Dev.* 10, 647–658.
- Hill, P., Wang, B., and Rüther, U. (2007). The molecular basis of Pallister Hall associated polydactyly. *Hum. Mol. Genet.* 16, 2089–2096.
- Hui, C.-C., and Angers, S. (2011). Gli proteins in development and disease. *Annu. Rev. Cell Dev. Biol.* 27, 513–537.
- Humke, E.W., Dorn, K.V., Milenkovic, L., Scott, M.P., and Rohatgi, R. (2010). The output of Hedgehog signaling is controlled by the dynamic association between Suppressor of Fused and the Gli proteins. *Genes Dev.* 24, 670–682.
- Hynes, M., Porter, J.A., Chiang, C., Chang, D., Tessier-Lavigne, M., Beachy, P.A., and Rosenthal, A. (1995). Induction of midbrain dopaminergic neurons by Sonic hedgehog. *Neuron* 15, 35–44.
- Jiang, J., and Struhl, G. (1995). Protein kinase A and hedgehog signaling in *Drosophila* limb development. *Cell* 80, 563–572.
- Kang, S., Graham, J.M., Jr., Olney, A.H., and Biesecker, L.G. (1997). GLI3 frameshift mutations cause autosomal dominant Pallister-Hall syndrome. *Nat. Genet.* 15, 266–268.
- Kim, J., Kato, M., and Beachy, P.A. (2009). Gli2 trafficking links Hedgehog-dependent activation of Smoothed in the primary cilium to transcriptional activation in the nucleus. *Proc. Natl. Acad. Sci. USA* 106, 21666–21671.
- Lee, C.W., Ferreón, J.C., Ferreón, A.C.M., Arai, M., and Wright, P.E. (2010). Graded enhancement of p53 binding to CREB-binding protein (CBP) by multisite phosphorylation. *Proc. Natl. Acad. Sci. USA* 107, 19290–19295.
- Lei, Q., Zelman, A.K., Kuang, E., Li, S., and Matise, M.P. (2004). Transduction of graded Hedgehog signaling by a combination of Gli2 and Gli3 activator functions in the developing spinal cord. *Development* 131, 3593–3604.
- Lepage, T., Cohen, S.M., Diaz-Benjumea, F.J., and Parkhurst, S.M. (1995). Signal transduction by cAMP-dependent protein kinase A in *Drosophila* limb patterning. *Nature* 373, 711–715.
- Li, W., Ohlmeyer, J.T., Lane, M.E., and Kalderon, D. (1995). Function of protein kinase A in hedgehog signal transduction and *Drosophila* imaginal disc development. *Cell* 80, 553–562.
- Mayya, V., Rezual, K., Wu, L., Fong, M.B., and Han, D.K. (2006). Absolute quantification of multisite phosphorylation by selective reaction monitoring mass spectrometry: determination of inhibitory phosphorylation status of cyclin-dependent kinases. *Mol. Cell. Proteomics* 5, 1146–1157.
- Méthot, N., and Basler, K. (1999). Hedgehog controls limb development by regulating the activities of distinct transcriptional activator and repressor forms of Cubitus interruptus. *Cell* 96, 819–831.
- Méthot, N., and Basler, K. (2001). An absolute requirement for Cubitus interruptus in Hedgehog signaling. *Development* 128, 733–742.
- Niewiadomski, P., Zhujiang, A., Youssef, M., and Waschek, J.A. (2013). Interaction of PACAP with Sonic hedgehog reveals complex regulation of the hedgehog pathway by PKA. *Cell. Signal.* 25, 2222–2230.
- Novitsch, B.G., Chen, A.I., and Jessell, T.M. (2001). Coordinate regulation of motor neuron subtype identity and pan-neuronal properties by the bHLH repressor Olig2. *Neuron* 31, 773–789.
- Okamura, H., Aramburu, J., García-Rodríguez, C., Viola, J.P., Raghavan, A., Tahiliani, M., Zhang, X., Qin, J., Hogan, P.G., and Rao, A. (2000). Concerted dephosphorylation of the transcription factor NFAT1 induces a conformational switch that regulates transcriptional activity. *Mol. Cell* 6, 539–550.
- Pan, D., and Rubin, G.M. (1995). cAMP-dependent protein kinase and hedgehog act antagonistically in regulating decapentaplegic transcription in *Drosophila* imaginal discs. *Cell* 80, 543–552.
- Pan, Y., Bai, C.B., Joyner, A.L., and Wang, B. (2006). Sonic hedgehog signaling regulates Gli2 transcriptional activity by suppressing its processing and degradation. *Mol. Cell. Biol.* 26, 3365–3377.
- Pan, Y., Wang, C., and Wang, B. (2009). Phosphorylation of Gli2 by protein kinase A is required for Gli2 processing and degradation and the Sonic Hedgehog-regulated mouse development. *Dev. Biol.* 326, 177–189.
- Park, K.-S., Mohapatra, D.P., Misonou, H., and Trimmer, J.S. (2006). Graded regulation of the Kv2.1 potassium channel by variable phosphorylation. *Science* 313, 976–979.
- Price, M.A., and Kalderon, D. (1999). Proteolysis of cubitus interruptus in *Drosophila* requires phosphorylation by protein kinase A. *Development* 126, 4331–4339.
- Pufall, M.A., Lee, G.M., Nelson, M.L., Kang, H.-S., Velyvis, A., Kay, L.E., McIntosh, L.P., and Graves, B.J. (2005). Variable control of Ets-1 DNA binding by multiple phosphates in an unstructured region. *Science* 309, 142–145.
- Ribes, V., Balaskas, N., Sasai, N., Cruz, C., Dessaud, E., Cayuso, J., Tozer, S., Yang, L.L., Novitsch, B., Marti, E., and Briscoe, J. (2010). Distinct Sonic Hedgehog signaling dynamics specify floor plate and ventral neuronal progenitors in the vertebrate neural tube. *Genes Dev.* 24, 1186–1200.
- Riobó, N.A., Lu, K., Ai, X., Haines, G.M., and Emerson, C.P., Jr. (2006). Phosphoinositide 3-kinase and Akt are essential for Sonic Hedgehog signaling. *Proc. Natl. Acad. Sci. USA* 103, 4505–4510.
- Salazar, C., and Höfer, T. (2009). Multisite protein phosphorylation—from molecular mechanisms to kinetic models. *FEBS J.* 276, 3177–3198.
- Sasaki, H., Hui, C., Nakafuku, M., and Kondoh, H. (1997). A binding site for Gli proteins is essential for HNF-3beta floor plate enhancer activity in transgenics and can respond to Shh in vitro. *Development* 124, 1313–1322.
- Sasaki, H., Nishizaki, Y., Hui, C., Nakafuku, M., and Kondoh, H. (1999). Regulation of Gli2 and Gli3 activities by an amino-terminal repression domain: implication of Gli2 and Gli3 as primary mediators of Shh signaling. *Development* 126, 3915–3924.
- Stamatakis, D., Ulloa, F., Tsoni, S.V., Mynett, A., and Briscoe, J. (2005). A gradient of Gli activity mediates graded Sonic Hedgehog signaling in the neural tube. *Genes Dev.* 19, 626–641.
- Strutt, D.I., Wiersdorff, V., and Mlodzik, M. (1995). Regulation of furrow progression in the *Drosophila* eye by cAMP-dependent protein kinase A. *Nature* 373, 705–709.
- Tempé, D., Casas, M., Karaz, S., Blanchet-Tournier, M.-F., and Concordet, J.-P. (2006). Multisite protein kinase A and glycogen synthase kinase 3beta phosphorylation leads to Gli3 ubiquitination by SCFbetaTrCP. *Mol. Cell. Biol.* 26, 4316–4326.
- Thomson, M., and Gunawardena, J. (2009). Unlimited multistability in multisite phosphorylation systems. *Nature* 460, 274–277.
- Torres, J.Z., Miller, J.J., and Jackson, P.K. (2009). High-throughput generation of tagged stable cell lines for proteomic analysis. *Proteomics* 9, 2888–2891.
- Tukachinsky, H., Lopez, L.V., and Salic, A. (2010). A mechanism for vertebrate Hedgehog signaling: recruitment to cilia and dissociation of SuFu-Gli protein complexes. *J. Cell Biol.* 191, 415–428.

- Tuson, M., He, M., and Anderson, K.V. (2011). Protein kinase A acts at the basal body of the primary cilium to prevent Gli2 activation and ventralization of the mouse neural tube. *Development* *138*, 4921–4930.
- Wang, B., and Li, Y. (2006). Evidence for the direct involvement of betaTrCP in Gli3 protein processing. *Proc. Natl. Acad. Sci. USA* *103*, 33–38.
- Wang, G., Wang, B., and Jiang, J. (1999). Protein kinase A antagonizes Hedgehog signaling by regulating both the activator and repressor forms of *Cubitus interruptus*. *Genes Dev.* *13*, 2828–2837.
- Wang, B., Fallon, J.F., and Beachy, P.A. (2000). Hedgehog-regulated processing of Gli3 produces an anterior/posterior repressor gradient in the developing vertebrate limb. *Cell* *100*, 423–434.
- Wen, X., Lai, C.K., Evangelista, M., Hongo, J.-A., de Sauvage, F.J., and Scales, S.J. (2010). Kinetics of hedgehog-dependent full-length Gli3 accumulation in primary cilia and subsequent degradation. *Mol. Cell. Biol.* *30*, 1910–1922.
- Zhou, C., Jacobsen, F.W., Cai, L., Chen, Q., and Shen, W.D. (2010). Development of a novel mammalian cell surface antibody display platform. *MAbs* *2*, 508–518.

Fate of iPSCs Derived from Azoospermic and Fertile Men following Xenotransplantation to Murine Seminiferous Tubules

Cyril Ramathal,¹ Jens Durruthy-Durruthy,¹ Meena Sukhwani,² Joy E. Arakaki,¹ Paul J. Turek,³ Kyle E. Orwig,² and Renee A. Reijo Pera^{1,4,*}

¹Institute for Stem Cell Biology & Regenerative Medicine, Departments of Genetics and Obstetrics and Gynecology, Stanford University, Stanford, CA 94305, USA

²Department of Obstetrics, Gynecology and Reproductive Sciences, University of Pittsburgh School of Medicine, Magee-Womens Research Institute, Pittsburgh PA 15213

³The Turek Clinic, San Francisco, CA 94133, USA

⁴Present address: Departments of Cell Biology and Neuroscience and Chemistry and Biochemistry, Montana State University, Bozeman, MT 59717, USA

*Correspondence: reneer@stanford.edu

<http://dx.doi.org/10.1016/j.celrep.2014.03.067>

This is an open access article under the CC BY license (<http://creativecommons.org/licenses/by/3.0/>).

SUMMARY

Historically, spontaneous deletions and insertions have provided means to probe germline developmental genetics in *Drosophila*, mouse and other species. Here, induced pluripotent stem cell (iPSC) lines were derived from infertile men with deletions that encompass three Y chromosome *azoospermia factor* (AZF) regions and are associated with production of few or no sperm but normal somatic development. AZF-deleted iPSC lines were compromised in germ cell development in vitro. Undifferentiated iPSCs transplanted directly into murine seminiferous tubules differentiated extensively to germ-cell-like cells (GCLCs) that localized near the basement membrane, demonstrated morphology indistinguishable from fetal germ cells, and expressed germ-cell-specific proteins diagnostic of primordial germ cells. Alternatively, all iPSCs that exited tubules formed primitive tumors. iPSCs with AZF deletions produced significantly fewer GCLCs in vivo with distinct defects in gene expression. Findings indicate that xenotransplantation of human iPSCs directs germ cell differentiation in a manner dependent on donor genetic status.

INTRODUCTION

Much progress has been made in recent years in elucidating the molecular genetic requirements of germline formation and differentiation in diverse organisms, including studies focused on murine germline development in vivo and in vitro from mouse embryonic stem cells (mESCs). Studies indicate that a key set of transcriptional regulators, including Prdm1, Prdm14, and Tfap2c, comprises a tripartite transcriptional core that functions

in suppression of somatic fate and acquisition of germline fate in vivo (Magnúsdóttir et al., 2013). In vitro studies have similarly demonstrated that induced expression of these factors converts mouse epiblast-like cells (mEpiLCs) to primordial germ-cell-like cells (PGCLCs); moreover, Prdm14 appears to be sufficient for this activity (Nakaki et al., 2013). The resulting PGCLCs are capable of contributing to spermatogenesis and fertile offspring following transplantation to murine seminiferous tubules (Hayashi et al., 2011, 2012). In parallel, in other studies, EpiSCs were shown to have an infinite capacity for generating PGCLCs as long as conditions were maintained to sustain pluripotency and self-renewal in vitro (Hayashi and Surani, 2009).

In contrast to mouse germline development, much less is known of the genetic and molecular requirements to establish the population of PGCs that ultimately gives rise to human sperm and oocytes. Indeed, this is in spite of the fact that infertility is remarkably common, affecting 10%–15% of couples (Skakkebaek et al., 1994). Moreover, genetic causes of infertility are surprisingly prevalent among men, most commonly due to the de novo deletion of one or more AZF (*azoospermia factor*) regions of the human Y chromosome (Reijo et al., 1995, 1996; Vogt et al., 1996; Foresta et al., 2000; Kuroda-Kawaguchi et al., 2001; Ferlin et al., 2003; Hopps et al., 2003; Navarro-Costa et al., 2010). Pure sterile phenotypes in men with deletions vary from the complete absence of germ cells and sperm (termed Sertoli cell-only [SCO] syndrome) to production of germ cells that arrest in development (early maturation arrest; EMA) to very low sperm counts (oligospermia) (Skakkebaek et al., 1994; Reijo et al., 1995, 1996). It is not known whether the genes of the Y chromosome AZF regions are required for PGC formation, maintenance of germline stem cell populations, and/or commitment to later stages of meiosis and haploid germ cell morphogenesis. Because of the unique nature of Y chromosome gene content in men, studies that probe the function of genes that map to the AZF regions must be conducted on a human genome background.

In order to recapitulate human germ cell formation in vivo, we tested the hypothesis that the somatic niche of murine seminiferous tubules can direct formation and maintenance of GCLCs

from undifferentiated human induced pluripotent stem cells (iPSCs). This hypothesis seemed reasonable given the extensive similarity between ESCs/iPSCs and PGCs in terms of pluripotency and gene expression and given that in both undifferentiated human ESCs (hESCs) and human iPSCs, *PRDM14*, the key inducer of PGC fate in mice, is very highly expressed and only reduced upon somatic differentiation (Chia et al., 2010). Thus, we generated patient-specific iPSCs from infertile men that harbor the most common genetic deletions of the *AZF* regions and then we induced germ cell formation from these iPSCs via xenotransplantation. Our studies offer a strategy for probing the function of naturally occurring mutations in germ cell development that is analogous to strategies used historically in species such as *Drosophila*.

RESULTS

Derivation and Characterization of iPSCs from Azoospermic Men with Y Chromosome Deletions

iPSC lines were derived from dermal fibroblasts from five males; lines were analyzed for Y chromosome deletions, and a deletion map was constructed (Figure 1A and Table S1). We verified that the fertile controls (*AZF1* and *AZF2*) had intact Y chromosomes, whereas all three infertile patients had deletions: one had a complete deletion of the *AZF_a* region (*AZF Δ _a*); the second, a deletion of both the *AZF_b* and *AZF_c* regions (*AZF Δ _{bc}*); and the third, an *AZF_c* deletion (*AZF Δ _c*). The men with *AZF Δ _a* and *AZF Δ _c* deletions presented with SCO syndrome and had no germ cells found in their testes upon extensive clinical examination; *AZF Δ _{bc}* was severely oligospermic. iPSCs generated from fibroblast cell lines (*iAZF1*, *iAZF2*, *iAZF Δ _a*, *iAZF Δ _{bc}*, and *iAZF Δ _c*) were isogenic with the parental fibroblast samples; no additional deletions occurred as a consequence of reprogramming. All iPSC lines met classic criteria of pluripotency (Figures 1 and S1). They expressed pluripotency markers at the mRNA and protein levels (Figures S1B and 1B), were karyotypically normal (Figure S1C; except for the presence of Y chromosome deletions as indicated), and differentiated in vitro and in vivo to cells of all three germ layers (Figures 1C and 1D).

In Vitro Differentiation of PGCs from Azoospermic Men and Controls

We and others previously reported germ cell differentiation from both hESCs and iPSCs in vitro (Clark et al., 2004; Kee et al., 2006, 2009; Park et al., 2009; Panula et al., 2011; Gkoutela et al., 2013). To assess germ cell development from azoospermic men relative to controls, we introduced a *VASA:GFP* reporter into all iPSCs, differentiated cells, and enriched for presumptive *VASA:GFP+* single-germ cells via FACS (fluorescence-activated cell sorting). We observed that the percentage of *GFP+* cells across all lines was similar (2%–8%) as determined from two independent clones per line (Figures S2A–S2E) but that germ cells differed in gene expression as a function of genotype. First, to determine similarities and differences between single cells differentiated from each of the four cell lines, we performed hierarchical clustering on single-cell expression (150–160 cells) and constructed a condensed heatmap of 25 single cells (iPGCs) expressing *VASA* and *GFP* mRNAs (Figure S2F). To evaluate germ-cell-spe-

cific gene expression of in-vitro-derived PGCs (iPGCs) from each line, we validated the identity of 50 individual cells that expressed the *GFP* transcript (Figure 2A) and queried expression of germ cell genes in a subset of cells for each line. Downregulation of key pluripotency genes and expression of *VASA* and other classical human PGC genes such as *DAZL* is considered indicative of a distinct PGC fate of iPSCs and hESCs following germ cell differentiation in vitro (Kee et al., 2009; Gkoutela et al., 2013).

We observed that iPGCs derived from all five lines expressed *PRDM1*, *PRDM14*, and *DAZL* mRNAs (Figure 2A). This was also reflected at the protein level for *DAZL* in *GFP+* cells (Figure 2B). However, the overall number of cells expressing *VASA*, *STELLA*, *IFITM3*, and *NANOS3* genes varied across the lines, with the greatest number observed in *iAZF1*-derived iPGCs compared to *AZF*-deleted iPGCs (Figure 2A). Moreover, we noted that *GFP+* cell populations derived from *iAZF Δ _a* and *iAZF Δ _{bc}* lines contained the fewest number of cells expressing at least seven germ-cell-specific genes. At the protein level, iPGCs expressed *VASA*, *STELLA*, and *DAZL*, but we detected fewer cells positive for each protein in *iAZF Δ _c*, *iAZF Δ _{bc}*, and *iAZF Δ _a* cells relative to controls (Figure 2B). For all iPGCs derived, core pluripotency genes were expressed at very low levels relative to undifferentiated cells (Figure 2A, right). Moreover, linear discrimination analysis of 12 candidate germ cell genes (Tables S2 and S3) in each population of *GFP+* single cells revealed that *iAZF1* and *iAZF Δ _c* iPGCs were distinct from *iAZF Δ _{bc}* and *iAZF Δ _a* iPGCs (Figure 2C). To further quantify these observations, we determined the percentage of *VASA+/GFP+* cells expressing between 1 and 12 candidate germ cell genes and observed that *iAZF1* *GFP+* cells expressed a minimum of 5–8 germ cell genes in 70% of the cell population (Figure 2D, left column, dashed lines). By comparison, 70% of *GFP+* single cells from each of the three *AZF*-deleted lines expressed a range of only one to six germ cell genes with the *iAZF Δ _a* and *iAZF Δ _{bc}* lines expressing the fewest germ-cell-specific genes within single cells. Further analysis of stage-specific gene expression revealed that, independent of genotype, the majority of *GFP+* iPGCs expressed at least four to six PGC markers (Figure 2D, right column). In contrast, *AZF*-deleted germ cells, particularly from *iAZF Δ _{bc}* and *iAZF Δ _a*, expressed zero to two spermatogonial markers, whereas *iAZF1* expressed two to four spermatogonial genes (Figure 2D). On the basis of germ-cell-specific gene expression at single-cell resolution, these analyses suggest that all lines can differentiate to iPGCs regardless of genetic background. However, when *iAZF Δ _a* and *iAZF Δ _{bc}* cells are differentiated, fewer germ cells are produced relative to control *iAZF1* cells.

Transplantation and Survival of Fetal Germ Cells to Murine Seminiferous Tubules

The gold standard for phenotypic characterization of stem cells is assessment of function in vivo (Hanna et al., 2007; Nelson et al., 2009; Weissman, 2012; Takahashi and Yamanaka, 2013). As previously reported, in transplantation with human spermatogonial stem cells, germ cells migrate to the seminiferous tubule basement membrane and proliferate to form chains and patches of spermatogonia that persist long term but do not appear to initiate or complete meiosis (Nagano et al., 2002; Hermann et al., 2010; Dovey et al., 2013). To date, the fate of human pluripotent stem

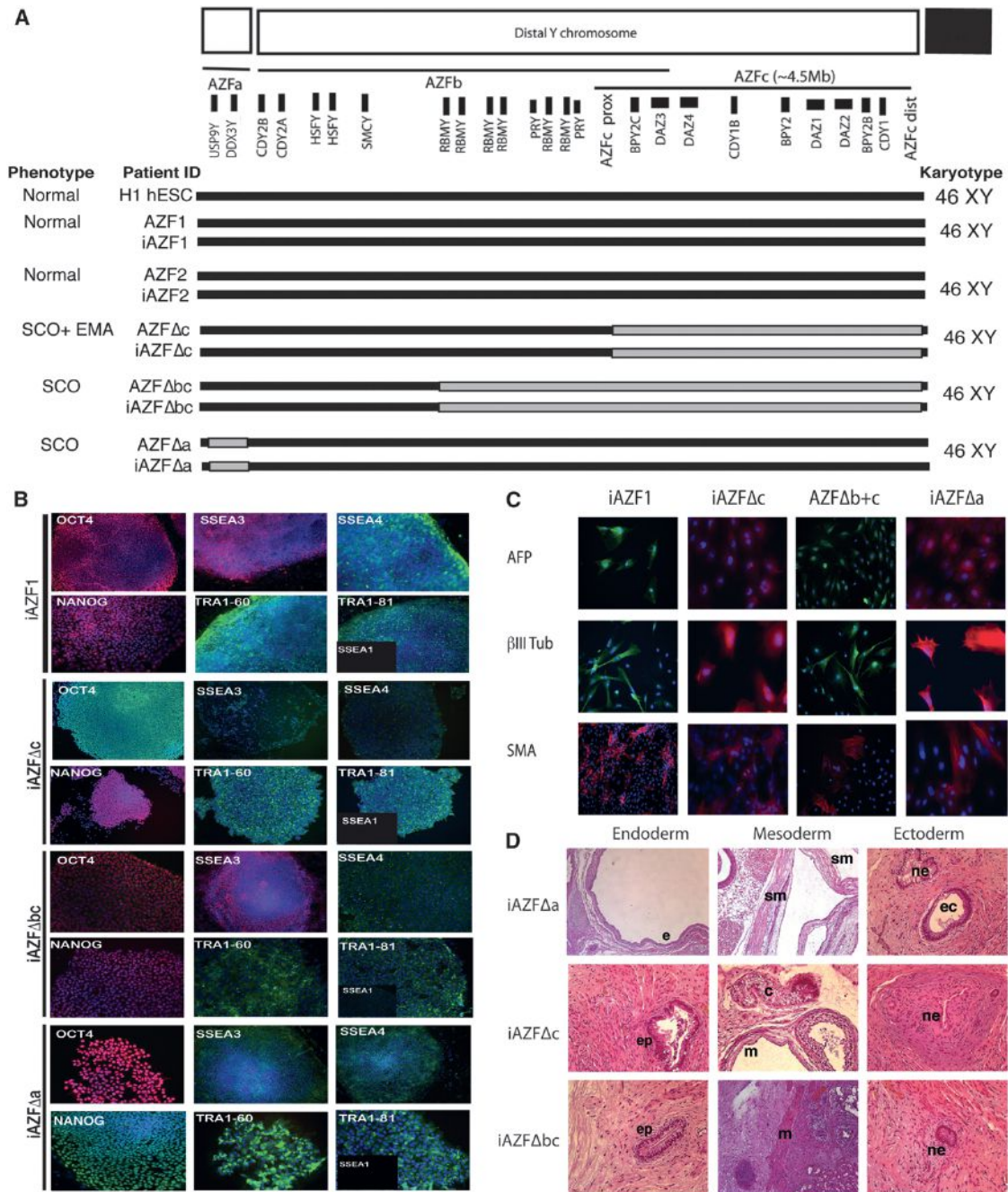


Figure 1. Derivation and Characterization of iPSCs from AZF-Intact and AZF-Deleted Patient Fibroblasts

(A) Genotype-phenotype map to visualize deletion of *AZF_a*, *AZF_b*, and *AZF_c* regions in hESC lines, patient samples, and patient-derived iPSCs used for this study. A deletion map was constructed for every hESC line, patient fibroblast, and iPSC line by testing for the presence of 20 major STSs by PCR. Vertical black bars (top) represent the STS amplification regions and genes we used to diagnose *AZF_a*, *AZF_b*, and *AZF_c* deletions. Gray boxes represent the deleted regions of the Y chromosome. The fertility phenotype (left; SCO and EMA) and karyotype (right) of each patient are listed. The triangle symbol (Δ) indicates the deletion of an *AZF* region in that cell line.

(B) Immunocytochemistry in all patient-derived iPSC lines for nuclear (OCT4 and NANOG) and cell surface (SSEA1/SSEA3/SSEA4, TRA1-60, and TRA1-81) markers of pluripotency.

(C) In vitro differentiation of four patient-derived lines to cells representative of all three germ layers: AFP, α -fetoprotein; β III-Tub, β -III-tubulin/Tuj1; SMA, smooth muscle actin.

(D) In vivo teratoma formation of *iAZF Δ bc*, *iAZF Δ c*, and *iAZF Δ a* lines showing evidence of all three germ layers. e, endoderm; ep, gut-like epithelium; m, mesoderm; sm, smooth muscle-like mesoderm; c, cartilage-like; ec, ectoderm; ne, neural ectoderm.

See also Figure S1 and Table S1.

cells in the mouse seminiferous tubule has not been explored. To verify that human germ cells could survive and engraft inside murine seminiferous tubules, we transplanted human fetal testicular cell suspensions (22 weeks old) into busulfan-treated testes of immunodeficient mice (Figure 3A). The use of busulfan treatment eliminates endogenous mouse germ cells from the seminiferous tubules (Figure 3B). Prior to transplantation, we observed that the 22-week-old human fetal testis contained a subset of cells positive for the germ-cell-specific protein VASA (Figure 3Ci). Using whole-mount staining analyses, we immunostained with a primate-specific antibody that is known to recognize all human donor cells only (regardless of germ cell fate) and, consistent with reports on adult testis transplants, observed single-donor cells, small chains (Figure 3Cii), or larger clusters of human donor cells on the basement membrane 2 months posttransplantation. In parallel, we also performed immunohistochemistry in cross-sections of testes transplanted with human fetal testis cells. In order to detect all human donor cells in recipient testes, we assessed expression of NuMA (Figure 3D), a well-characterized protein that exclusively labels human cells and tissues (Abad et al., 2007; Brüning-Richardson et al., 2012; Saadai et al., 2013). We observed significant human germ cell engraftment 8 weeks posttransplantation (Figure 3Ciii).

Xenotransplantation of hESCs and Human iPSCs to Seminiferous Tubules Directs Germ Cell Development

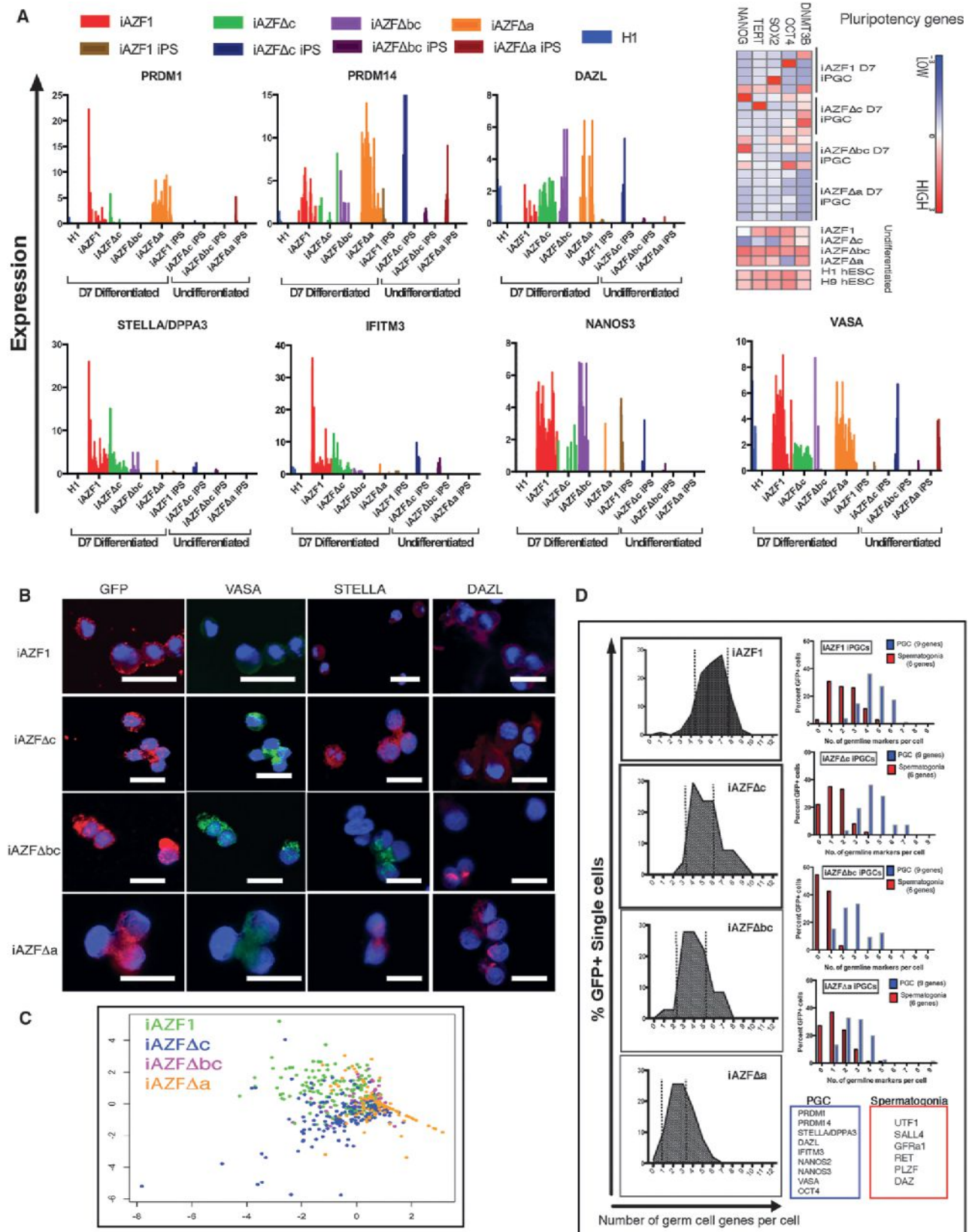
As noted above, we hypothesized that human iPSCs, which are distinct from mouse iPSCs (miPSCs), would survive, engraft, and be directed to a germ cell developmental fate if directly injected into the mouse seminiferous tubule, in response to instructive cues from the niche. Thus, we next transplanted undifferentiated male hESCs (H1) and the iAZF1 control iPSCs to eight recipient testes each and analyzed results by whole-mount immunohistochemistry as performed previously with human fetal testis transplants (Figure 3A). We observed that all donor-derived cells were detected either as single cells or in clusters of cells; no clear evidence of chain-like structures was observed (Figure S3B). We note that chain formation in human donor cells is a hallmark of spermatogonia but is not a property of PGCs and gonocytes (Nagano et al., 2002; Wu et al., 2009). Thus, we reasoned that engrafted cells might have differentiated to PGCLCs or gonocyte-like cells and tested systematically for the presence of germ-cell-specific proteins on NuMA+ surviving donor cells using serial immunohistochemical analysis across testis cross-sections. We observed that all transplantations, regardless of fertility status, resulted in two fates of donor undifferentiated iPSCs in the testes: (1) differentiation to GCLCs that were spatially located near or at the basement membrane of seminiferous tubules and (2) extensive proliferation of iPSCs distant from the basement membrane most often within the interstitial space. These proliferative cells resembled embryonal carcinoma (EC) and yolk sac tumors (YSTs).

Upon further analysis of H1 and iAZF1 xenotransplants, and as expected, we observed that a subset of tubules was occupied with NuMA+ donor cells (Figures S3C–S3I). In tubules containing donor cells, NuMA+ donor cells engrafted both near the basement membrane and in the center of the tubule. A significant number of NuMA+ cells coexpressed the germline protein,

VASA (henceforth referred to as NuMA+/VASA+ cells) (Figure 3E, white asterisks). We also observed that a few NuMA+ cells negative for VASA engrafted at the edges of seminiferous tubules (Figure 3E, red asterisk). To exclude the possibility that NuMA+ donor cells could differentiate to Sertoli cells, we costained for GATA4 and SOX9, two nuclear proteins expressed by mouse and human Sertoli cells (Figure S4). We did not observe the localization of SOX9 and GATA4 signals in nuclei of NuMA+ cells (Figures S4A and S4D), but only in cells that resemble human or mouse Sertoli cells at the edge of most tubules (Figures S4B, S4C, and S4E). Based on these results, we defined human GCLCs by the presence of NuMA+ cells that engrafted near the basement membrane of seminiferous tubules, colocalization of germ cell markers, especially VASA, and overall morphological resemblance to human fetal germ cells (Figure 3E). By comparison, staining of human fetal testis cross-sections revealed VASA+ germ cells near the tubule basement membrane (Figure 3Ci). Specifically, in testis xenografts, a large number of NuMA+/VASA+ cells localized to the basal membrane of the tubule either as single cells, rows or in clusters that bear clear resemblance to the arrangement of VASA+ germ cells of the human fetal testis (Figures 3E and 4A–4F).

Male Donor-Derived Cells Engrafted Outside Spermatogonial Tubules Remain Undifferentiated or Differentiate to Primitive Tumors

As noted above, in addition to cells that engrafted at the basement membrane, we observed that donor cells that filled the entire seminiferous tubule or exited the tubule proliferated extensively and did not demonstrate clear differentiation to either GCLCs or somatic cells. Instead, based on histology of xenografts, cells distant from the basement membrane, outside the tubules, resembled the histology of EC or, in some instances, YST cells (Figure S5A; Chaganti and Houldsworth, 2000; Nonaka, 2009). To verify, we stained xenografts for SOX2 and OCT4, protein markers diagnostic, at least in part, for EC formation and undifferentiated cells (Nonaka, 2009). We observed extensive SOX2 and OCT4 expression in NuMA+ nuclei in the interstitial space (Figure S5B). We reasoned that these cells likely resulted from leakage of donor hESCs and iPSCs from tubules into the interstitial spaces of the testis. Notably, donor cells in the interstitial spaces did not form teratomas as assessed by thorough histological analysis, suggesting that they did not receive the appropriate cues to differentiate to somatic lineages or that somatic cells are efficiently removed following differentiation. NuMA+ cells that filled the entire tubular space expressed OCT4 but did not appear to form GCLCs (VASA negative), suggesting that they remained undifferentiated (Figure S5C). We determined the efficiency of interstitial tumor formation across all testis xenografts performed and found that, except for human fetal testis transplantation, hESC and iPSC xenotransplants consistently produced interstitial tumors in more than half of all samples (Figure S5D). Curiously, iAZF1c iPSCs produced interstitial tumors only 30% of the time, but the tumors were always of EC or YST types. Altogether, these results suggested that the environment inside the seminiferous tubule is permissive for germ cell formation but appears to prevent differentiation of some donor cells to somatic lineages. In contrast, the



(legend on next page)

environment outside the tubules promotes somatic differentiation but not teratoma formation in donor cells that exited tubules.

Transplantation of iPSCs into Murine Seminiferous Tubules Reveals Differences in Germ Cell Differentiation between Control and *AZF*-Deleted Lines

We predicted that *AZF*-deleted iPSCs would form and/or maintain fewer GCLCs than *AZF*-intact iPSC lines. From our immunohistochemical analysis, we observed that transplanted human fetal testis cells, H1 hESCs, *iAZF1*, *iAZF2*, and *iAZFΔc* iPSCs were usually localized in NuMA+/VASA+ clusters containing at least three or more cells (Figures 3E and 4A–4D, arrows and white asterisks). In contrast, *iAZFΔbc* and *iAZFΔa* iPSCs gave rise to significantly fewer clusters of NuMA+/VASA+ cells (Figures 4E and 4F, arrows and white asterisks). To quantify this observation for each donor sample, we counted NuMA+/VASA+ cells and tubules across entire cross-sections (20× magnification) at three to four different depths of cross-sections and in at least four biological replicates per sample. Using this strategy, we extracted the average percentage of positive seminiferous tubules (Figure 4G). Although human fetal donor cells always produced the highest percentage of positive tubules (>30%), both *iAZF1* and *iAZF2* lines produced significantly higher tubule occupancy over *AZF*-deleted iPSCs (Figure 4G). We next determined the average number of NuMA+/VASA+ cells in each positively stained tubule (Figure 4H). We determined that, on average, >30 NuMA+/VASA+ cells per tubule were observed with human fetal donor cells and approximately 20–25 NuMA+/VASA+ cells per tubule with human *iAZF1* and *iAZF2* donor cells. These values were significantly higher than those observed in the case of *iAZFΔa*, *iAZFΔbc*, and *iAZFΔc* donor cells, where we observed four to eight NuMA+/VASA+ cells per tubule (Figure 4H). To determine the relative germ-cell-forming potential of each donor cell population, we multiplied the tubule occupancy (per 100 tubules) by NuMA+/VASA+ cells per tubule (Figure 4I). Our calculations reveal an approximate 50- to 100-fold reduction in formation of GCLCs from *AZF*-deleted iPSCs relative to *AZF*-intact iPSCs.

To further validate *in vivo* GCLC formation from donor cells, we examined expression of the germ-cell-specific proteins DAZL, PLZF, UTF1, STELLA, and DAZ in donor-derived GCLCs from xenotransplants (Figures 5 and S6). Based on previous reports, we predicted that STELLA, DAZL, and VASA would label iPSCs that had differentiated to PGCLCs, whereas UTF1, PLZF, and

DAZ proteins would label iPSCs that had entered the pool of gonocyte-like or prospermatogonia-like cells and would overlap with expression of VASA (Buaas et al., 2004; Anderson et al., 2007; Kristensen et al., 2008; Culty, 2009; Phillips et al., 2010; Wongtrakongate et al., 2013). Fetal testes at 22 weeks of gestation are expected to contain gonocytes and undifferentiated spermatogonia (Culty, 2009). Interestingly, fetal germ cells expressed DAZL, STELLA, and UTF1 simultaneously (Figure S6A). NuMA+/VASA+ cells derived from human fetal testis donor cells expressed the PGC proteins STELLA and DAZL in a similar nuclear and cytoplasmic pattern, respectively, to endogenous germ cells in the human fetal testis (Figure 5A, panel 1, and Figure S6A). Similarly, NuMA+/VASA+ cells derived from all *AZF*-intact and *AZF*-deleted donor lines expressed STELLA and DAZL proteins (Figures 5B–5F, panel 1). We further observed that expression of UTF1, PLZF, and DAZ proteins varied between donor cell lines dependent on genotype. In the control human fetal testis, UTF1, PLZF, and DAZ proteins were expressed in a few GCLCs in a subset of seminiferous tubules (Figure S6A). In a similar fashion to the fetal testis, UTF1 was localized in several DAZL+ donor-derived germ cells near the edges of tubules in all samples except *iAZFΔbc* and *iAZFΔa*, where we could not detect UTF1 signals (Figures 5A–5D, panel 2, and Figure S6). In addition, the prospermatogonial protein PLZF was detected in only a handful of VASA+ cells in *iAZF1* xenografts, but not in other samples (Figure 5C, panel 2). We further observed that none of the three *AZF*-deleted lines expressed the Y chromosome-encoded protein DAZ. In contrast, we detected cytoplasmic expression of DAZ proteins in NuMA+ cells of *AZF*-intact donor cells (H1, *iAZF1*, and *iAZF2*) and donor cells from the human fetal testis (Figures 5G and S6B). The pattern of DAZ expression closely corresponded to that of endogenous fetal germ cells in the human testis (Figure S6A). Collectively, results indicate that the human fetal testis donor cells and all patient-derived iPSCs are capable of forming PGCLCs but that, in general, *AZF*-deleted iPSCs form fewer GCLCs with altered expression of germ-cell-specific proteins (Figure 5H).

Epigenetic Analysis of Donor-Derived GCLCs from *AZF*-Intact iPSCs

In order to evaluate if epigenetic reprogramming, characteristic of endogenous germ cells, occurs in donor iPSC xenografts, we performed immunohistochemistry for 5-methylcytosine (5-mC)

Figure 2. Derivation and Characterization of iPSCs from *AZF*-Intact and *AZF*-Deleted iPSCs In Vitro

(A) Single-cell gene expression of VASA-GFP+ iPSCs derived from undifferentiated *AZF*-intact iPSCs (*iAZF1*), hESCs (H1), and *AZF*-deleted iPSCs (*iAZFΔc*, *iAZFΔbc*, and *iAZFΔa*). The relative expression of PGC genes *PRDM1*, *PRDM14*, *DAZL*, *STELLA* (*DPPA3*), *IFITM3*, *NANOS3*, and *VASA* was measured after normalization in all cells positive for *GFP* mRNA and plotted individually. Expression levels in undifferentiated single cells from each iPSC line are also shown in each graph. Each vertical bar represents 1 individual cell, and at least 25 cells are represented for differentiated samples and 20 cells for undifferentiated samples. See legend colors for sample identification. A heat index of pluripotency gene expression in five differentiated single cells and in undifferentiated iPSCs is shown (right). (B) Immunocytochemistry of GFP+ sorted cells for GFP and PGC proteins VASA, STELLA, and DAZL. Nuclei are counterstained with DAPI (blue). Scale bars represent 25 μm. (C) Two-component linear discrimination analysis of all single-cell RT-PCR measurements for 27 germ cell genes from all iPSC lines tested. Each single dot represents one single-cell measurement. (D) Percentage of GFP+ sorted single cells coexpressing 12 additional germ-cell-associated genes (see Table S3) as plotted by the number of markers within each individual cell. Dashed, vertical lines indicate the segment of the population of single cells from each line relative to the middle 70%–80% of control, *iAZF1* population. Coexpression of nine PGC (blue) and six gonocytic/spermatogonial genes (red) was quantified in GFP+ iPSCs and plotted by the number of respective markers within each cell.

See also Figure S2 and Tables S2 and S3.

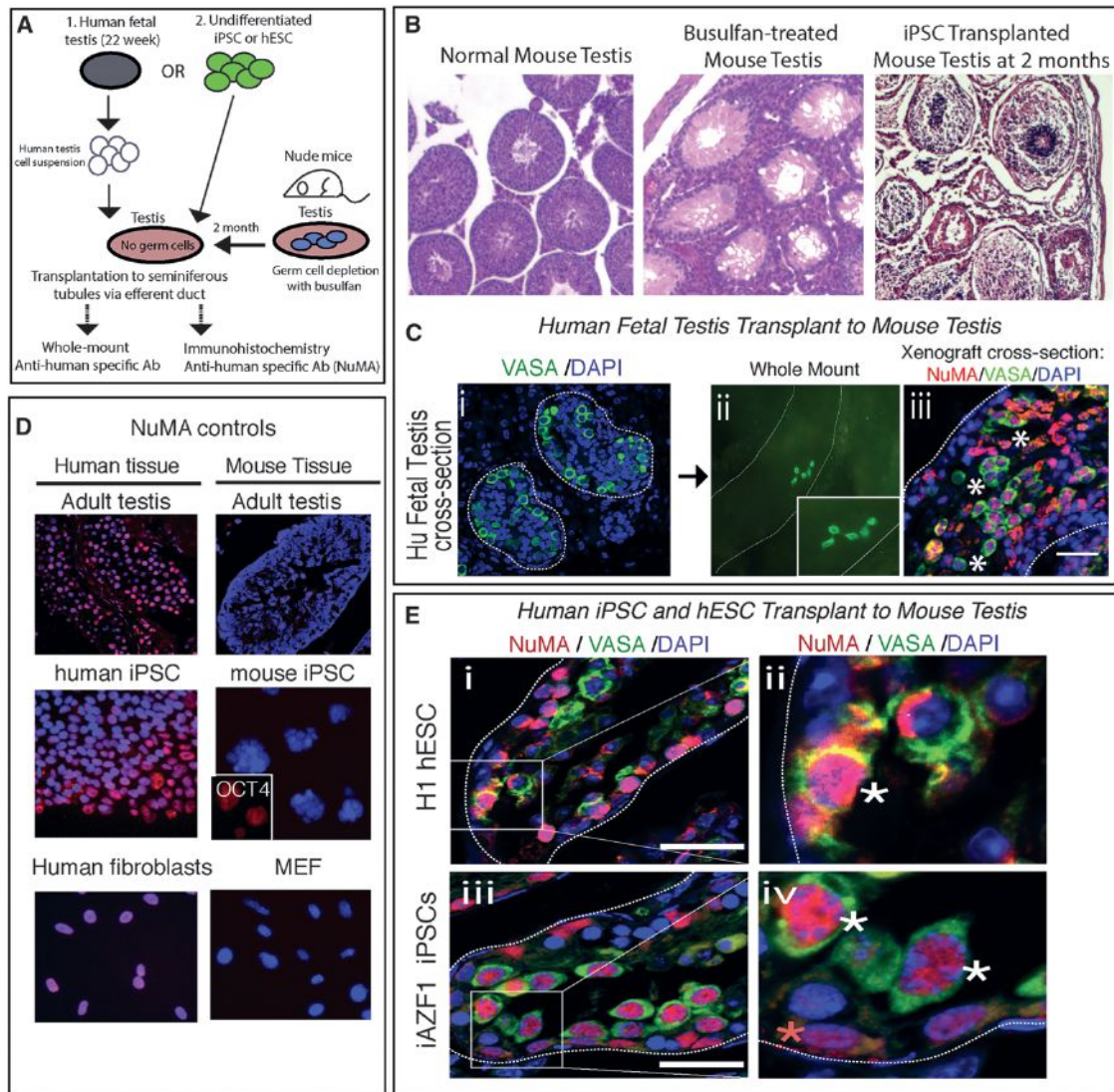


Figure 3. Survival and Germ Cell Differentiation of Fetal Germ Cells, hESCs, and iPSCs after Transplantation to Mouse Spermatogonial Tubules

(A) Transplantations were performed by independently injecting 22-week-old human fetal testicular cells, H1 hESCs, or human iPSCs directly into seminiferous tubules of busulfan-treated mouse testes (pink oval) that were depleted of endogenous germ cells. Testis xenografts were analyzed by (1) whole-mount histology using a human cell-specific antibody, or (2) immunohistochemistry using a human cell-specific antibody, NuMA, to detect donor cells.

(B) Hematoxylin and eosin histology of normal mouse recipient testes before busulfan treatment, after busulfan-mediated germ cell depletion, and 2 months posttransplantation of iPSCs.

(C) Human (Hu) fetal testis (22 weeks old) with cytoplasmic VASA expression (green) in germ cells (i). Nuclei are counterstained with DAPI. Human fetal testis was enzymatically dissociated, and fetal germ cells were transplanted and then detected after 2 months by (ii) whole-mount staining or (iii) cross-sectional immunohistochemistry for NuMA+/VASA+ cells (white asterisks).

(D) Human and mouse immunostaining controls for NuMA antibody specificity.

(E) Immunohistochemical analysis of testis xenografts derived from undifferentiated (i and ii) H1 hESC and (iii and iv) iAZF1 iPSCs. All images are merged from NuMA (red), VASA (green), and DAPI-stained nuclei. White rectangles indicate regions of interest of positive colocalization of NuMA and VASA and are magnified in (ii) and (iv). Red asterisks indicate NuMA+ donor cells adjacent to the basement membrane, whereas white asterisks represent NuMA+/VASA+ donor cells near the basement membrane.

In all panels, dashed white lines indicate the outer edges of spermatogonial tubules. Scale bars represent 50 μ m. See also Figure S3.

as a marker of global CpG methylation. We compared 5-mC status in endogenous germ cells of both human fetal and adult testes (Figures 6A and 6B) and in all recipient mouse testis xenografts (Figures 6C–6G). We observed that a majority of endogenous

VASA+ germ cells in fetal testes were 5-mC positive, with a subset of VASA+ cells 5-mC negative (Figure 6A, yellow arrowheads and white dotted circles, respectively). Intriguingly, NuMA+/VASA+ cells in all xenografts derived from human fetal testis

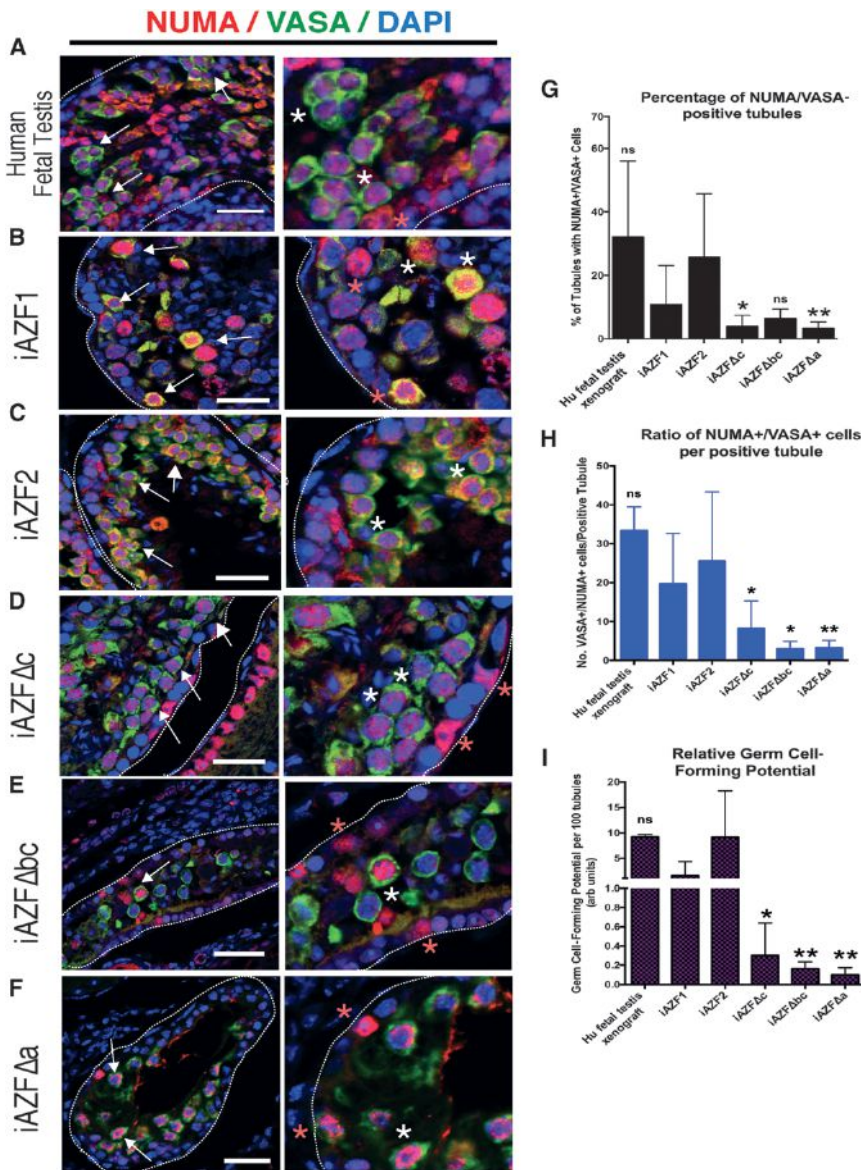


Figure 4. Differences in GCLC-Forming Potential between Patient-Derived iPSC Donor Cells in Mouse Spermatogonial Tubules

(A–F) Mouse testis xenografts were analyzed by immunohistochemistry using the human cell-specific antibody NuMA and an antibody recognizing the pan-germ cell marker VASA, marking PGCs, gonocytes, and spermatogonia. Cross-sections of testis xenografts derived from (A) 22-week-old human fetal testis cells, (B) iAZF1, (C) iAZF2, (D) iAZFΔc, (E) iAZFΔbc, and (F) iAZFΔa cell lines. All images are merged from NuMA (red), VASA (green), and DAPI-stained nuclei. Arrows indicate cells or clusters with positive colocalization of NuMA and VASA. Red asterisks indicate NuMA+ donor cells adjacent to the basement membrane, whereas white asterisks represent NuMA+ donor cells near the basement membrane. In all panels, dashed white lines indicate the outer edges of spermatogonial tubules. Scale bars represent 50 μm.

(G) Percentage of tubules positive for NuMA+/VASA+ cells was calculated across multiple cross-sections (relative to total number of tubules).

(H) For each positive tubule, the ratio of NuMA+/VASA+ cells per tubule was determined.

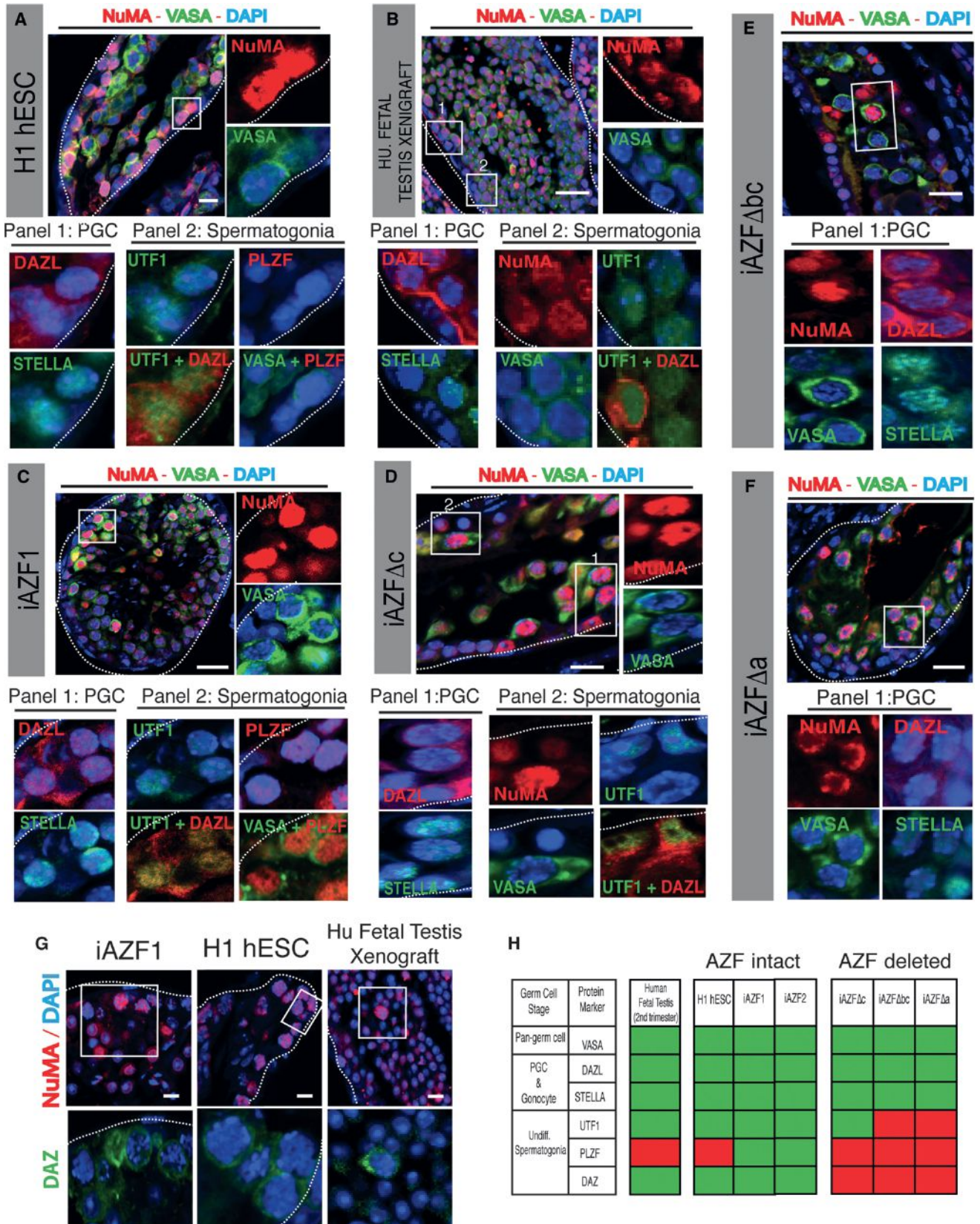
(I) Relative germ-cell-forming potential calculated by multiplying the fraction of positively stained tubules with the number of VASA/NuMA-cos-tained cells for each sample. Data are represented as mean ± SD of replicates. In each graph, significant differences in percentages/ratios between controls (iAZF1 or iAZF2) and AZF-deleted lines were determined by one-way ANOVA. *p < 0.05; **p < 0.001; ns, nonsignificant. See also Figure S3.

cells undergo global DNA demethylation upon initiation of germ cell differentiation inside the mouse seminiferous tubule.

DISCUSSION

A major emphasis in stem cell biology and regenerative medicine is focused on iPSC-derived cell transplantation to restore somatic cellular and tissue function (Wu and Hochedlinger, 2011; Takahashi and Yamanaka, 2013). Much less focus has been directed at the use of human iPSCs to derive germ cells for potential cell replacement therapies, despite elegant studies in the mouse that demonstrate the ability to completely reconstitute mouse germline development from ESCs and iPSCs (Hayashi et al., 2011, 2012; Grabole et al., 2013; Nakaki et al., 2013). Both mouse and human studies have demonstrated requirements for key germ-cell-specific genes and dependence of germ cell development on interaction with the niche (Nicholas et al., 2009; Hayashi et al., 2011; Kee et al., 2009; Panula et al., 2011; Easley et al., 2012; Medrano et al., 2012; Gkountela et al., 2013). Yet, there are difficulties in interpreting the human data given the low numbers of GCLCs formed in vitro, the extensive overlap of gene expression shared between ESCs and PGCs

donor cells or iPSC lines exhibited similar numbers of cells negative or positive for 5-mC (Figures 6C–6G, yellow arrowheads and white dotted circles, respectively). The 5-mC reduction was confined to germ cells within tubules (i.e., NuMA+ donor cells outside tubules were all 5-mC positive) (Figure 6H). Additionally, undifferentiated iPSC donor cells in culture exhibited uniform levels of 5-mC prior to transplantation (Figure 6H, bottom). In addition to immunohistochemical analysis, we quantified the pattern of 5-mC signals in NuMA+/VASA+ cells within tubules and observed a fairly uniform percentage (15%–20%) of 5-mC-negative cells in all xenografts, including those derived from human fetal testis donor cells. This observation mirrored the approximate 25% of endogenous fetal testis germ cells that were 5-mC negative (Figure 6I). Meanwhile, endogenous adult testis germ cells were highly methylated (only 3%–5% 5-mC negative). Collectively, our results suggest that human donor



(legend on next page)

such that fewer than a dozen genes may differ (Clark et al., 2004; Zwaka and Thomson, 2005; Johnson et al., 2008; Sabour et al., 2011), and the asynchrony in development of germ cells in vitro.

In this study, we observed that transplantation of normal and *AZF*-deleted iPSCs into the environment of the seminiferous tubule resulted in GCLC formation, whereas iPSCs outside the tubules failed to differentiate to GCLCs. Based on these results, we reason that iPSC and hESC donor cells inside seminiferous tubules may receive signals that permit them to engraft near the basement membrane. Our findings are supported by the observation that human spermatogonia transplanted to mouse testes “home” to the basement membrane but cannot differentiate to more mature stages (Nagano et al., 2002; Wu et al., 2009; Takashima et al., 2011). We suggest that cell-to-cell contacts between cells of the basement membrane niche, especially Sertoli cells, and donor cells enable exchange of instructive signals. Furthermore, we suggest that this crosstalk favors acquisition of a PGC- or gonocyte-like fate in human iPSCs with suppression of extensive proliferation and somatic cell differentiation (Resnick et al., 1992; Johnson et al., 2008; Kanatsu-Shinohara et al., 2012). In a similar fashion, undifferentiated murine spermatogonia self-renew or differentiate based on Sertoli cell density and factors secreted by Sertoli cells (Phillips et al., 2010; Oatley et al., 2011). These Sertoli cell-produced factors include paracrine growth factors such as transforming growth factor (TGF) and stem cell factor (SCF), which have been implicated in the survival and/or differentiation of PGCs (Mullaney and Skinner, 1991; Ewen and Koopman, 2010). In mice, the transition to epiblast stem cells and overexpression of *Prdm14* facilitates germ cell differentiation posttransplantation (Nakaki et al., 2013). In contrast, both undifferentiated hESCs and human iPSCs are believed to be “epiblast-like” and moreover express high levels of *PRDM14* endogenously as shown in this manuscript and other reports by Brons et al. (2007) and Tesar et al. (2007).

Our findings also bear some resemblance to reports in flies where the somatic cyst cells, which are immediately adjacent to germline stem cells, induce germline differentiation, whereas perturbation of the niche:germ cell environment leads to extensive proliferation resembling germ cell tumors (Karnis, 2012; Lim and Fuller, 2012). Based on our results and previously published studies, we posit that undifferentiated human iPSCs inside murine seminiferous tubules receive critical molecular cues from Sertoli cells and, potentially, from peri-tubular cells that assist in localization and physical interaction, accessibility to signaling cues, and ultimately direct germline differentiation. Moreover, if the niche is “overbooked” and iPSCs leak out of tubules or are

not able to contact Sertoli cells, we suggest that these cells will proliferate extensively to form EC outside the tubule or remain undifferentiated inside the tubule. Indeed, it is remarkable that in sharp contrast to studies with miPSCs, human iPSCs and hESCs never formed teratomas in our studies, perhaps due to their transient interaction with the intratubular environment.

Historically, it has not been possible to address when or how germ cells are depleted in men with spontaneous deletions; heterogeneity of clinical phenotypes associated with the same genetic deletions may be linked to depletion rate or time of presentation (Reijo et al., 1995, 1996). Moreover, it was not known whether *AZF* deletions might disrupt early germ cell development or maintenance. Here, we observed that iPSCs derived from men with *AZFa* and *AZFbc* deletions formed fewer and poor-quality PGCLCs both in vitro and in vivo. Regardless of genotype, however, we determined that human donor-derived GCLCs are induced to undergo global DNA demethylation from somatic methylation levels in a manner that is characteristic of the development of male PGCs to gonocytes (Wermann et al., 2010; Seisenberger et al., 2012). Importantly, our results indicate that there is a clear defect linked to expression of later genes such as *DAZ*, *PLZF*, and *UTF1* that coexpress with or follow expression of PGC markers (Culty, 2009); in particular, those with *AZF* deletions did not express Y chromosome *DAZ* and the genes *UTF1* and *PLZF* in any germ cells. Thus, our results of germ cell differentiation are well correlated with clinical outcomes but also provide some interesting insights. However, iPSCs formed PGCLCs, suggesting that men with these deletions likely form germ cells early in development but that these cells are depleted prior to clinical presentation. This concept is consistent with many mouse models of infertility in which initial populations of germ cells are not maintained (Modi et al., 2003; Rucker et al., 2000). Indeed, in mice, both XX and XY embryos form PGCs, which migrate to the gonad and begin differentiation to sperm or oocytes, independent of germ cell sex chromosome composition, depending on the sexual identity of the gonad proper (Gill et al., 2011). Human genetic data similarly indicate that the XO genotype (Turner syndrome) is compatible with formation of fetal germ cells, but they are depleted by birth or thereafter (Modi et al., 2003; Karnis, 2012).

Our results have been summarized into a working model for the efficiency and fate of human iPSCs during human germ cell formation in the mouse testes (Figure 7). Further studies should refine existing methods by performing transplantations with varying cell numbers, examining genetic complementation and hierarchy, and altering the xenotransplant recipient to a

Figure 5. Donor-Derived GCLCs from H1, Human Fetal Testis, and *iAZF1* Exhibit Multiple Markers of PGCs and Undifferentiated Spermatogonia, whereas *AZF*-Deleted Donor Cells Only Express PGC Markers

(A–F) Mouse testis xenografts derived from (A) H1 hESCs, (B) 22-week-old human fetal testicular cells, (C) *iAZF1*, and (D–F) *AZF*-deleted human iPSCs were stained in adjacent, serial cross-sections for the PGC markers *DAZL* and *STELLA* and for the gonocyte/spermatogonial markers *UTF1*, *PLZF*, and *DAZ* in NuMA+*VASA*+ regions. For each xenograft, low-magnification regions of the seminiferous tubule containing NuMA+*VASA*+ cells are shown, and boxed regions of interest are enlarged and shown to the right. In NuMA+*VASA*+ donor cells, immunostaining for germ cell proteins is shown as follows: Panel 1, positive immunostaining for *DAZL* (red) and *STELLA* (green); and Panel 2, *UTF1* (green), *UTF1*+*DAZL*, *PLZF* (green), or *PLZF*+*VASA*.

(G) Mouse testis xenografts derived from H1 hESCs, *iAZF1*, and human fetal testicular cells showing NuMA+ cells that coexpressed *DAZ* in boxed regions and enlarged in lower panels. In all panels, dashed white lines always indicate the outer edges of spermatogonial tubules. Wherever shown, nuclei are counterstained with DAPI (blue). Scale bar represents 50 μ m.

(H) Summary of positive (green) and negative (red) germ cell protein expression across all xenografts tested.

See also Figure S4.

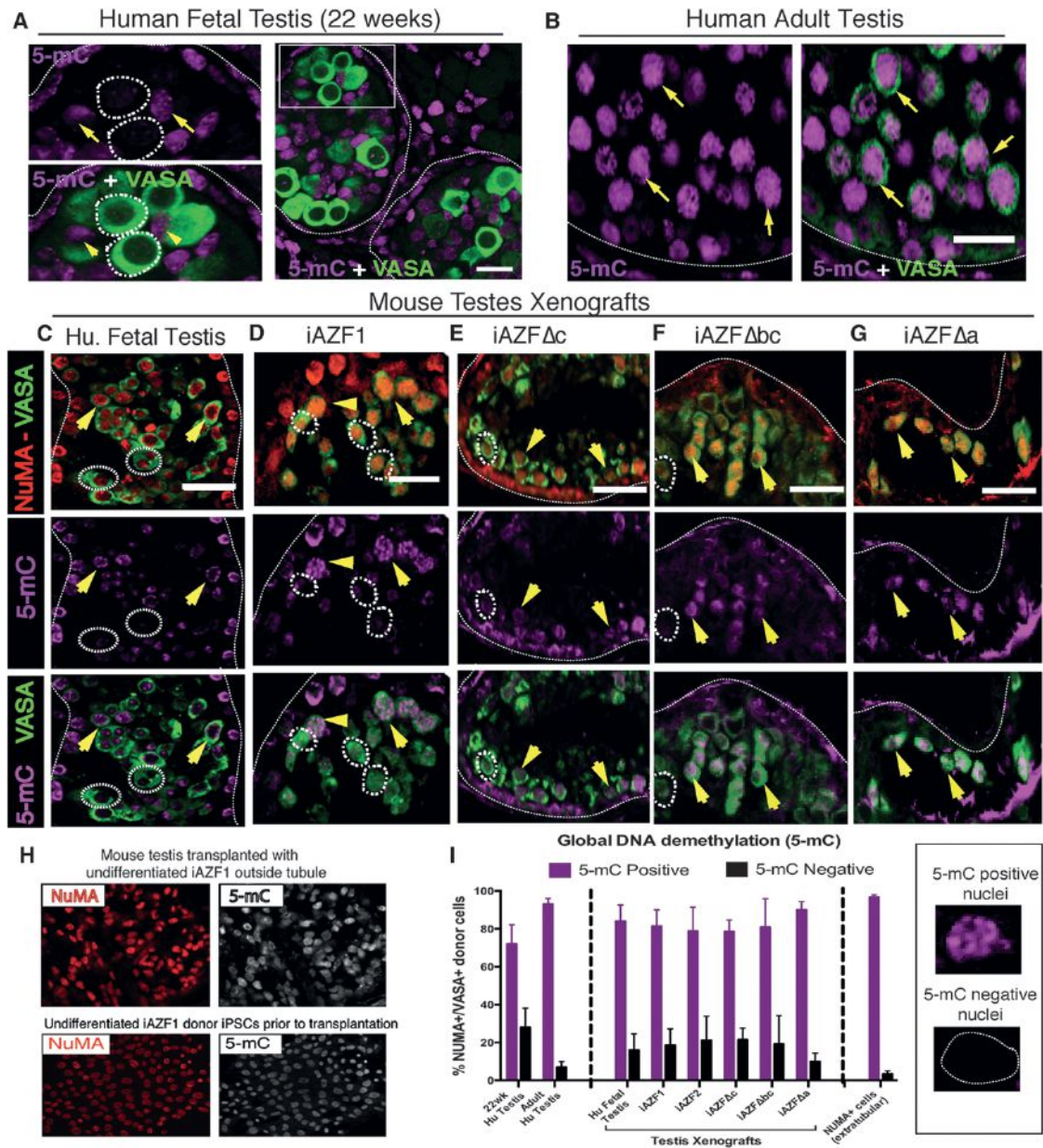


Figure 6. Global DNA Methylation Properties of Xenotransplanted iPSCs

Human fetal (22 weeks) testis (A), human adult testes (B), and mouse testis (C–G) xenografts derived from human fetal testicular cells and iPSCs were stained for VASA and 5-mC in NuMA+ regions.

(A) Cross-section of a human fetal testis (22 weeks) with positive immunostaining for 5-mC alone or VASA and 5-mC together. Enlarged panels on the left represent the region enclosed within the white rectangle of the right panel.

(B) Cross-section of a human adult testis with positive immunostaining for 5-mC alone or VASA and 5-mC together.

(C–G) Cross-sections of mouse testes transplanted with 22-week-old human fetal testicular cells (C) and undifferentiated iPSC donor cells from each line (D–G). For each xenografted line, immunostaining for NuMA+/VASA+ cells (top), 5-mC alone (middle), and 5-mC together with VASA (bottom) is shown. White dotted circles indicate NuMA+/VASA+ cells with complete loss of 5-mC signal; yellow arrowheads indicate NuMA+/VASA+ positive cells with positive 5-mC signals.

(H) Positive 5-mC signals in NuMA+ cells outside tubules (top) and in undifferentiated iPSCs prior to transplantation (bottom).

(I) Quantification of 5-mC positive and negative signals in human testes (left columns) and in NuMA+/VASA+ cells of testis xenografts (middle columns). 5-mC patterns in extratubular NuMA+ cells are shown (right column).

In all panels, dotted lines indicate edges of spermatogonial tubules. Scale bars represent 50 μ m. See also Figure S6.

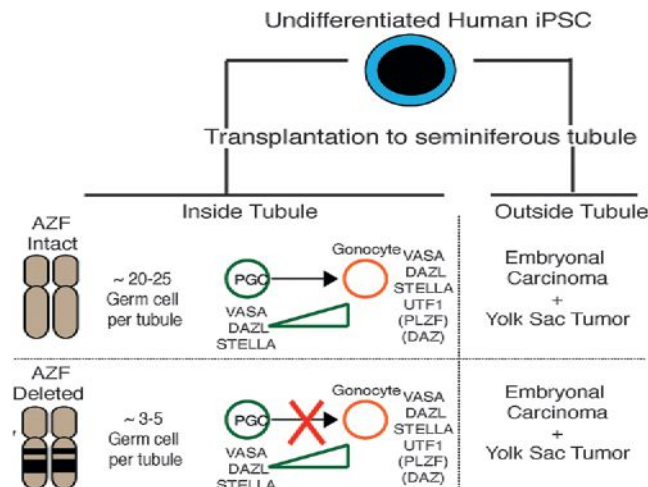


Figure 7. Schematic Illustration of Major Findings of This Study

iPSCs were derived from patients with AZF-intact and AZF-deleted Y chromosomes using the *OCT4*, *SOX2*, *KLF4*, and *CMYC* cocktail (OSKM). When transplanted, undifferentiated male iPSCs specifically differentiate to PGC-like and gonocyte-like germ cells inside the mouse spermatogonial tubule environment, presumably in the Sertoli cell niche. However, outside the tubule, all patient-derived iPSCs and hESCs remain undifferentiated as primitive tumors. AZF-deleted iPSCs appear to have a lower potential to make germ cells in vivo as compared to AZF-intact iPSCs and appear to be restricted to forming PGCLCs. See also Figure S5.

nonhuman primate in order to promote full reconstitution of spermatogenesis and overcome innate barriers in xenotransplantation of human cells to the mouse.

EXPERIMENTAL PROCEDURES

Derivation and Culture of iPSC Lines from Primary Human Skin Cells

The human skin-derived primary cell lines (*AZF1*, *AZF2*, *AZFΔa*, *AZFΔbc*, and *AZFΔc*) used in this study were obtained from a 4 mm adult skin punch biopsy and cultured as described by Byrne et al. (2009). *AZF2* iPSCs were derived from normal human fetal foreskin fibroblasts (Stemgent) as previously described (Durruthy Durruthy et al., 2014). Fibroblasts were allowed to expand to 80%–90% confluency before passaging and cryopreservation. Deletion mapping analysis of all patient-derived fibroblasts was determined by sequence-tagged site (STS) PCR analysis with the Y Chromosome Deletion Analysis Kit (Promega) according to manufacturer's instructions. Dermal fibroblasts were infected with a polycistronic lentiviral-reprogramming vector as previously described for reprogramming by Sommer et al. (2010) and Sebastian et al. (2011). Briefly, 10^5 fibroblasts were seeded in mouse embryonic fibroblast (MEF) medium and infected. After 6 days, cells were transferred onto inactivated MEFs. After replacement with hESC medium, the cells were grown for up to 8 weeks until hESC-like colonies started to emerge. iPSC colonies were manually picked, expanded on MEFs, and after approximately 15–20 passages, transferred to feeder-free culture conditions in mTeSR1 medium (STEMCELL Technologies).

Transduction, Differentiation, and FACS of iPSCs and hESCs with VASA:GFP Reporter Lentivirus

Undifferentiated iPSCs and hESCs were transduced, selected, and differentiated on Matrigel-coated plates with a VASA:GFP lentivirus as previously described by Kee et al. (2009) and Medrano et al. (2012). As controls, transduced cells and nontransduced cells were also used in all differentiation experiments. Differentiation medium was supplemented

with 50 ng/ml bone morphogenetic proteins 4 and 8 (BMP4 and BMP8, respectively), 10 nM retinoic acid (RA), and 2 ng/ml human recombinant leukemia inhibitory factor (hLIF) and changed every 3.5 days. Cells were sorted for GFP+ and GFP- populations on a Becton Dickinson FACSarias II instrument.

Xenotransplantation Assay

Human cell lines were transplanted into the testes of busulfan-treated, immune-deficient nude mice (NCr nu/nu; Taconic) as previously described for primate and human spermatogonia by Hermann et al. (2010). Briefly, immunodeficient nude mice were treated with a single dose of busulfan (40 mg/kg; Sigma-Aldrich) at 6 weeks of age to eliminate endogenous spermatogenesis. Xenotransplantation was then performed 5 weeks after busulfan treatment by injecting 7–8 μ l cell suspensions containing 10% trypan blue (Invitrogen) into the seminiferous tubules of each recipient testes via cannulation of the efferent ducts. At 8 weeks after transplantation, recipient mouse testes were harvested for histology and immunohistochemical analyses.

Immunohistochemistry

Formalin-fixed human testes or mouse testes xenotransplants were paraffin embedded and sectioned into serial cross-sections of 5–10 μ m thickness each (AML Laboratories). Testis sections were deparaffinized in xylene, rehydrated through an ethanol-graded series. For all samples, antigen retrieval was performed by boiling the sections in 0.01 M sodium citrate buffer (pH 6.0) for 20 min, followed by incubation at room temperature for 30 min. For DNA methylation analysis, sections were incubated in 4 N HCl for 20 min prior to blocking. A 10% solution of normal donkey serum (Jackson ImmunoResearch) in PBS was used as a blocking buffer. Sections were incubated with the following primary antibodies diluted in blocking solution (1.0% Normal Donkey Serum, 0.1% Triton X-100, and sterile PBS) overnight at 4°C: VASA (1:200) and GFR α 1 (1:250) (R&D Systems); NuMA (1:200), STELLA (1:200), DAZL (1:250) (Abcam); UTF1 (1:200; Millipore); PLZF (1:250; Chemicon); OCT4 (1:500), SOX2 (1:500), and GATA4 (1:250) (Santa Cruz Biotechnology); SOX9 (1:250; Sigma Aldrich); 5-mC (1:1500; Eurogentec); and 5-hmC (1:1500; Active Motif). The sections were washed and labeled with Alexa dye-conjugated secondary antibodies. Sections were mounted in ProLong Gold Antifade mounting media containing DAPI (Life Technologies). Negative controls included incubation with rabbit immunoglobulin G antibodies and omission of the primary antibody for all samples. Quantification of sections for NuMA/VASA double staining was determined manually from three to five independent 20 \times fields taken from three different testis tissue depths and from at least three separate biological replicates. Quantification of positive and negative 5-mC signals was determined by counting at least 150 NuMA+/VASA+ cells inside seminiferous tubules across five 20 \times fields of view from two independent biological replicates. For human testis cross-sections, 5-mC patterns were quantified in only VASA+ cells inside tubules. Data for statistical analysis follow a normal distribution.

SUPPLEMENTAL INFORMATION

Supplemental Information includes Supplemental Experimental Procedures, six figures, and three tables and can be found with this article online at <http://dx.doi.org/10.1016/j.celrep.2014.03.067>.

AUTHOR CONTRIBUTIONS

C.R. performed the majority of experiments and wrote the first draft of the manuscript with assistance from J.D.-D. for transplantation analysis and single-cell gene expression analysis. J.E.A. derived and characterized iPSCs, and M.S. helped with differentiation experiments and performed transplantations. P.J.T. coordinated patient recruitment and consents. R.A.R.P. initiated the research project and provided oversight. K.E.O. and R.A.R.P. assisted with planning and execution of transplantation experiments. C.R. and R.A.R.P. wrote the manuscript with valuable insights provided by other coauthors.

ACKNOWLEDGMENTS

The authors thank members of the R.A.R.P. laboratory for helpful support, advice, and suggestions. The authors are grateful to J.V. Medrano, P. Schanes, H. Steyer, and V. Sebastiano for assistance with technical aspects of the project. Funding for this project was obtained from the National Institutes of Health (NHLBI #U01HL100397) and as part of the Specialized Cooperative Centers Program in Reproduction and Infertility Research and National Institute for Child Health Development through grant #U54 HD068158.

Received: November 8, 2013

Revised: February 27, 2014

Accepted: March 27, 2014

Published: May 1, 2014

REFERENCES

- Abad, P.C., Lewis, J., Mian, I.S., Knowles, D.W., Sturgis, J., Badve, S., Xie, J., and Lelièvre, S.A. (2007). NuMA influences higher order chromatin organization in human mammary epithelium. *Mol. Biol. Cell* **18**, 348–361.
- Anderson, R.A., Fulton, N., Cowan, G., Coutts, S., and Saunders, P.T. (2007). Conserved and divergent patterns of expression of DAZL, VASA and OCT4 in the germ cells of the human fetal ovary and testis. *BMC Dev. Biol.* **7**, 136.
- Brons, I.G., Smithers, L.E., Trotter, M.W., Rugg-Gunn, P., Sun, B., Chuva de Sousa Lopes, S.M., Howlett, S.K., Clarkson, A., Ahrlund-Richter, L., Pedersen, R.A., and Vallier, L. (2007). Derivation of pluripotent epiblast stem cells from mammalian embryos. *Nature* **448**, 191–195.
- Brüning-Richardson, A., Bond, J., Alsiary, R., Richardson, J., Cairns, D.A., McCormac, L., Hutson, R., Burns, P.A., Wilkinson, N., Hall, G.D., et al. (2012). NuMA overexpression in epithelial ovarian cancer. *PLoS ONE* **7**, e38945.
- Buaas, F.W., Kirsh, A.L., Sharma, M., McLean, D.J., Morris, J.L., Griswold, M.D., de Rooij, D.G., and Braun, R.E. (2004). Plzf is required in adult male germ cells for stem cell self-renewal. *Nat. Genet.* **36**, 647–652.
- Byrne, J.A., Nguyen, H.N., and Reijo Pera, R.A. (2009). Enhanced generation of induced pluripotent stem cells from a subpopulation of human fibroblasts. *PLoS ONE* **4**, e7118.
- Chaganti, R.S., and Houldsworth, J. (2000). Genetics and biology of adult human male germ cell tumors. *Cancer Res.* **60**, 1475–1482.
- Chia, N.Y., Chan, Y.S., Feng, B., Lu, X., Orlov, Y.L., Moreau, D., Kumar, P., Yang, L., Jiang, J., Lau, M.S., et al. (2010). A genome-wide RNAi screen reveals determinants of human embryonic stem cell identity. *Nature* **468**, 316–320.
- Clark, A.T., Bodnar, M.S., Fox, M., Rodriguez, R.T., Abeyta, M.J., Firpo, M.T., and Pera, R.A. (2004). Spontaneous differentiation of germ cells from human embryonic stem cells in vitro. *Hum. Mol. Genet.* **13**, 727–739.
- Culty, M. (2009). Gonocytes, the forgotten cells of the germ cell lineage. *Birth Defects Res. C Embryo Today* **87**, 1–26.
- Dovey, S.L., Valli, H., Hermann, B.P., Sukhwani, M., Donohue, J., Castro, C.A., Chu, T., Sanfilippo, J.S., and Orwig, K.E. (2013). Eliminating malignant contamination from the therapeutic human spermatogonial stem cells. *J. Clin. Invest.* **123**, 1833–1843.
- Durruthy Durruthy, J., Ramathal, C., Sukhwani, M., Fang, F., Cui, J., Orwig, K.E., and Reijo Pera, R.A. (2014). Fate of induced pluripotent stem cells following transplantation to murine seminiferous tubules. *Hum. Mol. Genet.* <http://dx.doi.org/10.1093/hmg/ddu012>
- Easley, C.A., 4th, Phillips, B.T., McGuire, M.M., Barringer, J.M., Valli, H., Hermann, B.P., Simerly, C.R., Rajkovic, A., Miki, T., Orwig, K.E., and Schatten, G.P. (2012). Direct differentiation of human pluripotent stem cells into haploid spermatogenic cells. *Cell Rep* **2**, 440–446.
- Ewen, K.A., and Koopman, P. (2010). Mouse germ cell development: from specification to sex determination. *Mol. Cell. Endocrinol.* **323**, 76–93.
- Ferlin, A., Moro, E., Rossi, A., Dallapiccola, B., and Foresta, C. (2003). The human Y chromosome's azoospermia factor b (AZFb) region: sequence, structure, and deletion analysis in infertile men. *J. Med. Genet.* **40**, 18–24.
- Foresta, C., Moro, E., Rossi, A., Rossato, M., Garolla, A., and Ferlin, A. (2000). Role of the AZFa candidate genes in male infertility. *J. Endocrinol. Invest.* **23**, 646–651.
- Gill, M.E., Hu, Y.C., Lin, Y., and Page, D.C. (2011). Licensing of gametogenesis, dependent on RNA binding protein DAZL, as a gateway to sexual differentiation of fetal germ cells. *Proc. Natl. Acad. Sci. USA* **108**, 7443–7448.
- Gkoutela, S., Li, Z., Vincent, J.J., Zhang, K.X., Chen, A., Pellegrini, M., and Clark, A.T. (2013). The ontogeny of cKIT+ human primordial germ cells proves to be a resource for human germ line reprogramming, imprint erasure and in vitro differentiation. *Nat. Cell Biol.* **15**, 113–122.
- Grabole, N., Tischler, J., Hackett, J.A., Kim, S., Tang, F., Leitch, H.G., Magnúsdóttir, E., and Surani, M.A. (2013). Prdm14 promotes germline fate and naive pluripotency by repressing FGF signalling and DNA methylation. *EMBO Rep.* **14**, 629–637.
- Hanna, J., Wernig, M., Markoulaki, S., Sun, C.W., Meissner, A., Cassady, J.P., Beard, C., Brambrink, T., Wu, L.C., Townes, T.M., and Jaenisch, R. (2007). Treatment of sickle cell anemia mouse model with iPS cells generated from autologous skin. *Science* **318**, 1920–1923.
- Hayashi, K., and Surani, M.A. (2009). Self-renewing epiblast stem cells exhibit continual delineation of germ cells with epigenetic reprogramming in vitro. *Development* **136**, 3549–3556.
- Hayashi, K., Ohta, H., Kurimoto, K., Aramaki, S., and Saitou, M. (2011). Reconstitution of the mouse germ cell specification pathway in culture by pluripotent stem cells. *Cell* **146**, 519–532.
- Hayashi, K., Ogushi, S., Kurimoto, K., Shimamoto, S., Ohta, H., and Saitou, M. (2012). Offspring from oocytes derived from in vitro primordial germ cell-like cells in mice. *Science* **338**, 971–975.
- Hermann, B.P., Sukhwani, M., Hansel, M.C., and Orwig, K.E. (2010). Spermatogonial stem cells in higher primates: are there differences from those in rodents? *Reproduction* **139**, 479–493.
- Hopps, C.V., Mielnik, A., Goldstein, M., Palermo, G.D., Rosenwaks, Z., and Schlegel, P.N. (2003). Detection of sperm in men with Y chromosome microdeletions of the AZFa, AZFb and AZFc regions. *Hum. Reprod.* **18**, 1660–1665.
- Johnson, L., Thompson, D.L., Jr., and Varner, D.D. (2008). Role of Sertoli cell number and function on regulation of spermatogenesis. *Anim. Reprod. Sci.* **105**, 23–51.
- Kanatsu-Shinohara, M., Inoue, K., Takashima, S., Takehashi, M., Ogonuki, N., Morimoto, H., Nagasawa, T., Ogura, A., and Shinohara, T. (2012). Reconstitution of mouse spermatogonial stem cell niches in culture. *Cell Stem Cell* **11**, 567–578.
- Karnis, M.F. (2012). Fertility, pregnancy, and medical management of Turner syndrome in the reproductive years. *Fertil. Steril.* **98**, 787–791.
- Kee, K., Gonsalves, J.M., Clark, A.T., and Pera, R.A. (2006). Bone morphogenetic proteins induce germ cell differentiation from human embryonic stem cells. *Stem Cells Dev.* **15**, 831–837.
- Kee, K., Angeles, V.T., Flores, M., Nguyen, H.N., and Reijo Pera, R.A. (2009). Human DAZL, DAZ and BOULE genes modulate primordial germ-cell and haploid gamete formation. *Nature* **462**, 222–225.
- Kristensen, D.M., Nielsen, J.E., Skakkebaek, N.E., Graem, N., Jacobsen, G.K., Rajpert-De Meyts, E., and Leffers, H. (2008). Presumed pluripotency markers UTF-1 and REX-1 are expressed in human adult testes and germ cell neoplasms. *Hum. Reprod.* **23**, 775–782.
- Kuroda-Kawaguchi, T., Skaletsky, H., Brown, L.G., Minx, P.J., Cordum, H.S., Waterston, R.H., Wilson, R.K., Silber, S., Oates, R., Rozen, S., and Page, D.C. (2001). The AZFc region of the Y chromosome features massive palindromes and uniform recurrent deletions in infertile men. *Nat. Genet.* **29**, 279–286.
- Lim, J.G., and Fuller, M.T. (2012). Somatic cell lineage is required for differentiation and not maintenance of germline stem cells in *Drosophila* testes. *Proc. Natl. Acad. Sci. USA* **109**, 18477–18481.

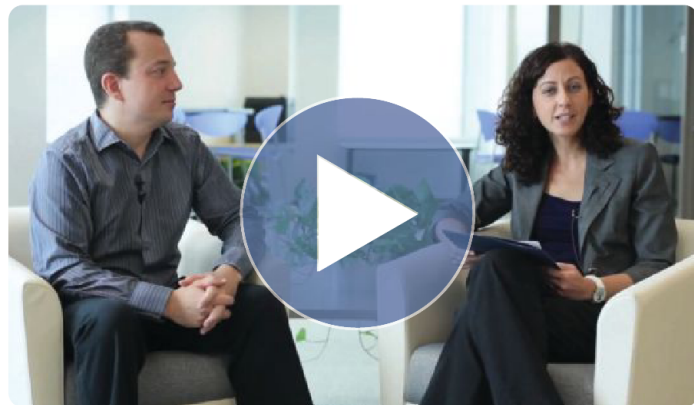
- Magnúsdóttir, E., Dietmann, S., Murakami, K., Günesdogan, U., Tang, F., Bao, S., Diamanti, E., Lao, K., Gottgens, B., and Azim Surani, M. (2013). A tripartite transcription factor network regulates primordial germ cell specification in mice. *Nat. Cell Biol.* **15**, 905–915.
- Medrano, J.V., Ramathal, C., Nguyen, H.N., Simon, C., and Reijo Pera, R.A. (2012). Divergent RNA-binding proteins, DAZL and VASA, induce meiotic progression in human germ cells derived in vitro. *Stem Cells* **30**, 441–451.
- Modi, D.N., Sane, S., and Bhartiya, D. (2003). Accelerated germ cell apoptosis in sex chromosome aneuploid fetal human gonads. *Mol. Hum. Reprod.* **9**, 219–225.
- Mullaney, B.P., and Skinner, M.K. (1991). Growth factors as mediators of testicular cell-cell interactions. *Baillieres Clin. Endocrinol. Metab.* **5**, 771–790.
- Nagano, M., Patrizio, P., and Brinster, R.L. (2002). Long-term survival of human spermatogonial stem cells in mouse testes. *Fertil. Steril.* **78**, 1225–1233.
- Nakaki, F., Hayashi, K., Ohta, H., Kurimoto, K., Yabuta, Y., and Saitou, M. (2013). Induction of mouse germ-cell fate by transcription factors in vitro. *Nature* **501**, 222–226.
- Navarro-Costa, P., Gonçalves, J., and Plancha, C.E. (2010). The AZFc region of the Y chromosome: at the crossroads between genetic diversity and male infertility. *Hum. Reprod. Update* **16**, 525–542.
- Nelson, T.J., Martinez-Fernandez, A., Yamada, S., Perez-Terzic, C., Ikeda, Y., and Terzic, A. (2009). Repair of acute myocardial infarction by human stemness factors induced pluripotent stem cells. *Circulation* **120**, 408–416.
- Nicholas, C.R., Haston, K.M., Grewall, A.K., Longacre, T.A., and Reijo Pera, R.A. (2009). Transplantation directs oocyte maturation from embryonic stem cells and provides a therapeutic strategy for female infertility. *Hum. Mol. Genet.* **18**, 4376–4389.
- Nonaka, D. (2009). Differential expression of SOX2 and SOX17 in testicular germ cell tumors. *Am. J. Clin. Pathol.* **131**, 731–736.
- Oatley, M.J., Racicot, K.E., and Oatley, J.M. (2011). Sertoli cells dictate spermatogonial stem cell niches in the mouse testis. *Biol. Reprod.* **84**, 639–645.
- Panula, S., Medrano, J.V., Kee, K., Bergström, R., Nguyen, H.N., Byers, B., Wilson, K.D., Wu, J.C., Simon, C., Hovatta, O., and Reijo Pera, R.A. (2011). Human germ cell differentiation from fetal- and adult-derived induced pluripotent stem cells. *Hum. Mol. Genet.* **20**, 752–762.
- Park, T.S., Galic, Z., Conway, A.E., Lindgren, A., van Handel, B.J., Magnusson, M., Richter, L., Teitell, M.A., Mikkola, H.K., Lowry, W.E., et al. (2009). Derivation of primordial germ cells from human embryonic and induced pluripotent stem cells is significantly improved by coculture with human fetal gonadal cells. *Stem Cells* **27**, 783–795.
- Phillips, B.T., Gassei, K., and Orwig, K.E. (2010). Spermatogonial stem cell regulation and spermatogenesis. *Philos. Trans. R. Soc. Lond. B Biol. Sci.* **365**, 1663–1678.
- Reijo, R., Lee, T.Y., Salo, P., Alagappan, R., Brown, L.G., Rosenberg, M., Rozen, S., Jaffe, T., Straus, D., Hovatta, O., et al. (1995). Diverse spermatogenic defects in humans caused by Y chromosome deletions encompassing a novel RNA-binding protein gene. *Nat. Genet.* **10**, 383–393.
- Reijo, R., Alagappan, R.K., Patrizio, P., and Page, D.C. (1996). Severe oligozoospermia resulting from deletions of azoospermia factor gene on Y chromosome. *Lancet* **347**, 1290–1293.
- Resnick, J.L., Bixler, L.S., Cheng, L., and Donovan, P.J. (1992). Long-term proliferation of mouse primordial germ cells in culture. *Nature* **359**, 550–551.
- Rucker, E.B., 3rd, Dierisseau, P., Wagner, K.U., Garrett, L., Wynshaw-Boris, A., Flaws, J.A., and Hennighausen, L. (2000). Bcl-x and Bax regulate mouse primordial germ cell survival and apoptosis during embryogenesis. *Mol. Endocrinol.* **14**, 1038–1052.
- Saadai, P., Wang, A., Nout, Y.S., Downing, T.L., Lofberg, K., Beattie, M.S., Bresnahan, J.C., Li, S., and Farmer, D.L. (2013). Human induced pluripotent stem cell-derived neural crest stem cells integrate into the injured spinal cord in the fetal lamb model of myelomeningocele. *J. Pediatr. Surg.* **48**, 158–163.
- Sabour, D., Araúzo-Bravo, M.J., Hübner, K., Ko, K., Greber, B., Gentile, L., Stehling, M., and Schöler, H.R. (2011). Identification of genes specific to mouse primordial germ cells through dynamic global gene expression. *Hum. Mol. Genet.* **20**, 115–125.
- Sebastiano, V., Maeder, M.L., Angstman, J.F., Haddad, B., Khayter, C., Yeo, D.T., Goodwin, M.J., Hawkins, J.S., Ramirez, C.L., Batista, L.F., et al. (2011). In situ genetic correction of the sickle cell anemia mutation in human induced pluripotent stem cells using engineered zinc finger nucleases. *Stem Cells* **29**, 1717–1726.
- Seisenberger, S., Andrews, S., Krueger, F., Arand, J., Walter, J., Santos, F., Popp, C., Thienpont, B., Dean, W., and Reik, W. (2012). The dynamics of genome-wide DNA methylation reprogramming in mouse primordial germ cells. *Mol. Cell* **48**, 849–862.
- Skakkebaek, N.E., Giwercman, A., and de Kretser, D. (1994). Pathogenesis and management of male infertility. *Lancet* **343**, 1473–1479.
- Sommer, C.A., Sommer, A.G., Longmire, T.A., Christodoulou, C., Thomas, D.D., Gostissa, M., Alt, F.W., Murphy, G.J., Kotton, D.N., and Mostoslavsky, G. (2010). Excision of reprogramming transgenes improves the differentiation potential of iPS cells generated with a single excisable vector. *Stem Cells* **28**, 64–74.
- Takahashi, K., and Yamanaka, S. (2013). Induced pluripotent stem cells in medicine and biology. *Development* **140**, 2457–2461.
- Takashima, S., Kanatsu-Shinohara, M., Tanaka, T., Takehashi, M., Morimoto, H., and Shinohara, T. (2011). Rac mediates mouse spermatogonial stem cell homing to germline niches by regulating transmigration through the blood-testis barrier. *Cell Stem Cell* **9**, 463–475.
- Tesar, P.J., Chenoweth, J.G., Brook, F.A., Davies, T.J., Evans, E.P., Mack, D.L., Gardner, R.L., and McKay, R.D. (2007). New cell lines from mouse epiblast share defining features with human embryonic stem cells. *Nature* **448**, 196–199.
- Vogt, P.H., Edelmann, A., Kirsch, S., Henegariu, O., Hirschmann, P., Kiesewetter, F., Köhn, F.M., Schill, W.B., Farah, S., Ramos, C., et al. (1996). Human Y chromosome azoospermia factors (AZF) mapped to different subregions in Yq11. *Hum. Mol. Genet.* **5**, 933–943.
- Weissman, I. (2012). Stem cell therapies could change medicine... if they get the chance. *Cell Stem Cell* **10**, 663–665.
- Wermann, H., Stoop, H., Gillis, A.J., Honecker, F., van Gurp, R.J., Ammerpohl, O., Richter, J., Oosterhuis, J.W., Bokemeyer, C., and Looijenga, L.H. (2010). Global DNA methylation in fetal human germ cells and germ cell tumours: association with differentiation and cisplatin resistance. *J. Pathol.* **221**, 433–442.
- Wongtrakoon, P., Jones, M., Gokhale, P.J., and Andrews, P.W. (2013). STELLA facilitates differentiation of germ cell and endodermal lineages of human embryonic stem cells. *PLoS ONE* **8**, e56893.
- Wu, S.M., and Hochedlinger, K. (2011). Harnessing the potential of induced pluripotent stem cells for regenerative medicine. *Nat. Cell Biol.* **13**, 497–505.
- Wu, X., Schmidt, J.A., Avarbock, M.R., Tobias, J.W., Carlson, C.A., Kolon, T.F., Ginsberg, J.P., and Brinster, R.L. (2009). Prepubertal human spermatogonia and mouse gonocytes share conserved gene expression of germline stem cell regulatory molecules. *Proc. Natl. Acad. Sci. USA* **106**, 21672–21677.
- Zwaka, T.P., and Thomson, J.A. (2005). A germ cell origin of embryonic stem cells? *Development* **132**, 227–233.

Want to learn how to prepare, submit and publish an article in a Cell Press journal?

Watch the Cell Press publication guide.



Chapter 1: Before manuscript submission



Chapter 2: After initial submission



Chapter 3: Decision process



Chapter 4: After manuscript acceptance

for more information visit
www.cell.com/publicationguide



Pain without Nociceptors? Nav1.7-Independent Pain Mechanisms

Michael S. Minett,¹ Sarah Falk,² Sonia Santana-Varela,¹ Yury D. Bogdanov,¹ Mohammed A. Nassar,¹ Anne-Marie Heegaard,² and John N. Wood^{1,*}

¹Molecular Nociception Group, Wolfson Institute for Biomedical Research, University College London, Gower Street, London WC1E 6BT, UK

²Department of Drug Design and Pharmacology, Faculty of Health and Medical Sciences, University of Copenhagen, Universitetsparken 2, 2100 Copenhagen, Denmark

*Correspondence: j.wood@ucl.ac.uk

<http://dx.doi.org/10.1016/j.celrep.2013.12.033>

This is an open-access article distributed under the terms of the Creative Commons Attribution-NonCommercial-No Derivative Works License, which permits non-commercial use, distribution, and reproduction in any medium, provided the original author and source are credited.

SUMMARY

Nav1.7, a peripheral neuron voltage-gated sodium channel, is essential for pain and olfaction in mice and humans. We examined the role of Nav1.7 as well as Nav1.3, Nav1.8, and Nav1.9 in different mouse models of chronic pain. Constriction-injury-dependent neuropathic pain is abolished when Nav1.7 is deleted in sensory neurons, unlike nerve-transection-related pain, which requires the deletion of Nav1.7 in sensory and sympathetic neurons for pain relief. Sympathetic sprouting that develops in parallel with nerve-transection pain depends on the presence of Nav1.7 in sympathetic neurons. Mechanical and cold allodynia required distinct sets of neurons and different repertoires of sodium channels depending on the nerve injury model. Surprisingly, pain induced by the chemotherapeutic agent oxaliplatin and cancer-induced bone pain do not require the presence of Nav1.7 sodium channels or Nav1.8-positive nociceptors. Thus, similar pain phenotypes arise through distinct cellular and molecular mechanisms. Therefore, rational analgesic drug therapy requires patient stratification in terms of mechanisms and not just phenotype.

INTRODUCTION

Pain afflicts a fifth of the population; there is an urgent need for new analgesic drugs with minimal side effects. There is strong evidence that, in most chronic pain conditions arising from nerve damage or inflammation, peripheral nerve block can cause pain relief in humans, proving that peripheral drive is critical to chronic pain (Aguirre et al., 2012). However, our understanding of the functional diversity of peripheral sensory neurons is limited, although attempts have been made to link histochemical markers to function with limited success. The developmental complexity of sensory neuron specification has been extensively

analyzed (Lallemend and Ernfors, 2012), but the links to function remain obscure. Here, we explore the role of voltage-gated sodium channels in different pain syndromes and provide evidence for a diversity of mechanisms in peripheral pain pathways that may help to explain recent failures to develop new analgesic drugs targeting peripheral neurons.

Studies of human monogenic disorders of pain perception have drawn attention to the voltage-gated sodium channels in sensory neurons (Eijkelkamp et al., 2012; Waxman, 2013), particularly Nav1.7 as a potential drug target, because loss of function in this channel leads to chronic insensitivity to pain (CIP) (Cox et al., 2006, Goldberg et al., 2007). Modeling this loss-of-function syndrome in mice recapitulates the human pain-free phenotype; acute thermal and mechanical insults have no behavioral consequences, whereas inflammatory pain is also abolished in inbred mouse strains lacking Nav1.7 in peripheral neurons (Minett et al., 2012; Nassar et al., 2004). Although the analgesia associated with loss of Nav1.7 function is dramatic, modality-specific pain therapies are more desirable for most chronic pain conditions where general analgesia could lead to inadvertent self-harm.

Earlier studies suggested that seemingly similar neuropathic pain models differed mechanistically (Kim et al., 1997). Neuropathic pain can be either sympathetically maintained or sympathetically independent (Roberts, 1986). Here, we examined a number of models including the spinal nerve transection (SNT) model (Kim and Chung, 1992) and the chronic constriction injury (CCI) model (Bennett and Xie, 1988). In the SNT model, mechanical and cold allodynia are associated with the invasion of the dorsal root ganglion (DRG) by postganglionic adrenergic sympathetic axons (Ramer and Bisby, 1998a, 1998c). In contrast, CCI is thought to trigger an immune response leading to a “neuritis” (Campbell and Meyer, 2006), where surgical lumbar sympathectomy produces no significant change in mechanical or cold allodynia (Kim et al., 1997). A further model associated with nerve damage, the oxaliplatin model of chemotherapeutic-induced neuropathic pain, was investigated (Renn et al., 2011) because painful neuropathies affect a third of all patients who undergo chemotherapy (Velasco and Bruna, 2010). Additionally, we examined spontaneous and movement-evoked pain behavior associated with cancer-induced bone pain in a syngeneic model

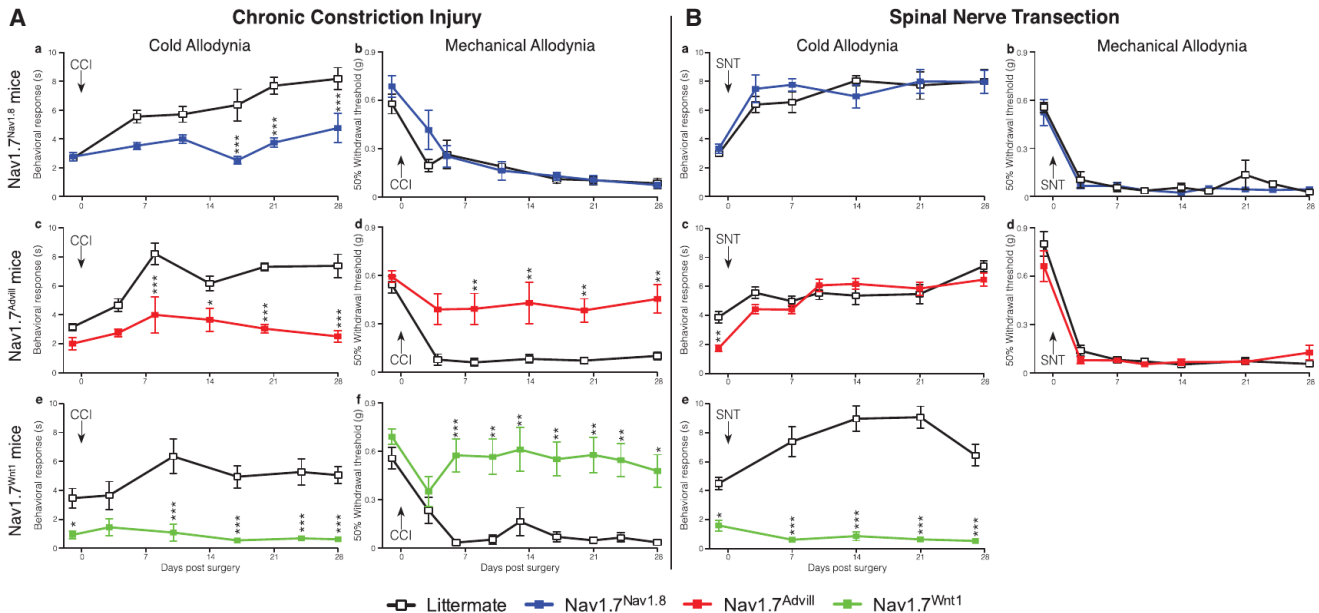


Figure 1. Comparison of Transgenic Mice Reveals Tissue-Specific Roles for Nav1.7 in Mechanical and Cold Allodynia after CCI Surgery as Well as a Role Specifically in Sympathetic Neurons after SNT Surgery

Behavioral responses of different Nav1.7 tissue-specific knockouts to the von Frey and acetone test following CCI (A) and L5 SNT surgery (B). Nav1.7^{Nav1.8} (blue squares, n = 9) do not develop CCI-induced cold allodynia (Aa) but do develop mechanical allodynia (Ab) in comparison to littermate mice (white squares, n = 8). Nav1.7^{Advill} (red squares, n = 8) do not develop CCI-induced cold (Ac) or mechanical allodynia (Ad) in comparison to littermate mice (white squares, n = 9). Nav1.7^{Wnt1} (green squares, n = 9) do not develop CCI-induced cold (Ae) nor mechanical allodynia (Af) in comparison to littermate mice (white squares, n = 6). Nav1.7^{Nav1.8} (blue squares, n = 6) develop both SNT-induced cold (Ba) and mechanical allodynia (Bb) in comparison to littermate mice (white squares, n = 6). Nav1.7^{Advill} (red squares, n = 6) develop both SNT-induced cold (Bc) and mechanical allodynia (Bd) in comparison to littermate mice (white squares, n = 9). Nav1.7^{Wnt1} (green squares, n = 9) do not develop SNT-induced cold allodynia (Be) in comparison to littermate mice (white squares, n = 12). Data analyzed by two-way analysis of variance followed by the Bonferroni post hoc test. Results are presented as mean ± SEM. **p < 0.01 and ***p < 0.001 (individual points). See also Figure S1.

of metastatic bone cancer. Bone metastasis is a common complication for patients suffering from advanced lung, breast, prostate, or skin cancers and is the most common source of severe cancer pain (Kinnane, 2007; Mercadante, 1997).

Here, we have used models of neuropathic and cancer-induced bone pain to investigate the role of Nav1.7, as well as other voltage-gated sodium channels in the development of pain syndromes. We crossed floxed (*Scn9a*) Nav1.7 mice with different tissue-restricted Cre mouse strains to generate nociceptor-specific (Nav1.7^{Nav1.8}), pan-DRG (Nav1.7^{Advill}), and pan-DRG and sympathetic (Nav1.7^{Wnt1}) Nav1.7 knockout mouse strains and examined the effects on pain behavior. We also compared the effects of deleting Nav1.7 in utero or in adult animals to examine any developmental effects that may contribute to CIP. Surprisingly, we found that classical nociceptors defined by the presence of the sodium channel Nav1.8, or the sodium channel Nav1.7 that have been linked to all forms of acute and inflammatory pain (Minett et al., 2012; Nassar et al., 2004) are not required for ongoing pain in models of cancer-induced bone pain or oxaliplatin-induced neuropathic pain. We also found that phenotypically identical pain syndromes are induced through different molecular mechanisms in distinct sets of sensory and sympathetic neurons. This functional redundancy raises questions about the organization of peripheral pain pathways and strategies for treating pain.

RESULTS

Generation of Nav1.7 Conditional Knockout Mouse Strains

We used the Cre-loxP system to generate a number of conditional Nav1.7 knockout mouse strains. Floxed (*Scn9a*) Nav1.7 mice were crossed with strains where Cre expression is driven by either the Nav1.8 promoter (Nav1.7^{Nav1.8}), expressed in >90% of neurons expressing markers of nociceptors (Nassar et al., 2004; Shields et al., 2012), the Advillin promoter (Nav1.7^{Advill}), expressed in all DRG neurons (Minett et al., 2012), and the Wnt1 promoter (Nav1.7^{Wnt1}), expressed in tissue derived from the neural tube, including sensory and sympathetic neurons (Danielian et al., 1998).

Pain-Modality-Specific Neurons and Nav1.7 in Neuropathic Pain Models

The three different tissue-specific Nav1.7 transgenic knockout mouse strains were examined after CCI of the sciatic nerve, or SNT of the fifth lumbar segment. Both surgical models produce robust cold and mechanical allodynia. In DRG neurons, Nav1.7 mediates the increased sensitivity to both the acetone and the von Frey test following CCI surgery (Figure 1A). A comparison of the Nav1.7^{Nav1.8} and Nav1.7^{Advill} behavioral responses reveals a modality-specific role for Nav1.7 within different DRG

subpopulations. Nav1.7^{Nav1.8} mice do not develop acetone-induced cold allodynia (Figure 1Aa) but show normal mechanical allodynia (Figure 1Ab). This is also true for the partial nerve ligation (Seltzer et al., 1990) surgically induced neuropathic pain model (Figures S1A and S1B). In contrast, deleting Nav1.7 from all DRG neurons attenuates both cold and mechanical allodynia (Figures 1Ac–1Af). Figure 1B demonstrates that Nav1.7 expression within DRG neurons is not critical for cold or mechanical allodynia in the sympathetically mediated SNT model. Both Nav1.7^{Nav1.8} and Nav1.7^{Advill} mice develop both cold and mechanical allodynia normally following SNT surgery (Figures 1Ba–1Bd), demonstrating that pain associated with the SNT model does not directly arise from Nav1.7-positive nociceptors, unlike the CCI model. In contrast, Nav1.7^{Wnt1} mice develop neither cold (Figure 1Be) nor mechanical allodynia (Minett et al., 2012) demonstrating that Nav1.7 expressed within peripheral sympathetic neurons is essential for the SNT-induced mechanical and cold allodynia.

Interactions between sympathetic neurons and the neuronal somata of DRG neurons have been described since the era of Ramón y Cajal in the 19th century (García-Poblete et al., 2003). Nerve injury has been shown to induce increased sympathetic sprouting into the DRG (McLachlan et al., 1993; Ramer and Bisby, 1998c). A high innervation density of sympathetic axons (highlighted by yellow arrow heads) was found within ipsilateral L4 DRG 30 days following SNT surgery (Figure 2A), in comparison to contralateral L4 DRG (Figure 2B). These sprouting sympathetic axons form “baskets” around the DRG cell body of large myelinated DRG neurons (McLachlan et al., 1993; Ramer and Bisby, 1998a), an example of which can be seen in Figure 2C. Quantification of sympathetic sprouting following SNT surgery shows that Nav1.7^{Nav1.8} and Nav1.7^{Advill} mice are indistinguishable from littermate controls (Figure 2D). In contrast, Nav1.7^{Wnt1} mice show the same low level sympathetic sprouting density in the ipsilateral as the contralateral L4 DRG following SNT surgery. No significant change in DRG size was observed in the three Nav1.7 knockout mouse strains or littermate controls. Nav1.7 expression within sympathetic neurons is therefore required for sympathetic sprouting following nerve injury. Inhibition of Nav1.7-mediated sympathetic sprouting is associated with a loss of cold (Figure 1Be) and mechanical allodynia in Nav1.7^{Wnt1} mice (Minett et al., 2012).

Global deletion of other voltage-gated sodium channels, such as Nav1.3, Nav1.8, or Nav1.9 does not reduce the sympathetic sprouting density following nerve damage (Figure 2E). Performing a chemical sympathectomy on Nav1.7^{Advill} mice prior to SNT surgery (Figure 2F) recapitulates the Nav1.7^{Wnt1} behavioral phenotype (Minett et al., 2012). It has previously been reported that approximately 10% of lumbar DRG neurons are tyrosine hydroxylase (TH) positive, although they are thought to be dopaminergic because they lack the enzymes required for norepinephrine or epinephrine production (Brumovsky et al., 2006). Microarray analysis of DRG from mice where the Nav1.8-positive DRG population has been ablated (Nav1.8^{DTA}) shows a significant decrease in TH (10-fold) in comparison to littermates, indicating an overlap between the Nav1.8 and TH-positive neurons (Abrahamsen et al., 2008). However, the disruption of the Nav1.8-positive DRG population in the

Nav1.7^{Nav1.8} mice does not alter the development of pain following SNT. Together this suggests that TH-positive DRG subpopulation is not critical for the development SNT-induced cold and mechanical allodynia.

The combination of chemical sympathectomy and the loss of Nav1.7 from all DRG neurons shows greater attenuation of SNT-induced mechanical allodynia than chemical sympathectomy alone (Figure 2F), suggesting the nociceptors contribute to SNT-evoked mechanical allodynia. Cutaneous injection of the sympathetic transmitter norepinephrine rekindles the spontaneous pain and dynamic mechanical hyperalgesia in posttraumatic neuralgia patients, which had been relieved by sympathetic block (Torebjörk et al., 1995). Peripheral sensory neurons have been shown to develop noradrenergic sensitivity following nerve lesion through an upregulation of α 2-adrenoceptors in intact afferent fibers (Baron et al., 1999). Interestingly, intraplantar injection of norepinephrine induces mechanical allodynia in Nav1.7^{Wnt1} mice 14 days after SNT surgery (Figure 2G). This means that peripheral pain pathways can be activated in the absence of Nav1.7 after nerve damage. Norepinephrine-induced SNT mechanical allodynia can be detected within 10 min and is still apparent 5 days postinjection. Importantly, intraplantar injection of norepinephrine does not induce mechanical allodynia in naive mice (Figure S2). Norepinephrine-mediated coupling between sympathetic and DRG neurons is thus critical for the development of pain in the sympathetically mediated SNT neuropathic pain model. Sympathetic sprouting following SNT is mainly associated with large diameter sensory neurons (Xie et al., 2011), as is the vast majority of norepinephrine-evoked spontaneous neuronal activity following SNT (Liu et al., 1999).

Distinct Modality-Specific Roles for Nav1.3, Nav1.8, and Nav1.9 in Neuropathic Pain

A comparison of the behavioral responses of Nav1.3, Nav1.8, and Nav1.9 global knockout mouse strains in the CCI (Figure 3A) and SNT (Figure 3B) neuropathic pain models reveals modality-specific roles for these sodium channels. Deletion of Nav1.3 reduces cold allodynia (Figure 3Aa) as well as the magnitude of mechanical allodynia (Figure 3Ab) following CCI surgery. However, mice lacking Nav1.8 show an attenuated response to acetone-induced cold allodynia (Figure 3Ac) but develop mechanical allodynia normally (Figure 3Ad). The same is also true for Nav1.9 knockout mice (Figures 3Ae and 3Af). Interestingly, Figure 3B shows that all these behavioral phenotypes are restricted to the CCI models of neuropathic pain. Both cold and mechanical allodynia develop normally in mice lacking Nav1.3 (Figures 3Ba and 3Bb), Nav1.8 (Figures 3Bc and 3Bd), and Nav1.9 (Figures 3Be and 3Bf) following SNT surgery. Additionally, sympathetic sprouting into the DRG develops normally in the Nav1.3, 1.8, and 1.9 global knockout mouse strains (Figure 2E), demonstrating that only Nav1.7 is required for sympathetic sprouting following SNT surgery.

Oxaliplatin-Induced Pain and Cancer-Induced Bone Pain Are Nav1.7 Independent

Both Nav1.7^{Advill} (Figures S3A and S3B) and Nav1.7^{Wnt1} (Figures 4A and 4B) mice develop mechanical and cold allodynia normally

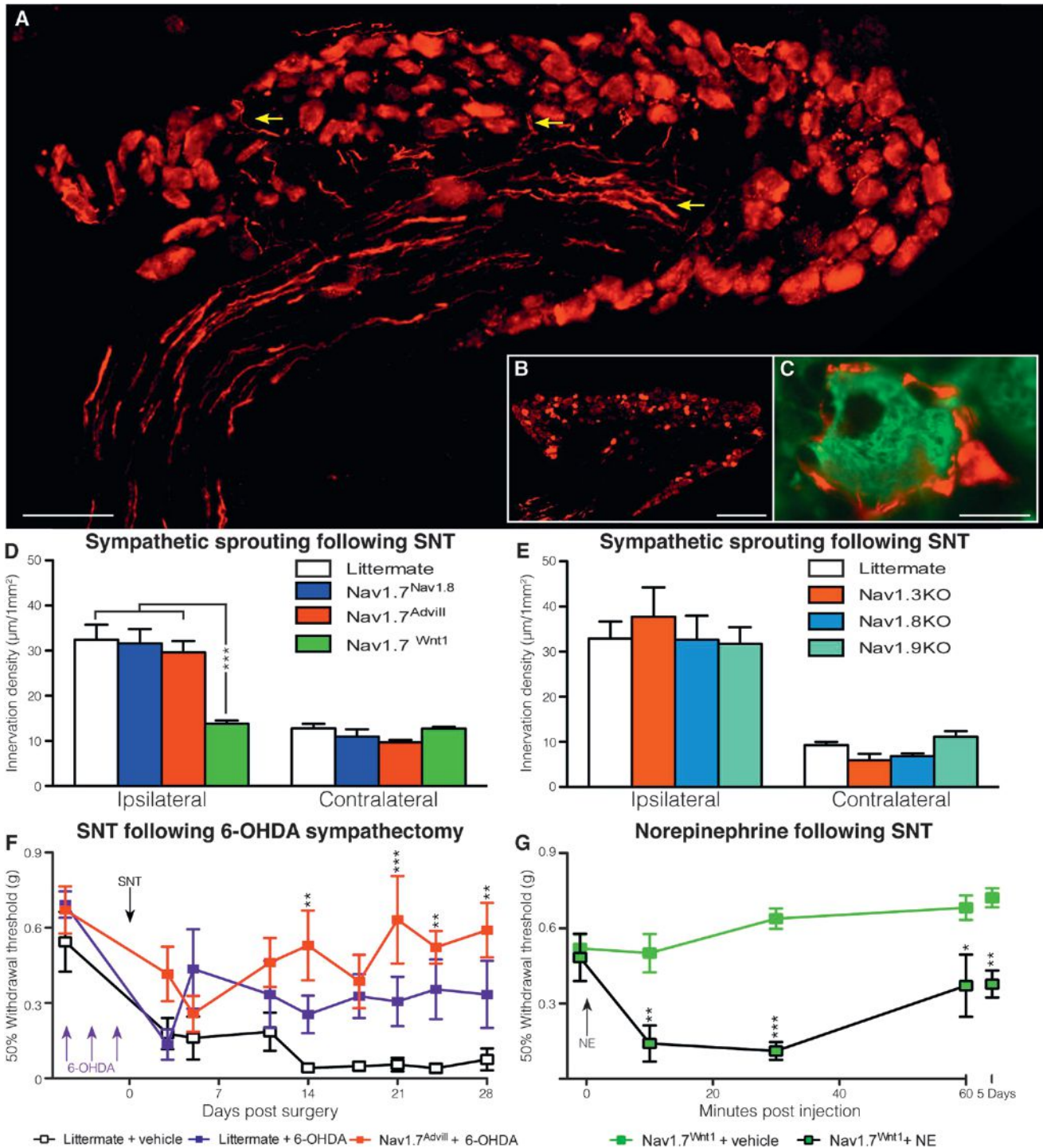


Figure 2. Spinal Nerve Transection Fails to Trigger Sympathetic Sprouting in Nav1.7^{Wnt1} Mice, which Can Be Sensitized by Norepinephrine
 (A) Yellow arrows show examples of sympathetic sprouting (tyrosine hydroxylase, red) into the ipsilateral DRG following SNT surgery (scale bar = 100 μm).
 (B) An example of a contralateral DRG showing no sympathetic sprouting (tyrosine hydroxylase, red) following SNT surgery (scale bar = 200 μm).
 (C) An example of a sympathetic “basket” (tyrosine hydroxylase, red) formed around a large diameter (N52, green) DRG neuron (scale bar = 20 μm).
 (D) Quantitation of sympathetic sprouting into the ipsilateral and contralateral L4 DRG following SNT. Littermates (white columns, n = 3), Nav1.7^{Nav1.8} (blue columns, n = 3), Nav1.7^{Advill} (red columns, n = 3), and Nav1.7^{Wnt1} (green columns, n = 3).
 (E) Quantitation of sympathetic sprouting into the L4 DRG following SNT. Littermates (white columns, n = 3), Nav1.3KO (orange columns, n = 3), Nav1.8KO (light blue columns, n = 3), and Nav1.9KO (turquoise columns, n = 3).

(legend continued on next page)

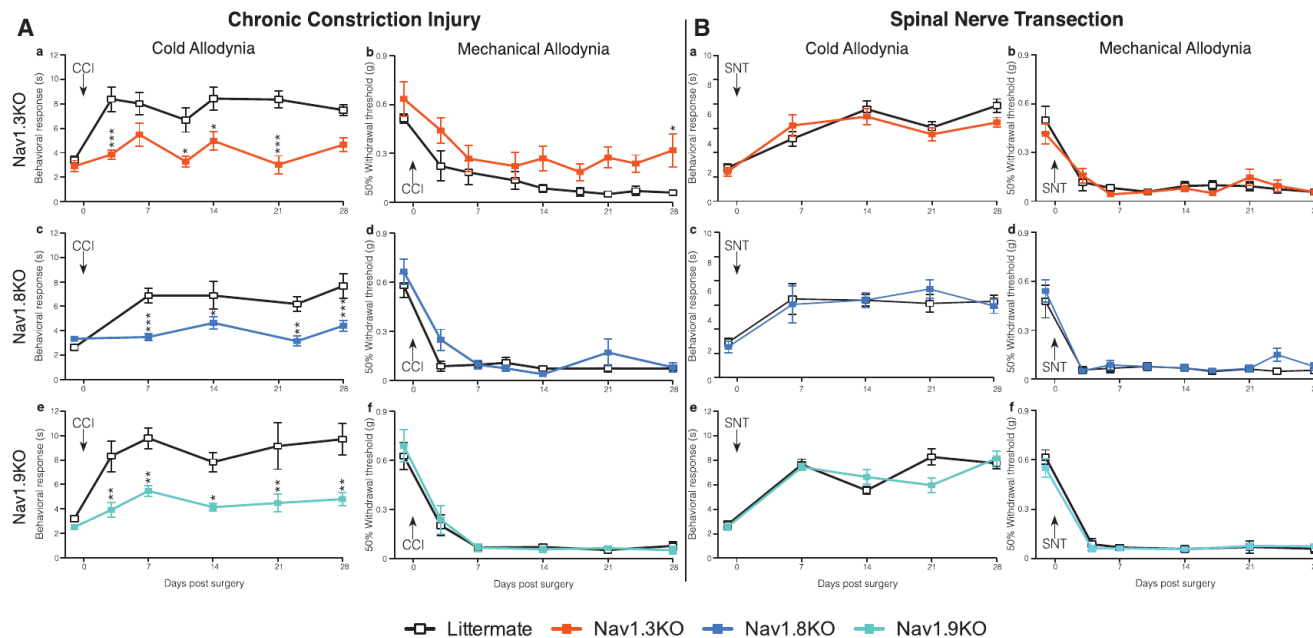


Figure 3. Behavioral Responses of Nav1.3, Nav1.8, and Nav1.9 Knockout Mice Reveal Critical Roles in Modality-Specific Responses to CCI-Induced Pain but Not Sympathetically Mediated SNT Pain

Behavioral von Frey and acetone responses of Nav1.3, Nav1.8, or Nav1.9 knockouts following CCI (A) and L5 SNT surgery (B). Nav1.3KO mice (orange squares, $n = 6$) show reduced CCI-induced cold allodynia (Aa) and mechanical allodynia (Ab) in comparison to littermate mice (white squares, $n = 10$). Nav1.8KO mice (light blue squares, $n = 8$) show diminished CCI-induced cold allodynia (Ac) but do develop mechanical allodynia (Ad) in comparison to littermate mice (white squares, $n = 10$). Nav1.9KO mice (turquoise squares, $n = 8$) show diminished CCI-induced cold allodynia (Ae) but do develop mechanical allodynia (Af) in comparison to littermate mice (white lines, $n = 8$). Nav1.3KO mice (orange squares, $n = 10$) develop both L5 SNT-induced cold (Ba) and mechanical allodynia (Bb) in comparison to littermate mice (white squares, $n = 8$). Nav1.8KO mice (light blue squares, $n = 8$) develop L5 SNT-induced cold (Bc) and mechanical allodynia (Bd) in comparison to littermate mice (white squares, $n = 8$). Nav1.9KO mice (turquoise squares, $n = 10$) develop L5 SNT-induced cold (Be) and mechanical allodynia (Bf) in comparison to littermate mice (white squares, $n = 7$). Data analyzed by two-way analysis of variance followed by the Bonferroni post hoc test. Results are presented as mean \pm SEM. ** $p < 0.01$ and *** $p < 0.001$ (individual points).

following oxaliplatin treatment when compared to littermate controls. This shows that the expression of Nav1.7, within either DRG or sympathetic neurons is not required for this pain syndrome. Similarly, global deletion of Nav1.3, Nav1.8, or Nav1.9 does not attenuate either mechanical or cold allodynia in this model (Figures S3C–S3H) despite the suggestion that enhanced Nav1.8 expression could contribute to oxaliplatin-induced cold pain (Descoeur et al., 2011). Finally, both mechanical and cold allodynia develop normally in Nav1.8^{DTA} mice (Figures 4C and 4D). The oxaliplatin model thus has a distinct underlying mechanism from both sympathetically dependent and independent surgically induced neuropathic pain models, as well as inflammatory pain (Minett et al., 2012; Nassar et al., 2004) and does not require the presence of Nav1.8-positive nociceptors.

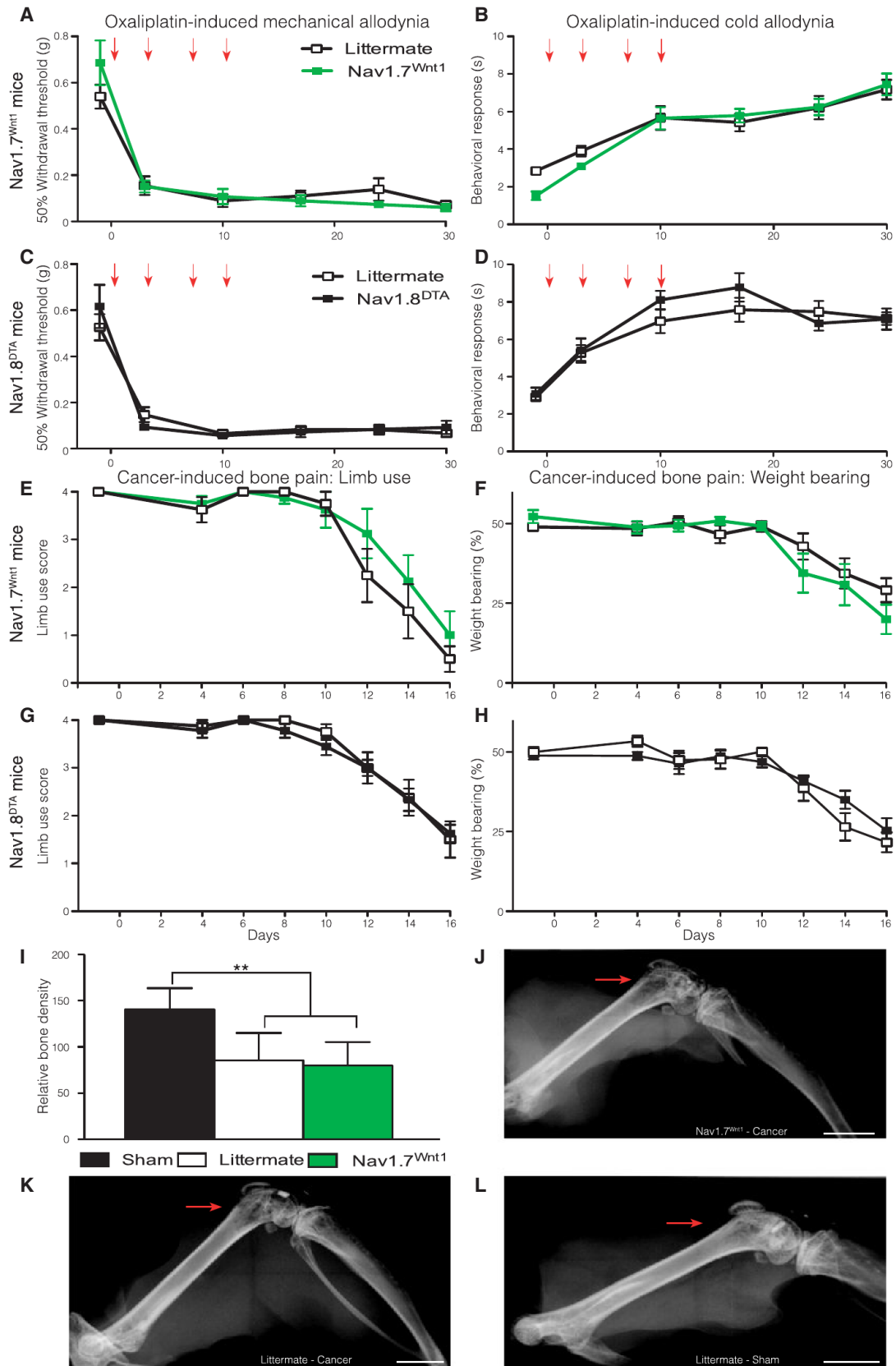
In a mouse model of metastatic cancer pain induced by intrafemoral injection of syngeneic LL/2 lung carcinoma cells, we found that, as with oxaliplatin-evoked pain, deleting Nav1.7

expression in the peripheral nervous system did not result in the loss of pain behavior. No behavioral deficits were observed in either limb use or weight-bearing ratio (Figures 4E and 4F), although deleting Nav1.7 from the peripheral nervous system produces striking behavioral deficits in all acute, inflammatory, and surgically induced neuropathic pain models tested (Minett et al., 2012; Nassar et al., 2004). Ablation of Nav1.8-positive neurons in the Nav1.8^{DTA} mouse strain leads to the loss of many pain modalities (Abrahamsen et al., 2008) but surprisingly does not diminish the development of cancer-induced bone pain (Figures 4G and 4H). No significant differences in the level of bone degradation were observed (Figure 4I). Example X-rays from a Nav1.7^{Wnt1} mouse (Figure 4J) and a littermate mouse (Figure 4K) both show pronounced bone degradation (highlighted by the red arrows) in comparison to sham-operated mice (Figure 4L). Furthermore, no overt fractures were observed in either Nav1.7^{Wnt1} or littermate mice demonstrating

(F) Behavioral von Frey responses following SNT surgery on 6-OHDA sympathectomized Nav1.7^{Advill} (red squares, $n = 8$) and littermate (purple squares, $n = 7$) mice, in comparison to unsympathectomized littermate controls (white squares, $n = 7$).

(G) Intraplantar norepinephrine (200 ng) injection sensitizes Nav1.7^{Wnt1} mice (black line/green square, $n = 7$) 14 days after SNT surgery, in comparison to vehicle alone in Nav1.7^{Wnt1} mice 14 days after SNT surgery (green line and squares, $n = 6$). Data analyzed by two-way analysis of variance followed by the Bonferroni post hoc test. Results are presented as mean \pm SEM. ** $p < 0.01$ and *** $p < 0.001$ (individual points).

See also Figure S2.



(legend on next page)

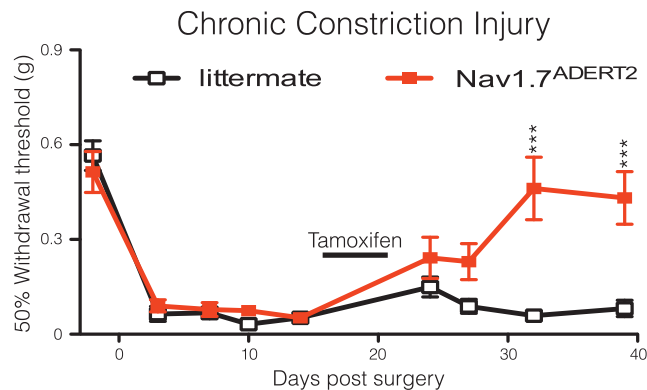


Figure 5. Reversal of CCI-Mediated Mechanical Allodynia after Tamoxifen-Induced Deletion of Nav1.7

Nav1.7^{ADERT2} (red squares, n = 8) mice develop mechanical allodynia normally in comparison to littermate controls (white squares, n = 9) following CCI surgery. However, activation of Advillin-CreERT2 through five daily intraperitoneal tamoxifen injections (2 mg per day) reverses this mechanical allodynia in Nav1.7^{ADERT2} mice but not Advillin-CreERT2 negative littermate controls. Data analyzed by two-way analysis of variance followed by the Bonferroni post hoc test. Results are presented as mean ± SEM. **p < 0.01 and ***p < 0.001 (individual points).

that the observed behavior is related to cancer-induced bone pain and not impaired mobility of the affected leg due to bone fractures.

Deleting Nav1.7 in Adult Mice Reverses Neuropathic Pain

Humans with recessive loss-of-function Nav1.7 mutations are pain free (Cox et al., 2006; Goldberg et al., 2007), but specific high-affinity antagonists of Nav1.7 have so far not produced dramatic analgesic effects (Schmalhofer et al., 2008). It is possible that developmental deficits related to the loss of Nav1.7 in utero could explain some aspects of Nav1.7-dependent pain. To address this, an inducible DRG-specific Nav1.7 knockout mouse strain (Nav1.7^{ADERT2}) was generated using Advillin-CreERT2 (Lau et al., 2011). Lau et al. (2011) show that Advillin-CreERT2 has the same expression pattern as Advillin-Cre, following tamoxifen induction. Figure 5 shows that uninduced Nav1.7^{ADERT2} mice develop mechanical allodynia following CCI surgery in the same manner as littermate controls. However, mechanical allodynia is reversed in Nav1.7^{ADERT2} but not in Advillin-CreERT2-negative, homozygous floxed (*Scn9a*) Nav1.7 littermate mice following tamoxifen treatment. These data provide further validation of Nav1.7 as a target for analgesic drug development in adult humans.

DISCUSSION

Present views of the organization of the peripheral nervous system have been formed by electrophysiological studies. Gasser showed that fast conducting myelinated A-fibers were involved in pain responses, together with slower conducting C-fibers (Gasser, 1941). There has been a subsequent focus on C-fiber-associated pain largely because the cells are easier to culture and characterize electrophysiologically. The role of specialized sensory neurons that only respond to damaging stimuli in pain pathways was experimentally demonstrated by Burgess and Perl (1967) and Bessou and Perl (1969) and the view that the intensity of a stimulus could change innocuous sensing neurons into damage-sensing neurons (intensity theory) was generally abandoned. Electrophysiological studies suggested that there were a range of different nociceptor subtypes, polymodal nociceptors, cold, mechano-heat (CMH) fibers, and so on, based on the electrical properties of teased fibers (often containing more than one axon) that depolarize in response to various, often superthreshold insults in anesthetized animals. These studies, combined with the now discredited gate-control theory of pain underpinned the view that pain was predominantly a C-fiber-mediated event.

Recent behavioral genetic studies in unanesthetized awake animals are incompatible with this analysis. For example, it is clear that the neurons that respond to noxious thermal (heat) insults are distinct from those involved in noxious mechanosensation when behavioral assays are employed (Abrahamsen et al., 2008; Minett et al., 2012; Mishra et al., 2011). Cell ablation or silencing strategies, where cell markers such as glutamate transporters or sodium channels are used to define and delete/disrupt subsets of sensory neurons, have shown that there is clear specialization in terms of noxious input into the dorsal horn (Abrahamsen et al., 2008; Lagerström et al., 2010, 2011; Minett et al., 2012; Mishra et al., 2011). It is also clear that some A-fibers are nociceptors and some C-fibers are low threshold mechanoreceptors or involved with definition of pleasurable stimuli (Vrontou et al., 2013).

Previously, we reported that neuropathic pain develops normally in mice lacking Nav1.7 and Nav1.8 in the Nav1.8-positive subset of sensory neurons (Nassar et al., 2005). However, the present study provides evidence that some neuropathic pain states depend upon sensory neuron input involving Nav1.7, whereas other neuropathic pain states depend upon the activity of Nav1.7 in both sensory and sympathetic neurons. Thus, Nav1.7 is required for the development of pain in surgical models of neuropathic pain. The sprouting of sympathetic neurons into DRG of damaged nerves depends, surprisingly, upon the

Figure 4. Oxaliplatin-Induced Pain and Cancer-Induced Bone Pain Do Not Require Nav1.7 Expression or Nav1.8⁺ Nociceptors

Nav1.7^{Wnt1} (green squares, n = 7) and littermate (white squares, n = 13) mice treated twice weekly (red arrows) with 3.5 mg/kg oxaliplatin (i.v.) develop both mechanical (A) and cold (B) allodynia. Nav1.8^{DTA} (black squares, n = 10) and littermate mice (white squares, n = 11) treated twice weekly with 3.5 mg/kg oxaliplatin (i.v.) develop both mechanical (C) and cold (D) allodynia. Limb use scores for the affected hind limb (E) and percentage of body weight placed on the affected hind limb (F) of Nav1.7^{Wnt1} (green squares, n = 8) and littermate (white squares, n = 8) mice following cancer induction in the femur. Limb use scores for the affected hind limb (G) and percentage of body weight placed on the affected hind limb (H) of Nav1.8^{DTA} (black squares, n = 9) and littermate (white squares, n = 8) mice following cancer induction in the femur. Both Nav1.7^{Wnt1} (green column, n = 8) and littermate (white column, n = 8) mice show similar decreases in bone density compared to sham operated mice (black column, n = 5) (I). Example of decreased bone density in a Nav1.7^{Wnt1} (J) and littermate (K) mouse, compared to a sham-operated mouse (L). Scale bars represent 2 mm. Data analyzed by two-way analysis of variance followed by the Bonferroni post hoc test. Results are presented as mean ± SEM. **p < 0.01 and ***p < 0.001 (individual points). See also Figure S3.

presence of Nav1.7 in these cells. The mechanism underlying this phenomenon is unknown, but since the studies of Dogiel and Ramón y Cajal in the 19th century, the existence of sympathetic bundles surrounding sensory neurons in normal animals has been described, with increased sprouting seen following neuronal damage (McLachlan et al., 1993; Ramer and Bisby, 1998b). Sympathetic nerve block has been used effectively in many pain states, and the application of beta blockers has also proved effective in some situations (López-Álvarez et al., 2012). Thus, norepinephrine acting on large diameter sensory neurons seems to be able to lower pain thresholds and cause ongoing pain (Roberts and Foglesong, 1988). Xie et al. showed that repeated stimulation of sympathetic postganglionic neurons within the dorsal ramus enhanced spontaneous activity in large and medium diameter neurons and reduced thresholds of activation in large neurons following SNT surgery (Xie et al., 2010). Interestingly, spontaneously active DRG neurons encapsulated by sympathetic baskets always had conduction velocities above 9 m/s and were clearly distinct from the much slower unmyelinated “classical” nociceptors (Xie et al., 2011). This spontaneous activity could be reduced or eliminated by applying norepinephrine antagonists, or by precutting the gray ramus through which sympathetic fibers innervate the DRG (Xie et al., 2010). We report here that exogenous norepinephrine can cause pain in the absence of Nav1.7, when sensory neurons are damaged (see Figure 2G). A role for EPAC-1-mediated sensitization of Piezo2 mechanotransducing molecules has recently been shown to be important for both touch and allodynia following SNT surgery and is an example of the type of mechanism that may involve peripheral sensitization through nonnociceptive sensory neurons (Eijkelkamp et al., 2013).

Increasing evidence suggests that cancer-induced bone pain is mechanistically different from other chronic pain states, such as neuropathic and inflammatory pain. It has been shown that the neurochemical changes observed in the spinal cord in models of cancer-induced bone pain are different from those observed in inflammatory and neuropathic pain states (Honore et al., 2000). Whereas inflammatory models display increased levels of substance P and calcitonin gene-related peptide in the spinal cord, models of cancer-induced bone pain display no changes in the levels of these neuropeptides (Honore et al., 2000). However, increases in c-Fos expression and dynorphin-expressing neurons have been reported in inflammatory, neuropathic, and cancer-induced bone pain models (Abbadie and Besson, 1992; Schwei et al., 1999; Wagner et al., 1993), suggesting that central pain mechanisms may partially overlap. The behavioral outcomes used to quantify cancer-induced bone pain are substantially different from neuropathic and inflammatory pain models consistent with the existence of distinct underlying mechanisms. Neuropathic and inflammatory pain states have traditionally been measured using threshold responses to evoked stimuli such as von Frey hairs, whereas alternative outcome measures, such as limb use scoring and weight-bearing ratios, have been developed for cancer-induced bone pain models, as measures of evoked pain have been inconsistent and unpredictable (Figures S4A and S4B).

In this study, we demonstrate that cancer-induced bone pain and oxaliplatin-induced pain do not require the peripheral

neuronal subpopulations that are essential for acute, inflammatory, and neuropathic pain. Nav1.7 expression within the peripheral nervous system is necessary for acute, inflammatory, and neuropathic pain behavior in mice (Minett et al., 2012; Nassar et al., 2004), as well as in human CIP (Cox et al., 2006; Goldberg et al., 2007) but not for either cancer-induced bone pain or oxaliplatin-induced pain. A role for inflammatory mediators such as tumor necrosis factor- α , nerve growth factor, bradykinins, prostaglandins, and ATP has been identified in the development of cancer-induced bone pain (Falk et al., 2012). Thus, tissue damage and subsequent activation of the immune system associated with the progression of cancer-induced bone pain could sensitize nociceptors to cause ongoing pain. However, the unilateral sensitization of the affected limb demonstrates the importance of peripheral input in ongoing pain. A role for the atypical sodium channel Nax implicated in sodium sensing has recently been described, where lentiviral siRNA knockdown of this channel reverses pain-related behavior associated with tumor growth (Ke et al., 2012). Nax is expressed in the medium to large diameter sensory neurons that are also implicated in oxaliplatin-evoked pain (Ke et al., 2012). Deleting Nav1.7, or ablating the Nav1.8-positive nociceptor population, does not diminish the pain-related behavior associated with either oxaliplatin or cancer-induced bone pain. However, the sodium channel blocker mexiletine is protective against oxaliplatin-induced pain (Egashira et al., 2010). This is consistent with the recent demonstration of an essential role for Nav1.6, in conjunction with delayed rectifier potassium channels in oxaliplatin-evoked pain (Sittl et al., 2012; Deuis et al., 2013). Nav1.6 expression is associated with myelinated A-fibers rather than classical C-fiber-associated nociceptors. Taken together, these observations are consistent with pain resulting from input from neurons that normally subserve innocuous sensation (Table 1).

Further evidence for the complexity of peripheral nociceptive mechanisms comes from sodium channel gene ablation studies. Global deletion of Nav1.3, Nav1.8, or Nav1.9 has quite different effects on cold and mechanical allodynia produced by different neuropathic pain models. These findings provide support for the existence of multiple mechanisms involving different subpopulations of sensory neurons that can produce apparently identical pain phenotypes. Microarray technology has been used to identify dysregulated transcripts common to different pain states (Maratou et al., 2009). The logic of this approach is that a single critical mechanism may underpin the pain caused by a variety of stimuli and provide a potentially useful target of new analgesic drug development. However, the evidence accumulated here suggests that different peripheral cell types and mechanisms lead to phenotypically similar pain states (see Table 2). Müller (1842) first suggested that the quality of a sensation is defined by the central terminations of sensory nerves. Recent advances in the use of genetically encoded calcium indicators should allow us to examine whether redundant mechanisms converge on similar pathways within the spinal cord and midbrain (Zariwala et al., 2012).

These findings have significant implications for clinical practice. Recent attempts to phenotype neuropathic pain patients as a prelude to rational drug treatment are a necessary first step (Backonja et al., 2013), but the present results suggest

Table 1. Peripheral Sodium Channels and Pain Pathways

Pain Modality	Essential Sodium Channel	Peripheral Neuronal Subpopulation
Classical nociceptive pain pathways		
Acute (spinal) heat pain	Nav1.7	Nav1.8-negative sensory neurons
Acute mechanical pain	Nav1.7	Nav1.8-positive sensory neurons
Acute cold pain	Nav1.8	Nav1.8-positive sensory neurons
Inflammatory hyperalgesia	Nav1.7	Nav1.8-positive sensory neurons
Nonnociceptive pain pathways		
Neuropathic mechanical allodynia	Nav1.7	Nav1.8-negative sensory neurons
Neuropathic cold allodynia	Nav1.7	Nav1.8-positive sensory neurons
Sympathetically maintained pain	Nav1.7	Nav1.7-positive sympathetic neurons
Atypical peripheral pain pathways		
Oxaliplatin-evoked allodynia	Nav1.6	A-fiber-associated neurons
Cancer-induced bone pain	Nax	A-fiber-associated neurons

that this useful analysis will require further subdivision into mechanistically distinct pain sets. Given the absence of biomarkers, and the uncertainty about mechanisms involved, the argument for polypharmacy becomes appealing. Triple therapy has proved revolutionary in HIV antiviral therapy (Bernardini and Maggiolo, 2013). There is no reason why multiple therapies should not be routinely used in pain treatment. The often-remarked-upon failure of new analgesic drugs may be linked to a failure to distinguish mechanistically distinct pain syndromes, and an inability to tease out useful effects of drugs on subsets of pain patients in the overall noise of nonresponders.

In summary, we have provided evidence that some pain states do not involve classical nociceptor activation, consistent with the proposal of the intensity theory that suggests neurons responding to innocuous stimuli may activate central pain pathways in some circumstances. The overwhelming evidence for redundancy in pain mechanisms coupled with a simplistic classification of nociceptive mechanisms on the basis of early electrophysiological studies helps to explain recent problems in developing analgesic drugs. Further mechanistic studies and a combined therapeutic attack on critical pain mediators such as norepinephrine and proinflammatory cytokines as well as the electrical apparatus that underpins peripheral signaling to the CNS is a logical route to pain treatment in the future.

EXPERIMENTAL PROCEDURES

Genotyping

Genomic DNA was isolated from ear notches as described previously (Akopian et al., 1999; Nassar et al., 2006; Abrahamsen et al., 2008; Minett et al., 2012; Ostman et al., 2008).

Behavioral Testing

Animal experiments were approved by the UK Home Office and UCL ethics committee. Touch perception thresholds were measured using the up-down method for obtaining the 50% threshold using von Frey hairs (Chaplan et al., 1994). Behavioral response to cooling (approximately 10°C–15°C) by acetone test was performed (Bautista et al., 2006).

Spinal Nerve Transection at the Fifth Lumbar Segment

A modified version of the Kim and Chung model (Kim and Chung, 1992) of peripheral neuropathy was adapted for use on mice (Minett et al., 2012). Acetone and von Frey thresholds were recorded at baseline and up to 28 days after surgery.

Chronic Constriction Injury of the Sciatic Nerve

The Bennett and Xie model of peripheral neuropathy (Bennett and Xie, 1988) was adapted for use on mice. Acetone and von Frey thresholds were recorded at baseline and up to 28 days after surgery.

Oxaliplatin-Induced Pain

Oxaliplatin (Sigma) was administered intravenously by tail vein injection (3.5 mg/kg). Mice received a total of four injections separated by 3 then 4 days (Renn et al., 2011).

Cancer-Induced Bone Pain

A model of metastatic bone pain was introduced by intrafemoral injection of LL/2 lung carcinoma cells (Clohisy et al., 1996). Spontaneous and movement-evoked pain response measures were used to evaluate pain behavior up to 16 days after induction (Falk et al., 2013).

Induction of Advillin-CreERT2

Advillin-CreERT2 expression was induced via a series of five consecutive daily 2 mg intraperitoneal (i.p.) injections of tamoxifen (Sigma-Aldrich) (Lau et al., 2011).

Chemical Sympathectomy

6-OHDA (Sigma) was dissolved in sterile saline containing 0.01% (w/v) ascorbic acid (vehicle) and was injected intraperitoneally at a concentration of 200 mg/kg (Leo et al., 1998). Control mice received an equivalent volume of vehicle alone.

Immunocytochemistry

DRGs were excised from animals perfused with 4% paraformaldehyde. Serial 10 μm sections were collected. Slides were washed and blocked in 10% goat serum in PBS +0.3% Triton for 1 hr at room temperature and incubated in the primary antibody overnight at 4°C. Primary antibodies were detected by incubating with the secondary antibody at room temperature for 2 hr.

Quantification of Sympathetic Sprouting

Tissue samples were visualized and captured in monochrome and pseudocolored using HClmage 2.0.1.16. ImageJ64 analysis software (NIH) was used to quantify sympathetic axons. To generate innervation density data, the total area of DRG cell layer, excluding axonal tracts, was measured. Following this, the length of TH-positive axons within the marked area was measured. A reference image with known grid size was used to calculate units.

Quantification of Bone Degradation

Following dissection and fixation, radiographic images of the distal femur head were obtained using a digital camera inside an enclosed cabinet during exposure to an X-ray source (Faxitron MX-20). Each X-ray image was calibrated to a standard aluminum wedge and the grayscale intensity quantified using ImageJ. The calibrated grayscale value was used to quantify the relative bone density of the distal femur for statistical analysis.

Statistics

Data were analyzed using the GraphPad Prism 5. Student's t test (two-tailed) was used for comparison of difference between two distributions. Multiple groups were compared using one-way or two-way analysis of variance with the Bonferroni post hoc test.

Table 2. Summary of Distinct Neuronal Subpopulations and Mechanisms Underlying Different Neuropathic Pain Models

VGSC	Deleted from	Chronic Constriction Injury		Spinal Nerve Transection		Oxaliplatin-Induced Pain	
		Cold Allodynia	Mechanical Allodynia	Cold Allodynia	Mechanical Allodynia	Cold Allodynia	Mechanical Allodynia
Nav1.3	CNS/PNS	attenuated	attenuated	normal	normal	normal	normal
Nav1.7	Nociceptors	lost	normal	normal	normal	normal	normal
	Sensory neurons	lost	lost	normal	normal	normal	normal
	Sympathetic and sensory neurons	lost	lost	lost	lost	normal	normal
Nav1.8	Nociceptors	attenuated	normal	normal	normal	normal	normal
Nav1.9	Nociceptors	attenuated	normal	normal	normal	normal	normal

VGSC, voltage-gated sodium channel; PNS, peripheral nervous system; CNS, central nervous system.

SUPPLEMENTAL INFORMATION

Supplemental Information includes Supplemental Experimental Procedures and four figures and can be found with this article online at <http://dx.doi.org/10.1016/j.celrep.2013.12.033>.

AUTHOR CONTRIBUTIONS

M.S.M. and S.S.-V. carried out behavioral experiments and immunohistochemistry. M.S.M. and S.S.-V. carried out neuropathic surgery and oxaliplatin studies. S.F. and M.S.M. carried out bone cancer studies. M.A.N. and Y.D.B. provided mouse lines and advice. A.-M.H. provided advice. J.N.W. and M.S.M. conceived the study and wrote the manuscript that was edited by all other coauthors.

ACKNOWLEDGMENTS

We thank the Medical Research Council, the Wellcome Trust, and the Danish Cancer Society trust for their generous support. Y.D.B. was supported by an EU IMI grant. We thank Rikke Rie Hansen at KCL for help with bone imaging. We thank James Cox, Anthony Dickenson, and other members of the lab for useful critical comments.

Received: August 22, 2013

Revised: November 22, 2013

Accepted: December 20, 2013

Published: January 16, 2014

REFERENCES

- Abbadie, C., and Besson, J.M. (1992). c-fos expression in rat lumbar spinal cord during the development of adjuvant-induced arthritis. *Neuroscience* **48**, 985–993.
- Abrahamsen, B., Zhao, J., Asante, C.O., Cendan, C.M., Marsh, S., Martinez-Barbera, J.P., Nassar, M.A., Dickenson, A.H., and Wood, J.N. (2008). The cell and molecular basis of mechanical, cold, and inflammatory pain. *Science* **321**, 702–705.
- Aguirre, J., Del Moral, A., Cobo, I., Borgeat, A., and Blumenthal, S. (2012). The role of continuous peripheral nerve blocks. *Anesthesiol. Res. Pract.* **2012**, 560879.
- Akopian, A.N., Souslova, V., England, S., Okuse, K., Ogata, N., Ure, J., Smith, A., Kerr, B.J., McMahon, S.B., Boyce, S., et al. (1999). The tetrodotoxin-resistant sodium channel SNS has a specialized function in pain pathways. *Nat. Neurosci.* **2**, 541–548.
- Backonja, M.M., Attal, N., Baron, R., Bouhassira, D., Drangholt, M., Dyck, P.J., Edwards, R.R., Freeman, R., Gracely, R., Haanpaa, M.H., et al. (2013). Value of quantitative sensory testing in neurological and pain disorders: NeuPSIG consensus. *Pain* **154**, 1807–1819.
- Baron, R., Levine, J.D., and Fields, H.L. (1999). Causalgia and reflex sympathetic dystrophy: does the sympathetic nervous system contribute to the generation of pain? *Muscle Nerve* **22**, 678–695.
- Bautista, D.M., Jordt, S.-E., Nikai, T., Tsuruda, P.R., Read, A.J., Poblete, J., Yamoah, E.N., Basbaum, A.I., and Julius, D. (2006). TRPA1 mediates the inflammatory actions of environmental irritants and proalgesic agents. *Cell* **124**, 1269–1282.
- Bennett, G.J., and Xie, Y.K. (1988). A peripheral mononeuropathy in rat that produces disorders of pain sensation like those seen in man. *Pain* **33**, 87–107.
- Bernardini, C., and Maggiolo, F. (2013). Triple-combination rilpivirine, emtricitabine, and tenofovir (Complera™/Eviplera™) in the treatment of HIV infection. *Patient Prefer Adherence* **7**, 531–542.
- Bessou, P., and Perl, E.R. (1969). Response of cutaneous sensory units with unmyelinated fibers to noxious stimuli. *J. Neurophysiol.* **32**, 1025–1043.
- Brumovsky, P., Villar, M.J., and Hökfelt, T. (2006). Tyrosine hydroxylase is expressed in a subpopulation of small dorsal root ganglion neurons in the adult mouse. *Exp. Neurol.* **200**, 153–165.
- Burgess, P.R., and Perl, E.R. (1967). Myelinated afferent fibres responding specifically to noxious stimulation of the skin. *J. Physiol.* **190**, 541–562.
- Campbell, J.N., and Meyer, R.A. (2006). Mechanisms of neuropathic pain. *Neuron* **52**, 77–92.
- Chaplan, S.R., Bach, F.W., Pogrel, J.W., Chung, J.M., and Yaksh, T.L. (1994). Quantitative assessment of tactile allodynia in the rat paw. *J. Neurosci. Methods* **53**, 55–63.
- Clohisey, D.R., Palkert, D., Ramnaraine, M.L., Pekurovsky, I., and Oursler, M.J. (1996). Human breast cancer induces osteoclast activation and increases the number of osteoclasts at sites of tumor osteolysis. *J. Orthop. Res.* **14**, 396–402.
- Cox, J.J., Reimann, F., Nicholas, A.K., Thornton, G., Roberts, E., Springell, K., Karbani, G., Jafri, H., Mannan, J., Raashid, Y., et al. (2006). An SCN9A channelopathy causes congenital inability to experience pain. *Nature* **444**, 894–898.
- Danielian, P.S., Muccino, D., Rowitch, D.H., Michael, S.K., and McMahon, A.P. (1998). Modification of gene activity in mouse embryos in utero by a tamoxifen-inducible form of Cre recombinase. *Curr. Biol.* **8**, 1323–1326.
- Descoeur, J., Pereira, V., Pizzoccaro, A., Francois, A., Ling, B., Maffre, V., Couette, B., Busserolles, J., Courteix, C., Noel, J., et al. (2011). Oxaliplatin-induced cold hypersensitivity is due to remodelling of ion channel expression in nociceptors. *EMBO Mol Med* **3**, 266–278.
- Deuis, J.R., Zimmermann, K., Romanovsky, A.A., Possani, L.D., Cabot, P.J., Lewis, R.J., and Vetter, I. (2013). An animal model of oxaliplatin-induced cold allodynia reveals a crucial role for Nav1.6 in peripheral pain pathways. *Pain* **154**, 1749–1757.
- Egashira, N., Hirakawa, S., Kawashiri, T., Yano, T., Ikeshue, H., and Oishi, R. (2010). Mexiletine reverses oxaliplatin-induced neuropathic pain in rats. *J. Pharmacol. Sci.* **112**, 473–476.

- Eijkelkamp, N., Linley, J.E., Baker, M.D., Minett, M.S., Cregg, R., Werdehausen, R., Rugiero, F., and Wood, J.N. (2012). Neurological perspectives on voltage-gated sodium channels. *Brain* 135, 2585–2612.
- Eijkelkamp, N., Linley, J.E., Torres, J.M., Bee, L., Dickenson, A.H., Gringhuis, M., Minett, M.S., Hong, G.S., Lee, E., Oh, U., et al. (2013). A role for Piezo2 in EPAC1-dependent mechanical allodynia. *Nat Commun* 4, 1682.
- Falk, S., Uldall, M., and Heegaard, A.-M. (2012). The role of purinergic receptors in cancer-induced bone pain. *J. Osteoporos.* 2012, 758181.
- Falk, S., Uldall, M., Appel, C., Ding, M., and Heegaard, A.-M. (2013). Influence of sex differences on the progression of cancer-induced bone pain. *Anticancer Res.* 33, 1963–1969.
- García-Poblete, E., Fernández-García, H., Moro-Rodríguez, E., Catalá-Rodríguez, M., Rico-Morales, M.L., García-Gómez-de-las-Heras, S., and Palomar-Gallego, M.A. (2003). Sympathetic sprouting in dorsal root ganglia (DRG): a recent histological finding? *Histol. Histopathol.* 18, 575–586.
- Gasser, H.S. (1941). The classification of nerve fibers. *Ohio J. Sci.* 41, 145–159.
- Goldberg, Y.P., MacFarlane, J., MacDonald, M.L., Thompson, J., Dube, M.P., Mattice, M., Fraser, R., Young, C., Hossain, S., Pape, T., et al. (2007). Loss-of-function mutations in the Nav1.7 gene underlie congenital indifference to pain in multiple human populations. *Clin. Genet.* 71, 311–319.
- Honore, P., Rogers, S.D., Schwei, M.J., Salak-Johnson, J.L., Luger, N.M., Sabino, M.C., Clohisey, D.R., and Mantyh, P.W. (2000). Murine models of inflammatory, neuropathic and cancer pain each generates a unique set of neurochemical changes in the spinal cord and sensory neurons. *Neuroscience* 98, 585–598.
- Ke, C.B., He, W.S., Li, C.J., Shi, D., Gao, F., and Tian, Y.K. (2012). Enhanced SCN7A/Nax expression contributes to bone cancer pain by increasing excitability of neurons in dorsal root ganglion. *Neuroscience* 227, 80–89.
- Kim, S.H., and Chung, J.M. (1992). An experimental model for peripheral neuropathy produced by segmental spinal nerve ligation in the rat. *Pain* 50, 355–363.
- Kim, K.J., Yoon, Y.W., and Chung, J.M. (1997). Comparison of three rodent neuropathic pain models. *Exp. Brain Res.* 113, 200–206.
- Kinnane, N. (2007). Burden of bone disease. *Eur. J. Oncol. Nurs.* 11 (Suppl 2), S28–S31.
- Lagerström, M.C., Rogoz, K., Abrahamsen, B., Persson, E., Reinius, B., Nordenankar, K., Olund, C., Smith, C., Mendez, J.A., Chen, Z.-F., et al. (2010). VGLUT2-dependent sensory neurons in the TRPV1 population regulate pain and itch. *Neuron* 68, 529–542.
- Lagerström, M.C., Rogoz, K., Abrahamsen, B., Lind, A.-L., Olund, C., Smith, C., Mendez, J.A., Wallén-Mackenzie, Å., Wood, J.N., and Kullander, K. (2011). A sensory subpopulation depends on vesicular glutamate transporter 2 for mechanical pain, and together with substance P, inflammatory pain. *Proc. Natl. Acad. Sci. USA* 108, 5789–5794.
- Lallemend, F., and Erfors, P. (2012). Molecular interactions underlying the specification of sensory neurons. *Trends Neurosci.* 35, 373–381.
- Lau, J., Minett, M.S., Zhao, J., Dennehy, U., Wang, F., Wood, J.N., and Bogdanov, Y.D. (2011). Temporal control of gene deletion in sensory ganglia using a tamoxifen-inducible Advillin-Cre-ERT2 recombinase mouse. *Mol. Pain* 7, 100.
- Leo, N.A., Callahan, T.A., and Bonneau, R.H. (1998). Peripheral sympathetic denervation alters both the primary and memory cellular immune responses to herpes simplex virus infection. *Neuroimmunomodulation* 5, 22–35.
- Liu, X., Chung, K., and Chung, J.M. (1999). Ectopic discharges and adrenergic sensitivity of sensory neurons after spinal nerve injury. *Brain Res.* 849, 244–247.
- López-Álvarez, S., Mayo-Moldes, M., Zaballos, M., Iglesias, B.G., and Blanco-Dávila, R. (2012). Esmolol versus ketamine-remifentanyl combination for early postoperative analgesia after laparoscopic cholecystectomy: a randomized controlled trial. *Can. J. Anaesth.* 59, 442–448.
- Maratou, K., Wallace, V.C.J., Hasnie, F.S., Okuse, K., Hosseini, R., Jina, N., Blackbeard, J., Pheby, T., Orengo, C., Dickenson, A.H., et al. (2009). Comparison of dorsal root ganglion gene expression in rat models of traumatic and HIV-associated neuropathic pain. *Eur. J. Pain* 13, 387–398.
- McLachlan, E.M., Jänig, W., Devor, M., and Michaelis, M. (1993). Peripheral nerve injury triggers noradrenergic sprouting within dorsal root ganglia. *Nature* 363, 543–546.
- Mercadante, S. (1997). Malignant bone pain: pathophysiology and treatment. *Pain* 69, 1–18.
- Minett, M.S., Nassar, M.A., Clark, A.K., Passmore, G., Dickenson, A.H., Wang, F., Malcangio, M., and Wood, J.N. (2012). Distinct Nav1.7-dependent pain sensations require different sets of sensory and sympathetic neurons. *Nat Commun* 3, 791–799.
- Mishra, S.K., Tisel, S.M., Orestes, P., Bhango, S.K., and Hoon, M.A. (2011). TRPV1-lineage neurons are required for thermal sensation. *EMBO J.* 30, 582–593.
- Müller, J. (1842). *Elements of Physiology* (London: Taylor and Walton).
- Nassar, M.A., Stirling, L.C., Forlani, G., Baker, M.D., Matthews, E.A., Dickenson, A.H., and Wood, J.N. (2004). Nociceptor-specific gene deletion reveals a major role for Nav1.7 (PN1) in acute and inflammatory pain. *Proc. Natl. Acad. Sci. USA* 101, 12706–12711.
- Nassar, M.A., Levato, A., Stirling, L.C., and Wood, J.N. (2005). Neuropathic pain develops normally in mice lacking both Na(v)1.7 and Na(v)1.8. *Mol. Pain* 1, 24.
- Nassar, M.A., Baker, M.D., Levato, A., Ingram, R., Mallucci, G., McMahon, S.B., and Wood, J.N. (2006). Nerve injury induces robust allodynia and ectopic discharges in Nav1.3 null mutant mice. *Mol. Pain* 2, 33.
- Ostman, J.A., Nassar, M.A., Wood, J.N., and Baker, M.D. (2008). GTP up-regulated persistent Na⁺ current and enhanced nociceptor excitability require Nav1.9. *J. Physiol.* 586, 1077–1087.
- Ramer, M.S., and Bisby, M.A. (1998a). Sympathetic axons surround neuro-peptide-negative axotomized sensory neurons. *Neuroreport* 9, 3109–3113.
- Ramer, M.S., and Bisby, M.A. (1998b). Normal and injury-induced sympathetic innervation of rat dorsal root ganglia increases with age. *J. Comp. Neurol.* 394, 38–47.
- Ramer, M.S., and Bisby, M.A. (1998c). Differences in sympathetic innervation of mouse DRG following proximal or distal nerve lesions. *Exp. Neurol.* 152, 197–207.
- Renn, C.L., Carozzi, V.A., Rhee, P., Gallop, D., Dorsey, S.G., and Cavaletti, G. (2011). Multimodal assessment of painful peripheral neuropathy induced by chronic oxaliplatin-based chemotherapy in mice. *Mol. Pain* 7, 29.
- Roberts, W.J. (1986). A hypothesis on the physiological basis for causalgia and related pains. *Pain* 24, 297–311.
- Roberts, W.J., and Foglesong, M.E. (1988). Spinal recordings suggest that wide-dynamic-range neurons mediate sympathetically maintained pain. *Pain* 34, 289–304.
- Schmalhofer, W.A., Calhoun, J., Burrows, R., Bailey, T., Kohler, M.G., Weinglass, A.B., Kaczorowski, G.J., Garcia, M.L., Koltzenburg, M., and Priest, B.T. (2008). ProTx-II, a selective inhibitor of Nav1.7 sodium channels, blocks action potential propagation in nociceptors. *Mol. Pharmacol.* 74, 1476–1484.
- Schwei, M.J., Honore, P., Rogers, S.D., Salak-Johnson, J.L., Finke, M.P., Ramnaraine, M.L., Clohisey, D.R., and Mantyh, P.W. (1999). Neurochemical and cellular reorganization of the spinal cord in a murine model of bone cancer pain. *J. Neurosci.* 19, 10886–10897.
- Seltzer, Z., Dubner, R., and Shir, Y. (1990). A novel behavioral model of neuropathic pain disorders produced in rats by partial sciatic nerve injury. *Pain* 43, 205–218.
- Shields, S.D., Ahn, H.-S., Yang, Y., Han, C., Seal, R.P., Wood, J.N., Waxman, S.G., and Dib-Hajj, S.D. (2012). Nav1.8 expression is not restricted to nociceptors in mouse peripheral nervous system. *Pain* 153, 2017–2030.
- Sittl, R., Lampert, A., Huth, T., Schuy, E.T., Link, A.S., Fleckenstein, J., Alzheimer, C., Grafe, P., and Carr, R.W. (2012). Anticancer drug oxaliplatin induces acute cooling-aggravated neuropathy via sodium channel subtype

- Na(V)1.6-resurgent and persistent current. *Proc. Natl. Acad. Sci. USA* 109, 6704–6709.
- Torebjörk, E., Wahren, L., Wallin, G., Hallin, R., and Koltzenburg, M. (1995). Noradrenaline-evoked pain in neuralgia. *Pain* 63, 11–20.
- Velasco, R., and Bruna, J. (2010). [Chemotherapy-induced peripheral neuropathy: an unresolved issue]. *Neurologia* 25, 116–131.
- Vrontou, S., Wong, A.M., Rau, K.K., Koerber, H.R., and Anderson, D.J. (2013). Genetic identification of C fibres that detect massage-like stroking of hairy skin in vivo. *Nature* 493, 669–673.
- Wagner, R., DeLeo, J.A., Coombs, D.W., Willenbring, S., and Fromm, C. (1993). Spinal dynorphin immunoreactivity increases bilaterally in a neuropathic pain model. *Brain Res.* 629, 323–326.
- Waxman, S.G. (2013). Painful Na-channelopathies: an expanding universe. *Trends Mol. Med.* 19, 406–409.
- Xie, W., Strong, J.A., and Zhang, J.-M. (2010). Increased excitability and spontaneous activity of rat sensory neurons following in vitro stimulation of sympathetic fiber sprouts in the isolated dorsal root ganglion. *Pain* 151, 447–459.
- Xie, W., Strong, J.A., Mao, J., and Zhang, J.-M. (2011). Highly localized interactions between sensory neurons and sprouting sympathetic fibers observed in a transgenic tyrosine hydroxylase reporter mouse. *Mol. Pain* 7, 53.
- Zariwala, H.A., Borghuis, B.G., Hoogland, T.M., Madisen, L., Tian, L., De Zeeuw, C.I., Zeng, H., Looger, L.L., Svoboda, K., and Chen, T.W. (2012). A Cre-dependent GCaMP3 reporter mouse for neuronal imaging in vivo. *J. Neurosci.* 32, 3131–3141.

Ribosome Profiling Reveals Pervasive Translation Outside of Annotated Protein-Coding Genes

Nicholas T. Ingolia,^{1,5,*} Gloria A. Brar,^{2,5} Noam Stern-Ginossar,^{2,6} Michael S. Harris,^{1,3,5} Gaëlle J.S. Talhouarne,^{1,3} Sarah E. Jackson,⁴ Mark R. Wills,⁴ and Jonathan S. Weissman²

¹Department of Embryology, Carnegie Institution for Science, Baltimore, MD 21218, USA

²Department of Cellular and Molecular Pharmacology, Howard Hughes Medical Institute, Center for RNA Systems Biology, California Institute for Quantitative Biosciences, University of California, San Francisco, San Francisco, CA 94158, USA

³Department of Biology, The Johns Hopkins University, Baltimore, MD 21218, USA

⁴Department of Medicine, University of Cambridge, Cambridge CB2 0QQ, UK

⁵Present address: Department of Molecular and Cell Biology, University of California, Berkeley, Berkeley, CA 94720, USA

⁶Present address: Department of Molecular Genetics, Weizmann Institute of Science, Rehovot 76100, Israel

*Correspondence: ingolia@berkeley.edu

<http://dx.doi.org/10.1016/j.celrep.2014.07.045>

This is an open access article under the CC BY license (<http://creativecommons.org/licenses/by/3.0/>).

SUMMARY

Ribosome profiling suggests that ribosomes occupy many regions of the transcriptome thought to be noncoding, including 5' UTRs and long noncoding RNAs (lncRNAs). Apparent ribosome footprints outside of protein-coding regions raise the possibility of artifacts unrelated to translation, particularly when they occupy multiple, overlapping open reading frames (ORFs). Here, we show hallmarks of translation in these footprints: copurification with the large ribosomal subunit, response to drugs targeting elongation, trinucleotide periodicity, and initiation at early AUGs. We develop a metric for distinguishing between 80S footprints and nonribosomal sources using footprint size distributions, which validates the vast majority of footprints outside of coding regions. We present evidence for polypeptide production beyond annotated genes, including the induction of immune responses following human cytomegalovirus (HCMV) infection. Translation is pervasive on cytosolic transcripts outside of conserved reading frames, and direct detection of this expanded universe of translated products enables efforts at understanding how cells manage and exploit its consequences.

INTRODUCTION

Identifying the genomic regions that are transcribed and translated is a fundamental step in annotating a genome and understanding its expression. A variety of microarray- and sequencing-based approaches can reveal the mRNA content of the cell (Bertone et al., 2004; Carninci et al., 2005; Wang et al., 2009), but it has proven more challenging to experimentally define translated sequences within the genome or the transcriptome. Historically,

protein-coding sequences were discovered by search for long (>100 codon) open reading frames, which are unlikely to occur in the absence of selection against stop codons. Widespread use of this approach has also been based on the assumption that short peptides are unlikely to fold into stable structures and thus perform robust biological functions. Recently, more-sophisticated conservation-based metrics, such as PhyloCSF, were developed for the computational identification of sequences that appear to encode proteins over a broad size range (Lin et al., 2008, 2011). However, these approaches focus on identifying regions of the genome experiencing selective pressure to maintain a reading frame encoding a functional protein. The questions of which parts of the genome are translated and whether or not the protein product has an adaptive function in the cell are related but distinct; the former can be answered by experimentally finding the locations of ribosomes on mRNAs.

Global profiling of transcription and mRNA abundance has revealed a class of transcripts with no clear protein-coding potential (Bertone et al., 2004; Carninci et al., 2005; Guttman et al., 2009). Many of these RNAs were long RNA polymerase II products, transcribed from genomic regions far from known protein-coding genes and thus were named long noncoding RNAs (lncRNAs).

The discovery of these surprising RNAs in the transcriptome as well as the existence of short upstream open reading frames (uORFs) in 5' leader regions (often referred to as 5' UTRs; Calvo et al., 2009; Wethmar et al., 2014) highlight the need for comparable direct, experimental maps of translation. Whereas, based on both lack of conservation and the distribution of ribosome-protected fragments, there is strong evidence that most lncRNAs do not encode proteins with conserved adaptive cellular roles (Cabili et al., 2011; Chew et al., 2013; Guttman et al., 2013), these computational approaches could miss functional coding sequences, particularly those that are short and/or species specific (Reinhardt et al., 2013). Furthermore, translation and protein synthesis have impacts beyond the production of stable proteins with discrete molecular functions—polypeptide products from all cellular translation must be degraded and noncanonical translation products yield unanticipated

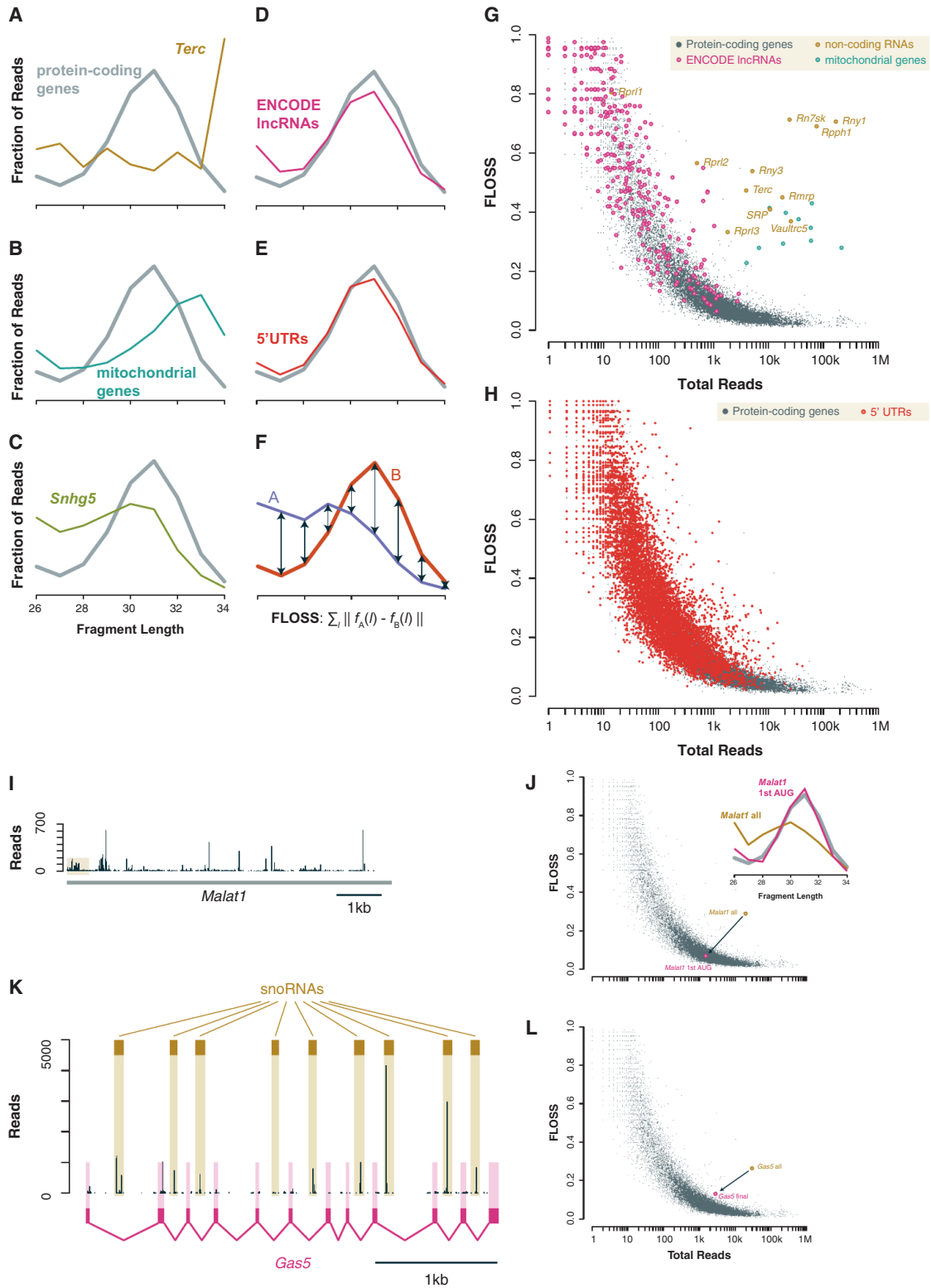


Figure 1. Fragment Length Analysis Distinguishes True Ribosome Footprints on Coding and Noncoding Sequences

(A–E) Distribution of fragment lengths mapping to nuclear coding sequences (CDSs) compared to (A) the telomerase RNA *Terc*, (B) mitochondrial coding sequences, (C) snoRNA host gene *Snhg5*, (D) ENCODE lncRNAs, and (E) 5' UTRs of protein-coding genes in ribosome-profiling data from etemine-treated mESCs. (F) Metric comparing the similarity of two length distributions.

(legend continued on next page)

antigens that may play roles in viral detection or in autoimmunity (Starck et al., 2012). Finally, the process of translation can affect the stability of the template message by triggering cotranslational decay pathways including nonsense-mediated decay (NMD) (Rebbapragada and Lykke-Andersen, 2009). Knowing what transcripts are translated has important implications for the fate of the RNA, the ribosome, and the cell. The ribosome-profiling technique provides a unique opportunity to experimentally address this question.

Ribosome profiling is an approach for mapping the exact position of translating ribosomes across the transcriptome by deep sequencing of the mRNA footprints that are occupied by the ribosomes and thereby physically protected from nuclease digestion (Ingolia et al., 2009; Steitz, 1969; Wolin and Walter, 1988). Analysis of these ribosome-protected mRNA fragments yields a quantitative and detailed map of ribosome occupancy that reveals translation in the cell with single-nucleotide resolution. Most ribosome footprints fall within known coding sequences, where they showed three-nucleotide periodicity reflecting the triplet nature of the genetic code. However, ribosome-profiling data suggested that some predicted noncoding regions of the transcriptome were translated (Ingolia et al., 2011). In some cases, these footprints were organized on single reading frames that closely resembled known coding sequences except for their shorter length (Brar et al., 2012; Stern-Ginossar et al., 2012). In other cases, footprints were not restricted to a single predominant reading frame based on metrics such as the ribosome release score (RRS) or the disengagement score (DS) (Chew et al., 2013; Guttman et al., 2013). This second group of predicted translated sequences, present on some lncRNAs as well as the 5' leaders of many mRNAs, can be distinguished both from conserved protein-coding genes, where one single reading frame does predominate, and from the 3' UTRs of most mRNAs, which are devoid of ribosome footprints (Chew et al., 2013). The high ribosome occupancy on some of these regions, comparable to that on protein-coding genes, suggests a similar stoichiometry of polypeptide production.

The broad implications of pervasive translation and the discrepancy between ribosome profiling and conservation analysis pose an immediate question: do the footprint sequences detected in these profiling experiments indicate the presence of assembled (80S) ribosomes? Here, we address this question and present several ways to distinguish true 80S footprints in ribosome-profiling data. We first classify protected RNA fragments based on their size distribution, a purely computational analysis that can be applied to existing data and to new profiling data collected without experimental modification. Our analysis discriminates cleanly between true footprints and known sources

of contamination. We validate the results from our fragment length classifier with two new lines of experimental evidence: drugs that target the elongating 80S ribosome specifically and affinity purification of the large ribosomal subunit, both of which support the translation of lncRNAs and 5' UTRs. We also show that footprints on these noncoding sequences demonstrate hallmarks of eukaryotic translation. Finally, we verify the accumulation of protein products from noncanonical translation and demonstrate the potential functional impact of novel human cytomegalovirus (HCMV) proteins as a source of viral antigens. Our results show that the universe of translated regions extends beyond long conserved regions encoding large, well-conserved proteins.

RESULTS

The Characteristic Length of Ribosome Footprints Distinguishes Them from Background RNA Fragments

The ribosome physically encloses its mRNA template and protects a characteristic length of this RNA from nuclease digestion (Steitz, 1969; Wolin and Walter, 1988). In ribosome-profiling data, the overall size distribution of fragments derived from protein-coding sequences, which should predominantly reflect true ribosome footprints, differs from the lengths of the abundant rRNA contamination found in profiling samples (Ingolia et al., 2009, 2011). We reasoned that fragment size could likewise distinguish true ribosome footprints from other, nonribosomal contaminants, such as RNA regions that are protected by protein complexes or stable RNA secondary structure. The exact length distribution of protected fragments can vary slightly between samples, likely due to differences in digestion conditions (Ingolia et al., 2012). Furthermore, distinct ribosome conformations can lead to significantly different mRNA footprint lengths (Lareau et al., 2014), and the predominant conformation may vary between samples. In order to avoid these confounding effects, we compared the size distributions of fragments derived from noncoding sequences to those on protein-coding genes within a single sample, treated with translation elongation inhibitors that should capture most ribosomes in a specific state (Lareau et al., 2014; Wolin and Walter, 1988).

We gathered new ribosome-profiling data from mouse embryonic stem cells (mESCs) treated with the translation elongation inhibitor emetine in order to obtain footprints with stronger reading frame bias (Ingolia et al., 2011, 2012). Fragment size distributions in this sample clearly distinguished true ribosome footprints, which predominate on coding sequences, from background RNA contained in nonribosomal ribonucleoprotein (RNP) complexes such as telomerase (Figure 1A). They also separated

(G) Fragment length analysis plot of total reads per transcript and FLOSS relative to the nuclear coding sequence average. An FLOSS cutoff is based on an extreme outlier threshold for annotated coding sequences. lncRNAs resemble annotated, nuclear protein-coding genes, whereas functional RNAs and mitochondrial coding sequences are distinct.

(H) As (G), comparing 5' UTRs and coding sequences of nuclear-encoded mRNAs.

(I) Read count profile on *Malat1* with an inset showing ribosomes on a non-AUG uORF and the first reading frame at the 5' end of the transcript. An inset shows the fragment length distribution for the first reading frame, which matches the overall coding sequence average, and the whole transcript, which does not.

(J) Fragment length analysis showing the shift from the entire *Malat1* transcript, which contains substantial background, to the first *Malat1* reading frame, which contains true ribosome footprints.

(K) Read count profile across the primary *Gas5* transcript with the snoRNAs and the fully spliced transcript shown.

(L) As (J) for the primary *GAS5* transcript, containing snoRNA precursors, and the fully spliced product.

footprints of the 80S ribosome from fragments of mitochondrial coding sequences that likely reflect footprints of the distinct mitochondrial ribosome (Figure 1B) and noncoding short RNAs that associate with the cytosolic ribosome or its precursors, such as small nucleolar RNAs (snoRNAs) (Figure 1C). By contrast, RNA fragments derived from lncRNAs and from 5' UTRs showed a size distribution much like that seen on coding sequences (Figures 1D and 1E). This similarity provides evidence that the protected fragments on these two classes of noncoding sequences consist principally of 80S ribosome footprints and, thus, that translation occurs outside of annotated protein-coding regions.

Classifying the Translation Status of Individual Transcripts and Subregions

We next adapted our fragment length distribution analysis to distinguish between individual transcripts that show substantial background fragments from those having true 80S footprints. When hundreds or thousands of ribosome-footprint-sequencing reads are available for a single transcript, their length distribution should converge to match the characteristic ribosome footprint size. We define a fragment length organization similarity score (FLOSS) that measures the magnitude of disagreement between these two distributions, with lower scores reflecting higher similarity (Figure 1F). Thousands of well-expressed protein-coding transcripts almost uniformly scored well, and the similarity improved with increasing read counts, as expected (Figure 1G). As with many sequencing-based analyses, this metric is less informative on transcripts with few reads—an inevitable consequence of sampling error in estimating the fragment length distribution—but we are most interested in the transcripts with many reads and, thus, clear FLOSS results.

In order to contrast nonribosomal background with true ribosome footprints, we needed canonical set of nontranslated RNAs to compare with annotated protein-coding sequences. We selected transcripts with well-established molecular functions as RNAs and features likely to suppress their translation, such as an absence of 5' methylguanosine caps or assembly into stable ribonucleoprotein structures inaccessible to the translational machinery. Many of these transcripts, defined in previous studies as “classical” noncoding RNAs (Guttman et al., 2013), in fact yielded very few protected fragments. We did find several (including telomerase RNA, vault RNA, and RNase P) that we could test, however, and found that each could be distinguished clearly from annotated coding sequences. Likewise, every individual mitochondrially encoded message stood out clearly from nuclear genes. We concluded that this metric discriminates reliably between true 80S ribosome footprints and background RNA fragments on specific transcripts as well as on broad classes of RNAs.

FLOSS analysis revealed that ribosome-profiling-derived reads from lncRNAs and 5' UTRs overwhelmingly reflect true ribosome footprints. Protected fragments on nearly every individual lncRNA showed a FLOSS value very similar to that seen on coding sequences, in contrast to background from classical noncoding RNAs (Figure 1G). Individual 5' UTRs also grouped very well with coding sequences (Figure 1H).

We formalized this classification by defining a threshold FLOSS value, excluding transcripts that differed greatly from annotated

protein-coding genes. We set this threshold based on the read counts and FLOSS values for known protein-coding genes using Tukey's method, a widely accepted nonparametric criterion for extreme outliers (Tukey, 1977). This cutoff eliminated all classical noncoding RNAs with substantial (>100 reads) expression while retaining almost all annotated mRNAs (99.6%). The perfect specificity and extraordinary sensitivity likely overestimate the true performance of this metric, especially on transcripts that contribute a mixture of true translation and background. Nonetheless, the vast majority of 5' UTRs (96%) and lncRNAs (90%) were classified with protein-coding genes (Figures S1A and S1B). Not all 5' UTRs or lncRNAs produced protected RNA fragments in profiling experiments, but when fragments did appear, they generally resembled the ribosome footprints of coding sequences, suggesting true translation in these regions.

We previously reported apparent ribosome occupancy on the abundant and prototypical lncRNA *Malat1*, which is predominantly nuclear and thus is largely separated from the translational apparatus (Wilusz et al., 2008). This surprising result led us to investigate protected *Malat1* RNA fragments more closely (see Figure 1I). We saw a pattern that was highly suggestive of ribosome occupancy near the 5' end of the transcript, covering the first AUG-initiated reading frame with substantially lower ribosome density after the corresponding in-frame stop codon. We also saw several other sites in *Malat1* that produced abundant protected RNA fragments. Whereas the overall distribution of *Malat1* fragment lengths did not resemble the profile of true ribosome footprints, the first short reading frame did appear to contain 80S ribosomes (Figures 1I and 1J). Similarly, whereas the full *Malat1* transcript stood out from protein-coding genes by fragment length analysis, the upstream reading frame resembled those of ordinary protein-coding genes. Thus, *Malat1* RNA fragments appear both to contribute nonribosomal background, like telomerase or RNase P, and also to represent footprints from ribosomes translating its first ORF. As *Malat1* is predominantly nuclear, whereas the translation occurs in the cytosol, it would be interesting to find the ribosome density and the relative background contribution in the cytoplasmic fraction. MALAT1 is also unusual in that the mature form is not polyadenylated, but the triple-helix structure that protects its nonadenylated 3' end also supports efficient translation (Wilusz et al., 2012); the role of these ribosomes, if any, in the function of *Malat1* remains to be determined.

The noncoding RNA *Gas5* also yielded a complex mixture of translation and background RNA that could be separated by fragment length analysis. *Gas5* is a snoRNA host gene whose introns contain several snoRNAs; there are no long or conserved reading frames in the mature message. Nonetheless, the spliced RNA associates with ribosomes in order to trigger its degradation by NMD (Smith and Steitz, 1998). Fragment length analysis of the primary *Gas5* transcript indicates that it is a source of background RNA in profiling experiments, corresponding principally to the intronic snoRNAs (Figure 1K). Fragments that mapped to the fully processed *Gas5* transcript, with no remaining snoRNA sequences, resembled 80S footprints on coding sequences (Figures 1K and 1L). They were also concentrated in reading frames near the 5' end of the transcript, where translation is expected to occur.

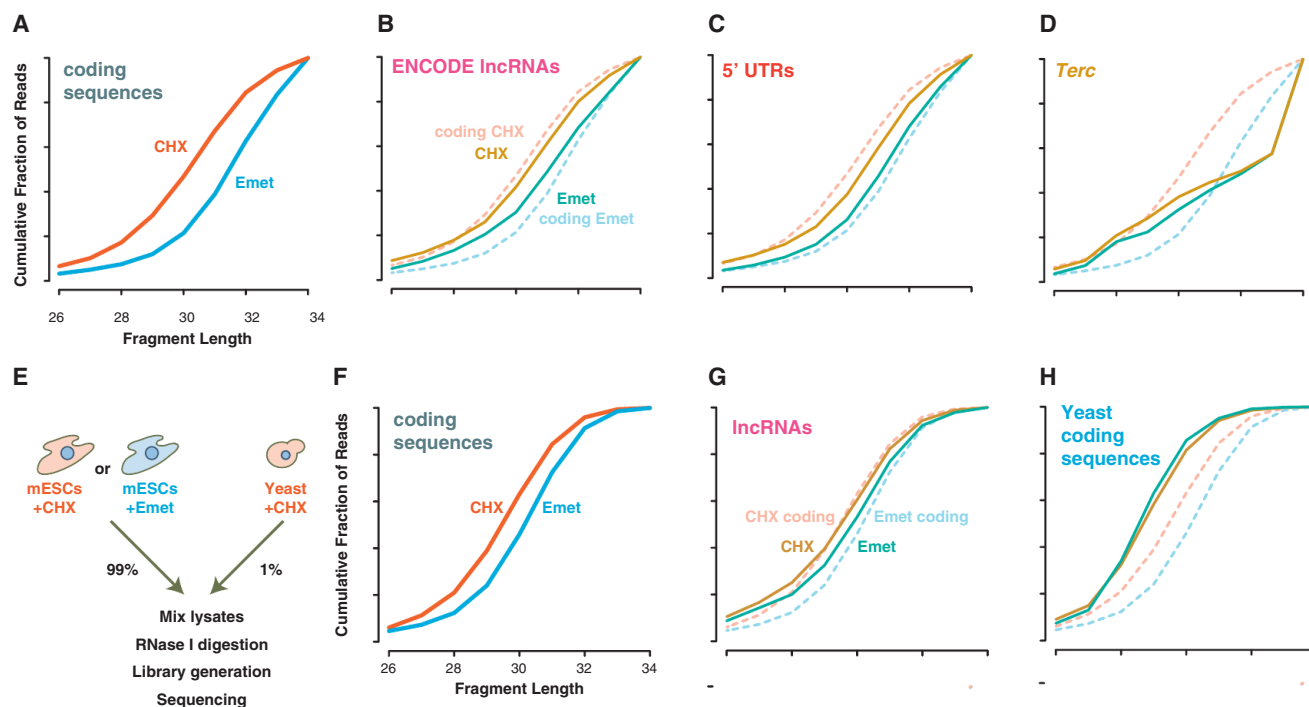


Figure 2. Elongation Inhibitors Shift Ribosome Footprint Sizes

(A) Cumulative length distribution shows ~ 1 nt larger footprints on annotated coding sequences from emetine- versus cycloheximide-treated cells (Ingolia et al., 2011).

(B–D) lncRNA (B) and 5' UTR (C) footprints from transcripts passing the FLOSS cutoff show a similar length shift, whereas background from (D) classical noncoding RNAs do not.

(E) Experimental design with cycloheximide-treated yeast polysomes as an internal standard for nuclease digestion and library generation.

(F and G) Annotated coding sequences (F) and lncRNAs (G) again show larger footprints in emetine-treated cells.

(H) Cycloheximide-stabilized footprints are not larger in the emetine-treated mESC lysate sample.

Taken together, these analyses show that fragment length analysis can discriminate between true 80S footprints and background RNA reads in ribosome-profiling data. Furthermore, this simple metric can be applied to existing profiling data sets as well as incorporated into computational workflows with no change to experimental protocols. It provides strong evidence for the presence of ribosomes based on comparisons with RNAs whose biology is well understood. As this analysis is correlative, however, we performed direct experimental tests to confirm that footprints on noncoding sequences reflected true translation.

Drugs that Inhibit Translation Specifically Affect Elongating Ribosome Footprints on Coding and Noncoding Sequences

Diverse translation inhibitors target distinct sites on the ribosome with high affinity and selectivity (McCoy et al., 2011; Schneider-Poetsch et al., 2010). We previously observed that mammalian cells treated with one such drug, cycloheximide, yielded ~ 1 nt shorter ribosome footprints over the body of open reading frames than those treated with another, emetine (Figure 2A; Ingolia et al., 2011). Both emetine and cycloheximide target the ribosome specifically, and so the differences observed in mammalian cells between these two drugs should appear only in true footprints of elongating ribosomes.

We set out to use the selectivity of these drugs for the ribosome as an additional test to distinguish true footprints. In aggregate, fragments on lncRNAs and on 5' UTRs showed a similar but more modest length shift to that seen on protein-coding genes—the cumulative length distribution on both noncoding regions is larger in emetine than in cycloheximide (Figures 2B and 2C). Drug treatment may affect footprints on noncoding RNAs less than those on coding sequences because the translated reading frames on these RNAs are short, and thus terminating ribosomes, whose footprints appear to differ slightly from elongating ribosomes (Ingolia et al., 2011), comprise a larger fraction of the total ribosomes. Alternately, a fraction of these footprints may reflect posttermination ribosome footprints, which can accumulate in yeast defective for ribosome-recycling factors and which should not respond to drugs targeting elongation (Guydosh and Green, 2014). Nonribosomal background fragments do not shift in length between these two elongation inhibitors (Figure 2D).

We gathered new ribosome-profiling data from cycloheximide- as well as emetine-treated mESCs and included a small amount of cycloheximide-stabilized yeast polysomes in each sample in order to monitor any differences in the extent of nuclease digestion between samples (Figure 2E). The true ribosome footprints on annotated coding sequences were again shorter from cycloheximide-treated than from emetine-treated

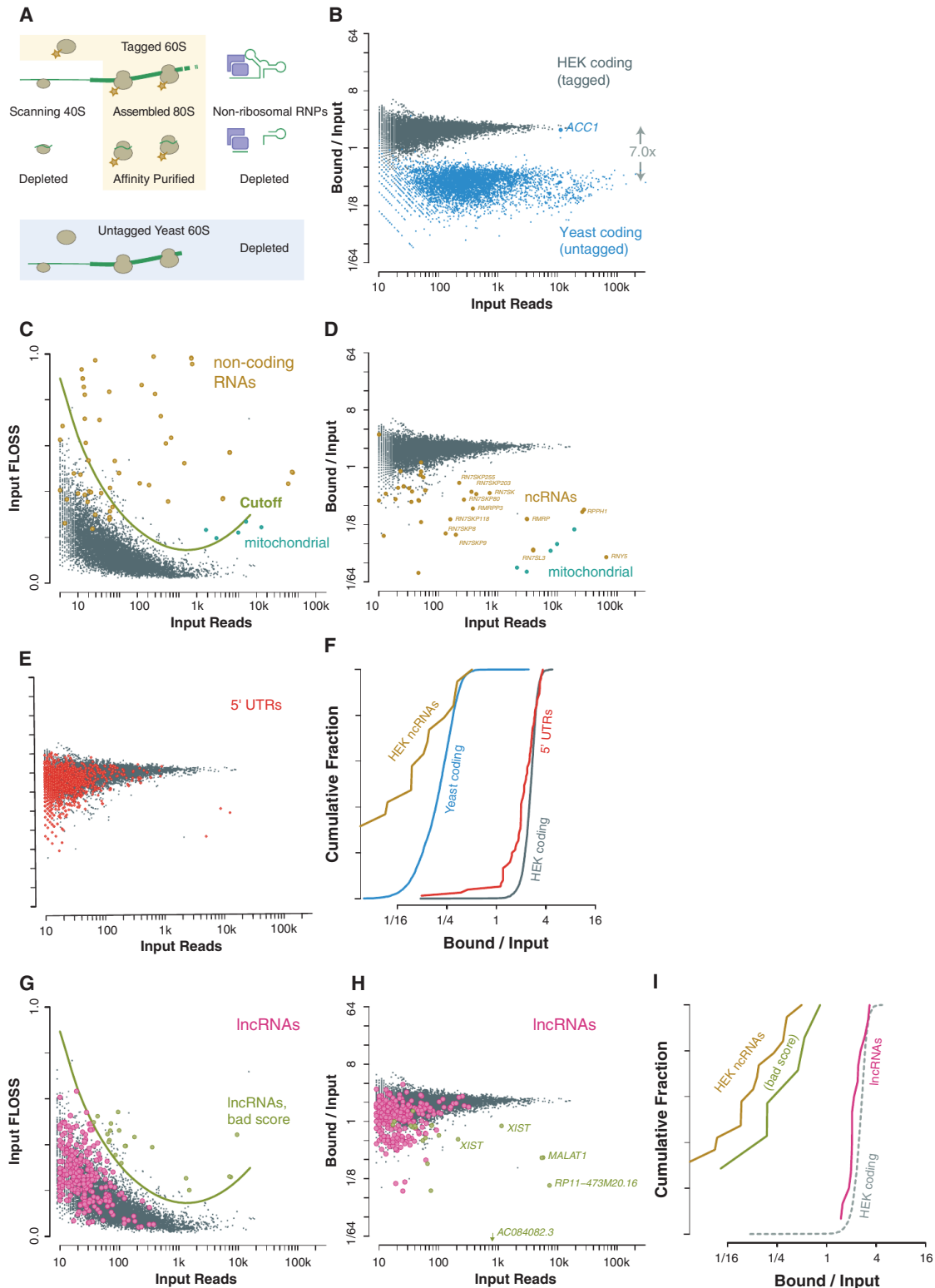


Figure 3. Ribosome Affinity Purification Separates 80S Footprints from Background RNA

(A) Schematic showing that affinity purification of tagged 60S ribosome subunits recovers 80S footprints but depletes background from nonribosomal RNPs, potential scanning 40S footprints, and footprints of untagged yeast 80S ribosomes.

(legend continued on next page)

cells, though the difference was less pronounced (Figure 2F). The length of footprints on lncRNAs also shifted in response to treatment with elongation inhibitors (Figure 2G), and these length shifts were significant on protein-coding genes ($p < 1 \times 10^{-4}$), 5' UTRs ($p < 1 \times 10^{-4}$), and on lncRNAs ($p < 0.01$; Figure S2). In contrast, the footprints from the yeast ribosomes included as an internal control showed, if anything, a very modest shift in the opposite direction (Figure 2H) that did not rise to the level of significance ($p > 0.05$; Figure S2), arguing that the reproducible difference between cycloheximide- and emetine-treated polysomes did not result from differences in nuclease digestion or library generation that affect all RNA fragments in a sample.

Ribosome Footprints on Classical Coding Sequences, 5' UTRs, and lncRNAs Copurify with the Large Ribosomal Subunit

We next sought to verify that footprints seen outside of annotated coding regions copurified specifically with the ribosome. Ribosome affinity purification would provide strong evidence that footprints on lncRNAs and on 5' UTRs were bound to the ribosome (Figure 3A). We typically recover ribosomes by sedimentation in an ultracentrifuge, but this purification provides little specificity for ribosomes over other large RNPs. The most prominent classical noncoding RNAs that contribute to background in ribosome-profiling experiments are components of nonribosomal RNPs, such as RNase P, telomerase, and the vault RNP (Figure 1G). We infer that these RNP assemblies both protect RNA fragments from digestion and then sediment with ribosomes, and it seemed possible that some apparent ribosome footprints on lncRNAs actually reflected the incorporation of the lncRNA into a similar RNP complex.

Specific affinity purification of the ribosome would deplete background from these RNPs. The large (60S) subunit joins at the last step in translation initiation and does not associate with mRNA prior to this time, and so any footprint associated with the 60S subunit derives from a ribosome that has completed initiation and begun translation (Aitken and Lorsch, 2012). Ribosome-profiling data are unlikely to include footprints of small (40S) subunits scanning 5' UTRs prior to initiation, because these complexes are unstable in the absence of chemical crosslinking and are expected to protect a different mRNA footprint size from assembled 80S ribosomes (Valásek et al., 2007). Nonetheless, we wished to verify that footprints on 5' UTRs reflected postinitiation-assembled (80S) ribosomes.

In order to purify 80S (and 60S) ribosomes specifically, we developed an affinity-tagged version of large subunit ribosomal protein L1 (formerly RPL10A). Several ribosome epitope tags have been developed for lineage-specific polysome isolation,

including the translating ribosome affinity purification tag, in which L1 is fused to enhanced GFP (Heiman et al., 2008). We believed that *in vivo* biotinylation of L1 would offer advantages over epitope tags, allowing us to exploit the high affinity and rapid association of biotin and streptavidin to purify tagged ribosomes. We placed a biotin acceptor peptide at the end of a long, flexible linker at the C terminus of L1 and coexpressed this tagged protein along with birA, the cognate *E. coli* biotin ligase, in human embryonic kidney 293 (HEK293) cells. Tagged L1 was biotinylated, dependent on the presence of birA, and L1-biotin was incorporated into ribosomes.

In order to test our enrichment of tagged ribosomes, we mixed lysate from human cells expressing L1-biotin (in addition to their endogenous L1) with a control yeast lysate lacking biotinylated ribosomes and compared the fate of the human ribosome footprints to footprints from yeast genes. We performed nuclease footprinting of this mixture, collected all ribosomes by filtration through Sephacryl S400 columns, and purified the tagged human ribosomes by streptavidin affinity. Footprints from human protein-coding genes were strongly enriched in the streptavidin-bound sample relative to footprints from yeast transcripts (Figure 3B). The only exception was the yeast gene *ACC1*, which encodes the endogenous yeast biotin carrier protein. We assume that it is biotinylated cotranslationally *in vivo* and so footprints recovered by affinity purification through the nascent chain. Consistent with this model, only footprints from the 3' end of *ACC1*, corresponding to ribosomes that have synthesized the biotin acceptor site of *Acc1p*, are enriched. Importantly, the observed specificity for human mRNAs also excluded postlysis association of human ribosomes to yeast mRNAs, arguing strongly that footprints seen in ribosome-profiling experiments reflect translation that initiated *in vivo* prior to cell lysis. Fragment length distribution analysis provided further evidence against human ribosomes subject to affinity enrichment on yeast mRNAs, as protected fragments on human and yeast ribosomes are distinct in the mixed lysate and there was no evidence for a shift toward human fragment lengths on yeast messages following affinity purification. Human snoRNA reads also copurified with biotinylated L1, though somewhat less efficiently than ribosome footprints, as we expect due to their binding to preribosomal complexes in order to guide pre-rRNA modification (Figures S3A–S3C).

We then investigated the fate of other human-derived background reads following affinity purification of ribosomes. As noted above, profiling data after conventional ribosome sedimentation in HEK cells contained fragments mapping to several classical noncoding RNAs that also appeared in the mESC profiling, such as RNase P. Fragment length analysis using the

(B) Human ribosome footprints are retained during ribosome affinity purification whereas yeast ribosome footprints (excepting the yeast biotin carrier *ACC1*) are depleted.

(C) Fragment length analysis of nuclear and mitochondrial coding sequences and of functional noncoding RNAs in HEK cells. A fragment length score cutoff based on extreme outliers relative to coding sequences excludes background fragments.

(D) Ribosome footprints are retained during ribosome affinity purification whereas mitochondrial footprints and noncoding RNAs are depleted.

(E and F) Ribosome footprints on 5' UTRs are retained during affinity purification of the 60S ribosomal subunit.

(G) Fragment length analysis of ENCODE lncRNAs, identifying a small number of transcripts with likely nonribosomal contamination.

(H and I) Ribosome footprints on lncRNAs are retained during ribosome affinity purification, whereas many sources of nonribosomal contamination, including the nuclear noncoding RNA *XIST*, are depleted.

FLOSS reliably discriminated this background from footprints on coding sequences (Figure 3D). These same transcript fragments were also depleted in affinity-purified profiling samples, at least as strongly as were yeast-coding sequences (Figures 3E and 3F). Fragments from mitochondrial coding sequences were also strongly depleted, as the mitochondrial ribosome, which is entirely distinct from the cytosolic ribosome, lacked a biotin tag.

Having established affinity purification as a physical separation of background RNA fragments from true ribosome footprints, we next turned to investigate the status of apparent ribosome footprints in noncoding regions. We first verified that, as in mESCs, the protected fragments size distribution on HEK cell 5' UTRs closely resembled ribosome footprints from the coding sequences (Figure S3D). These 5' UTR protected fragments also copurified with the large ribosomal subunit in nearly all cases (Figure 3C). We thus conclude that these fragments are true 80S ribosome footprints and do not reflect scanning 40S subunits. Likewise, we find that protected fragments on most HEK lncRNAs are physically bound to the ribosome and likely reflect true translation of these noncoding RNAs (Figures 3G–3I). Furthermore, the small number of lncRNAs yielding substantial non-ribosome-associated fragments were independently identified as sources of background by the FLOSS analysis.

Translation on lncRNAs Occurs in AUG-Initiated Reading Frames near the 5' End of the Transcript

lncRNAs lack a conserved, protein-coding reading frame by definition, and accordingly, ribosome footprints on these transcripts are not organized into a single, discrete reading frame without downstream translation in the manner seen on mRNAs (Chew et al., 2013; Guttman et al., 2013; Ingolia et al., 2011). Translation on lncRNAs and on mRNAs could differ fundamentally, however, and we wished to determine whether ribosome occupancy on lncRNAs show key features of eukaryotic translation. Whereas translation outside of annotated protein-coding regions often initiates at a variety of near-cognate codons in overlapping reading frames, obscuring some features of translation that manifest clearly on transcripts encoding a conserved protein, initiation should nonetheless be strongly biased toward AUG codons near the 5' end of RNAs, and elongating ribosomes should show enrichment in the reading frame that follows until it ends at a stop codon. In order to evaluate the pattern of translation on lncRNA, we analyzed the initiation-site-profiling data we gathered from mESCs (Ingolia et al., 2011). We previously reported that brief treatment with the drug harringtonine causes ribosomes to accumulate at start codons while allowing run-off depletion of ribosomes over the rest of the coding sequence. This can be used to robustly identify translation initiation sites (Ingolia et al., 2011; Stern-Ginossar et al., 2012). Here, we use a simplified criterion to detect peaks of ribosome occupancy over AUG codons following harringtonine treatment (Figure 4A). This approach is robust against the possibility of concurrent translation of other, overlapping reading frames. Whereas we considered only AUG codons as candidate start sites, we found that, on the majority of lncRNAs, the start site we selected was the highest occupancy ribosome position of the entire RNA (Figure 4B), suggesting that this assumption was reasonable.

Initiation sites on lncRNAs detected in harringtonine-profiling data showed hallmarks of eukaryotic translation. In the canonical initiation pathway, factors bound to the 5' cap recruit a preinitiation complex that scans the RNA directionally to identify a start codon. Consistent with this mechanism of translation, the start sites detected in harringtonine profiling generally fell near the beginning of the lncRNA, within a few hundred nucleotides of the 5' end (Figure 4C) and at one of the first AUG codons on the transcript (Figure 4D). This bias toward early AUG codons is well explained by the classical model of eukaryotic initiation. By contrast, it is not likely that background RNA fragments not indicative of translation would show a strong preference for AUG codons near the 5' end of transcripts.

Based on these observations, we next looked for evidence of elongating ribosome footprints in the reading frames associated with these initiation sites. Earlier studies argued against the predominance of a single open reading frame on lncRNAs. Both studies employed similar metrics—the RRS or the DS—to demonstrate that the abrupt drop in ribosome occupancy at the end of coding sequences was not seen for short reading frames in 5' UTRs and on lncRNAs (Chew et al., 2013; Guttman et al., 2013). The absence of clear termination in any single reading frame argues that multiple, overlapping reading frames are translated on these RNAs. Nonetheless, we expected that the start sites we detected should result in elevated ribosome occupancy in the downstream open reading frame relative to the overall transcript. Indeed, we found the observed number of ribosome footprints within predicted reading frames on lncRNAs exceeded the number expected based on the overall ribosome density the length of the reading frame, often 10-fold or more, and never strongly depleted relative to the transcript overall (Figure 4E). This comparison is related to the inside/outside score, the ratio of footprints inside versus outside a candidate reading frame, used by Chew et al. (2013). Furthermore, we found that footprints within the open reading frame immediately following the predicted strongest initiation site on a lncRNA showed codon periodicity relative to that start site, similar to the periodicity seen in annotated protein-coding genes, whereas footprints outside of these reading frames do not (Figure 4F). This pattern of footprint occupancy is consistent with substantial in-frame translation from the predicted start site occurring alongside translation of many other reading frames on the transcript, including those initiating at near-cognate, non-AUG sites. This translation, particularly the downstream component that lacks a reading frame signal relative to the strongest AUG start site and thus reflects overlapping translation in alternate reading frames, would reduce RRS and DS metrics on these lncRNAs relative to annotated mRNAs.

Fragment Length Analysis Supports Translation on Novel Reading Frames in Meiotic Yeast

In previous studies, we defined translated reading frames in meiotic budding yeast using ribosome-profiling data (Brar et al., 2012). We wished to determine whether FLOSS analysis could be applied in this distantly related organism to support our annotations. Cycloheximide-stabilized ribosome footprints lying within yeast-coding sequences show a tight size distribution, as we observed previously, which could be readily

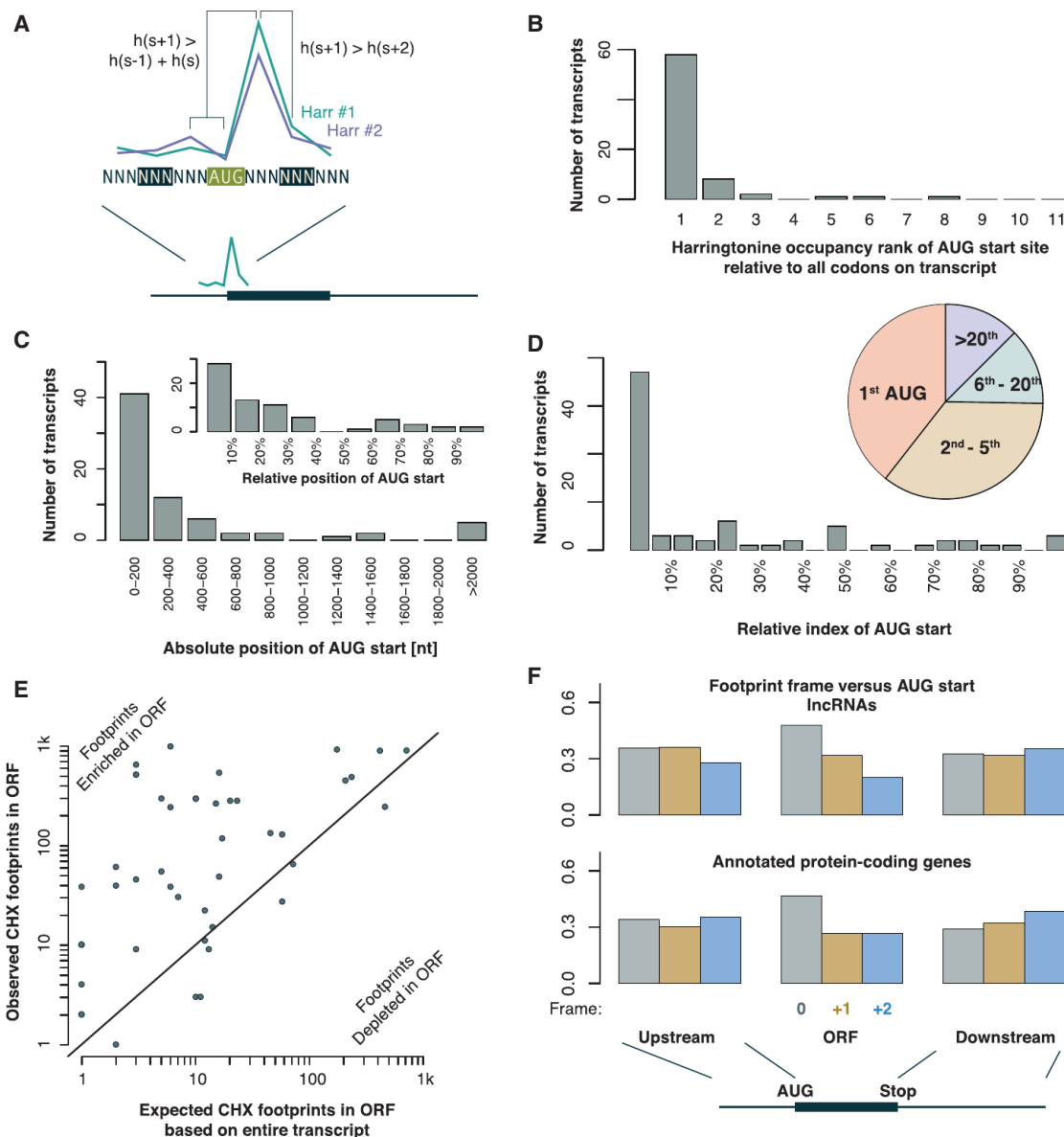


Figure 4. Ribosomes Translate Detectable Reading Frames on lncRNAs

(A) Schematic of AUG start site detection using two harringtonine samples (from 120 s and 150 s treatment). The start site is an AUG codon with a peak in footprint density—higher occupancy than flanking codons—selected as the highest occupancy among peaks at AUGs.
 (B) AUG start sites typically show the highest footprint density among all codons, not just all AUGs with peaks.
 (C) AUG start sites typically fall in the first few hundred nt of transcripts and (inset) near the beginning of the transcript.
 (D) AUG start sites are typically among the first AUG codons on transcripts, with relative positions shown in the histogram and absolute index shown in the pie chart (i.e., nearly half of AUG start sites are the first AUG on the transcript overall).
 (E) Overall ribosome occupancy is higher in the ORFs downstream of AUG start sites, relative to the overall density on the transcript.
 (F) Footprints on lncRNAs downstream of detected AUG start sites and upstream of the stop codon are biased toward the frame of the ORF. Annotated protein-coding genes show similar reading frame bias within the ORF, but not in the 5' UTR (upstream) or 3' UTR (downstream).

distinguished from background RNA fragments derived from nontranslated yeast RNAs, including tRNAs and isolated snoRNAs, and from the validated yeast meiotic noncoding RNAs *IRT1*, *RME2*, and *RME3* (Figure 5A). As in mammals, we also found fragments of mitochondrial mRNAs, likely representing footprints of the mitoribosome, which were larger than cyto-

solic ribosome footprints. By contrast, the protected fragments on the large majority of new, independent ORFs and on upstream ORFs in the 5' UTRs of annotated protein-coding genes matched the size of true ribosome footprints closely (Figures 5B–5D). FLOSS analysis discriminated well between individual annotated coding sequences and noncoding transcripts (Figure 5E)

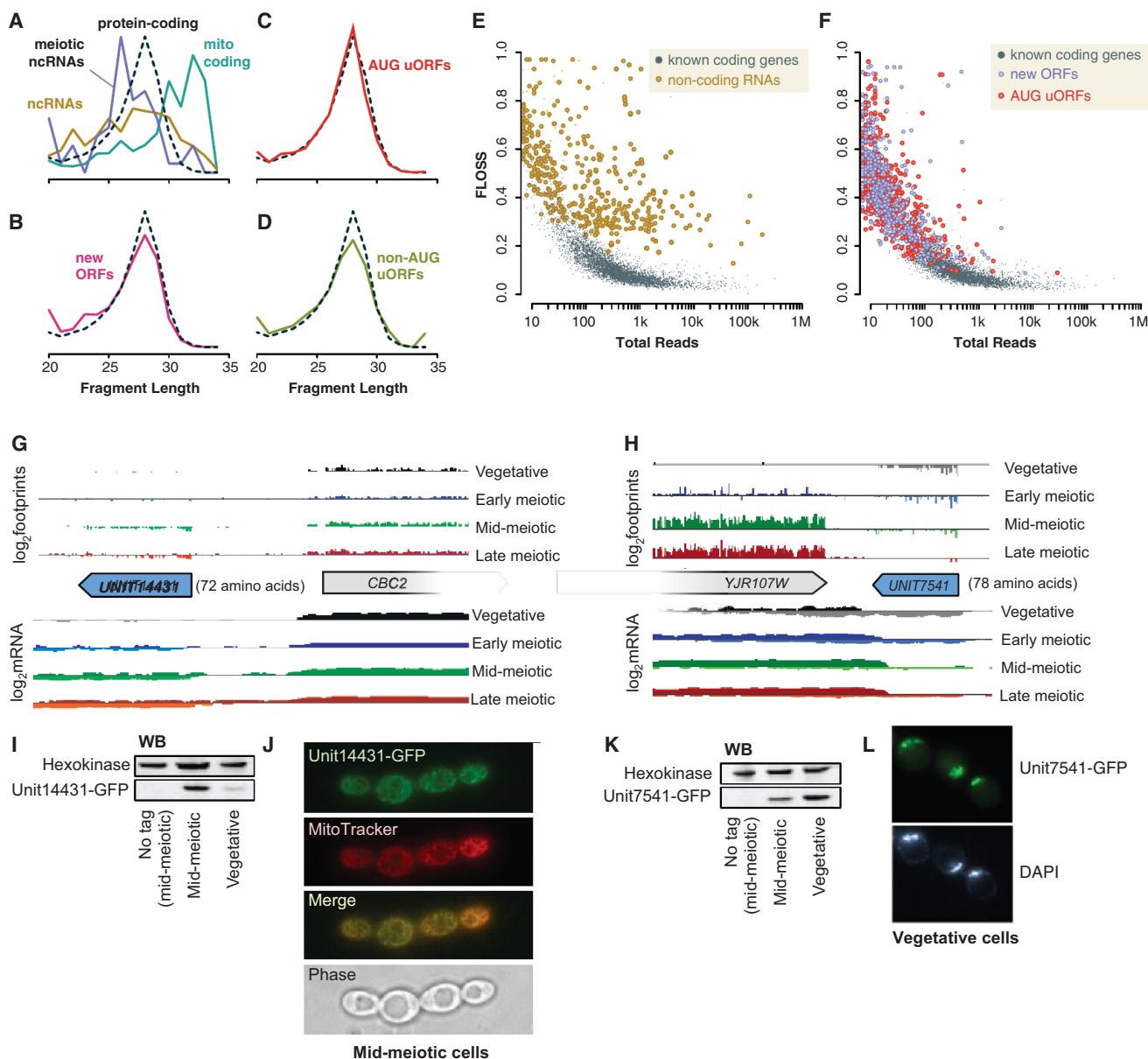


Figure 5. Novel Meiotic Reading Frames Based on True Ribosome Footprints Yield Protein Products

(A–D) Distribution of fragment lengths mapping to nuclear coding sequences compared to (A) classical noncoding RNAs, meiotic lncRNAs, and mitochondrial transcripts; (B) novel independent ORFs; (C) translated AUG uORFs; and (D) translated non-AUG uORFs.

(E and F) Fragment length analysis of yeast-coding sequences compared to (E) classical noncoding RNAs and (F) novel independent ORFs and AUG uORFs.

(G and H) Ribosome profiling and mRNA sequencing data for novel reading frames showing meiotic induction (G) or repression (H) of an ~75-codon ORF on an independent transcript (Brar et al., 2012).

(I) Western blot confirming meiotic expression of the Unit14431-GFP fusion. WB, western blot.

(J) Microscopy on meiotic yeast reveals mitochondrial targeting of the Unit14431-GFP fusion.

(K) Western blot confirming vegetative expression of the Unit7541-GFP fusion.

(L) Microscopy demonstrating nuclear localization of Unit7541-GFP.

and classified nearly all novel ORFs with known protein-coding genes (Figure 5F). Thus, considered singly or as a group, our reading frame annotations, defined solely by ribosome-profiling data, represent the presence of 80S ribosomes and not background RNA fragments.

We also sought to test whether productive translation could be detected from the ribosomes occupying these novel short reading frames. We integrated a GFP reading frame at the 3' end of meiotically regulated short reading frames in yeast (Figures 5G and 5H). Fusion protein from one short (72 codon)

reading frame accumulated in midmeiotic cells, as predicted from translation data, and localized to mitochondria (Figures 5I and 5J). GFP fused to another, 78-codon reading frame showed robust expression in vegetative cells that decreased in meiosis, consistent with expression-profiling data (Figure 5K). The fusion protein colocalized with the nucleus in vegetative cells (Figure 5L). The translational fusion of these short peptides with the large and well-folded GFP may artificially stabilize the protein products and enhance their accumulation. Nonetheless, these data confirm that the novel ORFs defined by ribosome profiling result in the synthesis of proteins and, further, that these short proteins can confer specific localization on a GFP fusion, suggesting that they can display some molecular activity in the cell.

Fragment Length Analysis Supports Translation on Novel Reading Frames in Human Cytomegalovirus

We recently published an annotation of HCMV open reading frames based on ribosome profiling of infected human foreskin fibroblasts (Stern-Ginossar et al., 2012). This annotation included many entirely novel reading frames as well as alternate versions of known proteins. The translation of many of our novel HCMV reading frames was confirmed previously by epitope tagging and by direct detection of native protein products through mass spectrometry (Stern-Ginossar et al., 2012). Our fragment length analysis revealed little difference between human protein-coding genes, well-known viral coding sequences, and newly identified ORFs (Figures 6A–6D). We next tested the FLOSS on individual HCMV ORFs and found that nearly all fell among the annotated human protein-coding genes (Figures 6E and 6F).

We may fail to detect proteins from other novel reading frames, despite the fact that they are actually synthesized in the cell, if they are highly unstable and thus low abundance. However, all translated polypeptides can serve as antigens, even if they are rapidly degraded and never accumulate within the cell. In fact, breakdown products from cotranslational degradation may be preferentially targeted for display as antigens. The adaptive immune system thus records signatures of past protein expression, and we wanted to mine this record by testing the antigenicity of the novel reading frames we identified in HCMV. We reasoned that, if humans with a history of CMV infection displayed T cell responses against novel peptides, as they do against canonical CMV proteins (Sylwester et al., 2005), it would indicate that these peptides were produced in the course of the normal viral life cycle in a human host. Furthermore, the T cell response would directly demonstrate the functional impact of short reading frame translation in viral infection.

We focused on the beta 2.7 transcript in HCMV. Despite its designation as a long noncoding RNA, ribosome-profiling data identified eight new, moderately sized ORFs, two of which (ORFL7C and ORFL6C) were identified in lysates from infected cells by mass spectrometry (Stern-Ginossar et al., 2012; Figure 6G). Human T cells from anonymous HCMV-positive donors revealed robust cellular immune responses to ORFL7C and ORFL6C, as well as to other short reading frames on beta 2.7 and other ORFs that we had identified by ribosome profiling (Figures 6H and 6I). These responses were absent from HCMV-negative individuals (Figure S2), supporting the natural exposure

of HCMV-infected individuals specifically to these newly annotated translation products. Neither ORFL6C nor ORFL7C resembled annotated reading frames by the RRS metric, consistent with the polycistronic and overlapping translation on the beta 2.7 transcript (Figure 6G), but the encoded proteins are synthesized in culture models and in infected humans.

DISCUSSION

In this study, we establish the validity of ribosome profiling as a global and experimental strategy for identifying translated regions of a genome. Profiling data are an excellent complement to computational analyses, which detect conserved protein-coding regions of the genome, and to proteomic approaches for identifying stable proteins. These three techniques answer different but related questions. Conserved functional proteins are a subset of the total polypeptide content of the cell, which in turn is a subset of all products that are produced, however transiently, by translation. Ribosome profiling thus provides the most expansive view of the proteome and has thereby helped us appreciate a wider universe of translated sequences.

We present multiple lines of evidence that true ribosome footprints are pervasive on cytosolic RNAs, independent of the presence of conserved reading frames. These footprints change in response to translation inhibitors, copurify with the large ribosomal subunit, and fall preferentially in reading frames near the 5' ends of transcripts. The size distribution of ribosome-protected mRNA fragments also distinguishes them from the background present in profiling data. This observation allowed us to develop a fragment length analysis, the FLOSS, that very accurately predicts the results of ribosome affinity purification, which separate true footprints from background RNA by physical rather than computational means. In fact, because some noncoding RNAs do associate with the ribosome for reasons that are unrelated to their actual translation, the FLOSS appears to exclude background more effectively than ribosome pull-down. The large majority of regions identified in profiling experiments reflect true translation; background originates from a handful of known, abundant noncoding RNAs. The FLOSS can be easily incorporated into ribosome-profiling workflows, and we here provide tools for applying it based on the widely used Bioconductor project (Gentleman et al., 2004). The specific length distribution and FLOSS cutoff for each individual data set can be determined empirically based on annotated protein-coding genes serving as examples of true translation. Adoption of the FLOSS should further increase confidence that profiling measurements on individual transcripts reflect their translation and aid in removing the small number of RNAs that yield nonribosomal background.

Pervasive ribosome occupancy outside of annotated coding regions has been seen in diverse organisms, and we here present further evidence for the existence of protein products resulting from translation by these ribosomes. The biological implications of this translation remain to be explored, however. In part, it may reflect an imprecision that leads to translation with no functional relevance. We do not know of molecular features that would enable the translational apparatus to distinguish an mRNAs from a capped, polyadenylated, cytosolic lncRNA, and so it may not be surprising to find ribosomes on many lncRNAs.

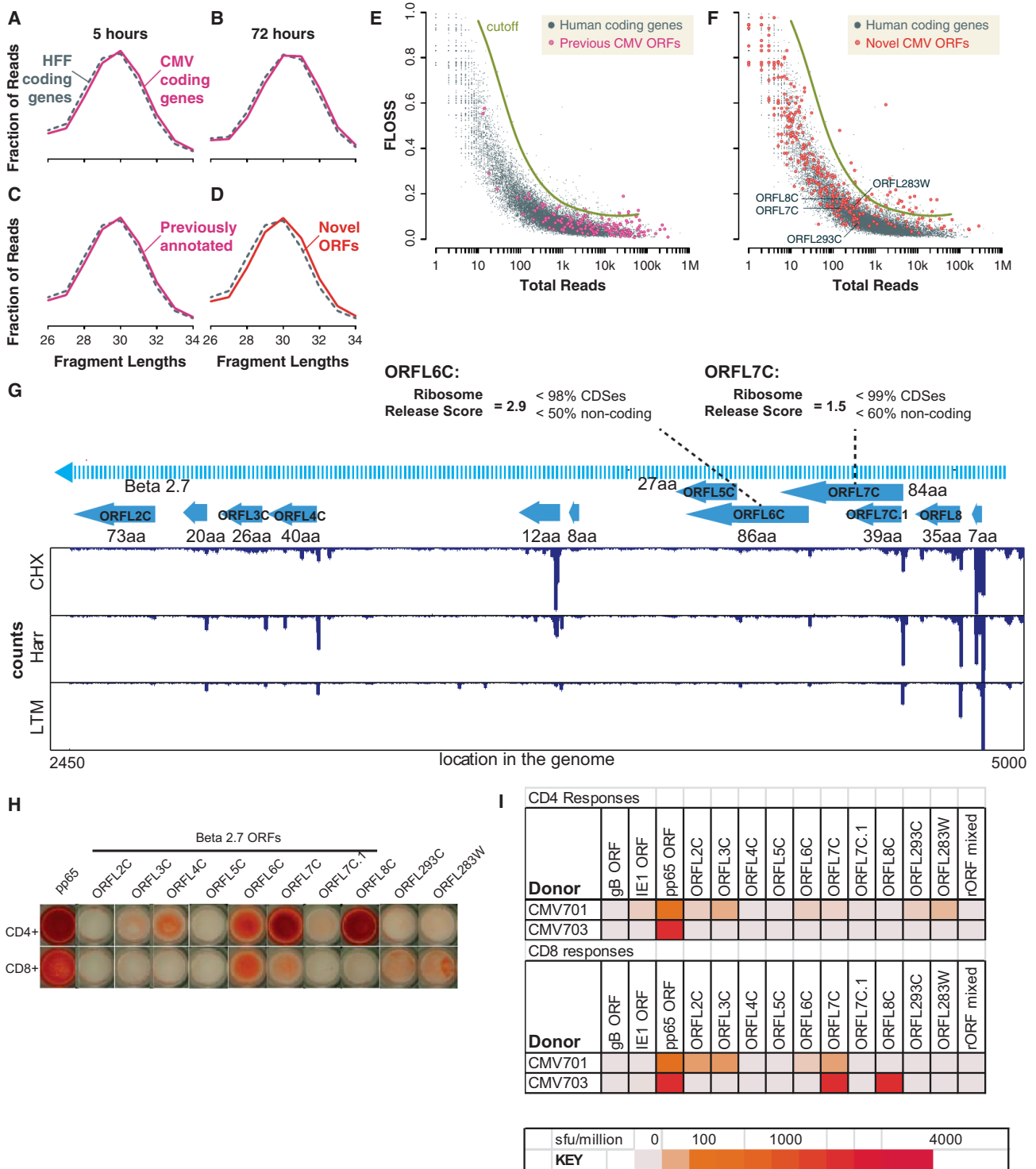


Figure 6. Novel Human Cytomegalovirus Reading Frames Based on True Ribosome Footprints Lead to Antigens in Humans

(A–D) Distribution of fragment lengths mapping to human nuclear CDSs compared to all annotated CMV-coding sequences after (A) 5 hr or (B) 72 hr of infection and of specifically the (C) previously annotated and (D) novel CMV-coding sequences after 5 hr of infection.

(E and F) Fragment length analysis of human coding sequences compared to (E) previously annotated CMV reading frames and (F) novel CMV annotations.

(G) Ribosome footprint organization on beta 2.7 transcript (Stern-Ginossar et al., 2012).

(H) ELISPOT assay of human donor T cell responses to novel CMV reading frames along with controls.

(I) Quantitation of ELISPOT data.

Imperfect rejection of near-AUG codons during translation initiation, combined with the presence of actual AUGs, could explain ribosome occupancy in many 5' UTRs. However, translation of these noncoding sequences has many potential consequences and noncoding sequences likely experience selection against translation with harmful effects. For example, AUG codons are depleted in many 5' UTRs, as they interfere with translation of the downstream protein-coding sequence, though this interference is exploited as a regulatory mechanism controlling the expression of genes such as *Atf4* (Sonenberg and Hinnebusch, 2009). Other side effects of noncoding translation may likewise be avoided in some RNAs and co-opted in others.

The translation of an RNA can impact the transcript itself, and lncRNAs with specific molecular functions are likely subject to selective pressure to manage this translation and avoid interference with their other activities. The translating ribosome acts as a potent helicase that can remodel RNA structure and remove RNA-binding proteins, potentially disrupting functional ribonucleoprotein complexes. We have shown that initiation and translation are biased toward the 5' ends of lncRNAs, as expected in eukaryotes, and so noncoding cytosolic transcripts may experience selection for benign 5' reading frames that capture ribosomes and protect functional elements occurring in the 3' end of the RNA (Ulitsky and Bartel, 2013). Short reading frames with atypical amino acid composition may resemble those found in aberrant mRNAs and trigger RNA decay through NMD or no-go decay, which were originally characterized as mRNA quality control pathways (Pérez-Ortín et al., 2013). Translated sequences may also exert *cis*-acting effects through the peptides they encode, for example, by cotranslational recruitment of the nascent chain attached to the ribosome and the transcript, to specific structures in the cell (Yanagitani et al., 2009).

Translation results in the synthesis of a polypeptide, regardless of whether an RNA sequence encodes a functional protein constrained by selection, and we have now detected proteins synthesized from novel translated sequences predicted by ribosome profiling in yeast and given evidence for their presence in humans during CMV infection. These unconstrained peptide sequences may not adopt a specific fold and may occupy cotranslational folding or degradation machinery, and those peptides escaping surveillance may aggregate and contribute to the burden of unfolded proteins. Some subset of this large pool of newly identified short peptides may play cellular roles that we have yet to discover, akin to the important roles recently shown for the 11- and 32-amino-acid peptides synthesized from the *polished rice* and *sarcolambin* loci in *Drosophila* and the 58-amino-acid peptide encoded by the zebrafish *toddler* gene (Kondo et al., 2010; Magny et al., 2013; Pauli et al., 2014).

All RNA sequences subject to translation will experience selection against encoding proteins with detrimental impact on the cell or on the organism. These benign proteins may occasionally provide an adaptive molecular function; for example, a surprisingly large fraction (~20%) of random nucleotide sequences encode functional secretion signals (Kaiser et al., 1987). Further evolution may refine their expression, folding, and activity, ultimately giving rise to the birth of a new gene (Carvunis et al., 2012; Reinhardt et al., 2013).

Regardless of their original cellular role, degraded proteins are the substrates for antigens presented to the cellular immune system, and proteins synthesized by noncanonical translation may be shunted preferentially for degradation and presentation as antigens, expanding the range of epitopes displayed by virus infected or transformed (Yewdell, 2011). The apparent elevation of noncanonical translation in stress could aid the body in detecting these pathological cells, and differences in translation between normal and transformed cells could yield cancer-specific antigens for immunomodulatory therapy (Mellman et al., 2011). The same processes producing cryptic viral and tumor antigens could also expose cryptic self-antigens that could initiate or sustain an autoimmune response.

In summary, translation of noncoding RNA has the potential to impact the cell directly and to constrain the evolution of genomic sequences. A better understanding of these molecular and evolutionary implications relies, first, on a reliable means for unbiased detection of translation. Ribosome profiling provides a starting point for exploring the role of the translational apparatus in truly noncoding RNAs as well as revealing novel short, functional proteins and offering a window into the murky gradations in between.

EXPERIMENTAL PROCEDURES

Ribosome Footprinting

Embryonic day 14 mESCs were pretreated with cycloheximide (100 $\mu\text{g}/\text{ml}$) or emetine (50 $\mu\text{g}/\text{ml}$) for 1 min as indicated, followed by detergent lysis and ribosome footprinting by RNase I digestion (Ingolia et al., 2012). Deep sequencing libraries were generated from 26–34 nt footprint fragments (Ingolia et al., 2012) and sequenced on an Illumina HiSeq.

Ribosome Affinity Purification

The ribosome affinity tag construct comprised human ribosomal protein L1 fused to the biotin acceptor peptide (Beckett et al., 1999; de Boer et al., 2003), coexpressed with a biotin ligase using a 2A peptide (de Felipe et al., 2006), as a stable transgene in HEK293 cells using the Flp-In system (Invitrogen). Yeast lysates were prepared as described (Ingolia, 2010). Following nuclease digestion, lysates were loaded onto a Sepharacryl S-400 gel filtration spin column (Boca Scientific) and the flowthrough was collected. One aliquot of flowthrough was bound to streptavidin-coated magnetic beads (Invitrogen), and RNA was recovered by Trizol extraction directly from beads; another aliquot was used directly for library generation following Trizol extraction. Extracted RNA was converted into deep sequencing libraries.

Footprint Sequence Alignment

Footprint sequences were trimmed to remove 3' adaptor sequence and aligned using TopHat v2.0.7 (Kim et al., 2013) with Bowtie v0.12.9.0 and samtools v0.1.18.0. The composite reference genomes comprised either the mm10 mouse genome with Ensembl GRCm38.72 transcripts or the human hg19 genome with Gencode v17 transcripts (Harrow et al., 2012), supplemented with the yeast genome with de novo transcript annotations (Brar et al., 2012). Alignments were filtered to remove those containing more than one mismatch.

Footprint Sequence Data Analysis

Footprints were assigned to specific A site nucleotide positions ~15 bases from their 5' ends, depending on the exact fragment length, as described previously. Reads assigned between 15 nucleotides before the start codon and 45 nucleotides after the start codon were excluded, as were all reads falling after the position 15 nucleotides upstream of the stop codon. All footprint data analysis was implemented in R/Bioconductor and is provided in a format allowing the direct reproduction of the analyses presented here.

We used our previously published (Stern-Ginossar et al., 2012), simplified approach to detect sites of AUG-mediated initiation in harringtonine-treated mESCs. We identified all AUG codons and selected harringtonine peaks by finding codons where A site occupancy on the +1 codon (i.e., AUG in the P site) as greater than occupancy on the +2 codon and greater than the sum of occupancy on the -1 and the 0 codon in both replicates. Among these AUG harringtonine peaks, we then selected the highest footprint occupancy on the +1 codon.

We computed the footprint A site occupancy at all codons on the transcript (not restricted to AUG codons with a harringtonine peak) and found the rank of the candidate initiation site relative to all other codons.

We also indexed all AUG codons on the transcript, starting from the 5' end, and found the candidate initiation site among all AUG codons on the transcript.

Fragment Length Organization Similarity Score

The FLOSS was computed from a histogram of read lengths for footprints on a transcript or reading frame. A reference histogram was produced using raw counts on all annotated nuclear protein-coding transcript, excluding those whose gene overlapped a gene annotated as noncoding. The FLOSS was defined as

$$0.5 \times \sum_{l=26}^{34} f(l) - f_{ref}(l),$$

where $f(l)$ is the fraction of reads at length l in the transcript histogram and $f_{ref}(l)$ is the corresponding fraction in the reference histogram. The FLOSS cutoff score, as a function of the total number of reads, was counted from a rolling window of individual annotated genes and the computing of the upper extreme outlier cutoff for each window.

Yeast Western Blotting and Microscopy

Novel ORFs were tagged with C-terminal GFP fusions by the Pringle method (Longtine et al., 1998). Samples were collected by trichloroacetic acid precipitation and subjected to western blotting (mouse anti-GFP antibody, Roche; rabbit anti-hexokinase antibody, Rockland Antibodies). Samples were also collected for microscopy, which was performed on a Zeiss Axioptot. Samples were costained with either DAPI or Mitotracker Orange (Molecular Probes).

T Cell Response Assays

Tiling peptides (15 amino acids long with ten-amino-acid overlap) for novel CMV ORFs were obtained from JPT Peptide Technologies and pooled at 2 $\mu\text{g}/\text{ml}$ of each individual peptide in RPMI 1640. Peripheral blood mononuclear cells were isolated by Lymphoprep (Axis-Shield) and depleted of either CD4+ or CD8+ T cells by magnetic-activated cell sorting (Miltenyi Biotec), yielding no more than 0.8% residual cells as accessed by flow cytometry. ELISPOT plates (EBioscience) were prepared, coated, and blocked, and T cells were plated at 3.0×10^5 cells in 100 μl RPMI-10.

ACCESSION NUMBERS

The NCBI GEO accession number for the ribosome profiling data reported in this paper is GSE60095.

SUPPLEMENTAL INFORMATION

Supplemental Information includes Supplemental Experimental Procedures, four figures, and three tables and can be found with this article online at <http://dx.doi.org/10.1016/j.celrep.2014.07.045>.

ACKNOWLEDGMENTS

We thank H. Chang, J. Darnell, R. Darnell, L. Lareau, and members of the N.T.I. and J.S.W. labs for valuable comments; C. Jan and C. Williams for insights into ribosome affinity purification; and A. Pinder for sequencing. This work was

supported by the Searle Scholars Program (to N.T.I.), the Howard Hughes Medical Institute (to J.S.W.), and by a Human Frontiers in Science postdoctoral fellowship (to N.S.-G.) and American Cancer Society Postdoctoral Fellowship 117945-PF-09-136-01-RMC (to G.A.B.). M.R.W. and S.E.J. were funded by British Medical Research Council grant G0701279 and the Cambridge BRC. N.T.I. and J.S.W. are inventors on a patent application encompassing the ribosome profiling technique.

Received: February 26, 2014

Revised: June 19, 2014

Accepted: July 24, 2014

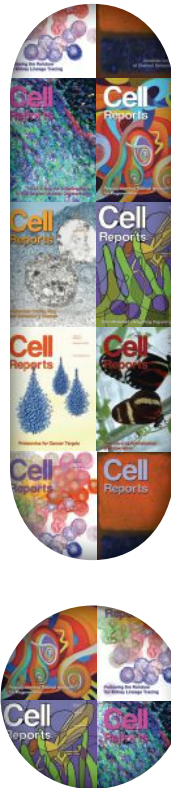
Published: August 21, 2014

REFERENCES

- Aitken, C.E., and Lorsch, J.R. (2012). A mechanistic overview of translation initiation in eukaryotes. *Nat. Struct. Mol. Biol.* *19*, 568–576.
- Beckett, D., Kovaleva, E., and Schatz, P.J. (1999). A minimal peptide substrate in biotin holoenzyme synthetase-catalyzed biotinylation. *Protein Sci.* *8*, 921–929.
- Bertone, P., Stolc, V., Royce, T.E., Rozowsky, J.S., Urban, A.E., Zhu, X., Rinn, J.L., Tongprasit, W., Samanta, M., Weissman, S., et al. (2004). Global identification of human transcribed sequences with genome tiling arrays. *Science* *306*, 2242–2246.
- Brar, G.A., Yassour, M., Friedman, N., Regev, A., Ingolia, N.T., and Weissman, J.S. (2012). High-resolution view of the yeast meiotic program revealed by ribosome profiling. *Science* *335*, 552–557.
- Cabili, M.N., Trapnell, C., Goff, L., Koziol, M., Tazon-Vega, B., Regev, A., and Rinn, J.L. (2011). Integrative annotation of human large intergenic noncoding RNAs reveals global properties and specific subclasses. *Genes Dev.* *25*, 1915–1927.
- Calvo, S.E., Pagliarini, D.J., and Mootha, V.K. (2009). Upstream open reading frames cause widespread reduction of protein expression and are polymorphic among humans. *Proc. Natl. Acad. Sci. USA* *106*, 7507–7512.
- Carninci, P., Kasukawa, T., Katayama, S., Gough, J., Frith, M.C., Maeda, N., Oyama, R., Ravasi, T., Lenhard, B., Wells, C., et al.; FANTOM Consortium; RIKEN Genome Exploration Research Group and Genome Science Group (Genome Network Project Core Group) (2005). The transcriptional landscape of the mammalian genome. *Science* *309*, 1559–1563.
- Carvunis, A.R., Rolland, T., Wapinski, I., Calderwood, M.A., Yildirim, M.A., Simonis, N., Charleoteaux, B., Hidalgo, C.A., Barbette, J., Santhanam, B., et al. (2012). Proto-genes and de novo gene birth. *Nature* *487*, 370–374.
- Chew, G.L., Pauli, A., Rinn, J.L., Regev, A., Schier, A.F., and Valen, E. (2013). Ribosome profiling reveals resemblance between long non-coding RNAs and 5' leaders of coding RNAs. *Development* *140*, 2828–2834.
- de Boer, E., Rodriguez, P., Bonte, E., Krijgsveld, J., Katsantoni, E., Heck, A., Grosveld, F., and Strouboulis, J. (2003). Efficient biotinylation and single-step purification of tagged transcription factors in mammalian cells and transgenic mice. *Proc. Natl. Acad. Sci. USA* *100*, 7480–7485.
- de Felipe, P., Luke, G.A., Hughes, L.E., Gani, D., Halpin, C., and Ryan, M.D. (2006). E unum pluribus: multiple proteins from a self-processing polyprotein. *Trends Biotechnol.* *24*, 68–75.
- Gentleman, R.C., Carey, V.J., Bates, D.M., Bolstad, B., Dettling, M., Dudoit, S., Ellis, B., Gautier, L., Ge, Y., Gentry, J., et al. (2004). Bioconductor: open software development for computational biology and bioinformatics. *Genome Biol.* *5*, R80.
- Guttman, M., Amit, I., Garber, M., French, C., Lin, M.F., Feldser, D., Huarte, M., Zuk, O., Carey, B.W., Cassady, J.P., et al. (2009). Chromatin signature reveals over a thousand highly conserved large non-coding RNAs in mammals. *Nature* *458*, 223–227.
- Guttman, M., Russell, P., Ingolia, N.T., Weissman, J.S., and Lander, E.S. (2013). Ribosome profiling provides evidence that large noncoding RNAs do not encode proteins. *Cell* *154*, 240–251.

- Guydosh, N.R., and Green, R. (2014). Dom34 rescues ribosomes in 3' untranslated regions. *Cell* 156, 950–962.
- Harrow, J., Frankish, A., Gonzalez, J.M., Tapanari, E., Diekhans, M., Kokocinski, F., Aken, B.L., Barrell, D., Zadissa, A., Searle, S., et al. (2012). GENCODE: the reference human genome annotation for The ENCODE Project. *Genome Res.* 22, 1760–1774.
- Heiman, M., Schaefer, A., Gong, S., Peterson, J.D., Day, M., Ramsey, K.E., Suárez-Fariñas, M., Schwarz, C., Stephan, D.A., Surmeier, D.J., et al. (2008). A translational profiling approach for the molecular characterization of CNS cell types. *Cell* 135, 738–748.
- Ingolia, N.T. (2010). Genome-wide translational profiling by ribosome footprinting. *Methods Enzymol.* 470, 119–142.
- Ingolia, N.T., Ghaemmaghami, S., Newman, J.R., and Weissman, J.S. (2009). Genome-wide analysis in vivo of translation with nucleotide resolution using ribosome profiling. *Science* 324, 218–223.
- Ingolia, N.T., Lareau, L.F., and Weissman, J.S. (2011). Ribosome profiling of mouse embryonic stem cells reveals the complexity and dynamics of mammalian proteomes. *Cell* 147, 789–802.
- Ingolia, N.T., Brar, G.A., Rouskin, S., McGeachy, A.M., and Weissman, J.S. (2012). The ribosome profiling strategy for monitoring translation in vivo by deep sequencing of ribosome-protected mRNA fragments. *Nat. Protoc.* 7, 1534–1550.
- Kaiser, C.A., Preuss, D., Grisafi, P., and Botstein, D. (1987). Many random sequences functionally replace the secretion signal sequence of yeast invertase. *Science* 235, 312–317.
- Kim, D., Pertea, G., Trapnell, C., Pimentel, H., Kelley, R., and Salzberg, S.L. (2013). TopHat2: accurate alignment of transcriptomes in the presence of insertions, deletions and gene fusions. *Genome Biol.* 14, R36.
- Kondo, T., Plaza, S., Zanet, J., Benrabah, E., Valenti, P., Hashimoto, Y., Kobayashi, S., Payre, F., and Kageyama, Y. (2010). Small peptides switch the transcriptional activity of Shavenbaby during *Drosophila* embryogenesis. *Science* 329, 336–339.
- Lareau, L.F., Hite, D.H., Hogan, G.J., and Brown, P.O. (2014). Distinct stages of the translation elongation cycle revealed by sequencing ribosome-protected mRNA fragments. *Elife (Cambridge)* 3, e01257.
- Lin, M.F., Deoras, A.N., Rasmussen, M.D., and Kellis, M. (2008). Performance and scalability of discriminative metrics for comparative gene identification in 12 *Drosophila* genomes. *PLoS Comput. Biol.* 4, e1000067.
- Lin, M.F., Jungreis, I., and Kellis, M. (2011). PhyloCSF: a comparative genomics method to distinguish protein coding and non-coding regions. *Bioinformatics* 27, i275–i282.
- Longtine, M.S., McKenzie, A., 3rd, Demarini, D.J., Shah, N.G., Wach, A., Brachat, A., Philippsen, P., and Pringle, J.R. (1998). Additional modules for versatile and economical PCR-based gene deletion and modification in *Saccharomyces cerevisiae*. *Yeast* 14, 953–961.
- Magny, E.G., Pueyo, J.I., Pearl, F.M., Cespedes, M.A., Niven, J.E., Bishop, S.A., and Couso, J.P. (2013). Conserved regulation of cardiac calcium uptake by peptides encoded in small open reading frames. *Science* 341, 1116–1120.
- McCoy, L.S., Xie, Y., and Tor, Y. (2011). Antibiotics that target protein synthesis. *Wiley Interdiscip. Rev. RNA* 2, 209–232.
- Mellman, I., Coukos, G., and Dranoff, G. (2011). Cancer immunotherapy comes of age. *Nature* 480, 480–489.
- Pauli, A., Norris, M.L., Valen, E., Chew, G.L., Gagnon, J.A., Zimmerman, S., Mitchell, A., Ma, J., Dubrulle, J., Reyon, D., et al. (2014). Toddler: an embryonic signal that promotes cell movement via Apelin receptors. *Science* 343, 1248636.
- Pérez-Ortín, J.E., Alepuz, P., Chávez, S., and Choder, M. (2013). Eukaryotic mRNA decay: methodologies, pathways, and links to other stages of gene expression. *J. Mol. Biol.* 425, 3750–3775.
- Rebbapragada, I., and Lykke-Andersen, J. (2009). Execution of nonsense-mediated mRNA decay: what defines a substrate? *Curr. Opin. Cell Biol.* 21, 394–402.
- Reinhardt, J.A., Wanjiru, B.M., Brant, A.T., Saelao, P., Begun, D.J., and Jones, C.D. (2013). De novo ORFs in *Drosophila* are important to organismal fitness and evolved rapidly from previously non-coding sequences. *PLoS Genet.* 9, e1003860.
- Schneider-Poetsch, T., Ju, J., Elyer, D.E., Dang, Y., Bhat, S., Merrick, W.C., Green, R., Shen, B., and Liu, J.O. (2010). Inhibition of eukaryotic translation elongation by cycloheximide and lactimidomycin. *Nat. Chem. Biol.* 6, 209–217.
- Smith, C.M., and Steitz, J.A. (1998). Classification of gas5 as a multi-small-nucleolar-RNA (snoRNA) host gene and a member of the 5'-terminal oligopyrimidine gene family reveals common features of snoRNA host genes. *Mol. Cell. Biol.* 18, 6897–6909.
- Sonenberg, N., and Hinnebusch, A.G. (2009). Regulation of translation initiation in eukaryotes: mechanisms and biological targets. *Cell* 136, 731–745.
- Starck, S.R., Jiang, V., Pavon-Eternod, M., Prasad, S., McCarthy, B., Pan, T., and Shastri, N. (2012). Leucine-tRNA initiates at CUG start codons for protein synthesis and presentation by MHC class I. *Science* 336, 1719–1723.
- Steitz, J.A. (1969). Polypeptide chain initiation: nucleotide sequences of the three ribosomal binding sites in bacteriophage R17 RNA. *Nature* 224, 957–964.
- Stern-Ginossar, N., Weisburd, B., Michalski, A., Le, V.T., Hein, M.Y., Huang, S.X., Ma, M., Shen, B., Qian, S.B., Hengel, H., et al. (2012). Decoding human cytomegalovirus. *Science* 338, 1088–1093.
- Sylwester, A.W., Mitchell, B.L., Edgar, J.B., Taormina, C., Pelte, C., Ruchti, F., Sleath, P.R., Grabstein, K.H., Hosken, N.A., Kern, F., et al. (2005). Broadly targeted human cytomegalovirus-specific CD4+ and CD8+ T cells dominate the memory compartments of exposed subjects. *J. Exp. Med.* 202, 673–685.
- Tukey, J.W. (1977). *Exploratory Data Analysis* (Reading, MA: Addison-Wesley).
- Ulitsky, I., and Bartel, D.P. (2013). lincRNAs: genomics, evolution, and mechanisms. *Cell* 154, 26–46.
- Valášek, L., Szamecz, B., Hinnebusch, A.G., and Nielsen, K.H. (2007). In vivo stabilization of preinitiation complexes by formaldehyde cross-linking. *Methods Enzymol.* 429, 163–183.
- Wang, Z., Gerstein, M., and Snyder, M. (2009). RNA-Seq: a revolutionary tool for transcriptomics. *Nat. Rev. Genet.* 10, 57–63.
- Wethmar, K., Barbosa-Silva, A., Andrade-Navarro, M.A., and Leutz, A. (2014). uORFdb—a comprehensive literature database on eukaryotic uORF biology. *Nucleic Acids Res.* 42, D60–D67.
- Wilusz, J.E., Freier, S.M., and Spector, D.L. (2008). 3' end processing of a long nuclear-retained noncoding RNA yields a tRNA-like cytoplasmic RNA. *Cell* 135, 919–932.
- Wilusz, J.E., JnBaptiste, C.K., Lu, L.Y., Kuhn, C.D., Joshua-Tor, L., and Sharp, P.A. (2012). A triple helix stabilizes the 3' ends of long noncoding RNAs that lack poly(A) tails. *Genes Dev.* 26, 2392–2407.
- Wolin, S.L., and Walter, P. (1988). Ribosome pausing and stacking during translation of a eukaryotic mRNA. *EMBO J.* 7, 3559–3569.
- Yanagitani, K., Imagawa, Y., Iwawaki, T., Hosoda, A., Saito, M., Kimata, Y., and Kohno, K. (2009). Cotranslational targeting of XBP1 protein to the membrane promotes cytoplasmic splicing of its own mRNA. *Mol. Cell* 34, 191–200.
- Yewdell, J.W. (2011). DRiPs solidify: progress in understanding endogenous MHC class I antigen processing. *Trends Immunol.* 32, 548–558.

Make your point with Cell Reports



Share your discoveries as you find them. Every breakthrough should get the attention it deserves. *Cell Reports* puts a spotlight on groundbreaking research with shorter, single-point stories.

Cell Reports is an open access journal that offers the quality, rigor, and visibility you've come to expect from Cell Press.

Do you have a new biological insight? Submit your paper to *Cell Reports*.

For more information www.cell.com/cell-reports

An open access journal with impact.
From Cell Press.

**Cell
Reports**

Conservation of mRNA and Protein Expression during Development of *C. elegans*

Dominic Grün,^{1,3} Marieluise Kirchner,^{2,3} Nadine Thierfelder,^{1,3} Marlon Stoeckius,¹ Matthias Selbach,² and Nikolaus Rajewsky^{1,*}

¹Systems Biology of Gene Regulatory Elements, Max Delbrück Center Berlin, Robert-Rössle-Strasse 10, 13125 Berlin, Germany

²Cell Signalling and Mass Spectrometry, Max Delbrück Center Berlin, Robert-Rössle-Strasse 10, 13125 Berlin, Germany

³These authors contributed equally to this work

*Correspondence: rajewsky@mdc-berlin.de

<http://dx.doi.org/10.1016/j.celrep.2014.01.001>

This is an open-access article distributed under the terms of the Creative Commons Attribution-NonCommercial-No Derivative Works License, which permits non-commercial use, distribution, and reproduction in any medium, provided the original author and source are credited.

SUMMARY

Spatiotemporal control of gene expression is crucial for development and subject to evolutionary changes. Although proteins are the final product of most genes, the developmental proteome of an animal has not yet been comprehensively defined, and the correlation between mRNA and protein abundance during development is largely unknown. Here, we globally measured and compared protein and mRNA expression changes during the life cycle of the nematodes *C. elegans* and *C. briggsae*, separated by ~30 million years of evolution. We observed that developmental mRNA and protein changes were highly conserved to a surprisingly similar degree but were poorly correlated within a species, suggesting important and widespread posttranscriptional regulation. Posttranscriptional control was particularly well conserved if mRNA fold changes were buffered on the protein level, indicating a predominant repressive function. Finally, among divergently expressed genes, we identified insulin signaling, a pathway involved in lifespan determination, as a putative target of adaptive evolution.

INTRODUCTION

Changes in gene expression are the basis of metazoan development. A new life starts with a totipotent zygote and requires many rounds of cell divisions and differentiation events to develop into a complex adult organism with a large diversity of tissues and cell types. Orchestrated differentiation of multiple cells within the developing animal is frequently driven by spatial or temporal changes in gene expression. Well-studied examples are spatial gene expression gradients that control the patterning of the *Drosophila* embryo (St Johnston and Nüsslein-Volhard, 1992) or temporal expression gradients of heterochronic genes in nematodes regulating the progression of larval development (Ruvkun and Giusto, 1989; Johnstone and Barry, 1996; Moss, 2007). Developmental gene expression is highly conserved, and alterations in gene expression levels are strong drivers of evolution

(Carroll, 2008; Haerty et al., 2008; Domazet-Lošo and Tautz, 2010; Kalinka et al., 2010). Comparing gene expression patterns across different species therefore provides insights into fundamental principles of development and evolution (Domazet-Lošo and Tautz, 2010; Kalinka et al., 2010; Levin et al., 2012). Notably, most of these conclusions were drawn from studies only interrogating transcript expression levels. However, gene expression is controlled at all molecular layers from genomic DNA to proteins, and changes in mRNA abundance are often a poor proxy for protein level changes (de Sousa Abreu et al., 2009; Schwanhäusser et al., 2011). Comprehensive simultaneous quantification of transcript and protein levels over the lifecycle of an organism would provide a highly informative data set describing developmental gene expression control. In particular, these data permit a quantification of the impact of posttranscriptional regulation on a genome-wide level. Here, we use two closely related nematode species to perform a global comparison of mRNA and protein abundance throughout the entire life cycle from embryogenesis to adulthood of a metazoan organism.

The nematodes *C. elegans* and *C. briggsae* are particularly attractive model organisms due to their highly reproducible development (Sulston et al., 1983; Zhao et al., 2008). The two species evolved from a common ancestor about 30–50 million years ago (Stein et al., 2003; Cutter, 2008) and are strongly diverged on the sequence level ($K_S = 1.78$ and $K_A = 0.11$) (Stein et al., 2003). Given that every neutral site in the genome should be substituted on average 1.78 times, a scenario of neutral evolution without any purifying selection would imply the loss of common regulatory sequences and reduce conservation of expression changes to background levels. However, despite the relatively long evolutionary distance, morphology, body plan and development of the two nematodes remained strikingly similar throughout the lifecycle. Even cell lineages are almost completely conserved (Zhao et al., 2008). Comparing developmental gene expression changes in the two nematodes will therefore help to elucidate the permitted evolutionary variability of gene expression that leaves the morphology and physiology of a species largely unaffected.

To quantify fold changes for thousands of proteins between defined developmental stages in both species, we used stable isotope labeling by amino acids combined with mass spectrometry. To perform a genome-wide comparative analysis of the evolution of transcript and protein abundance during

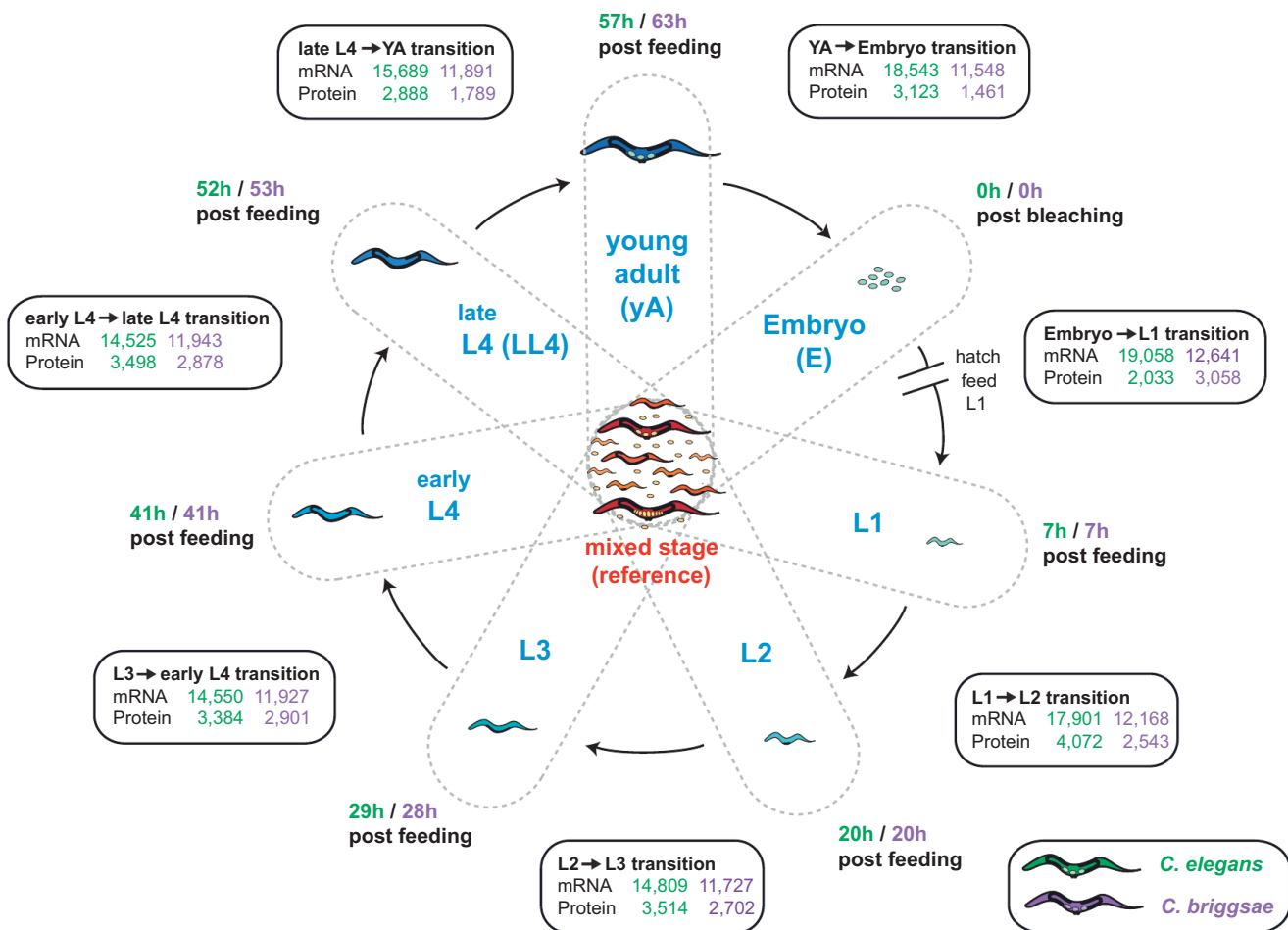


Figure 1. Nematode Life Cycle and Timing of Samples Used for Protein and Transcript Quantification

Experimental setup and time line for generation of *C. elegans* and *C. briggsae* samples for mRNA sequencing and mass spectrometry. Light-labeled synchronized worms (blue) were harvested at each stage (hours after feeding synchronized L1 larvae). A nonsynchronous heavy-labeled sample (red), containing a mixture of all time-contiguous stages, was used as a reference sample. For mRNA sequencing, all samples were analyzed independently. In order to quantify protein fold changes against the reference sample as SILAC ratios, each of the staged samples was mixed 2:1 with the reference sample. Numbers in the boxes represent quantified transcripts and proteins for each stage transition (*C. elegans*, green; *C. briggsae*, purple).

development, we complemented our protein data with mRNA quantification by mRNA sequencing. We observed that the degree of conservation is almost exactly the same for protein and transcript expression changes. Moreover, differences in protein and mRNA fold changes for the same gene were also conserved, preferentially if transcript changes were larger than protein changes, i.e., were buffered on the protein level.

We used our data to identify a pathway with accelerated evolution of expression changes and attempted to reproduce the observed cross-species changes within a single species by perturbation experiments.

RESULTS

Measuring Transcript and Protein Abundance in Parallel throughout Development

We sought to compare the developmental transcriptomes and proteomes of *C. elegans* and *C. briggsae* at well-defined develop-

mental stages covering the entire life cycle (Figure 1). The currently most accurate way to quantify changes in protein levels is stable isotope labeling and mass spectrometry (Heck and Krijgsveld, 2004), combining and coanalyzing differentially labeled samples. SILAC (stable isotope labeling with amino acids in cell culture) employs metabolic incorporation of heavy stable isotope-containing amino acids (Ong et al., 2002). The method was originally developed in cell culture and subsequently extended to several metazoan model organisms, including *C. elegans* (Krüger et al., 2008; Looso et al., 2010; Sury et al., 2010; Fredens et al., 2011; Larance et al., 2011). We generated SILAC worms by feeding worms on *E. coli* labeled with heavy lysine (Figure 2A; Supplemental Experimental Procedures). We did not observe any apparent difference between light and heavy worms (assessed by phenotype, developmental time, and number of worms obtained, $n > 1,000$). Efficient incorporation of heavy lysine was already observed in F1 adult worms (95% heavy-labeled peptides), with virtually complete labeling in F2 adult worms (99.5% heavy peptides).

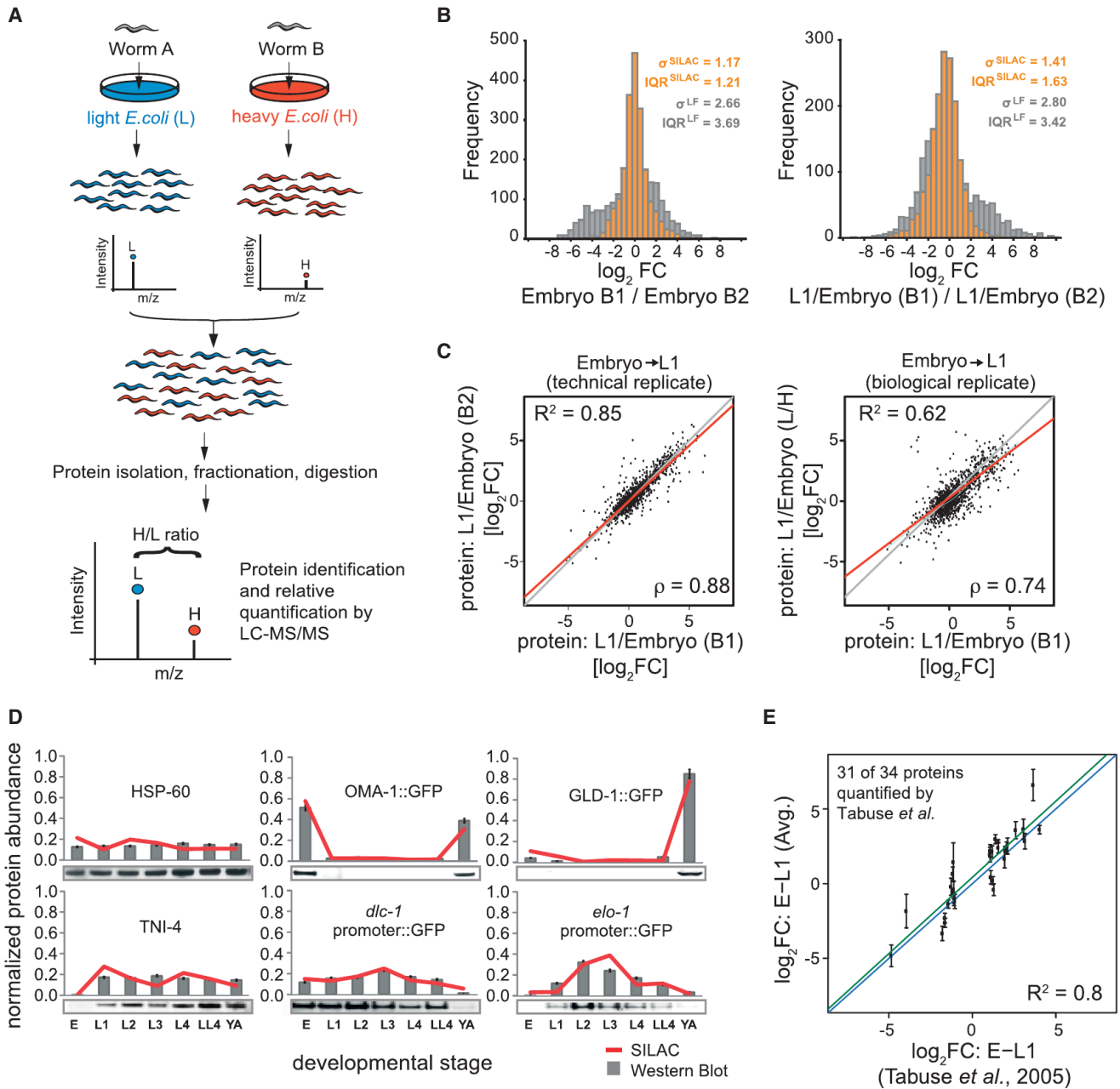


Figure 2. The SILAC Worm

(A) Stable isotope labeling with amino acids in nematodes. Nematodes are fed with either light- (L) or heavy- (H) labeled *E. coli* for at least two generations. Samples H and L are mixed at a defined ratio before processing and analysis by LC-MS/MS. Pairs of identical peptides with different stable-isotope compositions can be distinguished based on their mass difference. The ratio of peptide intensities reflects differences in protein abundance.

(B) Precision of label-free versus SILAC-based protein quantification. Two technical replicates of 1:1 mixtures were quantified based on intensity values (label-free, LF; gray) or based on SILAC ratios (SILAC; orange). SD (σ) and interquartile range (IQR) are shown for two replicates of the embryonic stage versus reference (left) and of the embryo-L1 fold changes (right).

(C) Pearson's R^2 and Spearman's correlation (ρ) between SILAC replicates of embryo-L1 \log_2 -fold changes for technical (left) and biological (right) replicates (see Supplemental Experimental Procedures for description and nomenclature of replicates).

(D) Validation of SILAC-based protein abundance by western blotting using antibodies for selected proteins, prepared from independent biological replicate samples and normalized against tubulin (TBA-2).

(E) Validation of SILAC-based embryo-L1 protein fold changes, averaged across biological replicates, by 2D difference gel electrophoresis (Tabuse *et al.*, 2005). Error bars indicate the SD across replicates; the blue line represents the diagonal. A regression (green line) yields $R^2 = 0.8$.

See also Figure S1.

We collected carefully staged unlabeled (light) worms of all major developmental stages (Figure 1; Supplemental Experimental Procedures) and combined these samples with a heavy SILAC reference sample (~99.5% heavy peptides) of asynchronously cultured worms, comprising a mixture of all time-contiguous developmental stages and serving as a common internal standard for the mass spectrometry runs (Figures 1 and 2A). For fold change quantification, we used revised high-quality gene models in *C. elegans* (Gerstein et al., 2010) comprising 21,774 genes and produced ab initio transcript annotations for *C. briggsae*. Our *C. briggsae* gene models were inferred based on sequencing read coverage, and we only maintained annotations supported by an alignment of *C. elegans* protein coding exons (Supplemental Experimental Procedures). This strategy yielded 13,938 *C. briggsae* orthologs. We note that our gene models largely overlap with a recently published annotation (Uyar et al., 2012). Of the 13,355 one-to-one orthologs based on reciprocal best protein blast alignments of these gene models to our *C. elegans* annotation, 12,008 (90%) correspond to orthology relations in our *C. briggsae* annotation. The respective gene models are highly overlapping: the sequence of 86% of the genes overlaps more than 80% between both annotations.

In total, we quantified 9,162 (5,552) proteins in *C. elegans* (*C. briggsae*) at a false discovery rate of 5%. In our hands, quantification based on the heavy SILAC reference was at least 2-fold more precise than label-free (LF) quantification according to a benchmark test ($\sigma^{\text{SILAC}} = 1.17$, $\sigma^{\text{LF}} = 2.66$; Figure 2B) and SILAC ratios reflect true protein fold changes inferred from mixing experiments (Figures S1A and S1B). Moreover, fold change variability across technical replicates was low (Spearman's rank coefficient $\rho = 0.88$) and increased slightly for biological replicates ($\rho = 0.74$), indicating moderate noise due to actual variation in protein abundance, a lack of timing precision or variable labeling efficiency for lowly expressed proteins (Figures 2C, S1E, and S1F). We first successfully validated the protein fold changes that we computed from in vivo SILAC by western blots for 20 proteins (Figures 2D, S1G, and S1H). Moreover, fold changes of 31 proteins measured by 2D gel electrophoresis (Tabuse et al., 2005) correlated strongly with our computed protein fold changes ($R^2 = 0.8$, Figure 2E).

We complemented our proteome data with transcript quantification by RNA sequencing (RNA-seq) of polyadenylated transcripts in the same biological samples. We obtained reliable expression for 19,549 (12,836) genes in *C. elegans* (*C. briggsae*) (Figures S1C and S1D; Table S1).

We validated our RNA-seq data, using quantitative RT-PCRs (qRT-PCRs) for 14 randomly selected genes covering the entire dynamic range of observed expression values, and measured a high correlation to RNA-seq-derived expression ($R^2 = 0.8/0.85$ for *C. elegans/C. briggsae*, Figure 3A). Moreover, reproducibility across biological replicates was high ($\rho > 0.82$, Figures S2A and S2B).

To examine how well our discrete set of developmental stages reflects transcript expression in our contiguous reference sample, we attempted to reproduce the composition of the reference sample by a mixture of all staged samples in silico. To this end, we defined for each developmental stage a vector with transcript

expression of all *C. elegans* genes and computed the linear combination of these vectors that best matches the expression vector for the reference sample by a multilinear regression. This in silico mixture reproduces the reference sample almost as good ($R^2 = 0.92$) as a true technical replicate ($R^2 = 0.93$). Contribution of each sample is essential because repeating the regression without, for instance, the young adult sample reduces the correlation ($R^2 = 0.81$, Figure 3B). Moreover, the optimized weights of the in silico mixture reflect the estimated contribution of the respective stage (determined by microscopy, $n > 1,000$) to the reference sample (Figure 3C). The in silico mixture for *C. briggsae* reproduces our composition estimates based on microscopic imaging equally well (Figure S2C). Developmental transcript expression changes are thus reflected by expression changes between our staged samples for the vast majority of genes.

In Figure 3D, examples are shown for a gene with conserved transcript and protein abundance, but differential embryo-L1 fold changes (*rpl-9*) and for a gene with nonconserved expression changes (*syd-2*).

A direct comparison of protein and transcript embryo-L1 fold change variability between biological replicates indicates that the level of noise is increased for protein quantification (Figure 3E). On average, the fold change error was comparable across the entire dynamic range (~0.5 for proteins versus ~0.25 for mRNAs), with slightly bigger errors for larger fold changes.

We supply transcript expression and SILAC protein ratios for all developmental stages in *C. elegans* and *C. briggsae* in Table S2, and graphical representations of expression profiles can be screened on our publicly available online database at <http://elegans.mdc-berlin.de>.

Transcript and Protein Abundance Changes Substantially during the Nematode Life Cycle

We first investigated temporal dynamics of transcript and protein abundance throughout *C. elegans* development. On both levels, pairs of larval stages were most highly correlated in comparison to pairs involving the young adult (YA) or the embryonic (E) stage (Figures 4A, 4B, and S3A). Therefore, transcript and protein abundances are relatively uniform throughout larval development and undergo pronounced changes at the embryo to larval transition and after completion of the final larval stage upon onset of oogenesis (Figure S3B).

Then, we assessed to what extent transcript expression changes explained protein abundance changes. Strikingly, only modest correlation was observed for the embryo-L1 ($\rho = 0.41$), the late L4 young adult ($\rho = 0.30$), and the young adult-embryo transition ($\rho = 0.17$) and almost no correlation at larval transitions ($\rho \sim 0$) (Figures 4C and S3). The pronounced differences between transcript and protein abundance changes suggest ubiquitous regulation at the posttranscriptional level.

Clustering of Temporal Expression Profiles Reveals Broad Posttranscriptional Regulation

We next searched for groups of genes with similar expression profiles throughout *C. elegans* development and analyzed to

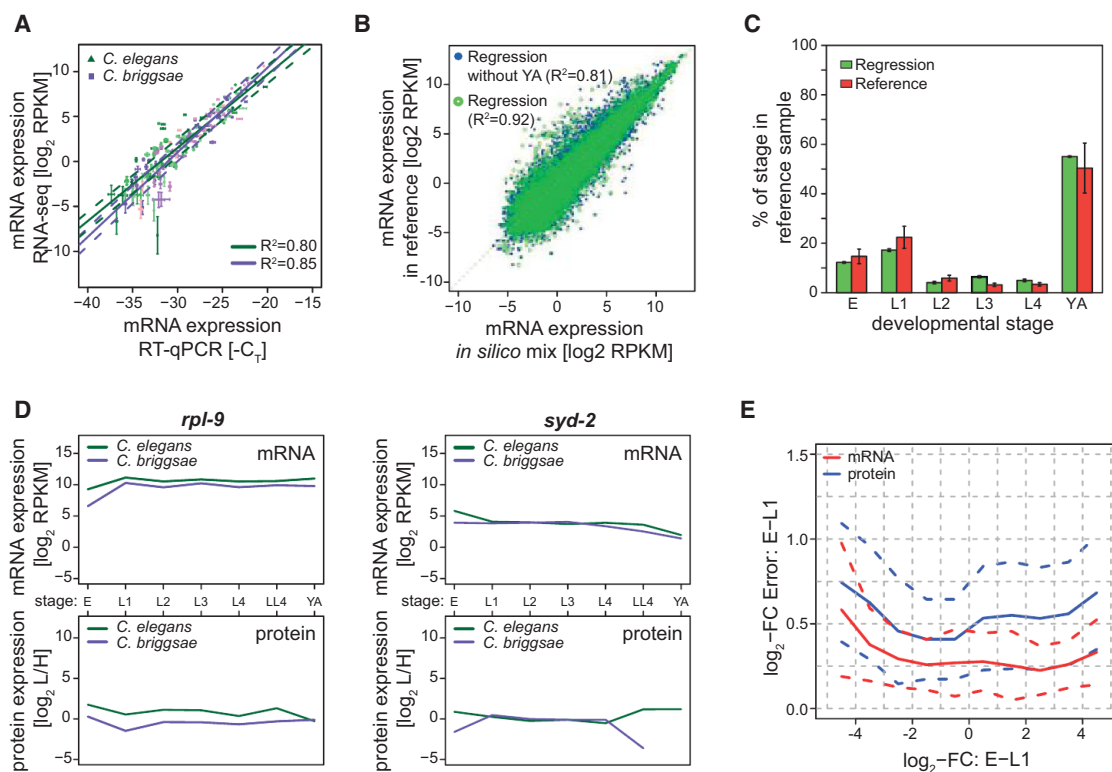


Figure 3. Validation of Transcript and Protein Quantification

(A) Validation of RNA-seq data by qRT-PCR for 14 genes with differential expression across development. Shown is the regression between \log_2 RPKM and $-C_T$. The broken lines represent a 2-fold interval around the regression line. Different shadings of green (*C. elegans*) and purple (*C. briggsae*) correspond to distinct developmental stages from embryos (dark) to young adults (light). Error bars represent the SD across replicates.

(B) Correlation between transcript expression in the reference sample and an in silico mixture of all stages (green circles) and after omitting the young adult sample (blue points).

(C) Comparison of the fraction of total mRNA from each stage in the reference sample as computed by the in silico mixture to estimates based on microscopic analysis for *C. elegans* ($n > 1,000$). Error bars indicate the error of the regression coefficients and the uncertainty of our estimates, respectively.

(D) Temporal expression profile for transcripts and proteins of the ribosomal gene *rpl-9* (left), which correlates well between the two species at all stages, and the gene *syd-2* (right), which shows divergent expression changes in the two species at the embryo-L1 transition.

(E) Variability of transcript (red) and protein (blue) \log_2 -fold changes quantified by the SD across biological replicates as a function of the fold change magnitude. Shown are the average (solid line) and the SD (broken line) of the variability across all genes.

See also Figure S2.

what extent transcript and protein level changes correlated within these groups. Hierarchical clustering of temporal expression profiles for all genes with quantified protein abundance for at least three developmental stages (Supplemental Experimental Procedures) yielded seven distinct expression clusters (Table S3A; Figure S3C). Four of those exhibited un- or even anticorrelated transcript and protein fold changes at the embryo-L1 transition, suggesting that posttranscriptional control modifies protein levels for a large fraction of genes. Next, we performed the same clustering procedure for *C. briggsae* (Table S3B; Figure S3D) and found that expression profiles in the two species looked similar and that the cluster composition was highly conserved (Table S3C). Hence, the majority of genes display conserved expression profiles.

As supplementary information, we computed enrichment of RNAi phenotypes (Table S3D; Supplemental Experimental Procedures) and identified overrepresented gene ontology

(GO) terms using the DAVID functional annotation tool (Huang et al., 2009; Table S4). For instance, the functional analysis reveals a strong enrichment of diverse developmental phenotypes (Table S3D) and developmental functions (Table S4) among genes with increased transcript and protein abundance in embryos (cluster 4 in Figure S3C). Metabolic functions, on the other hand, were enriched among genes upregulated on the transcript and protein level during larval development and adulthood (cluster 1 in Figure S3C).

Evidence for Oscillating Expression of Genes with Large Expression Changes at Larval Transitions

Many genes with highly dynamic transcript expression during larval development were discarded from clustering due to the lack of protein quantification. In *C. elegans*, these genes appear as a distinct population with strongly increased

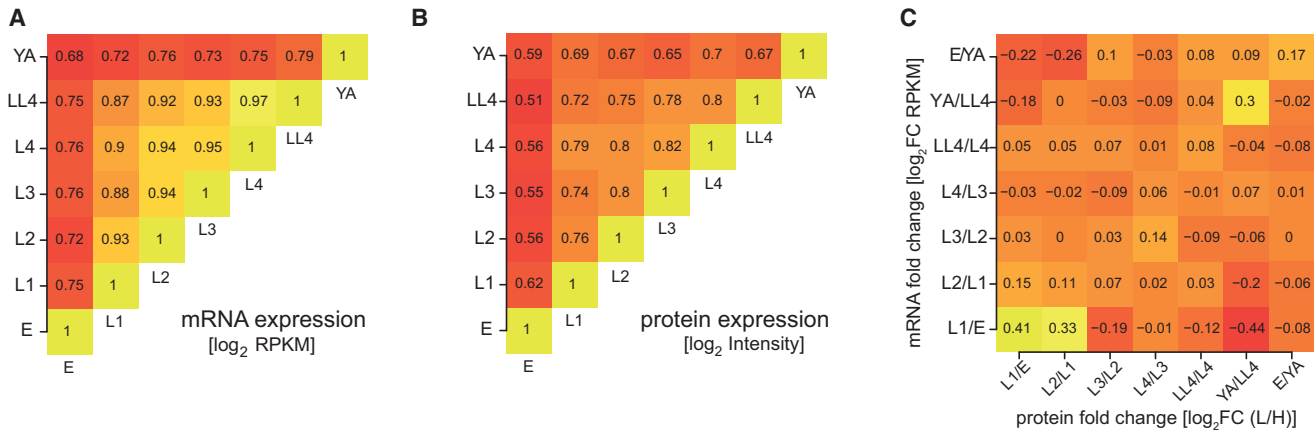


Figure 4. Correlation of Transcript and Protein Abundances Varies between Developmental Stages

The heatmaps indicate correlation between \log_2 -expression of transcripts (A) and proteins (B) for all possible pairs of stages. Protein abundance was quantified by normalized protein intensities. (C) Correlation between transcript and protein fold changes (measured by SILAC). See also Figure S3.

expression at the L3 stage and correlated temporal expression changes throughout development (Figures 5A and S4). To analyze the behavior of this group of 866 genes in more detail, we measured the expression of eight randomly selected candidates and five controls by qRT-PCRs in a 3 hr time course throughout *C. elegans* and *C. briggsae* development. Strikingly, we measured oscillating expression of these genes synchronized with larval transitions in both species (Figure 5B), whereas control genes remained overall uniformly expressed (Figure 5C). Given that oscillating expression could be validated for all eight randomly selected candidates, the majority of the 866 genes presumably show conserved expression oscillations in the two nematodes. Upon each larval transition, nematodes, like all ecdysozoans, replace their exoskeleton in a process called molting (Page and Johnstone, 2007). Noticeably, we found a 6-fold overrepresentation of molting phenotypes (Frand et al., 2005) among our cycling genes ($p < 7 \times 10^{-7}$). We note that a large number of genes oscillating throughout *C. elegans* larval development were independently discovered while this manuscript was submitted (Kim et al., 2013). However, evolutionary conservation of oscillatory expression was not addressed in this study. We compared our dynamically expressed genes to the 1,592 genes within oscillating clusters identified by Kim et al. and found that 497 out of the 866 candidates (57%) fall into one of these clusters ($p = 0$, hypergeometric test), which confirms that most of our candidates were truly oscillating.

Because we quantified protein abundance at more than three stages for only 99 out of the 866 genes, we could not reliably address the dynamics of protein expression. We note, however, that the average SILAC ratio of these proteins varies up to 2-fold between different larval stages (data not shown) suggesting dynamic regulation also on the protein level.

In summary, we discovered numerous genes with conserved oscillating mRNA levels during larval development that are enriched in molting phenotypes.

Transcript and Protein Fold Changes at the Embryo-to-Larva Transition Are Conserved

To further investigate evolutionary conservation of gene expression throughout development, we computed the cross-species correlation of mRNA and protein abundance changes at each developmental transition (Figures S5A and S5B). Both mRNA and protein fold changes correlated most strongly at the embryo-L1 transition (Spearman's correlation coefficient $\rho > 0.62$ [mRNA]/0.65 [protein]; Figure S5A). It has been postulated that gene expression is more evolutionarily constrained in developing animals compared to adults (Kalinka et al., 2010). However, we also observed well-conserved fold changes at the late L4 young adult transition ($\rho = 0.59/0.24$; Figure S5A) and speculated that these changes originate primarily from the germline, induced by the initiation of oogenesis. Analyzing transcript expression changes of germline enriched and somatic genes (Supplemental Experimental Procedures) separately revealed that these groups largely correspond to genes up- and downregulated in young adults versus late L4 larvae, respectively (Figures S5C and S5D). Hence, the well-conserved transcript fold changes at this transition are most likely induced by a conserved gene expression program in the maturing germline.

To evaluate cross-species conservation of transcript and protein fold changes comprehensively, we focused on the embryo-L1 transition, because synchronization at these stages was most reliable. We first tested if strong expression changes, i.e., transcript or protein fold changes exceeding the average fold-change variability (SD of \log_2 -fold changes), were conserved. About 15% (19%) of all genes display strong transcript (protein) expression changes with the same direction in both species, whereas only 0.7% (0.6%) of transcripts (proteins) change in opposite directions (Figure 6A). Hence, evolutionary reversion of strong expression switches is rare, and the on- or off-state of a gene is therefore well conserved.

Next, we examined conservation of fold change magnitudes. To correct for different levels of expression noise in transcript and protein quantification, we normalized by the average fold change variability. Interestingly, the majority of transcripts (68%)

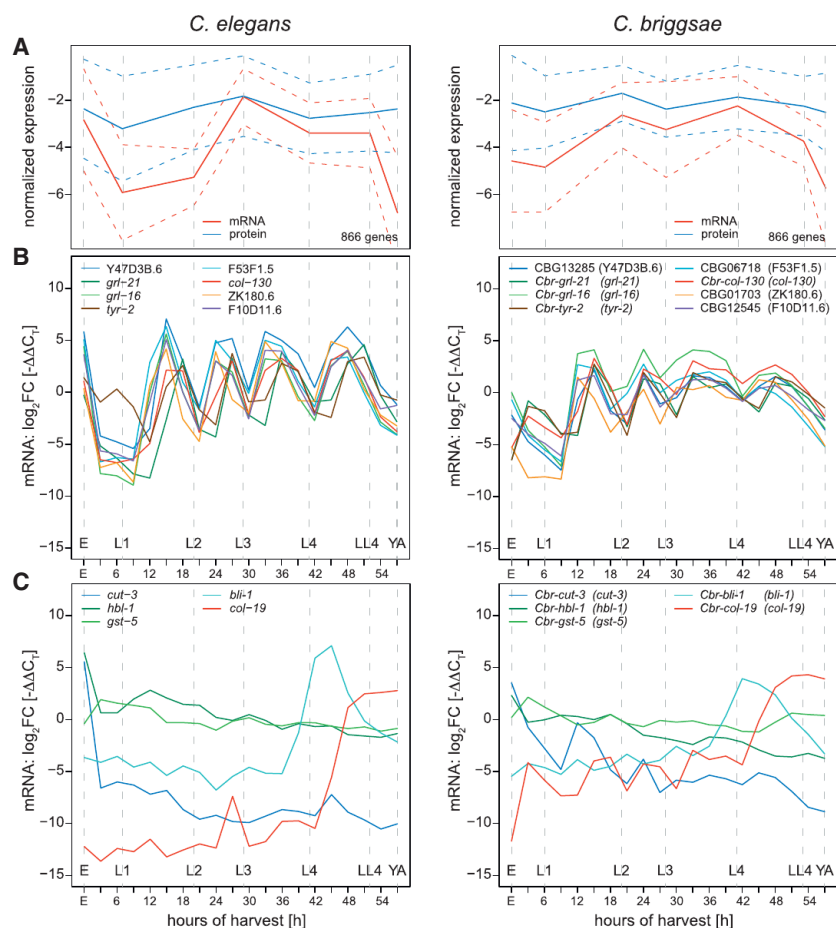


Figure 5. Transcriptome Analysis Reveals Genes with Cycling Expression

(A) Clusters of genes with dynamic expression during larval development in *C. elegans* (left) and *C. briggsae* (right). The average expression (solid line) and the SD (broken line) are shown.

(B) qRT-PCR of eight randomly selected genes for a 3 hr time series covering the entire development from embryo to young adult.

(C) qRT-PCR of five control genes with constant expression according to our data for a time series covering the entire development from embryo to young adult with samples taken every 3 hr. In (B) and (C), Y57G11C.34 was used as internal control for *C. elegans* and *Cbr-ero-1* for *C. briggsae*; $\Delta\Delta C_T$ was computed by comparing to expression in the reference sample. See also Figure S4.

scripts and proteins was found to be comparable across the entire dynamic range.

Next, we compared conservation of the fold change magnitude. We considered a transcript or protein fold change magnitude as conserved, if the variability intervals of the respective fold changes, inferred from the SD across biological replicates, overlapped between the two species (Figure S5E). We computed the fold enrichment of conserved genes above the background level obtained with shuffled orthology assignments of genes in the two species. We observed comparable fold enrichments for transcripts (2.02-fold) and proteins (2.05-

fold), confirming a similar degree of conservation on both levels at the embryo-L1 transition (Figure 6D). Thus, conservation of expression changes between both species is twice as high as expected by chance and surprisingly similar for transcripts and proteins, indicating that protein levels are not, on average, under stronger evolutionary constraint than mRNA levels.

Similar Conservation of Transcript and Protein Fold Changes at the Embryo-to-Larva Transition

Because proteins are the mediators of biological functions, whereas mRNAs are frequently considered only as coding intermediates, protein abundance could potentially be more highly conserved than transcript expression. We tested this hypothesis at the embryo-L1 transition by analyzing conservation of a given degree of up- or downregulation for transcripts or proteins. We extracted all *C. elegans* genes exceeding a given positive fold-change threshold and computed the fraction of genes with fold changes higher than the same threshold in *C. briggsae*. This fraction corresponds to the conservation probability of a given degree of upregulation. The conservation probability for downregulation was calculated accordingly (Figure 6C). To correct for expression noise, we subtracted the conservation probability obtained with shuffled orthology relations between genes in *C. elegans* and *C. briggsae*. For transcripts and proteins, the conservation probability above noise increases up to ~50% for 4-fold expression changes (Figure 6C). Conservation of tran-

servation of posttranscriptional regulation is enhanced if transcript fold changes are dampened on the protein level

Conservation of Posttranscriptional Regulation Is Enhanced if Transcript Fold Changes Are Dampened on the Protein Level

The lack of correlation between mRNA and protein level changes throughout development (Figure 4C) in each species suggests that protein abundance is controlled by substantial regulation on the posttranscriptional and/or (post)translational level, hereafter summarized as posttranscriptional regulation. To investigate evolutionary conservation of this component, we split the ensemble of all *C. elegans* genes into groups with up- and down-regulated transcripts at the embryo-L1 transition and subdivided these groups into genes whose protein fold changes exceed their transcript fold changes (amplifying posttranscriptional regulation), and genes whose protein fold changes buffered their transcript fold changes (dampening posttranscriptional regulation). To assess evolutionary conservation, we computed the fraction of *C. briggsae* genes that fall into the same subgroup

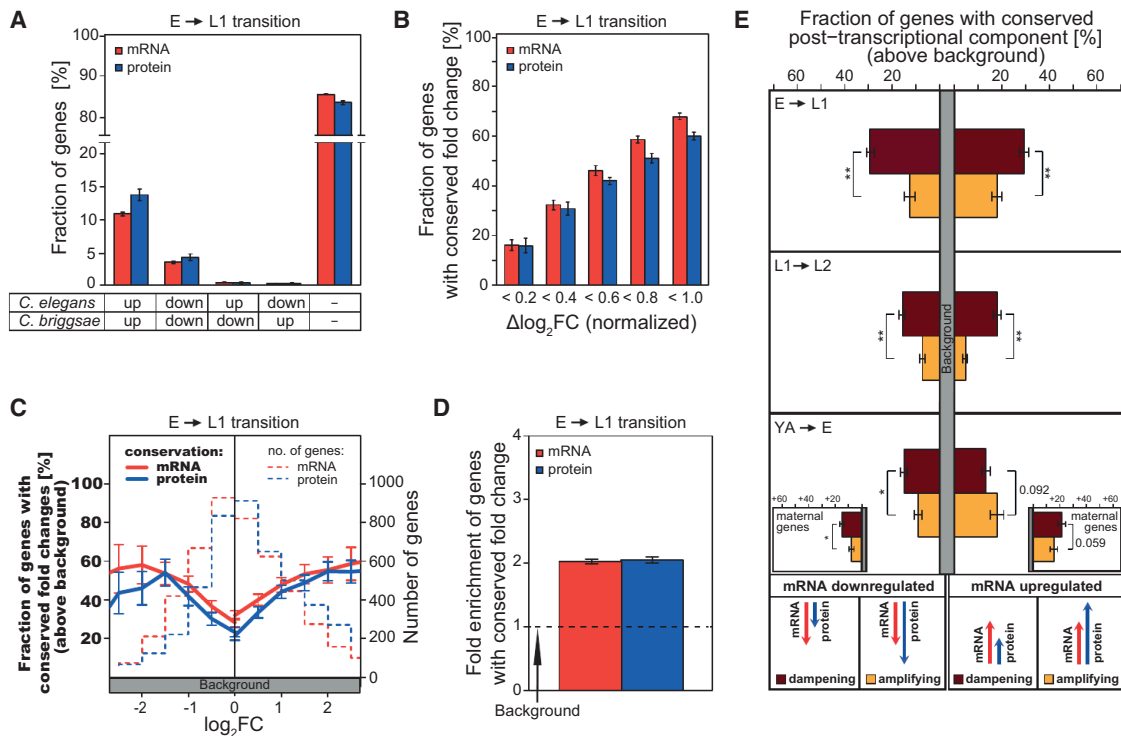


Figure 6. Cross-Species Comparison of Transcript and Protein Fold Changes at the Embryo-L1 Transition between *C. elegans* and *C. briggsae*

(A) Fraction of genes with conserved and nonconserved pronounced up- or downregulation, exceeding the fold change SD for proteins (3.0-fold) or transcripts (4.2-fold). Error bars are based on random counting statistics.

(B) Fraction of genes with a maximum \log_2 -fold-change difference between *C. elegans* and *C. briggsae* after normalizing fold changes by the SD to account for different dynamic ranges of transcript and protein fold changes. Error bars indicate the SE inferred by bootstrapping.

(C) Fraction of genes with conserved minimal up- or downregulation. For all genes with a fold change higher (right) or lower (left) than a given threshold in *C. elegans*, the fraction of genes with a fold change higher or lower than the same threshold in *C. briggsae* was computed. Background conservation has been subtracted. Error bars are based on random counting statistics.

(D) Fold enrichment of genes with strictly conserved transcript or protein fold change magnitudes, measured by overlapping intervals of variability. Error bars indicate the SE inferred by bootstrapping.

(E) Fraction of genes with a conserved posttranscriptional fold change component. For all *C. elegans* genes with a positive (negative) \log_2 -fold difference between protein and transcript fold changes, the fraction of genes with a positive (negative) \log_2 -fold difference in *C. briggsae* was computed. Background conservation has been subtracted. Conservation is shown for up- and downregulated transcripts with dampening and amplifying posttranscriptional regulation. The inset displays the conservation for maternal genes only. Error bars are based on random counting statistics (* $p < 0.05$, ** $p < 0.001$).

See also Figure S5.

like in *C. elegans*. After subtracting background conservation obtained for shuffled orthology relations, conservation increased up to 30% (Figure 6E). These data provide evidence that post-transcriptional control is highly conserved during metazoan development. Conservation is significantly enhanced for genes subject to posttranscriptional dampening, whereas amplifying changes are less well conserved.

In contrast, we observed that dampening and amplifying post-transcriptional regulation were equally well conserved at the young adult-to-embryo transition for transcripts upregulated in embryos. The embryonic transcriptome is composed of maternal genes and zygotic genes that are transcribed by the embryo after zygotic genome activation. We tested if maternal and zygotic genes (see Supplemental Experimental Procedures; Table S5) have different conserved modes of posttranscriptional regulation. We observed that dampening regulation of maternal mRNAs was more highly conserved than amplifying regulation (Figure 6E),

whereas zygotic mRNAs displayed enhanced conservation of amplifying posttranscriptional regulation (Figure S5F).

In summary, we find that strong positive and negative transcript expression changes are dampened by posttranscriptional regulation, potentially enforcing robust protein levels throughout longer developmental timescales. In the embryo, however, we observe preferential conservation of amplifying posttranscriptional gene regulation of genes transcribed in the embryo, which may be essential to ensure fast accumulation of crucial regulators of embryogenesis.

Fold Change Conservation at the Embryo-L1 Transition Coincides with Conservation of Exonic and 3' UTR Sequence

To compare conservation of mRNA and protein fold changes to conservation of regulatory sequence at the embryo-L1 transition, we downloaded three-way alignments of *C. elegans*,

C. briggsae, and *C. remanei* from the UCSC genome browser (Dreszer et al., 2012). We extracted alignments for promoter sequences (1 kb upstream), for 3' UTRs (Mangone et al., 2010) and for all exons. We only considered mRNAs and proteins, which change at least 2-fold at this transition in *C. elegans* and assessed conservation of up- or downregulation in *C. briggsae*. We then compared sequence conservation of genes with conserved and nonconserved fold changes. We also included genes with a conserved posttranscriptional component into this comparison (Figure S5G). Genes with conserved mRNA fold changes do not display significantly increased sequence conservation. Genes with conserved protein fold changes, on the other hand, are overall significantly more conserved and, in particular, have more highly conserved 3' UTRs, suggesting enrichment in binding sites for RNA binding proteins or microRNAs. Genes with conserved posttranscriptional component also have more highly conserved exons and 3' UTRs, with the only exception of downregulated transcripts subject to dampening regulation. However, among the nonconserved genes in this group are 125 genes with conserved but only 36 genes with nonconserved protein fold changes, explaining the high sequence conservation.

In summary, the observed patterns of conservation of expression fold changes are consistent with trends in sequence conservation.

Increased Evolutionary Fold Change Variability Identifies a Putative Target of Adaptive Evolution

Finally, we searched for classes of genes with strongly reduced or enhanced fold change conservation. Regulatory factors are presumably well conserved, because mutations of *trans*-acting factors can affect whole gene networks. We extracted a list of transcription factors from the literature (Haerty et al., 2008) and analyzed evolutionary variability of their expression changes at the embryo-L1 transition. The 761 (44) transcription factors with measured transcript (protein) expression changes show significantly less cross-species fold change variability than random sets of genes. On the transcript (protein) level, we observed a 16% (33%) reduction (Figure S6A), consistent with enhanced sequence conservation of transcription factors (Haerty et al., 2008).

Next, we explored genes with reduced fold change conservation and validated a subset of these by qRT-PCRs (Figure S6B). Among those were genes involved in an insulin/insulin-like growth factor (IGF) signaling pathway. The main downstream target of this pathway, DAF-16, is a deeply conserved FOXO-family transcription factor regulating lifespan in flies, worms, and mammals (Tatar et al., 2003). Strikingly, we observed a 4-fold reduction of *daf-16* transcript expression, aggregated across all isoforms, in *C. briggsae* embryos compared to *C. elegans* embryos, whereas larval expression was comparable in both species (Figure S6C). We successfully validated RNA-seq-based embryo-L1 fold changes by qRT-PCR for *daf-16* and four additional differentially regulated genes (*daf-12*, *daf-7*, *syd-2*, *ttr-1*), which are known DAF-16 targets (Figure 7A). We did not detect DAF-16 at the protein level in our mass spectrometry (MS) analysis, perhaps due to relatively low abundance. Therefore, to quantify DAF-16 protein levels, we used a poly-

clonal antibody directed against the C-terminal region of the protein, which is shared by all known isoforms and highly conserved in both species (78% amino acid identity). Western blotting indicated that DAF-16 protein levels are reduced in *C. briggsae* embryos compared to *C. elegans* (Figure 7B), whereas protein abundance increases in both species at the embryo-L1 transition to comparable level. Together, with the observation that mRNA levels remain unchanged at this transition in *C. elegans*, these data suggest amplifying posttranscriptional regulation of *daf-16*. To which degree the difference between mRNA and protein fold changes has evolved cannot be reliably assessed, given that the western method is not quantitative enough to determine precise fold changes. In any case, our data clearly suggest that differences in embryonic *daf-16* mRNA expression and protein abundance have evolved between both species. Next, we extracted a list of 446 predicted DAF-16 targets from the literature (Murphy et al., 2003). For these genes, we observed significantly increased evolutionary variability of transcript and protein fold changes in comparison to random sets of genes ($p < 0.001$, Figure 7C). To test whether this increase is driven by *daf-16*, we performed an RNAi-mediated knockdown of *daf-16* in *C. elegans* embryos (Figure 7D) and globally measured protein fold changes compared to wild-type L1 larvae. Interestingly, after knockdown of *daf-16* in *C. elegans*, protein fold changes at the embryo-L1 transition were slightly more correlated to *C. briggsae* ($R^2_{\text{RNAi}} = 0.50$ versus $R^2_{\text{control}} = 0.47$). Consistently, the distribution of residuals was shifted significantly ($p < 0.004$) to lower values for the *daf-16* knockdown versus the control sample (Figure 7E). Hence, the *daf-16* knockdown overall reduces the cross-species variability. Moreover, reduced expression of *daf-16* in *C. briggsae* embryos explains a fraction of the global proteome changes between the two species. To investigate whether the set of predicted DAF-16 targets accounts for this observation, we compared the difference in embryo-L1 \log_2 -fold changes between control and *daf-16* knockdown samples to the difference between *C. elegans* and *C. briggsae* wild-type samples. If both numbers were either positive or negative for a given gene, the cross-species fold change modulation is consistent with differential expression of *daf-16*. In contrast to the ensemble of all genes, with equal numbers of consistent and inconsistent fold changes, DAF-16 targets comprise almost twice as many consistent as inconsistent fold changes (Figure 7F). We could reproduce these observations with an independent biological replicate (Figures S6D–S6F). These data suggest that the enhanced expression divergence of DAF-16 targets is likely a result of differential expression of *daf-16* itself and that the *daf-16* regulatory network is a possible target of adaptive evolution.

DISCUSSION

In this study, we investigated joint dynamics and evolutionary conservation of transcript and protein abundance during development of a well-studied metazoan model organism on a genome-wide scale. Only a handful of studies have quantified developmental protein fold changes in *C. elegans* on a large scale, either using 2D-gel electrophoresis (Tabuse et al., 2005) or metabolic ^{15}N labeling combined with mass spectrometry

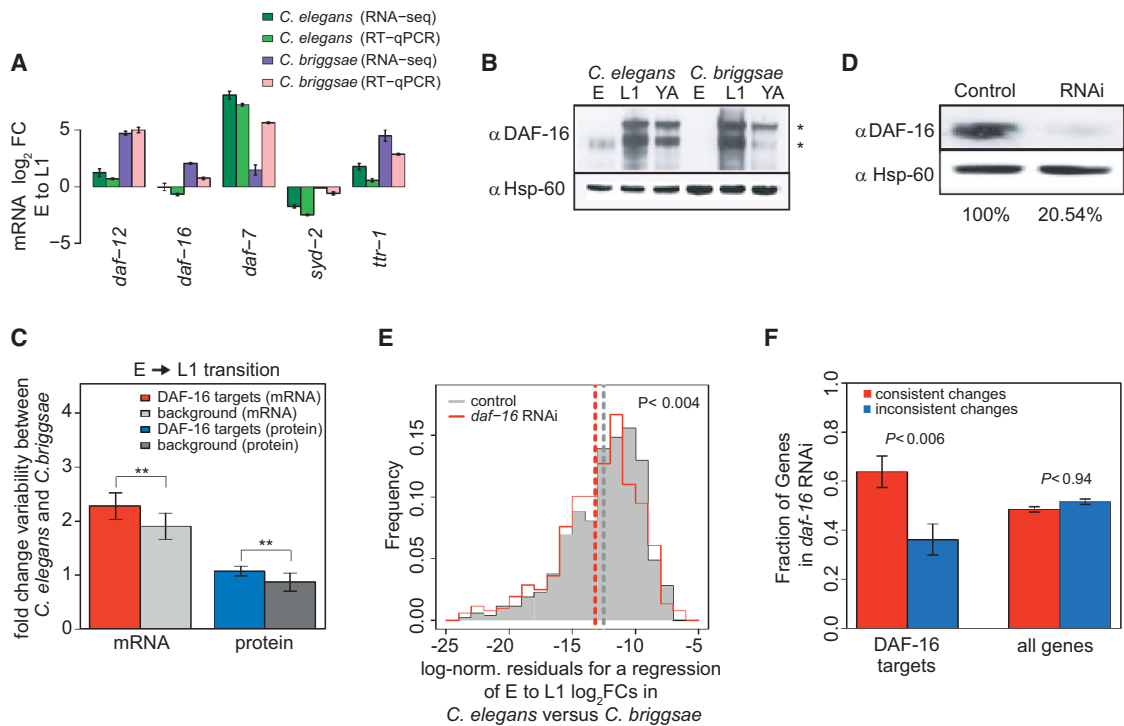


Figure 7. Identification of a Pathway with Enhanced Expression Divergence at the Embryo-L1 Transition

(A) Validation of RNA-seq-based quantification by qRT-PCR for *daf-16* and four known DAF-16 targets with diverged expression changes between *C. elegans* and *C. briggsae* at the embryo-L1 transition. qRT-PCR was performed for individual biological replicate samples. Error bars represent the SD across replicates ($n \geq 3$).

(B) Western blot analysis of DAF-16 protein abundance in *C. elegans* and *C. briggsae* embryos (E), L1 larvae (L1), and young adults (YA). Hsp-60 was used as loading control and for normalization. *Multiple bands represent expression of DAF-16 isoforms.

(C) Average of the absolute \log_2 -fold-change difference between *C. elegans* and *C. briggsae* for DAF-16 targets and random groups of nontargets. Mean and SE are inferred by bootstrapping (** $p < 0.001$).

(D) Western blot analysis of DAF-16 after RNAi-mediated knockdown of *daf-16*. Protein knockdown was quantified as a percentage of the control (set as 100%). Hsp-60 was used as a loading control and for normalization.

(E) Distribution of the logarithm of squared normalized residuals from a regression of protein \log_2 -fold changes between *C. elegans* and *C. briggsae*. Upon knockdown of *daf-16* in *C. elegans* embryos, the distribution (red line) is shifted compared to a control transfection (gray) ($p < 0.004$, Wilcoxon rank sum test).

(F) Genes with differences in \log_2 -fold changes between *daf-16* knockdown and control *C. elegans* embryos that exhibit consistent (red) or inconsistent (blue) differences between *C. elegans* and *C. briggsae*. Data are shown for all genes and for the subset of predicted DAF-16 targets (Murphy et al., 2003). Error bars are based on random counting statistics. A hypergeometric test was performed to assess an enrichment of consistent fold changes. See also Figure S6.

(Geillinger et al., 2012), and these studies were limited to a fold-change determination for a few hundred proteins. Tabuse et al. (2005) measured expression changes for a small number of proteins at the embryo-to-L1 transition and the fold change magnitude compares very well to our data ($R^2 = 0.8$; Figure 1E).

Evolution of transcript expression during *Caenorhabditis* embryogenesis was previously investigated in great detail (Levin et al., 2012), and, while our study was under review, a comparison of transcript expression and translation rate changes at a specific developmental transition was published (Stadler and Fire, 2013). Stadler et al. used ribosome profiling to compare changes in ribosome occupancy to transcript expression changes upon the L1 diapause exit. In contrast to protein quantification by mass spectrometry, however, this approach only reveals changes in ribosome association of mRNAs, not protein abundance changes, which are also affected by (post)translational modifications. Nonetheless, this study also

provides evidence for important posttranscriptional regulation at a different developmental transition.

We focused on the embryo-L1 transition to examine general properties of posttranscriptional versus transcriptional regulation. For most genes, protein abundance changes could not be explained by changes of the transcript level, suggesting ubiquitous posttranscriptional regulation that could be exerted by factors such as microRNAs or RNA binding proteins or a consequence of enzymatic protein modifications directly effecting protein levels.

At this transition we could also directly compare evolutionary conservation of transcript and protein fold changes. In previous studies, enhanced conservation of protein versus transcript abundance was derived for mixtures of homogenized whole animals of various developmental stages (Schimpf et al., 2009; Weiss et al., 2010). In contrast, our analysis suggests that transcript and protein fold changes are conserved to a very similar

degree. In order to arrive at this conclusion, we had to account for different levels of technical noise in protein and mRNA quantification. To address a possible ascertainment bias in our conservation measurements due to a selection of specific genes by our *C. briggsae* annotation, we computed fold change conservation of one-to-one orthologs inferred from recently published *C. briggsae* gene models (Uyar et al., 2012). This annotation was highly similar to our own gene models, and fold change conservation was invariant (Figures S5H and S5I).

Our finding implies that regulation on the level of mRNA and protein is of similar functional importance during metazoan development. This may seem surprising given that proteins are the functional products of most genes. However, posttranscriptional regulation presumably modulates protein levels produced from invariant mRNA levels in a developmental stage- or condition-specific way. The mRNA fold change as primary input for protein production is therefore read out in a context-dependent way and hence presumably under equally strong evolutionary constraint as the protein fold change.

Our results further include that the fold change magnitude of mRNAs and proteins is remarkably well conserved during ~30 million years of evolution separating the two nematodes. Therefore, not only the on- or off-state of a gene and the architecture of the regulatory circuits appear to be exposed to selective pressure, as postulated for gene regulatory networks during metazoan embryonic development (Peter and Davidson, 2011), but also the precise level of temporal up- or downregulation between developmental stages.

The posttranscriptional component of protein fold changes was also well conserved, in particular, if transcript fold changes were dampened on the protein level. We cannot rule out that this observation is partially due to technical reasons such as systematic underestimation of protein fold changes. However, predominance of amplifying regulation for zygotically transcribed genes and our SILAC mixing experiments argue against this possibility. Hence, gene regulation at the posttranscriptional level is ubiquitous and functionally relevant during animal development, in particular, when protein fold changes are buffered. Furthermore, it is thought that for microRNAs and most RNA binding proteins, which bind 3' UTRs of mature mRNAs, the regulatory effect on translation is negative.

Finally, we used our data to screen for pathways that could be a target of adaptive evolution. Among genes with enhanced cross-species variability, we recovered a number of target genes of DAF-16, a central regulator of the insulin/IGF pathway in nematodes (Murphy et al., 2003). Knocking down *daf-16* in embryos changed the gene expression profile of *C. elegans* toward the profile of *C. briggsae*. Thus, some of the evolutionary expression changes between both species seem to be a direct consequence of different DAF-16 levels in the embryo. Although the functional consequence of this difference remains to be explored, an adaptive evolution of the insulin/IGF pathway is conceivable because this pathway regulates stress resistance (Tatar et al., 2003; Baumeister et al., 2006) and is therefore likely affected by the environment and life conditions specific to each species.

In conclusion, our findings underscore the relevance of a combined analysis of transcript and protein levels when

studying gene regulation during animal development. We provide all of our expression data as a valuable resource to the research community and implemented a publicly available database with graphical representations of all developmental transcript and protein expression profiles at <http://elegans.mdc-berlin.de>.

EXPERIMENTAL PROCEDURES

Worm Culture and Stable Isotope Labeling and Sample Preparation

C. elegans wild-type strain N2 and *C. briggsae* wild-type strain AF16 were used in this study, cultured as described previously (Brenner, 1974). *C. elegans* and *C. briggsae* were metabolically labeled by feeding either light (Lys0; $^{12}\text{C}_6$, $^{14}\text{N}_2$) or heavy (Lys8; $^{13}\text{C}_6$, $^{15}\text{N}_2$) SILAC-labeled *E. coli* (Hanke et al., 2008) for at least two generations. Light-labeled staged animals were collected at different time points. An asynchronous reference sample (containing all stages) was produced using heavy-labeled bacteria. Detailed information can be found in the Supplemental Information.

Mass-Spectrometry-Based Protein Quantification

Light and heavy mixtures of SILAC protein extracts (150 μg per sample) were fractionated by SDS-PAGE, in-gel digested using Lysyl endopeptidase (LysC) and cleaned by STAGE tip purification (Rappsilber et al., 2003). Online liquid chromatography-tandem mass spectrometry (LC-MS/MS) analysis was performed essentially as previously described (Selbach et al., 2008), using 10%–60% acetonitril gradients (240 or 360 min) and an LTQ-Orbitrap hybrid mass spectrometer (Thermo Fisher Scientific). The MaxQuant software package and an in-house curated database for *C. elegans*, *C. briggsae* (see the Experimental Procedures), and *E. coli* (MG1655) plus common contaminants (e.g., trypsin, BSA) (v.1.0.13.13) was used to identify and quantify proteins (Cox and Mann, 2008; Cox et al., 2009). False discovery rate was set to 5% (FDR of 5) at both the peptide and protein level (further details are found in the Supplemental Information).

Proteomic Data Validation by Western Blotting

Total protein (20 μg) was separated by SDS-PAGE, blotted onto polyvinylidene fluoride membrane, and analyzed by immunodetection (primary antibodies and GFP strains are listed in the Supplemental Experimental Procedures) using chemiluminescence (PerkinElmer). Films were scanned and quantitative analysis was performed using ImageJ software. TBA-2 or HSP-60 was used for normalization (as indicated).

RNA Isolation and RNA-Seq Library Constructions

Total RNA isolation was performed with TRIzol Reagent (Invitrogen) by following the manufacturer's instructions. PolyA mRNA was purified from 10 μg of total RNA using the Dynabeads mRNA Purification Kit for mRNA Purification from Total RNA (Invitrogen). Details of the library preparation are outlined in the Supplemental Experimental Procedures. Cluster generation and sequencing was performed on the Illumina cluster station and Genome Analyzer Ix according to the manufacturer's instructions. Read lengths were 76 bases.

All details concerning sample collection, data generation, processing, analysis, and validation can be found in the Supplemental Information.

ACCESSION NUMBERS

Data analyzed herein have been deposited in the NCBI Gene Expression Omnibus under accession number GSE53359.

SUPPLEMENTAL INFORMATION

Supplemental Information includes Supplemental Experimental Procedures, six figures, and five tables and can be found with this article online at <http://dx.doi.org/10.1016/j.celrep.2014.01.001>.

AUTHOR CONTRIBUTIONS

D.G. carried out all computational experiments and most of the data analysis. M.K. performed mass spectrometry experiments and western blots. N.T. staged worms and performed RNA measurements. N.T., M.K., and M. Stoeckius developed the SILAC worm. M. Stoeckius performed RNAi and DAF-16 experiments. M. Selbach supervised M.K., N.R. supervised D.G., N.T., and M. Stoeckius. D.G. wrote the paper with guidance of N.R. and input from all other authors.

ACKNOWLEDGMENTS

We are grateful to R. Lin for providing us with the TX189[P(oma-1)::oma-1::GFP] strain and to T. Schedl for providing us with the BS1080[P(glp-4)::glp-4::GFP] strain. All other nematode strains used in this project were provided by the *Caenorhabditis* Genetics Center, which is funded by the National Center for Research Resources. D.G. received funding from the European Community's Seventh Framework Programme (FP7/2007-2013) under grant agreement HEALTH-F4-2010-241504 (EURATRANS). We thank all members of the N.R. lab for discussions and support. We thank S. Mackowiak for setting up our online expression database. We acknowledge C. Langnick and M. Feldkamp from the Wei Chen lab (BIMSB/MDC) for the sequencing runs. M. Stoeckius thanks BIMSB/NYU International PhD program for funding (BMBF funding ID 0315362). We thank F. Piano and K. Gunsalus for constructive discussions during the beginning of the project.

Received: September 22, 2013

Revised: November 14, 2013

Accepted: December 31, 2013

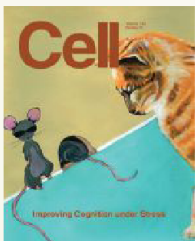
Published: January 23, 2014

REFERENCES

- Baumeister, R., Schaffitzel, E., and Hertweck, M. (2006). Endocrine signaling in *Caenorhabditis elegans* controls stress response and longevity. *J. Endocrinol.* **190**, 191–202.
- Brenner, S. (1974). The genetics of *Caenorhabditis elegans*. *Genetics* **77**, 71–94.
- Carroll, S.B. (2008). Evo-devo and an expanding evolutionary synthesis: a genetic theory of morphological evolution. *Cell* **134**, 25–36.
- Cox, J., and Mann, M. (2008). MaxQuant enables high peptide identification rates, individualized p.p.b.-range mass accuracies and proteome-wide protein quantification. *Nat. Biotechnol.* **26**, 1367–1372.
- Cox, J., Matic, I., Hilger, M., Nagaraj, N., Selbach, M., Olsen, J.V., and Mann, M. (2009). A practical guide to the MaxQuant computational platform for SILAC-based quantitative proteomics. *Nat. Protoc.* **4**, 698–705.
- Cutter, A.D. (2008). Divergence times in *Caenorhabditis* and *Drosophila* inferred from direct estimates of the neutral mutation rate. *Mol. Biol. Evol.* **25**, 778–786.
- de Sousa Abreu, R., Penalva, L.O., Marcotte, E.M., and Vogel, C. (2009). Global signatures of protein and mRNA expression levels. *Mol. Biosyst.* **5**, 1512–1526.
- Domazet-Lošo, T., and Tautz, D. (2010). A phylogenetically based transcriptome age index mirrors ontogenetic divergence patterns. *Nature* **468**, 815–818.
- Dreszer, T.R., Karolchik, D., Zweig, A.S., Hinrichs, A.S., Raney, B.J., Kuhn, R.M., Meyer, L.R., Wong, M., Sloan, C.A., Rosenbloom, K.R., et al. (2012). The UCSC Genome Browser database: extensions and updates 2011. *Nucleic Acids Res.* **40** (Database issue), D918–D923.
- Frand, A.R., Russel, S., and Ruvkun, G. (2005). Functional genomic analysis of *C. elegans* molting. *PLoS Biol.* **3**, e312.
- Fredens, J., Engholm-Keller, K., Giessing, A., Pultz, D., Larsen, M.R., Højrup, P., Møller-Jensen, J., and Færgeman, N.J. (2011). Quantitative proteomics by amino acid labeling in *C. elegans*. *Nat. Methods* **8**, 845–847.
- Geillinger, K.E., Kuhlmann, K., Eisenacher, M., Meyer, H.E., Daniel, H., and Spanier, B. (2012). Dynamic changes of the *Caenorhabditis elegans* proteome during ontogenesis assessed by quantitative analysis with ¹⁵N metabolic labeling. *J. Proteome Res.* **11**, 4594–4604.
- Gerstein, M.B., Lu, Z.J., Van Nostrand, E.L., Cheng, C., Arshinoff, B.I., Liu, T., Yip, K.Y., Robilotto, R., Rechtsteiner, A., Ikegami, K., et al.; modENCODE Consortium (2010). Integrative analysis of the *Caenorhabditis elegans* genome by the modENCODE project. *Science* **330**, 1775–1787.
- Haerty, W., Artieri, C., Khezri, N., Singh, R.S., and Gupta, B.P. (2008). Comparative analysis of function and interaction of transcription factors in nematodes: extensive conservation of orthology coupled to rapid sequence evolution. *BMC Genomics* **9**, 399.
- Hanke, S., Besir, H., Oesterheld, D., and Mann, M. (2008). Absolute SILAC for accurate quantitation of proteins in complex mixtures down to the attomole level. *J. Proteome Res.* **7**, 1118–1130.
- Heck, A.J.R., and Krijgsvel, J. (2004). Mass spectrometry-based quantitative proteomics. *Expert Rev. Proteomics* **1**, 317–326.
- Huang, D.W., Sherman, B.T., Zheng, X., Yang, J., Imamichi, T., Stephens, R., and Lempicki, R.A. (2009). Extracting biological meaning from large gene lists with DAVID. *Curr. Protoc. Bioinformatics* **13**, 13.11.
- Johnstone, I.L., and Barry, J.D. (1996). Temporal reiteration of a precise gene expression pattern during nematode development. *EMBO J.* **15**, 3633–3639.
- Kalinka, A.T., Varga, K.M., Gerrard, D.T., Preibisch, S., Corcoran, D.L., Jarrells, J., Ohler, U., Bergman, C.M., and Tomancak, P. (2010). Gene expression divergence recapitulates the developmental hourglass model. *Nature* **468**, 811–814.
- Kim, Dh., Grün, D., and van Oudenaarden, A. (2013). Dampening of expression oscillations by synchronous regulation of a microRNA and its target. *Nat. Genet.* **45**, 1337–1344.
- Krüger, M., Moser, M., Ussar, S., Thievensen, I., Luber, C.A., Forner, F., Schmidt, S., Zanivan, S., Fässler, R., and Mann, M. (2008). SILAC mouse for quantitative proteomics uncovers kindlin-3 as an essential factor for red blood cell function. *Cell* **134**, 353–364.
- Larance, M., Bailly, A.P., Pourkarimi, E., Hay, R.T., Buchanan, G., Coulthurst, S., Xirodimas, D.P., Gartner, A., and Lamond, A.I. (2011). Stable-isotope labeling with amino acids in nematodes. *Nat. Methods* **8**, 849–851.
- Levin, M., Hashimshony, T., Wagner, F., and Yanai, I. (2012). Developmental milestones punctuate gene expression in the *Caenorhabditis* embryo. *Dev. Cell* **22**, 1101–1108.
- Looso, M., Borchardt, T., Krüger, M., and Braun, T. (2010). Advanced identification of proteins in uncharacterized proteomes by pulsed in vivo stable isotope labeling-based mass spectrometry. *Mol. Cell. Proteomics* **9**, 1157–1166.
- Mangoni, M., Manoharan, A.P., Thierry-Mieg, D., Thierry-Mieg, J., Han, T., Mackowiak, S.D., Mis, E., Zegar, C., Gutwein, M.R., Khivansara, V., et al. (2010). The landscape of *C. elegans* 3'UTRs. *Science* **329**, 432–435.
- Moss, E.G. (2007). Heterochronic genes and the nature of developmental time. *Curr. Biol.* **17**, R425–R434.
- Murphy, C.T., McCarroll, S.A., Bargmann, C.I., Fraser, A., Kamath, R.S., Ahringer, J., Li, H., and Kenyon, C. (2003). Genes that act downstream of DAF-16 to influence the lifespan of *Caenorhabditis elegans*. *Nature* **424**, 277–283.
- Ong, S.-E., Blagoev, B., Kratchmarova, I., Kristensen, D.B., Steen, H., Pandey, A., and Mann, M. (2002). Stable isotope labeling by amino acids in cell culture, SILAC, as a simple and accurate approach to expression proteomics. *Mol. Cell. Proteomics* **1**, 376–386.
- Page, A.P., and Johnstone, I.L. (2007). The cuticle. *WormBook* **19**, 1–15.
- Peter, I.S., and Davidson, E.H. (2011). Evolution of gene regulatory networks controlling body plan development. *Cell* **144**, 970–985.
- Rappsilber, J., Ishihama, Y., and Mann, M. (2003). Stop and go extraction tips for matrix-assisted laser desorption/ionization, nanoelectrospray, and LC/MS sample pretreatment in proteomics. *Anal. Chem.* **75**, 663–670.

- Ruvkun, G., and Giusto, J. (1989). The *Caenorhabditis elegans* heterochronic gene *lin-14* encodes a nuclear protein that forms a temporal developmental switch. *Nature* 338, 313–319.
- Schrimpf, S.P., Weiss, M., Reiter, L., Ahrens, C.H., Jovanovic, M., Malmström, J., Brunner, E., Mohanty, S., Lercher, M.J., Hunziker, P.E., et al. (2009). Comparative functional analysis of the *Caenorhabditis elegans* and *Drosophila melanogaster* proteomes. *PLoS Biol.* 7, e48.
- Schwanhäusser, B., Busse, D., Li, N., Dittmar, G., Schuchhardt, J., Wolf, J., Chen, W., and Selbach, M. (2011). Global quantification of mammalian gene expression control. *Nature* 473, 337–342.
- Selbach, M., Schwanhäusser, B., Thierfelder, N., Fang, Z., Khanin, R., and Rajewsky, N. (2008). Widespread changes in protein synthesis induced by microRNAs. *Nature* 455, 58–63.
- St Johnston, D., and Nüsslein-Volhard, C. (1992). The origin of pattern and polarity in the *Drosophila* embryo. *Cell* 68, 201–219.
- Stadler, M., and Fire, A. (2013). Conserved translational remodeling in nematode species executing a shared developmental transition. *PLoS Genet.* 9, e1003739.
- Stein, L.D., Bao, Z., Blasiar, D., Blumenthal, T., Brent, M.R., Chen, N., Chinwalla, A., Clarke, L., Clee, C., Coghlan, A., et al. (2003). The genome sequence of *Caenorhabditis briggsae*: a platform for comparative genomics. *PLoS Biol.* 1, E45.
- Sulston, J.E., Schierenberg, E., White, J.G., and Thomson, J.N. (1983). The embryonic cell lineage of the nematode *Caenorhabditis elegans*. *Dev. Biol.* 100, 64–119.
- Sury, M.D., Chen, J.-X., and Selbach, M. (2010). The SILAC fly allows for accurate protein quantification in vivo. *Mol. Cell. Proteomics* 9, 2173–2183.
- Tabuse, Y., Nabetani, T., and Tsugita, A. (2005). Proteomic analysis of protein expression profiles during *Caenorhabditis elegans* development using two-dimensional difference gel electrophoresis. *Proteomics* 5, 2876–2891.
- Tatar, M., Bartke, A., and Antebi, A. (2003). The endocrine regulation of aging by insulin-like signals. *Science* 299, 1346–1351.
- Uyar, B., Chu, J.S.C., Vergara, I.A., Chua, S.Y., Jones, M.R., Wong, T., Baillie, D.L., and Chen, N. (2012). RNA-seq analysis of the *C. briggsae* transcriptome. *Genome Res.* 22, 1567–1580.
- Weiss, M., Schrimpf, S., Hengartner, M.O., Lercher, M.J., and von Mering, C. (2010). Shotgun proteomics data from multiple organisms reveals remarkable quantitative conservation of the eukaryotic core proteome. *Proteomics* 10, 1297–1306.
- Zhao, Z., Boyle, T.J., Bao, Z., Murray, J.I., Mericle, B., and Waterston, R.H. (2008). Comparative analysis of embryonic cell lineage between *Caenorhabditis briggsae* and *Caenorhabditis elegans*. *Dev. Biol.* 314, 93–99.

SHIFT YOUR PARADIGM



**Think you don't have a Cell paper?
Think again.**

If you've got an exciting paper that changes the way we think about a problem, submit it. We'd like to work with you.

PROTECT

Detect, eliminate and prevent cell culture contamination



Before mycoplasma contamination compromises your cell cultures, stop it. Biological Industries has everything you need.

Disinfect incubators, sterile benches and other surfaces regularly with our pharmacidal spray.

- Prevents contamination and growth of fungi, bacteria, mycoplasma and viruses
- Non-toxic, biodegradable and non-corrosive

Keep water baths clean and clear.

- **Aquaguard-1:** for disinfecting water baths of CO₂ incubators
- **Aquaguard-2:** for disinfecting various kinds of water baths from bacteria and fungi

Detect suspected contamination with our EZ-PCR Mycoplasma Test Kit.

- Complete, ready-to-use—including TAQ polymerase and positive template control cultures
- High sensitivity and selectivity—selective primers for over 20 species of mycoplasma DNA
- Results in less than 5 hours

Treat mycoplasma contamination effectively when it happens.

- **BIOMYC-1:** based on the antibiotic tiamutin
- **BIOMYC-2:** based on the antibiotic minocycline
- **BIOMYC-3:** based on the antibiotic ciprofloxacin

Protect your cell cultures 24/7 with mycoplasma detection and treatment products from Biological Industries. Available in the U.S. from Rainbow Scientific, Inc.



Download brochure



Visit www.shoprainbowsscientific.com for easy online ordering or call 860.298.8382.



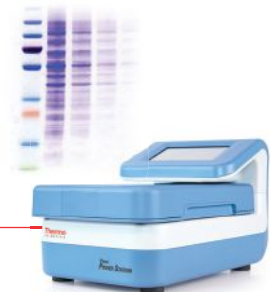
BI
Biological Industries
Culture of Excellence
www.bioind.com

Leading North American supplier of state-of-the-art products

more power to you.

Thermo Scientific™ Pierce™ Power System lets you power through two essential protein detection steps with one efficient system! Save hours in coomassie staining and protein transfer from gels to membranes without compromising the quality of your results. Efficiently stain or transfer protein gels in about 10 minutes with one system. Intuitive, color LCD touchscreen interface and pre-programmed methods make both coomassie staining and protein transfer easy. One power station + two cassettes = powerful possibilities.

• Request a demo at thermoscientific.com/powersystem



Thermo Scientific Pierce Power Stainer

Coomassie staining and destaining of proteins in about 10 minutes



Thermo Scientific Pierce Power Blotter

Transfer proteins in 5-10 minutes

